Environmental magnetism of eastern Mediterranean sediments and aeolian dust flux changes over orbital timescales

By

Yao Qian

A thesis submitted for the degree of
Doctor of Philosophy of
The Australian National University

March 2021

Declaration

The work presented in this thesis was carried out while I was a full-time student at the Research School of Earth Sciences, at the Australian National University, between October 2016 and March 2021. Except where mentioned in the text, the research described here is my own. No part of this thesis has been submitted to any other university or similar institution.

Yao Qian

March 2021

Acknowledgements

I would like to thank the following people, without whom I would not have been able to complete my study at the Australian National University (ANU). Firstly, I express my thanks to my primary supervisor, Andrew Roberts. Thanks for providing me an opportunity to join the Black Mountain paleomagnetic group at ANU and for your continuous guidance, great patience and timely feedback throughout my PhD study. You are so knowledgeable and have great vision on my research topics. Without your close supervision and continuous encouragement, it would be difficult for me to overcome those hard times during my study. Thank you!

I also thank the rest of my supervisory panel. David Heslop, thank you for sharing MATLAB codes to help me process data and for your patient explanation in analysing data, especially during the initial period of my PhD study. Eelco Rohling, thank you for taking time to discuss my project, especially for my paleoclimate manuscript. Katharine Grant, thank you for providing samples and other useful data to fulfil my research.

Of course, I really need to thank our group members: particularly, Xiang Zhao and Pengxiang Hu. Thank you both for your help in my research and personal life. Without your help, I could not have settled down in Canberra in such a short time, and I truly appreciate all your help in lab work and for your valuable discussions, especially for my first paper. Xiang, I will never forget the moment that you picked me up in front of the Black Mountain Library when I got lost. Pengxiang, thanks for your companionship and for organizing gatherings in Chinese festivals that made me feel at home at Canberra.

Thank you to Tiah Penny, for your time spent teaching me picking foraminifera. Laura Rodríguez-Sanz, thank you for all your help in the lab and with processing stable

isotope data. I also thank the China Scholarship Council and the ANU for offering me scholarships to pursue my PhD degree at the Research School of Earth Sciences at ANU.

A special thank you to all of my friends that I have made in Canberra. We have had so many good memories! Meinan Shi, I will never forget your ginger cake! Bei Chen, Yuwei Li, Congcong Gai, Mingkun Li, Victor Piedrahita Velez, Feng Wang, Yingxing Kou, and Lin Tian, thanks for your friendship and support, which mean a lot to me.

From the bottom of my heart, I would like to say a big thank you to my parents. Thank you for always supporting all of my decisions and also for your endless encouragement, support, and understanding. I love you! Last but definitely not least, Yang, thank you for being with me and for looking after me for these past four years. I appreciate everything you have done for me. Hope our future life will be more colourful!

Abstract

Magnetic techniques have been used widely in environmental studies for the past few decades. Environmental magnetism typically involves conventional room temperature measurements of bulk magnetic parameters and more advanced component-specific magnetic approaches. Conventional bulk parameters can provide continuous records of magnetic mineral concentration and/or particle size variations in sediments, respectively. However, such parameters are not necessarily well suited to identifying magnetic components within individual magnetic mineral assemblages. More advanced techniques, such as first-order reversal curve (FORC) diagrams and low-temperature (LT) magnetic measurements, can enable detailed discrimination of magnetic mineral assemblages. However, these measurements are time-consuming, so they cannot be used to develop high-resolution records. Furthermore, although these techniques have been used more frequently in recent years, much work remains to be done to unlock their full diagnostic power in environmental magnetism. In this thesis, I use marine sediments from the eastern Mediterranean Sea to assess bulk magnetic measurements, FORC diagrams, LT measurements, X-ray fluorescence core-scan elemental data, and transmission electron microscope (TEM) observations to investigate the benefits and limitations of conventional and advanced environmental magnetic techniques for sediments deposited under variable redox conditions, and to explore the use of LT magnetic properties for detecting different magnetic particle types in marine sediments. Eastern Mediterranean sediments were selected here because they contain complexly varying mixtures of detrital, biogenic, and diagenetically altered magnetic mineral assemblages that were deposited under varying oxic (organic-poor marls) to anoxic (organic-rich sapropels) conditions. I demonstrate in this work that conventional bulk magnetic parameters can be used to provide high-resolution records of environmental

magnetic variations, while advanced measurements provide direct ground-truthing of mineral magnetic assemblages that enables calculation of magnetization contributions of different end members. Thus, a combination of conventional bulk parameters and advanced magnetic techniques can provide detailed records from which the meaning of environmental magnetic signals can be unlocked. In this work, I also demonstrate that LT studies enable clear identification of the extent of the presence of biogenic magnetite, superparamagnetic particles, and surficial maghemitization of magnetite particles. Furthermore, new high-resolution magnetic and planktic foraminiferal stable oxygen isotope ($\delta^{18}O$) proxy records are presented together with published geochemical data from eastern Mediterranean sediments to discuss the causes of increased dust inputs from the Sahara Desert across the mid-Pleistocene Transition (MPT). After assessing hypotheses for increased Saharan dust inputs across the MPT, including increasing source-area aridity due to reduced precipitation, expanding dust source areas, and atmospheric CO_2 reduction that led to decreased vegetation and soil cohesion, I find that increasing climate extremes boosted wind-blown dust production and emissions. This is important because the resultant aeolian aerosols play a major role in both the radiative balance of climate and biogeochemical cycles in areas where the dust settles. This work provides valuable insights into the application of conventional bulk and more advanced component-specific methods in identifying mineral magnetic assemblages in paleoceanographic and paleoenvironmental reconstructions, and in explaining increased Saharan dustiness across the MPT.

List of Contents

List of Figures

List of Tables

Chapter 1

Introduction

1.1 The Mediterranean Sea

The Mediterranean Sea is a semi-enclosed marginal sea with the only connection with the open (Atlantic) Ocean through the narrow Strait of Gibraltar (Fig. 1.1). Much of the basin is surrounded by mountainous terrain with a maximum extent of ~1,600 km in the north-south direction and a maximum extent of ~3,860 km in the west-east direction, covering a total surface area of ~2,500,000 km^2. Due to its small volume and limited communication with the world ocean, it preserves and amplifies signals due to climatic change and various other biogeochemical and physical processes, as well as their interactions (Bethoux et al., 2005; Hecht & Gertman, 2001; Malanotte-Rizzoli & Hecht, 1988; MEDOC group, 1970; MerMex Group, 2011; Miller et al., 1970; Millot & Taupier-Letage, 2005; Pinardi & Masetti, 2000; POEM group, 1992; Ribera d'Alcalà et al., 2003; Samuel et al., 1999; Send et al., 1999; Theocharis et al., 2002; Wüst, 1961).

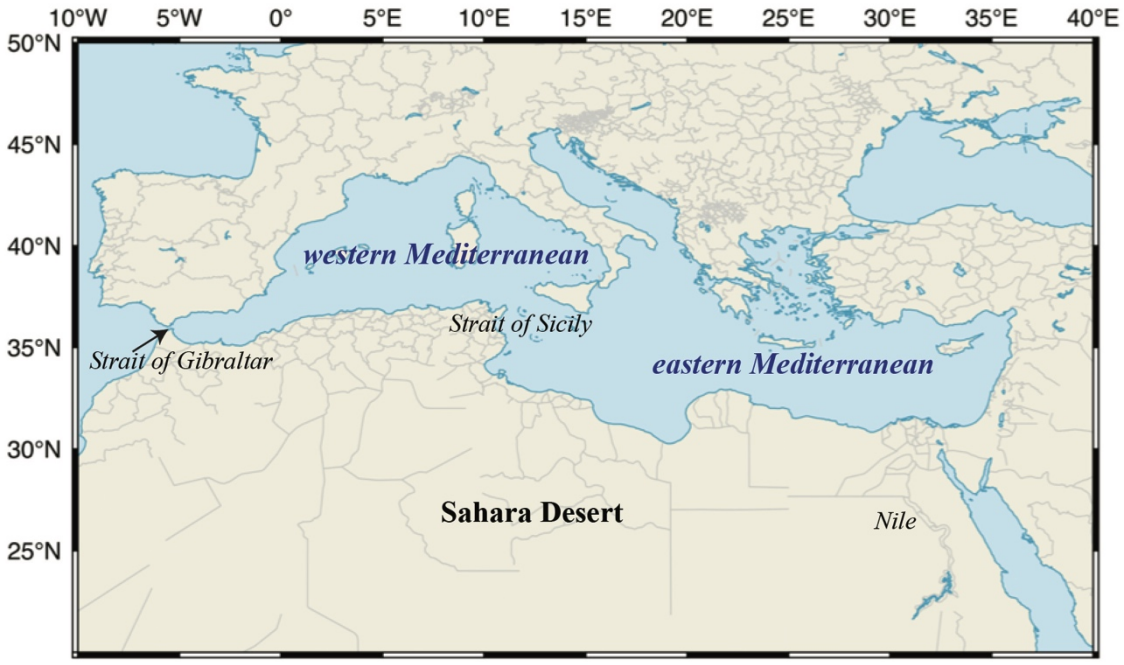

Fig. 1.1 Location of the Mediterranean Sea and North Africa.

The Mediterranean basin is located in the transition zone between the temperate westerlies across central and northern Europe and the subtropical high-pressure belt across North Africa, which results in a typical Mediterranean climate (Lolis et al., 2002). Specifically, in warm and dry summers, northward displacement of this transition brings warm and dry climates to the Mediterranean region (Lolis et al., 2002; Rohling & Hilgen, 1991). Conversely, in mild and wet winters, southward displacement of this transition brings wet and rainy conditions to the Mediterranean region (Lolis et al., 2002; Rohling & Hilgen, 1991; Rohling et al., 2015). Moreover, Atlantic depressions track seasonally eastward across Europe and may reach the western Mediterranean, with rarer movement over the eastern Mediterranean (Rohling & Hilgen, 1991).

The Mediterranean basin is divided into two parts by the Strait of Sicily, namely the eastern Mediterranean basin and the western Mediterranean basin (Fig. 1.1; de Lange et al., 2008; Emeis et al., 1991, 2003; Meyers, 2006; Rohling, 1994; Rohling & Thunell, 1999; Rohling et al., 2009, 2015; Rossignol-Strick, 1985). The Strait of Sicily has a maximum depth of 500 m, which limits water-mass exchange between the basins (e.g., Pinardi et al., 2015; Rohling et al., 2015). Considering its land-locked configuration and latitudinal position, the eastern Mediterranean Sea is particularly sensitive to astronomically-induced climatic changes that are well-preserved in the sedimentary record. Deposition of aeolian dust from the Sahara into the Mediterranean Sea during dry periods and dominantly riverine detrital input during wet periods, which coincide with deposition of marine sapropel-bearing sequences, provide high-resolution sedimentary records of climate variations. Paleoclimate proxy data from eastern Mediterranean sedimentary sequences have been used to reconstruct high-resolution astronomically-calibrated timescales for the past 9 Ma of Earth history by helping to constrain the timing of past geomagnetic reversals (Grant et al., 2017; Hilgen, 1987, 1991; Hilgen &

Langereis, 1993; Langereis & Hilgen, 1991; Langereis et al., 1997; Lourens et al., 1996; Rossignol-Strick, 1995). Furthermore, the extraordinary accuracy of these paleoclimatic records helps to improve our understanding of past Earth orbital changes (Hilgen, 1991; Lourens et al., 2001). For example, sapropel formation is associated with variations in Earth's orbit, so that sapropel occurrences enable fine alignment of sedimentary records to astronomical target curves (Hilgen, 1991; Larrasoaña et al., 2006; Lourens et al., 1996).

1.2 Eastern Mediterranean marine sediments

Distinctive (organic-rich) sapropels are deposited cyclically with (organic-poor) marls in Mediterranean sedimentary sequences of the past 13.5 Myr (Hilgen et al., 2003; Krijgsman et al., 1995, 2001; Lourens et al., 1996; Schenau et al., 1999; Sierro et al., 1999). Sapropel formation is controlled by periodic variations of solar energy generated from the northern low- to mid-latitudes during summer insolation maxima at ca 22-kyr precession minima (Emeis et al., 2000a; Hilgen, 1991; Larrasoaña et al., 2003a; Lourens et al., 1996). During these periods, strengthening and increased northward penetration of the African monsoon resulted in increased freshwater runoff into the eastern Mediterranean Sea via both the Nile and the whole North African margin (Larrasoaña et al., 2003a; Lourens et al., 2001; Rohling et al., 2002a; Rossignol-Strick, 1983). This led to reduced dust generation from the Sahara, increased riverine supply, enhanced primary productivity in eastern Mediterranean surface waters, and limited bottom-water ventilation, which facilitated organic matter delivery to deep basins and its subsequent preservation (Cramp & O'Sullivan, 1999; Rohling, 1994). Conversely, during insolation minima (precession maxima), North Africa is dominated by drier climates, which leads to nannofossil ooze deposition under (present-day type) environments of low monsoon

drainage, efficient bottom-water ventilation, limited surface water productivity, and enhanced aeolian dust transport from the Sahara.

Sapropels are important to paleoclimate studies because they record the pace of an orbitally driven climatic system that was magnified marked by the semi-enclosed morphology of the Mediterranean basin. Sapropel formation is associated with variations in Earth's orbit, so that sapropel occurrences enable the sedimentary record to be aligned to astronomical target curves (Hilgen, 1991; Larrasoaña et al., 2006; Lourens et al., 1996). Typically, this involves tuning the sedimentary record to summer insolation at 65°N, with sapropels adjusted to even-numbered insolation maxima (i-cycles) (Hilgen, 1991; Larrasoaña et al., 2006; Lourens et al., 1996). This helps to reconstruct accurate high-resolution age models that help to date geological processes such as paleoclimatic and paleoceanographic variations, and geomagnetic events.

Sapropels are dark-coloured laminated layers that are usually between 1 to 60 cm thick, and are more common in the eastern Mediterranean Sea than in the western Mediterranean Sea (e.g., Cramp & O'Sullivan, 1999; de Kaenel et al., 1999; Emeis et al., 1991; Meyers, 2006; Meyers & Doose, 1999; Murat, 1999; Rogerson et al., 2008; Rohling et al., 2015). Western Mediterranean Plio-Pleistocene sapropels normally have lower organic carbon (C_{org}) values compared to eastern Mediterranean sapropels except in the Tyrrhenian Sea (Murat, 1999). However, due to post-depositional oxidation (burn-down), sapropels can be partly or even entirely removed (Emeis et al., 2000a; Larrasoaña et al., 2006). During times of sapropel formation, increased organic carbon deposition led to sulphidization in anoxic sapropels and produced sulphide that diffused downward into earlier deposited oxic sediments (Larrasoaña et al., 2003b, 2006; Passier et al., 1996). These reduction intervals could be misinterpreted to mark the onset of sapropels (Passier et al., 1996). On the other hand, after sapropel formation, bottom waters are reoxygenated,

oxygen diffuses downward into the sapropel and oxidizes organic matter within the sapropel, which also affects how a sapropel is identified (Larrasoaña et al., 2006). Thus, sediment colour and C_{org} records cannot be used to identify oxidized sapropels. In order to identify the initial limits of a sapropel, geochemical, paleontological and magnetic techniques have been used widely in eastern Mediterranean studies (Grant et al., 2017; Larrasoaña et al., 2006).

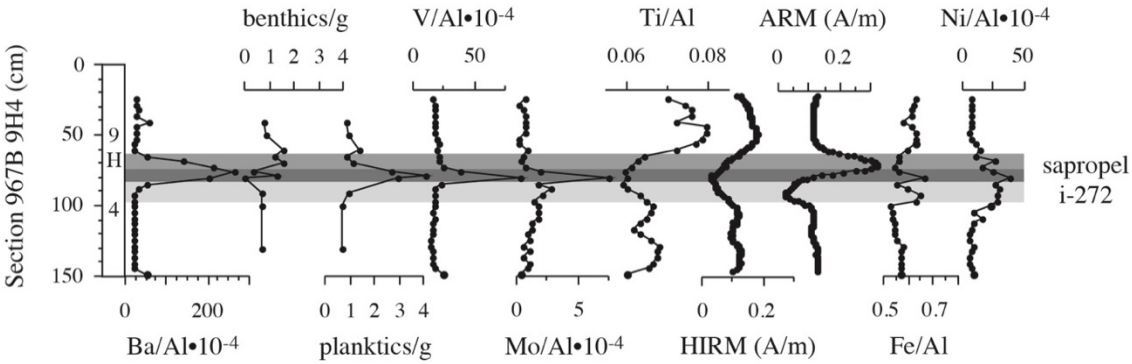

Fig. 1.2 Geochemical, paleontological, and magnetic data from ODP Site 967 for representative sapropel i-272. Grey, dark grey, and light grey shadings indicate the locations of the oxidation front, sapropel, and dissolution interval, respectively. Sapropel stratigraphy is based on Emeis et al. (2000). Modified from Larrasoaña et al. (2006).

Geochemical records, like barium/aluminium (Ba/Al) ratios and titanium/aluminium (Ti/Al) ratios, are used commonly to detect the presence of sapropels (e.g., Emeis et al., 2000a). Elevated Ba/Al ratios are observed in sapropels, which are associated with enhanced primary productivity of surface waters (Fig. 1.2; de Lange et al., 2008; Thomson et al., 1995; Wehausen & Brumsack, 1999). During sapropel formation, enhanced freshwater supply into the eastern Mediterranean Sea leads to enhanced primary productivity in the surface ocean, which enhances C_{org} deposition within sapropels. Compared with easily oxidized C_{org}, Ba is associated with export productivity, and can be well-preserved in sediments because it is not easily mobilized after deposition (Dymond et al., 1992). Thus, the Ba/Al ratio is an ideal proxy for identifying initial sapropel locations (Thomson et al., 1995). In addition, Ti/Al ratios

normally have distinctive minima in sapropels (Fig. 1.2). Ti/Al reflects relative variations of riverine (Al-rich) and Saharan (Ti-rich) supply that relate to African monsoon intensity changes (Calvert & Fontugne, 2001; Lourens et al., 2001; Wehausen & Brumsack, 2000). Moreover, redox-sensitive trace metals, like V and Mo, are enriched in sapropels. High values of these metals suggest that oxygen contents of bottom water were low during sapropel deposition (Fig. 1.2; Calvert & Fontugne, 2001; Larrasoaña et al., 2006; Passier et al., 2001; Thomson et al., 1995; van Santvoort et al., 1997; Wehausen & Brumsack, 2000). Lastly, sapropels are also characterized by high calcophilic elements such as Ni and Fe, which are incorporated into iron sulphide minerals, mainly pyrite, under the sulphate-reducing environments that resulted from organic matter accumulation and degradation (Fig. 1.2; Calvert & Fontugne, 2001; Larrasoaña et al., 2006; Passier et al., 2001; Pruysers et al., 1993; van Santvoort et al., 1997; Warning & Brumsack, 2000).

Paleontological records enable identification of sapropels because they commonly lack benthic foraminifera that indicate bottom water anoxia (such fauna usually return when suitably oxygenated conditions are re-established) (Fig. 1.2; Casford et al., 2003; Emeis et al., 2000b; Mercone et al., 2001; Nijenhuis et al., 1996; Rohling et al., 1993, 1997; Schmiedl et al., 2003). In most cases, benthic organisms did not survive anoxic conditions during sapropel formation, so that lack of bioturbation preserves undisturbed and highly-resolved sedimentary records (Rohling et al., 2002a). Sapropels are also marked commonly by negative anomalies in stable oxygen isotope ratios ($\delta^{18}O$), which are measured on the calcium carbonate shells of surface-layer dwelling planktonic foraminifera *Globigerinoides ruber (white) (G. ruber (w))* (Fig. 1.2). Compared to seawater, freshwater has distinctly low $\delta^{18}O$, especially for heavy (monsoon-type) precipitations, which are isotopically light (Abell & Hoelzmann, 2000; Beuning et al., 2002; Gasse, 2000; Hoelzmann et al., 2000; McKenzie, 1993; Rozanski, 1985; Sonntag

et al., 1979). Hence, a combination of Mediterranean surface waters and freshwater floods results in negative $\delta^{18}O$ anomalies of surface-dwelling planktonic foraminifera (e.g., Emeis et al., 1998, 2003; Rohling et al., 2004; Rohling & De Rijk, 1999a, b) and $\delta^{18}O$ records generated from shallow-dwelling planktonic foraminifera provide highly resolved time-series of past climate variability.

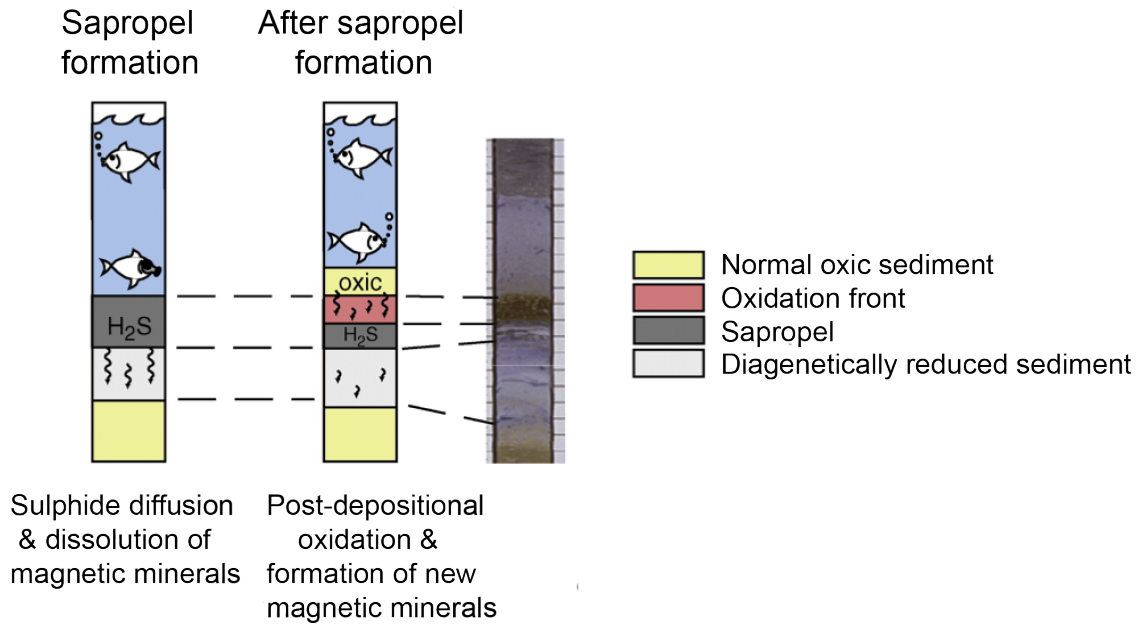

Fig. 1.3 Illustration of the paleoceanographic conditions of eastern Mediterranean sediments during sapropel formation (type 2 sapropel according to Larrasoaña et al. (2003b)). During sapropel formation, bottom waters are sulphidic. Downward H_2S diffusion sulphidizes sediments below sapropels. After sapropel deposition, bottom waters become reoxygenated, oxygen can diffuse downward into the previously sulphidic sediments, forming an oxidation front that provides a suitable environment for authigenic magnetic mineral formation (Larrasoaña et al., 2006; Passier et al., 2001; Passier & Dekkers, 2002). Modified from Roberts (2015).

1.3 Environmental magnetism of eastern Mediterranean sediments

Environmental magnetism is a useful technique for studying paleoceanographic conditions, both in relation to depositional processes and sedimentary diagenesis because magnetic minerals are sensitive to reductive dissolution (Larrasoaña et al., 2003b; Roberts et al., 1999; Robinson et al., 2000; Tarduno & Wilkinson, 1996; van Hoof et al.,

1993). Marine sediments contain magnetic minerals that originated primarily from detrital inputs, biomineralization, or post-depositional alteration of both types of minerals. The magnetic properties and grain size of marine sediments are sensitive to environmental variations, which helps to characterize geochemical environments and depositional regimes (Hilgenfeldt, 2000; Just et al., 2012; Liu et al., 2012a; Roberts et al., 2013; Rowan et al., 2009; Thompson & Oldfield, 1986).

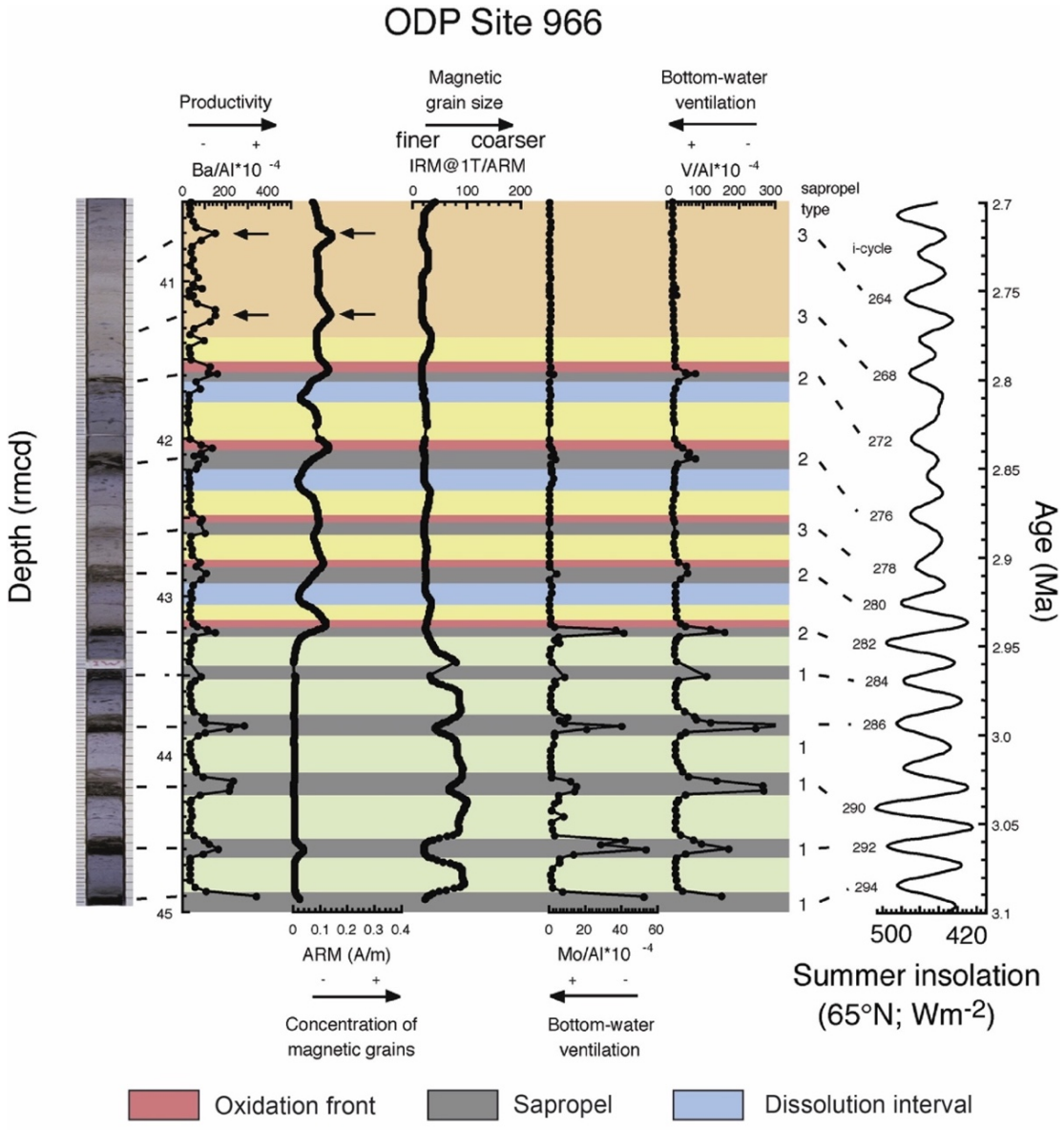

Fig. 1.4 Illustration of magnetic property variations related to three sapropel types in eastern Mediterranean sediments. Data are derived from ODP Site 966 (Larrasoaña et al., 2003b) and rmcd depths are based on Emeis et al. (2000). From Roberts (2015).

During sapropel formation, organic matter accumulation and burial results in sulphate-reducing diagenetic conditions, which causes reductive dissolution of the main low coercivity ferrimagnetic mineral (magnetite) in eastern Mediterranean sediments (Dekkers et al., 1994; Kruiver & Passier, 2001; Larrasoaña et al., 2003a, 2006; Passier et al., 2001), and formation of iron sulphides, mainly pyrite (Fig. 1.3; Dekkers et al., 1994; Passier et al., 1996; Pruysers et al., 1993; Roberts et al., 1999; van Santvoort et al., 1997). Hence, the magnetite concentration-dependent parameter, the anhysteretic remanent magnetization (ARM), decreases gradually within sapropels (Fig. 1.4). Under strong sulphate-reducing conditions, excess sulphide generated within a sapropel can diffuse downward into earlier formed normal sediments, resulting in coincident magnetite dissolution and pyritization (Figs. 1.3-1.4; Dekkers et al., 1994; Kruiver & Passier, 2001; Larrasoaña et al., 2003b; Passier et al., 1996, 2001; Roberts et al., 1999; van Hoof et al., 1993; van Santvoort et al., 1997). These intervals that have been subjected to downward sulphidization are referred to as 'dissolution fronts' (Larrasoaña et al., 2003b, 2006). ARM values remain low in these intervals (Fig. 1.4). After sapropel formation, bottom waters become reoxygenated, the oxidation of organic matter within sapropels stimulates the formation of diagenetic magnetite at paleo-oxidation fronts which develop on tops of sapropels, namely 'oxidation fronts' (Figs. 1.3-1.4; Passier et al., 2001; Kruiver & Passier, 2001; Larrasoaña et al., 2003b, 2006). ARM has its highest values at oxidation fronts. In addition to their sensitivity to non-steady-state diagenesis, information about depositional processes can be provided by magnetic minerals. For example, comparison between magnetic results and Ti/Al data demonstrates that changes in the amount of hematite reflect variations of Saharan (aeolian) dust supply (Larrasoaña et al., 2003a). These variations are driven by orbitally forced cycles that cause changes in the northward penetration and intensity of the African monsoon across the northern Sahara, where

hematite (dust) minima coincide with sapropels and dust maxima occur between sapropels (Figs. 1.2-1.3; Emeis et al., 2000a; Larrasoaña et al., 2003a; Lourens et al., 2001).

According to their distinctive magnetic properties, sapropels in the eastern Mediterranean Sea can be grouped into three main types. Type 1 sapropels have extremely low ARM concentrations (Fig. 1.4). This reflects their formation in times of sustained bottom water anoxia during which sulphidic diagenetic conditions removed all magnetite by development of thick dissolution intervals (Larrasoaña et al., 2003b). In some cases, type 1 sapropels have been magnetically enhanced. This results from the formation of a magnetic iron sulphide mineral (Roberts et al., 1999), which is likely to be greigite magnetofossils (Reinholdsson et al., 2013). Type 2 sapropels are representative sapropels, which contain both dissolution intervals and oxidation fronts (Fig. 1.4). The presence of dissolution intervals suggests that sufficient organic matter accumulated to generate excess sulphide that diffused downward and dissolved magnetic minerals. After sapropel formation, diagenetic conditions must have then become oxic to promote development of oxidation fronts (Larrasoaña et al., 2003b). Type 3 sapropels are weakly developed sapropels and are characterized by well-developed oxidation fronts and a lack of dissolution intervals (Fig. 1.4). The absence of dissolution intervals means that no excess sulphide was generated because anoxic conditions in this type of sapropel were less severe compared to type 2 sapropels (Larrasoaña et al., 2003b).

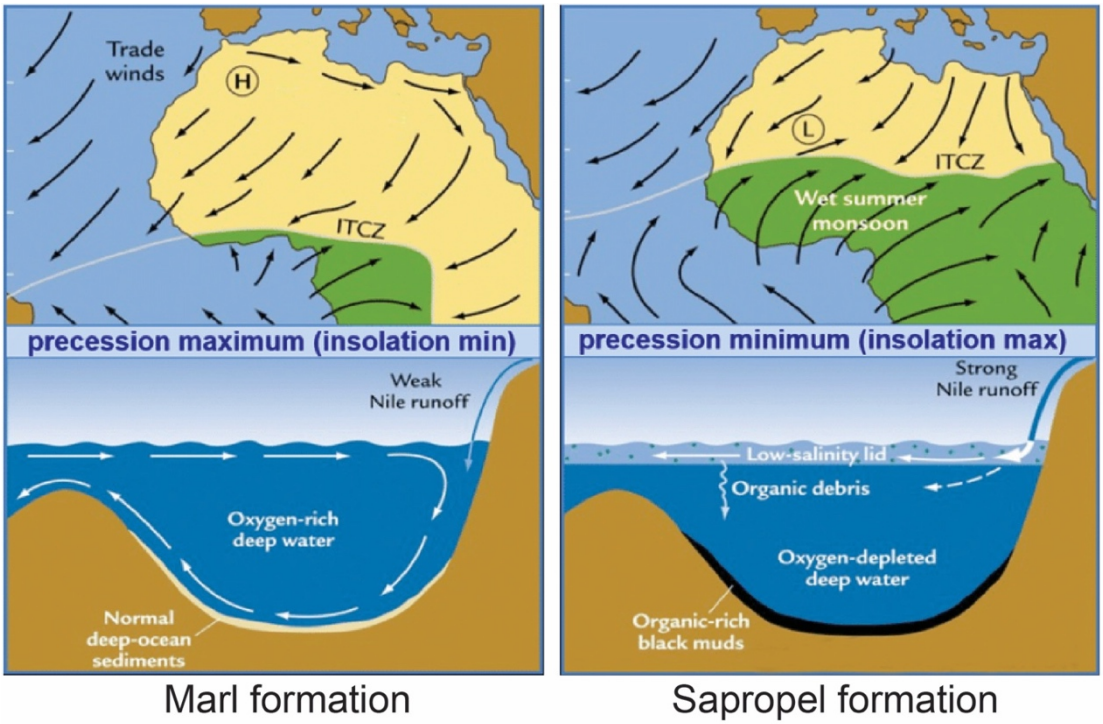

Fig. 1.5 Illustration of conditions that give rise to deposition of sapropels or normal marine sediments depending on the African summer monsoon strength, associated with the orbital configuration at precession maxima (left) and minima (right). From Ruddiman (2001). ITCZ= Inter-Tropical Convergence Zone.

1.4 African monsoon

Eastern Mediterranean sediments provide valuable archives not only of mid/high latitude climate processes, but also of African monsoon variations. Although the monsoon does not itself penetrate into the basin, it plays a 'remote' influence. On orbital timescales, enhancement and northward penetration of African monsoon rainfall during boreal summer insolation maxima leads to considerably increased freshwater supply into the eastern Mediterranean Sea, which provides conditions conducive to sapropel formation (Fig. 1.5; Osborne et al., 2008; Rohling et al., 2002a, 2004; Rossignol-Strick et al., 1982; Rossignol-Strick, 1983). In contrast, desertification of North Africa (Sahara) when the monsoon rain belt lay further to the south caused enhanced dust production and

deposition into eastern Mediterranean sediments, particularly during boreal summer insolation minima (Fig. 1.5; Larrasoaña et al., 2003a). This pattern recurs over many glacial-interglacial cycles to produce a marine paleoclimate record that complements ice core records of climate change. Analysis of sediments from areas down-wind of major Saharan dust sources provides an excellent means to study long-term African monsoon changes.

Due to their sensitivity to African monsoon variability, well-preserved Mediterranean sediments can provide an archive of humid periods in North Africa. The most recent monsoon interval, known as the Holocene 'African Humid Period' (Ritchie et al., 1985), together with three other "wetter" periods within the most recent glacial cycle, are well-recorded by marine proxy records and clear continental evidence (deMenocal, 2000; Drake et al., 2013; Larrasoaña et al., 2013). However, the extent and timing of older 'Green Sahara periods' (GSPs) is poorly constrained in continental environments because of a lack of well-preserved and well-dated continental deposits. Understanding of GSPs is important for studying the potential routes and timing of early human emigration and settlements in Africa (Osborne et al., 2008; Drake et al., 2011; Larrasoaña et al., 2013; Rohling et al., 2013; Timmermann & Friedrich, 2016), particularly in combination with increasing evidence of relatively humid periods in East Africa across the past few million years (Maslin et al., 2014). The timing of older GSPs is usually determined from sedimentary sequences that contain sapropels. However, sapropels can be partially or even completely oxidized during redox processes after deposition (de Lange et al., 2008; Higgs et al., 1994; Larrasoaña et al., 2003b, 2006; Thomson et al., 1999). Therefore, it can be inaccurate to determine the presence and/or timing of GSPs according to visual sapropel identification if sapropels have been oxidized (hidden or 'ghost' sapropels; Larrasoaña et al., 2006).

1.5 Aeolian dust

Climate can be influenced by airborne mineral dust both directly and indirectly (Kaufman et al., 2002; Maher et al., 2010; Tegen et al., 1996). Specifically, climate is influenced directly by dust by absorbing and scattering terrestrial and solar radiation that further affect the radiative properties of the atmosphere (IPCC, 2007). Dust also behaves as ice nuclei in clouds and changes cloud properties (Sassen et al., 2003), which affects the formation and life span of clouds and influences the hydrological cycle and Earth's radiative balance (Arimoto, 2001; Spracklen et al., 2008). Mineral dust fluxed from North Africa to the Mediterranean region influences the regional radiation balance by affecting the pH of precipitation and cloud microphysical properties (Levin & Ganor, 1996; Loye-Pilot et al., 1986). Dust can also affect climate indirectly by providing iron (Fe), which is a micronutrient, to Fe-limited waters upon its deposition onto the surface ocean, which improves phytoplankton productivity (Boyd & Ellwood, 2010; Jickells et al., 2005; Wolff et al., 2006). Increased productivity leads to the reduction of atmospheric CO_2, and the transport of biogenic carbon from surface ocean to deep ocean can result in long-term carbon sequestration (Martínez-Garcia et al., 2009). Thus, it is well recognized that aeolian dust has a close connection with climate change (Jickells et al., 2005; Maher et al., 2010).

Dust transportation accounts for a large part of the total sediment deposited into the eastern Mediterranean Sea, in which two short deposition events can constitute as much as 30% of the total annual sediment flux. The small and semi-enclosed Mediterranean basin receives dust that is transported from the deserts of the Arabian Peninsula and Syria (the Middle East), and Sahara (North Africa). Climatological conditions are conducive to dust transportation from North Africa to the eastern Mediterranean region in spring and from the Middle East during autumn (Alpert et al.,

1990; Dayan 1986). Other conditions are conducive to summer dust transport to the western Mediterranean (Moulin et al., 1998). However, it is difficult to obtain accurate dust transportation and deposition estimates on a regional scale because long-term, large-scale observations are needed. Besides, land use changes from anthropogenic activities have a significant influence on dust production (Mulitza et al., 2010). Dust cycle models predict that anthropogenic modification will dramatically affect aeolian transportation from land to sea over the coming centuries (Mahowald et al., 2006a). These models rely on understanding how dust aerosols respond to past and present radiative forcing and how dust flux variations affect ocean productivity and related atmospheric CO_2 variations. Several dust cycle models have been created to predict aeolian dust trajectories from the continents to the oceans. These models usually focus on dust collection and leaching studies, which is important for identifying mineral dust sources, particle size distributions, and transportation history. To address key uncertainties, we need to understand the dust cycle, such as the relationship between aeolian dust and climate forcing, by obtaining long stratigraphic records of dust deposition.

A specific climatic mechanism, which linked African monsoon variations to dust generation during the previous (Eemian) interglacial maximum, was proposed by Rohling et al. (2002). This mechanism suggests that the African summer monsoon penetrates significantly northward beyond the central Saharan watershed (~21°N) with simultaneously enhanced monsoon flooding through the Nile and across the North African margin. This is an effective concept to explain the observed modulation of aeolian dust flux into the eastern Mediterranean Sea on orbital time scales. Larrasoaña et al. (2003a) produced an important but relatively low-resolution dust flux record of Saharan dust to the eastern Mediterranean Sea, using an environmental magnetic proxy for hematite variation ($IRM_{0.9T@AF120mT}$) derived from sediments from Ocean Drilling

Program (ODP) Site 967. The sensitivity of eastern Mediterranean records to subtropical and mid/high latitude climate forcing makes development of Saharan dust proxy records a valuable approach for seeking a better understanding of the dust cycle, African monsoon variations and GSPs, and for understanding climate change across the Mid-Pleistocene transition, as discussed below.

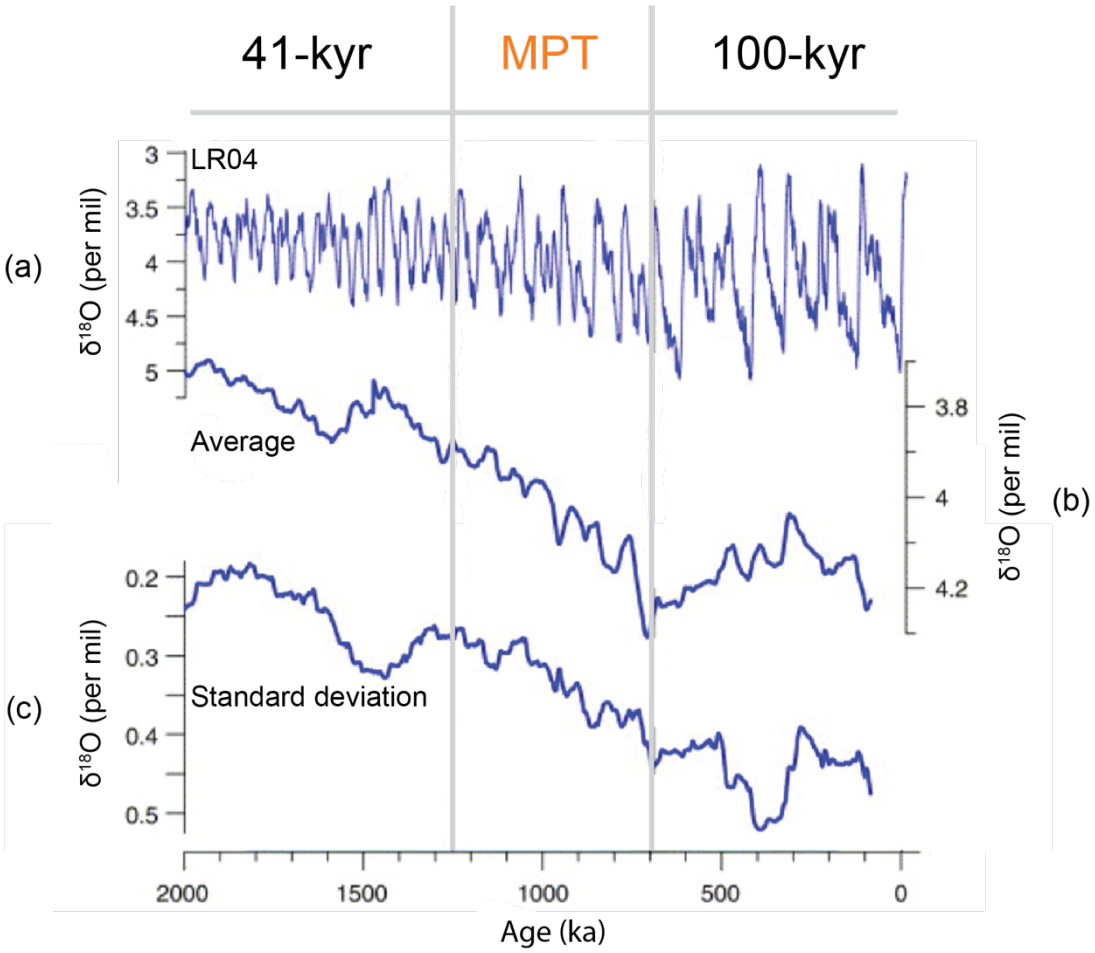

Fig. 1.6 Variations of glacial-interglacial cycles before and after the MPT. (a) The LR04 $\delta^{18}O_b$ stack (Lisiecki & Raymo, 2005), and (b) among average of the LR04 stack calculated by a 200-kyr sliding window, and (c) the standard deviation of the moving average from LR04 stack. The timing of the MPT is indicated by light grey vertical lines. Modified from Clark et al. (2006).

1.6 The Mid-Pleistocene Transition

The Mid-Pleistocene Transition (MPT), which occurred over a time interval from approximately 1250 ka to 700 ka (Clark et al., 2006; Elderfield et al., 2012), was a transitional period for Earth's climate where previously dominant 41-kyr glacial-interglacial cycles evolved into 100-kyr cycles (Fig. 1.6). Climate cycle amplitudes also increased after the MPT, with 100-kyr cycles associated with much more intense glacials and an asymmetric 100-kyr rhythm (Clark et al., 2006; Mudelsee & Schulz, 1997; Park & Maasch, 1993; Schmieder et al., 2000). Whilst the 41-kyr cycles had similar rates of glaciation and deglaciation, the asymmetry of 100-kyr cycles involves prolonged glaciation rates and rapid deglaciation events (Fig. 1.6). This basic climate reorganization obviously occurred without any major changes in orbital forcing, which led to the concept that MPT is affected by internal climate system changes (Clark et al., 2006). These changes caused the Earth system to cross a climate threshold to the asymmetrical sawtooth glacial-interglacial variations over the past 800-kyr; however, the mechanisms for this change have yet to be identified conclusively (Clark et al., 2006). Uncertainty surrounding the MPT highlights our lack of knowledge regarding the climatic responses to large-scale forcings and feedbacks on glacial-interglacial timescales.

Several driving hypotheses along with a variety of feedback mechanisms have been discussed for the MPT. Hypotheses to explain the MPT include: (1) a threshold response to a decrease in atmospheric temperature driven by CO_2 concentration decreases that resulted in gradual global cooling (Berger & Jansen, 1994; Raymo & Horowitz, 1996); (2) the regolith hypothesis, in which continuous erosion of glacial bedrock resulted in the accumulation of larger ice sheets, which in turn generated steeper terminations and more unstable ice sheets that represented the past 600-kyr (Clark & Pollard, 1998; Clark et al., 2006); (3) variations in ice sheet dynamics that led to the

formation of large ice sheets (Bintanja et al., 2005; Clark et al., 2006; Elderfield et al., 2012; Pollard & DeConto, 2009), and (4) oceanic thermohaline circulation reorganization (Peña & Goldstein, 2014; Schmieder et al., 2000; Sexton & Barker, 2012).

Several studies of aridity and humidity variations during the MPT in Africa from marine and other records have focused on the early to mid-Pleistocene. deMenocal et al. (2000) proposed that there are two obvious minima in the early Holocene and in marine isotope stage (MIS) 5.1, which are known to be related to GSPs and minimum dust production. During glacial MIS 22, dust flux enhanced dramatically at 950 ka after a long period with generally low dust flux and slight glacial/interglacial fluctuations (Larrasoaña et al., 2003a; Trauth et al., 2009). The increase in dust flux from ~800 ka correlates with minima in 65°N solar forcing and 400-kyr eccentricity, as well as with weak African monsoon precession periodicity (Trauth et al., 2007; 2009). This led to the expansion of hyper-arid environments throughout North Africa, where lakes in East Africa had their lowest levels and Nile River source areas had their lowest rainfall (Trauth et al., 2007). The abrupt dust flux increase indicates that African aridity responded only after a large ice volume threshold was obtained across the MPT (Clark et al., 2006; Sosdian & Rosenthal, 2009).

Most of our knowledge of the MPT comes from $^{18}O_{benthic}$ ($\delta^{18}O_b$) records, which reflects a combination of seawater oxygen isotope composition ($^{18}O_{seawater}$) and bottom water temperature combination (Labeyrie et al., 1987; Lisiecki & Raymo, 2005, 2007; Maasch, 1988; Mudelsee & Schulz, 1997; Pisias & Moore, 1981; Ruddiman et al., 1989; Rutherford & D'Hondt, 2000; Saltzman & Maasch, 1991; Shackleton, 1967). Although it has been studied and analysed statistically for years, disagreement remains about its origins and whether the MPT reflects a gradual transition that began at ~1.2 Ma and finished at ~0.65 Ma (Clark et al., 2006; Lisiecki & Raymo, 2007; McClymont et al.,

2013; Pisias & Moore, 1981; Raymo et al., 2006; Ruddiman et al., 1989; Rutherford & D'Hondt, 2000; Sosdian & Rosenthal, 2009). To better understand the development of a major global climate shift at that time, a continuous and high-resolution aeolian dust record from the eastern Mediterranean Sea is presented in this study, to seek to obtain clearer insights into the mechanisms and climate feedbacks that contributed to climate changes across the MPT.

1.7 Thesis objectives

My PhD project focuses on past aeolian dust flux changes to the eastern Mediterranean Sea over orbital timescales using magnetic and geochemical proxies. In my work, I propose to combine environmental magnetic and geochemical analyses to develop high-resolution (~150-year) records of aeolian dust flux for ODP Site 967 (Shipboard Scientific Party, 1996; Emeis et al., 2000a), which is a highly suitable site for acquiring a long and high-resolution dust fluctuation record (Larrasoaña et al., 2003a; Lourens et al., 2001; Wehausen & Brumsack, 2000) for the last 2 Ma to seek a better understanding of climate forcings and responses across the MPT.

My work includes the following objectives.

1. Integration of high-resolution bulk magnetic, low-temperature (LT) magnetic, and first-order-reversal curve (FORC) measurements, transmission electron microscope (TEM) observations, X-ray fluorescence (XRF) measurements, and FORC-principal component analysis (PCA) to identify magnetic mineral components within sapropel-rich sediments from the eastern Mediterranean Sea.

2. Integration of hysteresis loop analyses, FORC measurements, TEM observations, and LT measurements, together with previous published calibrated XRF

core-scan data (Grant et al., 2017) and high-resolution bulk magnetic results (Qian et al., 2020) to investigate the LT magnetic properties of the main eastern Mediterranean sediment types (representative sapropel, weakly developed sapropel, and normal sediments).

3. Integration of new continuous and high-resolution magnetic and planktic foraminiferal oxygen isotope data, published calibrated XRF core-scanning data (Grant et al., 2017) from eastern Mediterranean sediments, and published atmospheric CO_2 data to assess hypotheses proposed to explain increased glacial Saharan dustiness across the MPT. These hypotheses include increased source-area aridity due to reduced precipitation, expanding dust source areas, and atmospheric CO_2 reduction that led to decreased vegetation and soil cohesion, and a newly proposed hypothesis, an increase of wet/dry cycle intensity.

1.8 Thesis outline

Basic environmental magnetic theory is described in Chapter 2. The main results obtained in this study are presented in Chapters 3 to 5. A manuscript named "Assessment and integration of bulk and component-specific methods for identifying mineral magnetic assemblages in environmental magnetism" is presented in Chapter 3, which provides information to compare and illustrate the benefits and limitations of both techniques in identifying mineral magnetic assemblages (this work has been published in the *Journal of Geophysical Research – Solid Earth*). A detailed study of the LT magnetic properties of eastern Mediterranean sediments is presented in Chapter 4. This study illustrates the usefulness of LT analyses in identifying signals of interest in environmental magnetic studies and provides new insights into investigating the effects

of diagenesis on magnetic mineralogy (this work has been submitted for publication). In Chapter 5, I test several hypotheses that have been proposed to explain increased Saharan dustiness across the MPT. The finding that increasing climate extremes boosted wind-blown dust emissions is important because the resultant aeolian aerosols play major roles in both the radiative balance of climate and biogeochemical cycles in areas where the dust settles. Chapter 6 comprises the overall conclusions of these studies and provides suggestions for further work.

Chapter 2

Theory of environmental magnetism

2.1 Introduction

Environmental magnetism is versatile and applicable in a wide variety of settings. Environmental magnetism includes use of the magnetic properties of natural materials to investigate diverse environmental processes, and is based on the same mineral-magnetic principles that are used in paleomagnetism and rock magnetism (Liu et al., 2012a). Specifically, the magnetic properties of natural magnetic minerals and variations in their concentration, particle shape or size are used as proxy parameters to indicate environmental processes. These include provenance analysis of sedimentary basins, depositional and ensuing diagenetic processes within sediments, iron biomineralization, pollution assessment and paleoclimate studies (e.g., Maher & Thompson, 1999; Oldfield, 1991; Thompson et al., 1980; Thompson & Oldfield, 1986; Verosub & Roberts, 1995).

Environmental magnetism was formally defined as a discipline for the first time by Thompson et al. (1980) in a landmark article in *Science*. Before 1980, magnetic tools had been used for many years in many types of environmental studies (Verosub & Roberts, 1995). The seminal textbook *Environmental Magnetism* by Thompson & Oldfield (1986) provides a comprehensive introduction to, and definition of, the subject. This work helped the rapid expansion in use of magnetic measurements in environmental science. Review papers on environmental magnetism by Oldfield (1991) and King & Channell (1991) suggested that magnetic parameters can be complex to interpret because natural magnetic mineral assemblages tend to contain complex mixtures and because the theoretical and quantitative basis for environmental magnetism needs to be improved. Verosub & Roberts (1995) concluded that magnetic techniques have significant advantages, such as their nondestructive nature and sensitivity, and emphasized that their

value is based on the fact that they can be used to address research questions that often cannot be resolved with other methods. In 1999, the textbook *Quaternary Climates, Environments and Magnetism* by Maher & Thompson (1999) systematically introduced progress in environmental magnetic techniques with a focus on Quaternary studies. Evans & Heller (2003) summarized new developments in environmental magnetism, especially in loess studies, biomagnetism, and magnetic pollution monitoring. More recently, Liu et al. (2012a) presented the theory of magnetic parameters and reviewed recent developments in using magnetic tools to unravel environmental changes both in past geological settings and modern environments.

In order to understand the fundamentals of magnetic parameters used in this thesis, a specific explanation of the principles of environmental magnetism is presented here. In this chapter, a microscopic view of the origins of magnetism is presented first, followed by a brief summary of basic magnetic properties, and the three main types of natural magnetic minerals. A detailed description of the main natural pathways by which magnetic particles are deposited in sedimentary environments and the magnetic parameters used in environmental magnetism are introduced in the latter part of this chapter.

2.2 Fundamentals of magnetism

All magnetic fields are caused by electrical currents. Magnetic fields originate from the motion of electrons, which can take two forms. One is the orbital motion of an electron about an atomic nucleus; the other is the motion of an electron about its own axis (Cracknell, 1975). The magnetic moment **M** produced by the spin and the orbital motion of an electron in an atom can be calculated as:

$$\boldsymbol{M} = -\left(\frac{e}{2m_e}\right)\boldsymbol{L}, \tag{2.2.1}$$

where e indicates the charge, m_e represents the mass, and $\boldsymbol{L}$ is the angular momentum of the electron. This ratio (magnetic moment or orbital angular momentum) is a universal constant. In addition, the constant $e/2m_e$ is known as the gyromagnetic ratio of an electron. The magnetic moment of an electron in an atom in the z component is:

$$\left(\frac{e}{2m_e}\right)L_z = \left(\frac{e}{2m_e}\right)m_l\hbar = \frac{e\hbar}{2m_e}m_l, \tag{2.2.2}$$

where $\frac{e\hbar}{2m_e}$ is the Bohr magneton (μ_B). μ_B is the quantum of magnetic moment related to the orbital angular momentum of an electron in an atom or ion, $\hbar$ is the Planck constant divided by 2π, and m_l indicates the number of magnetic quanta. For a complete electron shell, the total orbital angular momentum is zero, so a magnetic moment associated with orbital motion only occurs for incomplete electron shells.

For most geological materials, the contributions of orbital magnetic moments cancel, so the magnetization is caused mainly by electron spins. The algebraic characteristics of the spin angular momentum operator S, which represents the intrinsic angular momentum of an electron, with eigenvalue of $S^2 = s(s+1)\hbar^2$, means that the only allowed value of s is ½. A fourth quantum number, m_s, in addition to n, l, and m_l, was introduced to reflect the electronic state of an atom. The z component of the spin angular momentum is:

$$S_z = m_s\hbar, \tag{2.2.3}$$

where m_s is equal to ±½. The magnetic moment related to the spin angular momentum is:

$$\boldsymbol{M_L} = -\left(\frac{e}{2m_e}\right)\boldsymbol{L} \text{ or } \boldsymbol{M_S} = -2\left(\frac{e}{2m_e}\right)\boldsymbol{S}. \tag{2.2.4}$$

The spin angular momentum of an atom mainly comes from unpaired electrons, so the total magnetic moment produced by both the orbital and spin motion (**L** and **S**) is:

$$\boldsymbol{M_J} = -g\left(\frac{e}{2m_e}\right)\boldsymbol{J}, \tag{2.2.5}$$

where g indicates the Landé g-factor, and **J** is the angular momentum operator.

Magnetization $\boldsymbol{M}$ is the magnetic moment per mass/volume. After being placed in a magnetic field, a material will produce its own magnetic field. Some materials will produce a magnetic field spontaneously without any additional magnetic field. Therefore, the magnetization can be divided into two types: an induced magnetization (which exists only in the presence of an external magnetic field) and a remanent magnetization (which can exist in zero field). Magnetism can originate in two ways: microscopic current loops and magnetic dipoles, which produce magnetic fields $\boldsymbol{H}$ or $\boldsymbol{B_0}$. The source of $\boldsymbol{H}$ or $\boldsymbol{B_0}$ comes from Coulomb's law or the Biot-Savart law, which introduces how $\boldsymbol{H}$ derives from a specified set of either magnetic charges or current elements. The volume magnetic susceptibility (κ) or the mass susceptibility (χ) indicates the ratio of the magnetization $\boldsymbol{M}$ and the applied external magnetic field:

$$\kappa = \boldsymbol{M/H} \text{ or } \chi = \boldsymbol{M/H}, \tag{2.2.6}$$

where χ can be defined as κ/ρ, in units of m^3/kg, where ρ indicates the density of a material. Magnetic susceptibility is generally regarded as a scalar quantity for bulk materials. $\boldsymbol{M}$ and $\boldsymbol{H}$ have the same units, so κ is dimensionless. In environmental magnetism, the original low-field susceptibility, χ, is used more commonly. In the SI unit system, Maher & Thompson (1999) state that the magnetic induction $\boldsymbol{B}$ is given by:

$$\boldsymbol{B} = \mu_0(\boldsymbol{H} + \boldsymbol{M}), \tag{2.2.7}$$

where μ_0 ($4\pi \times 10^{-7}$ N/m^2) is the permeability of free space.

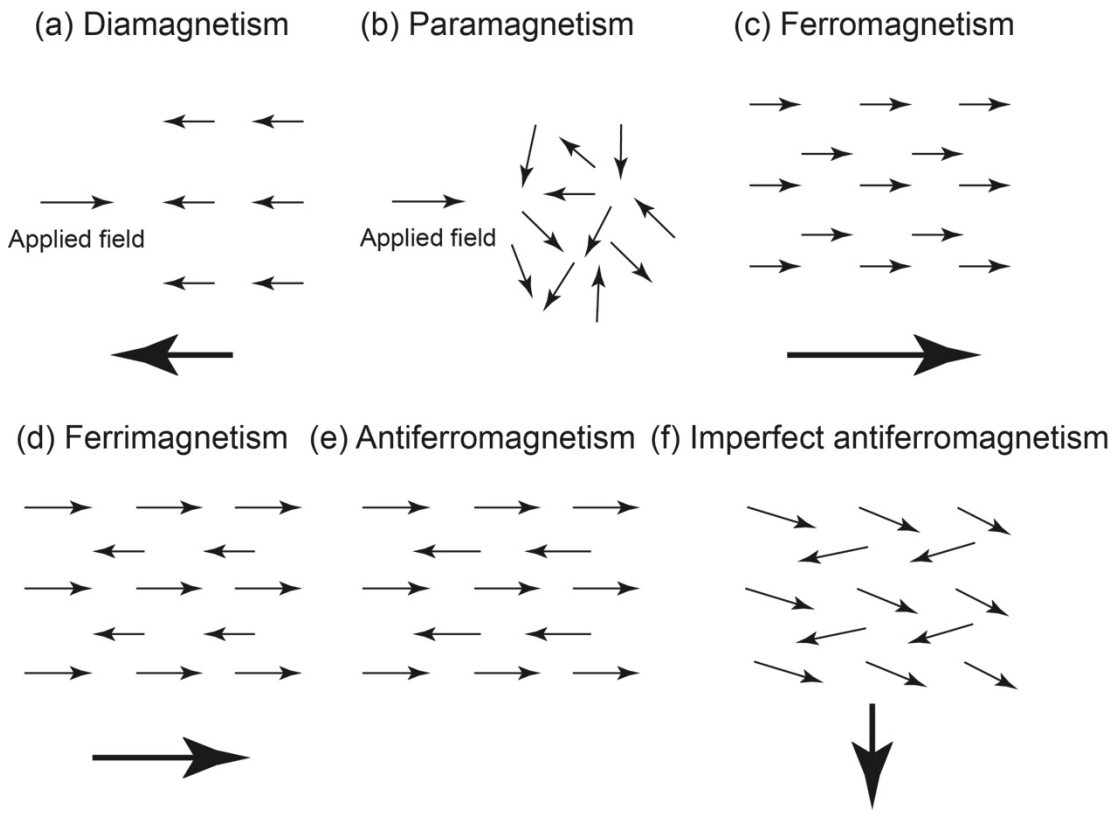

Fig. 2.1 Illustration of the spin structures of different kinds of magnetic materials. Black arrows at bottom of each plot indicate the net magnetization. The net magnetization in (b) and (e) is zero.

2.3 Magnetic properties of materials

As mentioned above, at atomic scale, electron spins are the main cause of magnetic phenomena. The electron spins of natural materials normally appear in pairs or are disturbed by thermal energy, so they can only produce diamagnetic or paramagnetic responses. However, for some materials, exchange interactions cause atomic magnetic moments to be aligned in a given direction and without cancelation of atomic magnet moments, which causes the material to have a spontaneous magnetization. Such materials can be strongly magnetic, and are referred to as ferromagnetic and ferrimagnetic materials.

2.3.1 Diamagnetism

All materials that contain electrons are diamagnetic. Diamagnetism is caused by the interaction between the orbital motion of electrons and an external magnetic field, which leads to a weak negative magnetization. Upon removal from an external magnetic field, the precession of electrons, or the distortion of the wave functions disappears, so that the weak induced magnetization is lost. For diamagnets, the spin magnetic moments of electrons do not contribute to the magnetization because these electrons are paired and cancel each other out (Fig. 2.1a). An external magnetic field only affects the orbital electron motion, so diamagnetism is independent of temperature. Due to its extremely weak magnetization, diamagnetism is mostly swamped by other kinds of stronger magnetic behaviour when non-diamagnetic materials are also present. Some natural non-iron-bearing materials, such as water, feldspar, calcite, and quartz, have diamagnetic behaviour.

2.3.2 Paramagnetism

The second weak magnetic property is paramagnetism. Due either to the spin of unpaired electrons or to the orbital motions of electrons, or to both, individual ions, molecules, or atoms can have a permanent magnetic dipole moment that results in paramagnetic behaviour. These dipoles are oriented randomly owing to thermal agitation before being placed in an external magnetic field (Fig. 2.1b). Once in an applied magnetic field, these permanent magnetic dipoles tend to align parallel to the direction of the external magnetic field, which leads to a positive, weak induced magnetization. After removal of the magnetic field, the weak magnetic ordering can be overcome by thermal effects, so that the magnetization disappears. Thus, the magnetic moment is controlled by a combination of the applied magnetic field magnitude and the absolute temperature. The M-H relationship for paramagnets is described by the *Langevin function*. Many

natural iron- and manganese minerals, e.g., olivine, garnet, pyroxene, lepidocrocite, and biotite are paramagnetic at 300 K. Several common elements, e.g., Fe^{2+}, Fe^{3+}, and Mn^{2+} ions, have incompletely filled outer 3*d* orbitals that cause the paramagnetic behaviour of natural materials. This is because these ions have unpaired electrons with free spin magnetic moments.

2.3.3 Ferromagnetism

For ferromagnetic materials below a certain temperature, all magnetic moments of atoms or ions align parallel to some particular crystallographic direction, resulting in large permanent magnetic moments even in the absence of an external field (Fig. 2.1c). The total magnetic moment is much larger than that of diamagnetic and paramagnetic materials. Moreover, regardless of continuous thermal disturbance, the exchange energy between neighbouring atoms is large enough to maintain alignment of ferromagnetic atomic moments.

An important characteristic of a ferromagnet (e.g., iron), is that its magnetic properties change significantly at a certain ordering temperature, known as the Curie temperature (T_c) for ferrimagnets or ferromagnets or the Néel temperature (T_N), for antiferromagnets. Below this temperature, ferromagnetic materials have a strong remanent magnetization, and above this temperature, ferromagnetic order can be broken by thermal energy and the material becomes paramagnetic. Strong remanent magnetization is another significant feature of ferromagnetism. This strong spontaneous magnetization means that the permanent magnetization of a ferromagnet exists even without an external magnetic field. Spontaneous magnetizations result from exchange interactions among neighbouring atoms, whereby the elementary magnetic moments of adjacent electrons are arranged in parallel by quantum mechanical effects.

2.3.4 Ferrimagnetism and antiferromagnetism

The number of natural magnetic minerals is not large. Only metallic iron, which is rare in Earth's crust, and some natural Fe-Ni alloys are ferromagnetic. Most natural magnetic materials are ferrimagnets (Néel, 1948) or antiferromagnets (Néel, 1936). Ferrimagnetic and antiferromagnetic behaviour in natural materials, especially iron and manganese minerals, are due to the first series of transition elements, in which the spin magnetic moment of electrons can be generated by the exchange force ordering in the incompletely filled 3*d* shells. The magnetic behaviour of ferrites (ferrimagnets) relies on their special crystal structure. In a ferrimagnetic crystal, there are two kinds of magnetic sites with antiparallel magnetic moments of different magnitudes. However, due to the moment difference in these two directions, the elementary magnetic moments of a ferrite do not cancel fully and normally have a net permanent magnetization (Fig. 2.1d). Magnetite and maghemite are ferrimagnetic minerals.

Antiferromagnetic minerals also have two magnetic sublattices with antiparallel magnetizations (Fig. 2.1e). However, their magnetic moments are identical, so no net spontaneous magnetization is produced. Some antiferromagnets can possess a net spontaneous magnetization due to modification of the basic arrangement of ferromagnetic moments. These minerals are known as imperfect antiferromagnets, which result from heterogeneities caused by the presence of impurities, lattice defects, and spin canting that produce a minor modification of antiparallel sublattice magnetic moments in antiferromagnets (Fig. 2.1f). For example, due to spin canting, the naturally occurring hematite has an imperfect antiferromagnetic structure and a weak permanent moment.

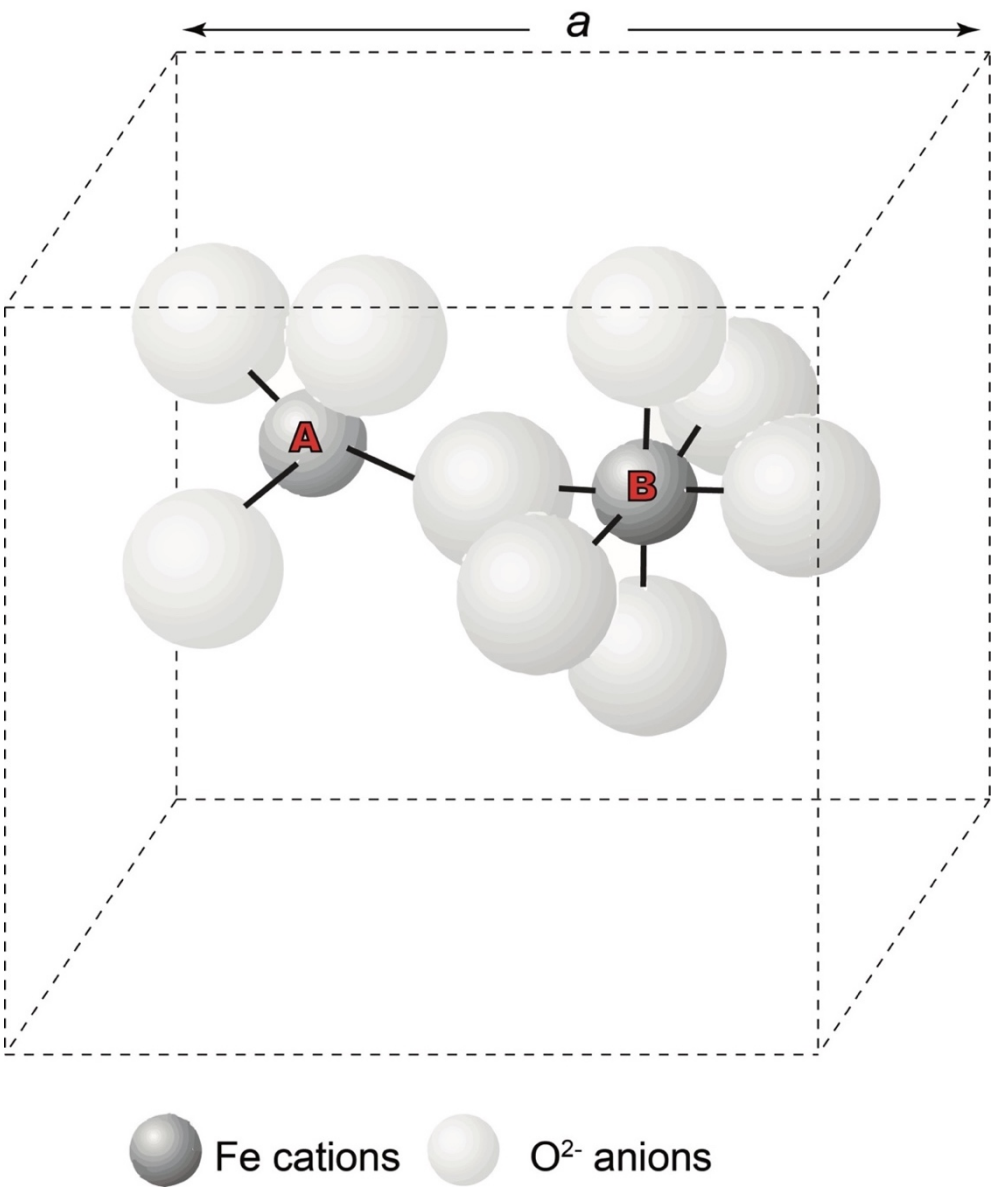

Fig. 2.2 Sketch of a unit cell of magnetite. The lattice parameter for the cubic cell is *a*. Fe cations are indicated by dark shaded spheres, and O^{2-} anions are indicated by light shaded spheres. Two types of coordination of Fe cations with O^{2-} occur in magnetite: A-sublattice cations (left) are in tetrahedral coordination with 4 O^{2-} anions; B-sublattice cations (right) are in octahedral coordination with 6 O^{2-} anions. Redrawn after Butler (1998).

2.4 Magnetic mineralogy

Natural magnetic minerals can be divided into three main types: iron oxides (e.g., magnetite, titanomagnetite, maghemite, and hematite); iron oxyhydroxides (e.g., goethite); and the iron sulphides (e.g., greigite and pyrrhotite). All of these magnetic

minerals have strong magnetic properties and most retain magnetic remanences at room temperature. Magnetite and titanomagnetite are the most commonly occurring ferrimagnetic minerals. These strongly magnetic iron oxide minerals generally dominate the magnetic properties of natural samples, although other magnetic minerals can become important in settings that are more appropriate for their occurrence.

2.4.1 The iron oxides

Iron oxides are types of ionic crystals that are composed of a compact lattice of oxygen anions with metallic cations in the interstices. Fe^{3+} and Fe^{2+} cations are the main interstitial species in iron oxides; however, these cations can also be substituted by other elements, for example, Ti, Al, Mn, and Cr. Titanomagnetite is one of the most frequently occurring terrestrial magnetic minerals (e.g. Dunlop & Özdemir, 1997; Mollo et al., 2013). Al may occur as a minor constituent in spinels in basalts, soils, and other weathering environments. The Mn-end member jacobsite occurs in carbonatites and the Cr-end member chromite occurs in various Mg-rich rocks. Hematite and goethite, with usually some Al-substitution, are common in red beds and soils (Fritsch et al., 2005).

Natural iron oxide structures can be divided into two main groups. One crystallizes with a spinel structure, and the other crystallizes with a corundum structure. Most iron oxide minerals, such as magnetite and titanomagnetite, crystallize with a spinel structure. The spinel structure is a face-centered cube (Fig. 2.2). In the cube, there are twenty-four interstitial sites of two types, A and B (Fig. 2.2). A sites contain 4 oxygen ions that form a tetrahedral cell, and B sites are surrounded by 6 oxygen ions that form an octahedral cell (Fig. 2.2). Cation sites are fixed in spinels, whereas the locations of the thirty-two oxygen sites are flexible. These oxygen ions develop an approximately compact cubic framework. Other elements can occur as cations within this framework in natural oxide spinels. The corundum structure is rhombohedral. Hematite and ilmenite,

and the intermediate titanohematite series, are important magnetic minerals with rhombohedral structure (Fig. 2.3).

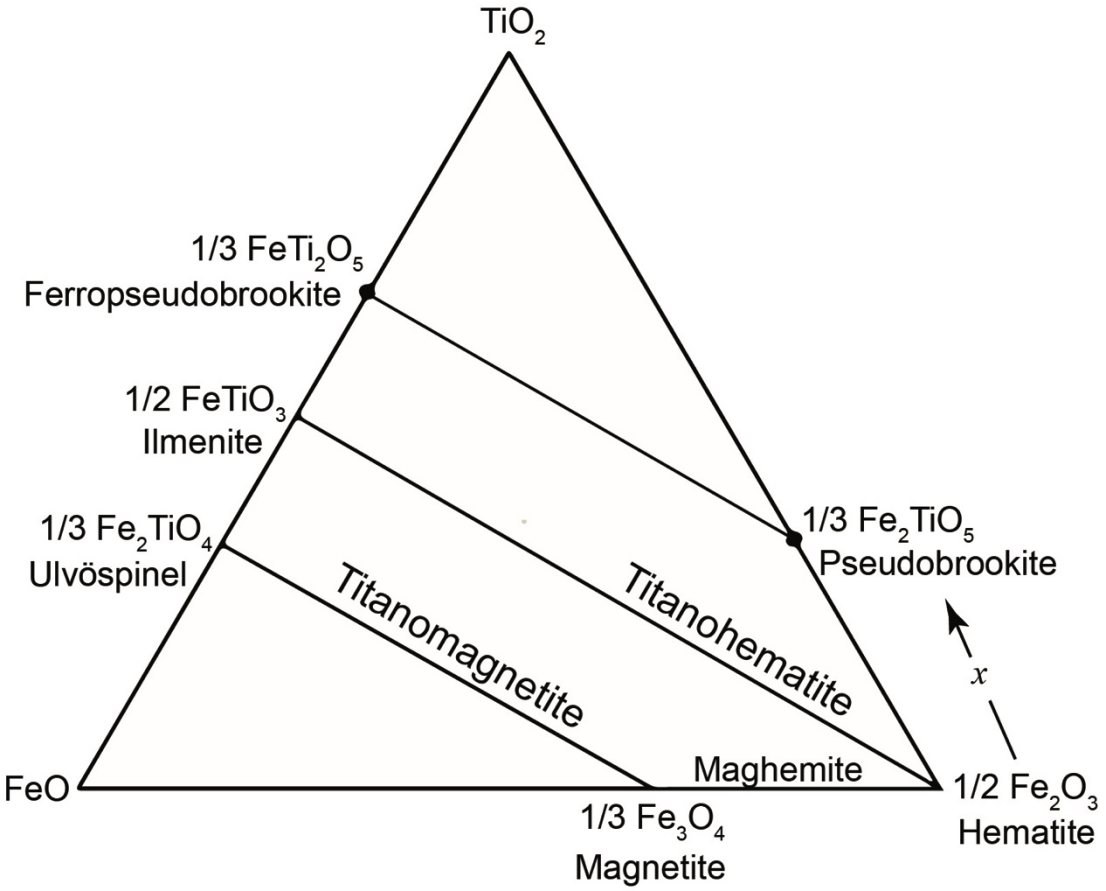

Fig. 2.3 The TiO_2-FeO-Fe_2O_3 ternary diagram in which *x* indicates the mole percent of Ti^{4+}, and the main FeTi-oxide mineral names are labelled with their respective chemical compositions.

Magnetite

Magnetite (Fe_3O_4; $Fe^{2+}Fe^{3+}{}_2O_4$) has the strongest magnetization of the natural magnetic minerals. Magnetite is a cubic mineral with an inverse spinel structure. In stoichiometric magnetite, all twenty-four Fe sites are occupied, with 8 Fe^{3+} cations located in the A sites and a mixture of 8 remaining Fe^{3+} cations and 8 Fe^{2+} cations hosted in the B sites. Due to the opposite spin direction of Fe^{3+} in the A and B sites, the moment due to Fe^{3+} is canceled. The net magnetic moments provided by Fe^{2+} in the B sites give rise to the characteristic ferrimagnetic properties of magnetite.

Magnetite is a major magnetic mineral on Earth and can be found in continental and oceanic crust. Magnetite occurs as a primary or secondary mineral in igneous, sedimentary, and metamorphic rocks. Pure magnetite can also be produced intracellularly by magnetotactic bacteria or extracellularly by iron-reducing bacteria and then preserved in sediments and water-logged soils. Magnetite can be identified easily by temperature-dependent magnetic measurements because the dynamics of magnetic structures change dramatically with temperature. Stoichiometric magnetite has a T_c of 580 °C (Thompson & Oldfield, 1986). Above this temperature, physical properties change dramatically, with a maximum in the specific heat and the coefficient of thermal expansion (Thompson & Oldfield, 1986). Below room temperature, the magnetic and physical properties of magnetite change dramatically at a magnetic transition at around 120 K, which is known as the Verwey transition (T_v) (Verwey, 1939). Below 120 K, there is an ordered arrangement of Fe^{2+} and Fe^{3+} ions with the unit cell distorted slightly from cubic to monoclinic symmetry.

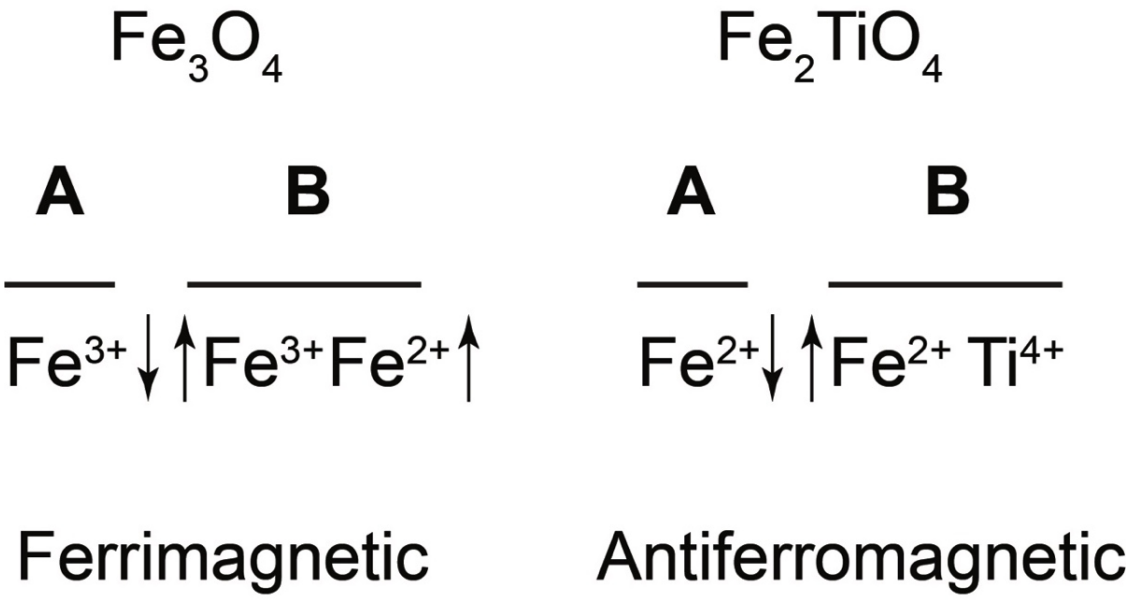

Fig. 2.4 Cation distributions in magnetite (left) and titanomagnetite (right). **A** and **B** indicate the respective A and B sublattice cations. Directions of cationic magnetic moments are indicated by black arrows. Redrawn after McElhinny (1973).

Titanomagnetite

Titanomagnetite has the chemical formula $Fe_{3-x}Ti_xO_4$, where x varies from zero for magnetite (Fe_3O_4) to one for ulvöspinel (Fe_2TiO_4). The mole percent of Ti^{4+} is measured by the composition parameter x. Ti-rich ulvöspinel is antiferromagnetic, with the same inverse spinel structure as magnetite. Fe^{3+} cations in the B sublattice are substituted by Ti^{4+}, and the remaining cations in the B sublattice are occupied by Fe^{2+} to maintain charge balance (Fig. 2.4). This means there are 8 Fe^{2+} cations on the octahedral sites and 8 Fe^{2+} cations on the tetrahedral sites. Antiparallel coupling of A and B sublattices results in zero net magnetic moment. In addition, the packed electron orbital for Ti^{4+} suggests that this cation has no atomic magnetic moment. The T_N of ulvöspinel is below -100°C, so at or above room temperature, it is paramagnetic.

Titanomagnetite is also an inverse spinel. A common titanomagnetite composition is $Fe_{2.4}Ti_{0.6}O_4$ (or TM_{60}), which has a T_c of 150-200 °C. Increasing Ti^{4+} substitution weakens exchange coupling between the A and B sublattices and T_c decreases almost linearly with increasing x (Fig. 2.5; O'Reilly, 1984). T_c also decreases with inclusion of other non-magnetic ions, e.g., due to subsititution of Ca, Mg, Al, V, Si, or Cu impurities into the spinel structure. For example, inclusion of 10% Al reduces T_c to 535 °C (Pouillard, 1950). The magnetization of titanomagnetite can be calculated as:

$$M_s = 4\mu_B(1 - x), \tag{2.4.1}$$

where μ_B is the magnetic moment related to the orbital angular momentum of an electron in an atom, and x is the mole percent of Ti^{4+}. The decreasing exchange interactions mean that M_s decreases with increasing x (Fig. 2.5; O'Reilly, 1984). In the titanomagnetite series, with the increase in Ti content, Ti^{4+} replaces Fe^{3+}. Specifically, the ionic substitution is 2 Fe^{3+} to Fe^{2+} and Ti^{4+}. This indicates that for each Ti^{4+} introduced, the

remaining Fe cations must be transformed from Fe^{3+} to Fe^{2+}. The radius of a Ti^{4+} ion is larger than that of Fe^{3+}, so cell size increases with increasing x (O'Reilly, 1984). Oxidation of titanomagnetite also affects the magnetic properties, especially the cell parameter, a, and T_c. With increasing oxidation, a decreases because Fe^{3+} is smaller than Fe^{2+}, while T_c increases (Dunlop & Özdemir, 1997). As for the magnetization, low-temperature oxidation decreases the net magnetic moment between the A and B sites, leading to a magnetization decrease (Dunlop & Özdemir, 1997).

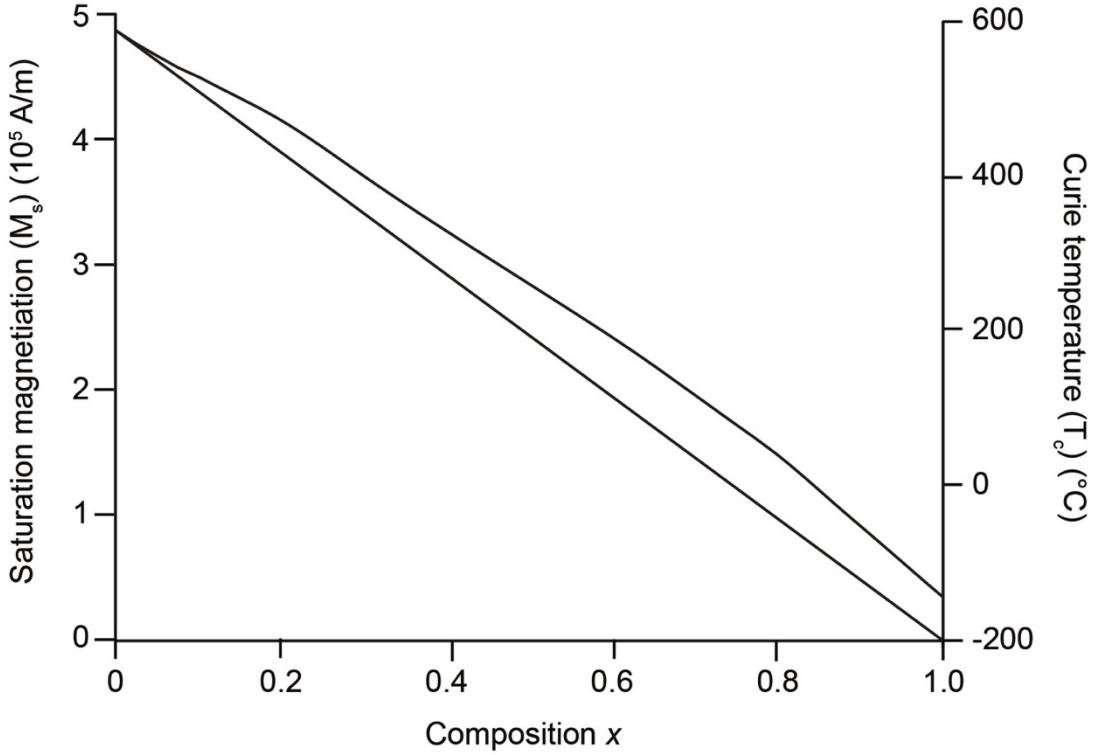

Fig. 2.5 Saturation magnetization and Curie temperature for the titanomagnetite series. Parameter x indicates composition. The left-hand axis is the saturation magnetization (M_s), and the right-hand axis is the Curie temperature (T_c). Modified from Nagata (1961).

Maghemite

Maghemite (γ-Fe_2O_3) is the low-temperature oxidation or weathering product of magnetite. It occurs commonly in both subaerial and oceanic environments, where it can be indicative of soil formation and alteration processes in igneous rocks. Maghemite shares the same composition as hematite but has the same structure as magnetite. By

comparing the structural formula for magnetite $Fe^{3+}[Fe^{3+}Fe^{2+}]O_4$ and maghemite $Fe^{3+}[Fe^{3+}_{5/3}\square_{1/3}]O_4$, it is considered that by changing the 2/3 valence state of original Fe^{2+} to Fe^{3+} together with simultaneously removing 1/3 of the initial Fe^{2+} cations from the B sublattice, magnetite can be oxidized to maghemite. This removal occurs by diffusion, resulting in vacancies (□) in the spinel structure in place of Fe^{2+} cations. The ferrimagnetism of maghemite mainly results from the net magnetic moment of the 2/3 Fe^{3+} cations in the B sublattice. The magnetization decreases from 4.8×10^5A/m for magnetite to 4.2×10^5 A/m for maghemite due to removal of 1/3 of the cations, and *a* decreases from 8.396 Å for magnetite to 8.337 Å for maghemite. Maghemite is usually metastable, and inverts upon heating above about 250 °C to hematite. This instability can make it difficult to determine T_c for maghemite.

Hematite

Hematite (αFe_2O_3) is the ultimate oxidation product of magnetite at ambient temperatures. It can also form by primary high-temperature oxidation during cooling from a melt or as a secondary inversion product of titanomaghemite during later reheating of a rock. Thus, hematite mainly occurs in oxidizing conditions, including humid environments. Fine hematite grains normally have a distinctive bright-red colour. Hematite has a hexagonal close-packed oxygen lattice, which forms a rhombohedral structure with offset, stacked layers of Fe^{3+} cations and triplets of oxygen ions on both sides that make up tetrahedral Fe-O_3-Fe packages (Fig. 2.6). Due to exchange coupling of the Fe-O_3-Fe triplets, the two Fe^{3+} cations in each unit have antiparallel spin moment coupling. This spin arrangement gives hematite its basic antiferromagnetic structure. Although the spins in each unit are parallel to each other, the spins of neighbouring layers are not exactly antiparallel, which gives rise to a canted antiferromagnetism in hematite. The angle between the magnetic moments of these layers results in a weak but stable net

magnetic moment and significant positive susceptibility. Although the magnetization of hematite is more than 200 times weaker than magnetite, it is extremely stable due to its corundum structure. The T_N of hematite is around 675 °C. At low temperatures, hematite undergoes a magnetic phase transition, which is known as the Morin transition. In pure synthetic crystals, the transition occurs at -10 °C; however, the transition temperature decreases in imperfect or impure crystals, including hematite nanoparticles.

2.4.2 The iron oxyhydroxides

Iron oxyhydroxides are observed commonly in weathered metamorphic and igneous rocks, sediments, and soils. Goethite (αFeOOH) is the most important magnetic iron oxyhydroxide, and is stable in soils from humid climates. Goethite can also occur due to the weathering of pyrite (FeS_2) in limestones. Goethite has an orthorhombic crystal system, arranged in double strands, and separated by two rows of vacancies. Goethite is mostly antiferromagnetic, but due to uncompensated spins generated from oxygen ion vacancies and other lattice defects, natural goethite commonly has a weak imperfect antiferromagnetism with a T_N of 120 °C. Below the T_N, goethite acquires a weak but stable thermoremanent magnetization. Hematite can be produced by natural dehydration of goethite and by laboratory heating to 250-400 °C. Goethite also transforms gradually to hematite at ambient temperature in hot, dry climates and is an essential constituent of red sediments. Compared with goethite, lepidocrocite (γFeOOH) is a minor constituent of soils and sediments. It is a paramagnetic oxyhydroxide at room temperature with antiferromagnetic T_N far below 0 °C. Lepidocrocite can convert to maghemite or to goethite by dehydration when heated above 250 °C (Morris & Lauer, 1981; Laberty & Navrotsky, 1998).

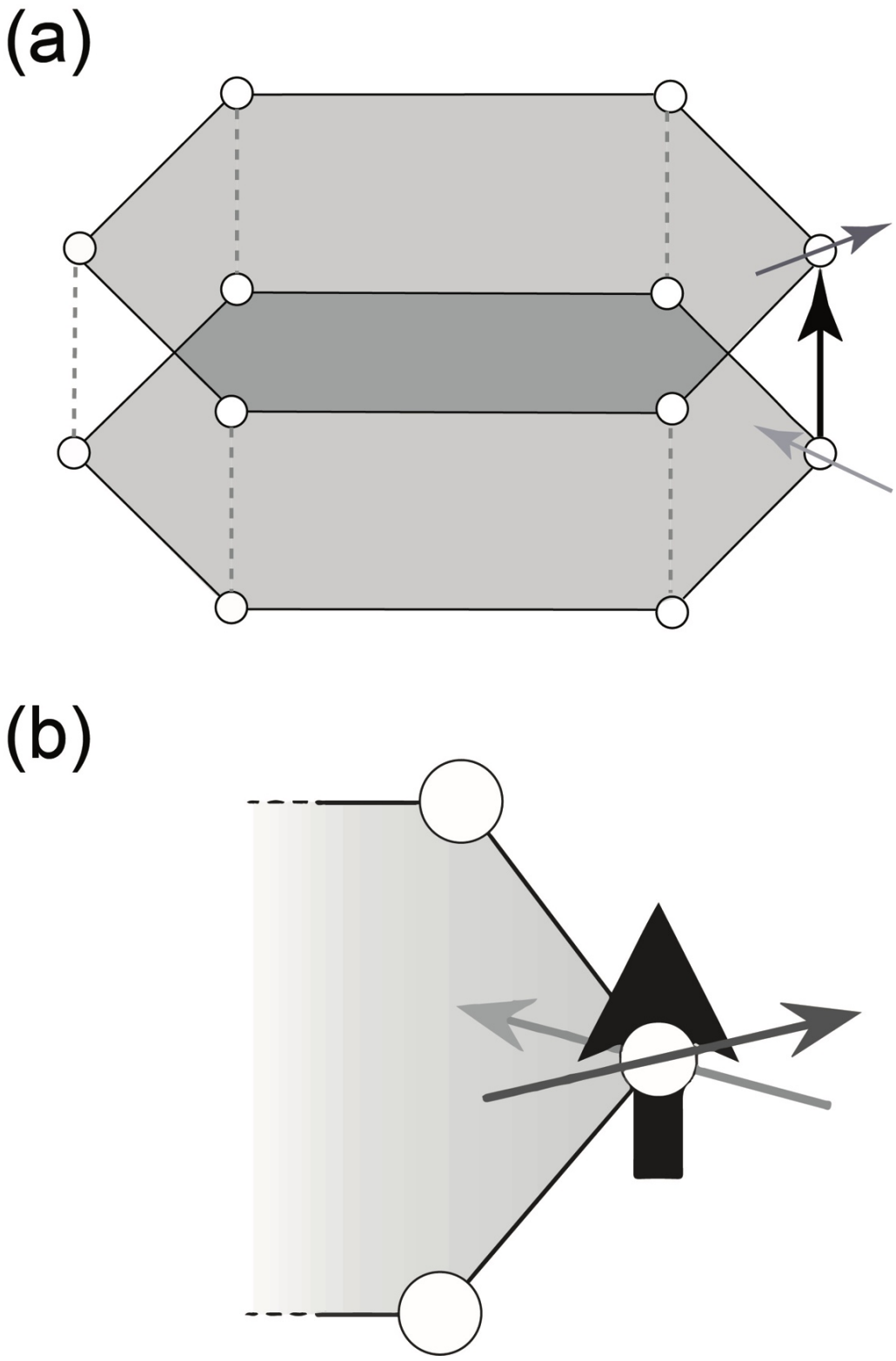

Fig. 2.6 Coupling of Fe^{3+} cationic magnetic moments in hematite (a). The magnetic moment is indicated by the dark (light) grey arrow in the upper (lower) plane. The bold black arrow represents the vector sum of these two almost anti-parallel magnetic moments using a greatly expanded and exaggerated scale (b). Redrawn after Butler (1998).

2.4.3 The iron sulphides

Iron sulphides range in composition from pyrite (FeS_2) to troilite (FeS), although the latter is generally only found in meteorites. FeS_{1+x} ($0 \leq x \leq 1$) is the general formula of iron sulphide, where the compositional parameter x indicates iron sulphide compositions. Pyrrhotite ($Fe_{1-x}S$) ($0 \leq x \leq 0.2$) forms in igneous rocks, in regional metamorphic belts, and in metamorphic aureoles surrounding igneous intrusives; some types of pyrrhotite can form in sediments during diagenesis. Monoclinic pyrrhotite (Fe_7S_8) is a ferrimagnetic iron sulphide. Pyrrhotite polytypes have compositions ranging from Fe_7S_8 to Fe_9S_{10} ($0.11 \leq x \leq 0.14$). Two antiparallel coupled sublattices containing Fe^{2+} ions exist in pyrrhotite, but in the opposite sublattices the number of Fe^{2+} ions is not equal due to the arrangement of lattice vacancies. Thus, monoclinic pyrrhotite is ferrimagnetic. It has a T_c at 320 °C, and its saturation magnetization can reach 1.3×10^5 A/m. Greigite (Fe_3S_4) occurs commonly in sediments formed under sulphate-reducing conditions, and can also form by biomineralization within magnetotactic bacteria. Greigite is the sulphide counterpart of magnetite and has the same inverse spinel structure (Wu et al., 2016). It is ferrimagnetic but thermally unstable, so its T_c remains unknown but is constrained to be >330 °C (Chang et al., 2008; Roberts et al., 2011a).

2.5 Origins of magnetic materials

Environmental magnetism focuses mainly on the variation of magnetic properties of iron-bearing materials in the rock cycle. Magnetic minerals can be affected by chemical, physical, and biological mechanisms. Therefore, environmental magnetism is concerned generally with constraining research questions associated with the following processes: (1) weathering of igneous rocks and soil formation; (2) erosion,

transportation, and deposition of sediments, including biogenic contributions; and (3) postdepositional processes, such as burial and early diagenetic reactions within sediments (Fig. 2.7; Liu et al., 2012a). Overall, through geological time, the flow of material through parts or the entire rock cycle provides the source material for the formation of various soils, sediments, and rocks, including specific magnetic assemblages that are related to physical and chemical conditions specific to the respective formation process. Furthermore, biological activity is also important in driving mineralization processes, including diagenetic degradation and fermentation of organic matter in sediments and soils.

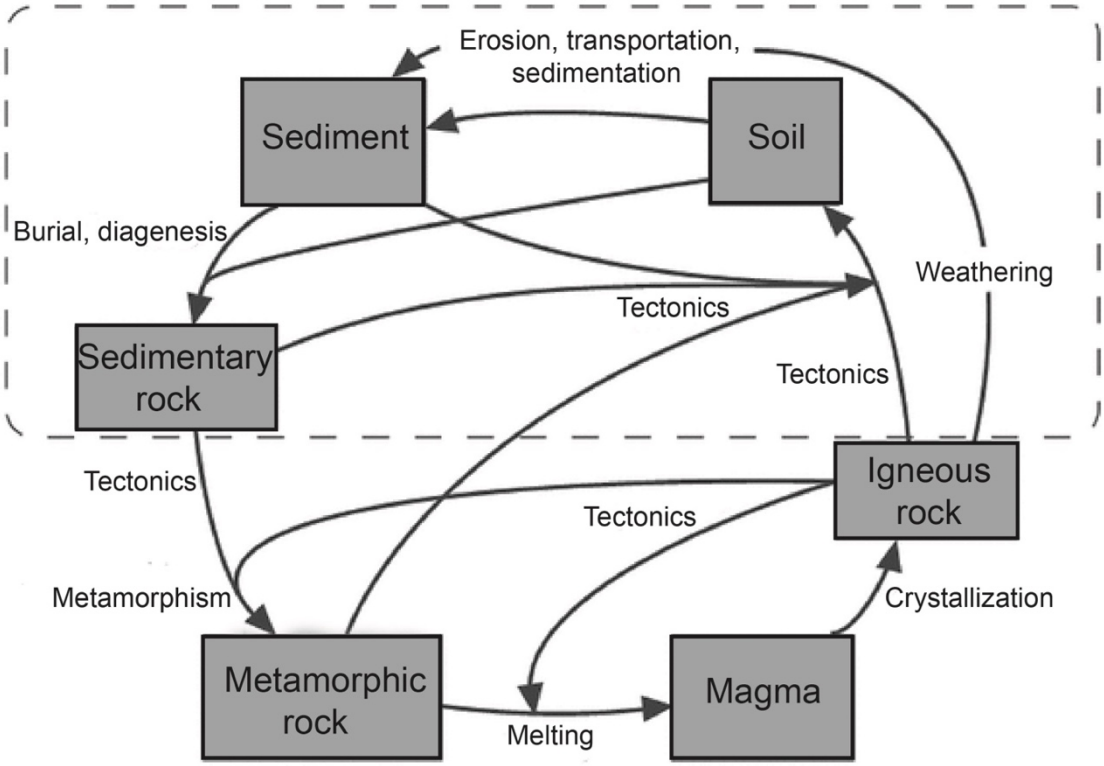

Fig. 2.7 Pathways by which magnetic minerals are produced in Earth's lithosphere, which illustrate the processes that can be studied using environmental magnetism. The dashed boxes represent the settings that are the focus of environmental magnetism. Redrawn after Liu et al. (2012a).

Natural magnetic materials

Magnetic minerals in igneous and metamorphic rocks are derived from crystallization and precursor minerals, respectively. Magnetite normally occurs in oceanic and continental intrusive rocks due to primary or other mineral alteration, such as high temperature oxidation, hydrothermal alteration, or serpentinization (Dunlop & Özdemir, 1997). Monoclinic pyrrhotite also occurs in continental intrusive and plutonic rocks. Titanomagnetite and titanomaghemite occur typically in subaqueous basalts, whereas titanohematites can largely be found in felsic volcanic rocks. In terms of magnetic grain size, coarser particles are common in slowly cooled plutonic and intrusive rocks within Earth's crust, while finer grained minerals typically exist in rapidly cooled extrusive rocks at Earth's surface (Dunlop & Özdemir, 1997).

Detrital particles

In sediments and soils, magnetic mineral assemblages can be a mixture of several components. Magnetic minerals in sediments are often dominated by detrital particles, which are eroded and then transported to the depositional site. Specifically, magnetic minerals in igneous rocks are released through weathering, which begins after they are exposed to air or water. Some of these magnetic and other minerals can be further altered to form new (authigenic) magnetic minerals. After being eroded by wind, water, or ice, these magnetic minerals are transported through a series of mechanisms with variable durations, such as aeolian, riverine, lacustrine or marine processes, and are subsequently deposited in sediments under subaqueous (lacustrine or marine) or subaerial (terrestrial) environmental conditions (Maher, 2011). During these processes, detrital particles may be weathered physically and/or chemically to some extent; however, coarse-grained lithogenic magnetic minerals can be well preserved after deposition. Furthermore, variable diagenetic alteration usually takes place shortly after deposition as a

consequence of the changing sedimentary geochemical environment. During these processes, due to dissolution and recrystallization, detrital magnetic minerals can be replaced by authigenic magnetic minerals. In soils and paleosols, these processes are referred to as pedogenesis and in sediments, post-depositional change is referred to as diagenesis.

Biogenic particles

Another important contributor to the magnetization of sediments is biogenic particles. Biogenic minerals are usually produced by biological processes within sedimentary environments in two major ways, namely biologically induced mineralization (BIM) and biologically controlled mineralization (BCM) (Lowenstam, 1981). Iron ions are used as terminal electron acceptors by BIM bacteria. Magnetite formed by BIM bacteria normally grows outside bacterial cells. This kind of magnetite is usually fine-grained, but poorly crystalline. In the BCM category, magnetotactic bacteria (MTB) produce highly crystalline single-domain (SD) magnetite or greigite within their cells. The SD particles produced by MTB normally grow in a chain structure (Fig. 2.8). After MTB die, their remains, which are referred to as magnetofossils, can record a natural remanent magnetization in sediments. Magnetofossils can potentially record environmental changes because a given MTB species is often associated with specific environmental and redox conditions (Li et al., 2020a).

Authigenic particles

Authigenesis of hematite, maghemite, and magnetite occur typically under oxic conditions, while greigite and pyrrhotite form in anoxic environments. In addition, magnetite and, in some cases, pyrrhotite are found in metamorphic rocks, which form under specific chemical environments at elevated temperatures and pressures. These

chemical transformations are caused by deep burial or by the influence of metamorphism within sedimentary rocks. High temperatures and/or pressures can cause melting, so that the rock cycle returns to its starting point (Fig. 2.7).

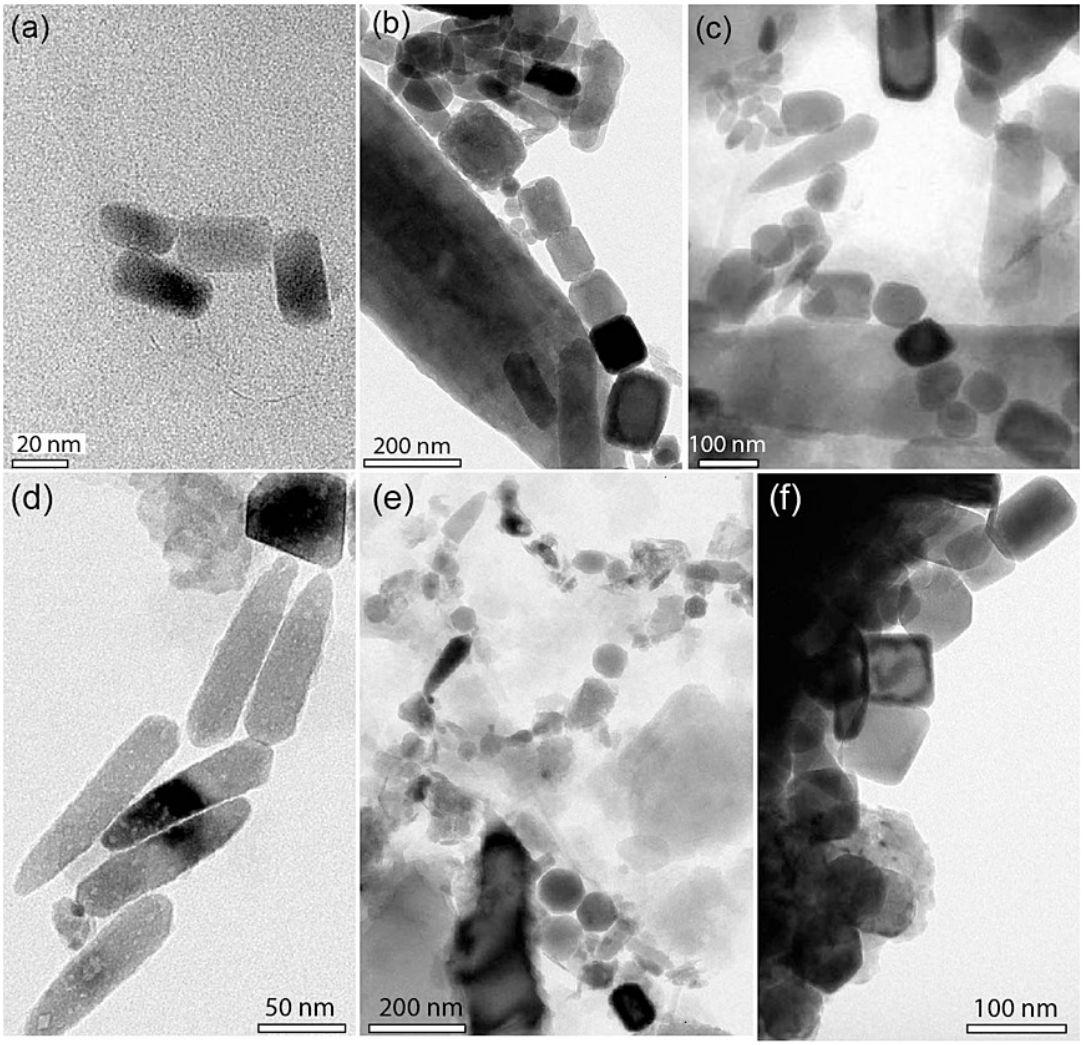

Fig. 2.8 TEM images of magnetofossils from Chang et al. (2014).

2.6 Magnetic properties of natural materials

2.6.1 Room temperature properties

Magnetic susceptibility

Low-field magnetic susceptibility (χ, mass susceptibility; κ, volume susceptibility) is an extensively used magnetic parameter. χ can be measured rapidly with an inductance bridge and is used frequently as a proxy for magnetic mineral concentration, especially

magnetite concentration. Compared with other parameters that can indicate magnetite concentration, χ is a complex parameter because all material contributes to the magnetic susceptibility, such as ferrimagnetic, antiferromagnetic, paramagnetic, and diamagnetic minerals. When the magnetite concentration is larger than 1%, the paramagnetic contribution of χ is negligible compared to the contribution of ferrimagnetic minerals. In sediments and soils, the paramagnetic contribution is often significant and the ferrimagnetic contribution (χ_{ferri}) can only be obtained after subtracting the paramagnetic or high-field susceptibility (χ_{high}): $\chi_{ferri} = \chi - \chi_{high}$. For strongly magnetic minerals, χ varies mildly with grain size within the SD-MD (multidomain) range; χ also varies strongly for different magnetic minerals. However, superparamagnetic (SP) grains have a markedly higher χ than stable SD (SSD) or MD grains. The response of small (submicron) magnetic particles near the SP/SSD boundary (with sizes of tens of nanometres) depends on applied field frequency so that the frequency-dependent magnetic susceptibility can be used to detect SP particles (Maher, 1988; Worm, 1998). By increasing the measurement frequency of χ, the relaxation time(s) of the grains can become longer than the measurement time, and a grain that has SP behaviour at low frequency has SD behaviour at a higher frequency, which lowers its χ distinctly. The absolute frequency-dependent susceptibility (χ_{fd}) can be calculated as: $\chi_{fd} = \chi_{low} - \chi_{high}$, where χ_{low} is the low-field susceptibility. Besides, χ_{fd}% (= $\chi_{fd} \times 100\%$) is associated with the grain size distribution of the SP/SD fraction. SP behaviour is also closely related to temperature, which means that it can also be useful to measure χ as a function of temperature below room temperature to detect SP particles.

Anhysteretic remanent magnetization (ARM)

The anhysteretic remanent magnetization (ARM) is a key magnetic parameter related to magnetic particle concentration and size. ARM is acquired in the laboratory by

placing a sample in an asymmetric alternating field (AF) created by the imposition of a small direct current (DC) bias field. ARM is sometimes regarded as an ideal remanence because it is free from hysteresis. ARM is usually expressed as the susceptibility of ARM (χ_{ARM} = ARM/DC bias field) because it is proportional to the DC bias field. Banerjee et al. (1981) proposed that the different behaviours of χ and ARM (or χ_{ARM}) can be a useful indicator of magnetic grain size variation. χ_{ARM} is especially sensitive to the presence of small grain sizes (SD and vortex state grains), whereas χ is relatively insensitive to particle size. Thus, χ_{ARM}/χ can be used to detect relative abundance variations of fine and coarse magnetic grains in samples.

Isothermal remanent magnetization (IRM)

The isothermal remanent magnetization (IRM) is also used to indicate magnetic mineral concentration variations. An IRM is imparted by placing a sample in a strong magnetic field, thus magnetizing it along the applied field direction. The saturation remanent magnetization (M_r) is the magnetization that remains after removal of an applied field above which its remanent magnetization no longer increases, and is equivalent to the saturation IRM (SIRM).

χ_{ARM}/SIRM, like χ_{ARM}/χ, is also grain size dependent. χ_{ARM}/SIRM is sometims preferred because it is only affected by particles with a stable remanence (i.e., stable SD and coarser particles), while χ_{ARM}/χ can be also be affected by SP, paramagnetic, and diamagnetic minerals. Tauxe (1993) proposed that SIRM/χ may be better than χ_{ARM}/χ for estimating relative grain size variations because SIRM is comparatively insensitive to variations in the inducing field, and can generally be used to indicate the magnetic mineral concentration in sediments. SIRM/χ can also indicate the presence of SD greigite grains in sedimentary environments, where enhanced SIRM compared to χ suggests that SD particles have greater magnetic remanence recording ability.

Hysteresis

For ferrimagnetic materials, a remanent magnetization is preserved after removal of an applied magnetic field, which is due to magnetic hysteresis. At lower applied fields, and starting from a demagnetized state, the magnetization will increase dramatically with increasing external field; at higher fields, the magnetization curve flattens as magnetic saturation is approached (Fig. 2.9). If the applied field cycles between high values of both forward and reversed polarity, the sample magnetization follows a so-called hysteresis loop (Fig. 2.9). The hysteresis loop reflects the whole magnetization process, and key hysteresis parameters include the saturation magnetization (M_s), saturation isothermal remanent magnetization (M_r), coercivity (B_c), and coercivity of remanence (B_{cr}), which can can be used to understand the magnetic properties of samples. M_s refers to the saturation magnetization when the external field is large enough to magnetically saturate the sample. When a critical field is reached, the induced magnetization ceases to respond to increasing external fields because the electronic spins are totally aligned (Fig. 2.9). M_s is independent of particle size variations and composition, and is only affected by magnetic mineral content, so it can be used to express magnetic mineral concentration variations. Due to the partial loss of magnetic moment alignment that occurrs after removal of an applied field, M_r is normally lower than M_s. B_c is the reversed field required to return the magnetization from saturation to zero, and B_{cr} is the external back-field required to drive the remanence of the sample from saturation to zero.

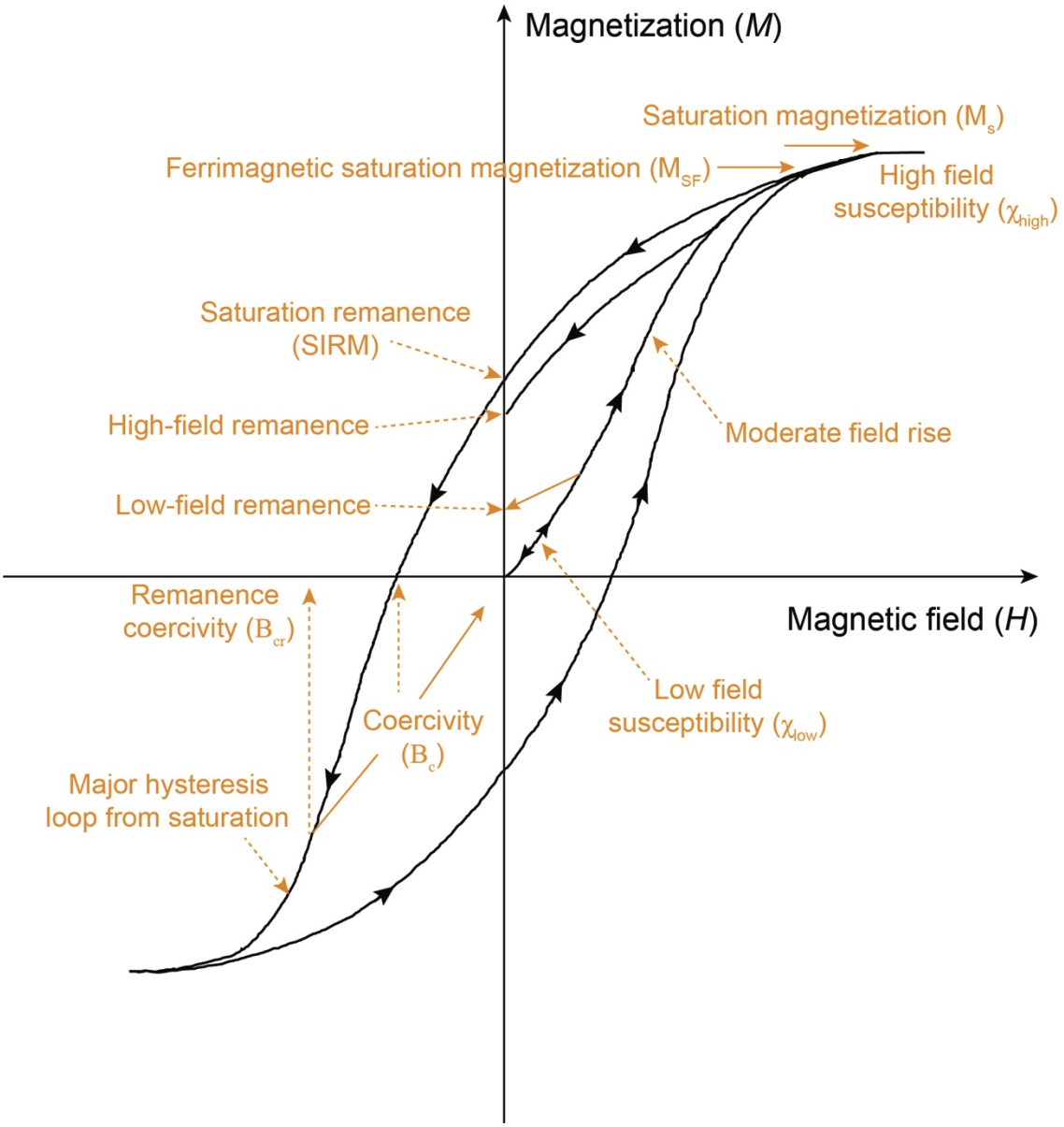

Fig. 2.9 Magnetic hysteresis loop and magnetization curve indicating M_s, B_c, and B_{cr}.

First-order reversal curves (FORCs) are partial hysteresis loops that are used to detect magnetic grain size distributions and magnetostatic interactions among particles. FORCs are measured cyclically between a large positive field and a reversal field (Mayergoyz, 1986). FORC measurement begins with saturating a sample in a large positive applied field. The field is then reduced to a reversal field B_a (Fig. 2.10). The FORC is the magnetization curve that is measured as the applied field increases from B_a

back to saturation at field steps B_b. The magnetization $M(B_a, B_b)$ is acquired for various B_b field values between a B_a value and the saturation field, where B_b is normally larger than B_a (Fig. 2.10). The same measurement procedure is repeated for different B_a values to obtain a series of FORCs. A FORC distribution is defined as the mixed second derivative (Pike et al., 1999; Roberts et al., 2000):

$$\rho(B_a, B_b) = -\frac{\partial^2 M(B_a, B_b)}{2 \times \partial B_a \partial B_b}, \quad (2.6.1)$$

which is well defined for $B_b > B_a$.

A FORC diagram is normally plotted in the transformed coordinate system from (B_a, B_b) to $(B_i = (B_a + B_b)/2, B_c = (B_a - B_b)/2)$, which provides useful information about magneitc mineral properties. Specifically, variations along the vertical B_i axis are indicative of magnetostatic interactions in SD particle systems, while variations along the horizontal B_c axis are indicative of the coercivity distribution of the sample (Pike et al., 1999; Roberts et al., 2000).

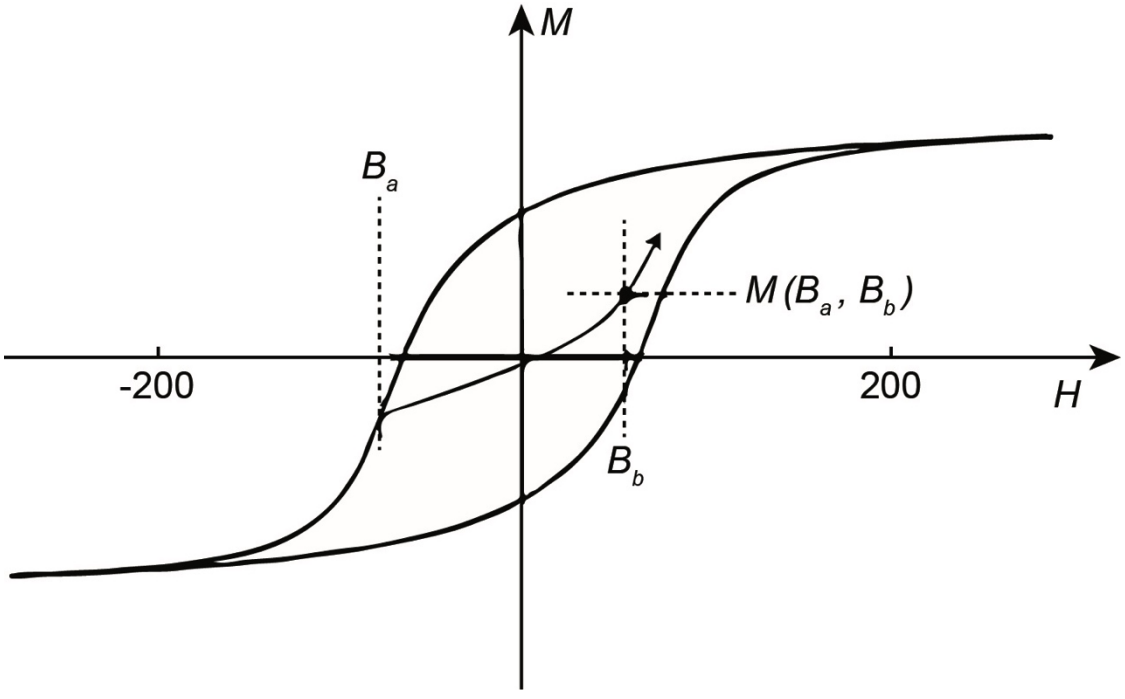

Fig. 2.10 Illustration of a FORC measurement.

Coercivity-dependent parameters

B_{cr} is useful for assessing magnetic mineralogy and particle size variations. The micro-coercivity represents the magnitude of the magnetic field needed to shift the magnetization of an individual particle from one easy axis direction to another. The presence of weakly magnetic imperfect antiferromagnetic particles is generally masked by strongly magnetic ferrimagnetic minerals, which makes it difficult to detect these weakly magnetic minerals within mixed magnetic mineral assessblages. Imperfect antiferromagnetic minerals generally have much higher coercivities than ferrimagnetic minerals and are referred to as being magnetically "hard". Thus, it is possible to discriminate between minerals on the basis of their magnetic "hardness" by measuring IRM acquisition as a function of applied field strength. The "hard" IRM (HIRM) was introduced as a proxy for the mass concentration of high-coercivity minerals, such as goethite and hematite. HIRM is expressed as $(SIRM + IRM_{-0.3T})/2$, in which $IRM_{-0.3T}$ is the residual IRM after the SIRM is exposed to a reversed field of 0.3 T. The S-ratio = $(- IRM_{-0.3T}/SIRM)$ is used as a proxy for relative abundance variations of low- to high-coercivity minerals (King & Channell, 1991). High S-ratios suggest that ferrimagnetic minerals, such as magnetite, are dominant, whereas low values indicate relative increases in hematite (goethite) contents. The magnetic coercivity of a single mineral also varies with grain size. Liu et al. (2007) introduced the L-ratio $(= (SIRM + IRM_{-0.3T})/(SIRM + IRM_{-0.1T}))$, which indicates coercivity or grain size distribution variations of the high-coercivity mineral component.

2.6.2 Temperature-dependence of magnetic properties

The most significant temperature-dependent characteristic is T_c for ferrimagnets and T_N for antiferromagnets. Above T_c (or equivalently T_N), thermal energy overcomes magnetic exchange anisotropy. Below T_c, a remanent magnetization is "blocked" at the blocking temperature (T_b). Above T_b a material is superparamagnetic and in turn becomes paramagnetic above T_c. When a material passes through its T_b, χ increases dramatically, resulting in a χ peak at a temperature below T_c. This feature is referred to as a Hopkinson peak. A Hopkinson peak can also be caused by the domain wall unpinning in coarse MD grain near T_c. In nature, samples normally have a distribution of grain sizes. Thus, the maximum T_b in an assemblage of particles will typically coincide with T_c.

Low-temperature magnetic analyses can also provide information to assess magnetic mineralogy. Below room temperature, several magnetic minerals undergo phase transitions, with marked magnetic behaviour changes occurring upon cooling or warming through a specific temperature. The T_N for siderite and rhodochrosite occur at around 30-40 K (Housen et al., 1996), the Besnus transition for monoclinic pyrrhotite occurs at 34 K (Dekkers et al., 1989; Rochette et al., 1990), the Verwey transition for magnetite occurs at 110-120 K (Verwey, 1939), and the Morin transition for hematite occurs at about 250-260 K (Morin, 1950). Expression of these magnetic transitions is also affected by grain size and stoichiometry of the respective minerals.

For stoichiometric magnetite, with decreasing grain size from the MD state to the SD state, the corresponding amplitude of the magnetization change at T_v decreases progressively. The Verwey transition also becomes less evident with increasing oxidation (Cui et al., 1994; Özdemir et al., 1993), with increased nonstoichiometry depressing and broadening the Verwey transition and shifting T_v to lower temperatures.

Overall, mineral magnetic properties and environmental magnetism have widespread applicability in understanding the magnetic signals recorded by eastern Mediterranean sediments. The above described environmental magnetic theory is applied to address questions related to mineral magnetic signals and environmental signals recorded in eastern Mediterranean sediments, as outlined in the following chapters.

Chapter 3

Assessment and integration of bulk and component-specific methods for identifying mineral magnetic assemblages in environmental magnetism

---

This chapter has been published as: **Qian, Y**., Roberts, A. P., Liu, Y., Hu, P., Zhao, X., Heslop, D., Grant, K. M., Rohling, E. J., Hennekam, R., & Li, J. (2020). Assessment and integration of bulk and component-specific methods for identifying mineral magnetic assemblages in environmental magnetism. *Journal of Geophysical Research*: *Solid Earth*, *125*(8), e2019JB019024. https://doi.org/10.1029/2019jb019024 with permission of use for thesis from John Wiley and Sons (license number: 5030780609105).

Abstract

Magnetic parameters are used extensively to interpret magnetic mineral assemblage variations in environmental studies. Conventional room temperature measurements of bulk magnetic parameters, like the anhysteretic remanent magnetization (ARM) and the ratio of the susceptibility of ARM to magnetic susceptibility (χ), can reflect, respectively, magnetic mineral concentration and/or particle size variations in sediments, although they are not necessarily well suited for identifying magnetic components within individual magnetic mineral assemblages. More advanced techniques, such as first-order reversal curve (FORC) diagrams and low-temperature (LT) magnetic measurements, can enable detailed discrimination of magnetic assemblages. Here, we integrate conventional bulk magnetic measurements alongside FORC diagrams, LT measurements, and X-ray fluorescence core-scan data, transmission electron microscope observations, and principal component analysis of FORC diagrams to identify and quantify magnetic mineral assemblages in eastern Mediterranean sediments. The studied sediments were selected because they contain complexly varying mixtures of detrital, biogenic, and diagenetically altered magnetic mineral assemblages that were deposited under varying oxic (organic-poor marls) to anoxic (organic-rich sapropels) conditions. Conventional bulk magnetic parameters provide continuous records of environmental magnetic variations, while more time-consuming LT and FORC measurements on selected samples provide direct ground-truthing of mineral magnetic assemblages that enables calculation of magnetization contributions of different end members. Thus, a combination of conventional bulk parameters and advanced magnetic techniques can provide detailed records from which the meaning of environmental magnetic signals can be unlocked.

3.1. Introduction

Magnetic parameters have been used widely in paleoenvironmental studies since the 1980s (e.g., Kent, 1982; Thompson et al., 1980) to detect variations in minute quantities of magnetic minerals within sedimentary strata. For example, Banerjee et al. (1981) proposed that the ratio of the susceptibility of anhysteretic remanent magnetization (χ_{ARM}) to magnetic susceptibility (χ) can be used for rapid estimation of magnetic grain size variations. Parameters such as χ, χ_{ARM}, and the isothermal remanent magnetization (IRM) or saturation IRM (SIRM) are used commonly to indicate variations in the concentration of magnetic particles (e.g., Evans & Heller, 2003; Liu et al., 2012a; Maher & Thompson, 1999; Thompson & Oldfield, 1986; Verosub & Roberts, 1995). These parameters are generally measured at room temperature with focus on detecting ferrimagnetic minerals. More advanced methods such as first-order-reversal curve (FORC) (Pike et al., 1999; Roberts et al., 2000) and low-temperature (LT) magnetic measurements (e.g., Chang et al., 2016; Passier & Dekkers, 2002) are more time-consuming, but can provide more detailed information for characterizing magnetic mineral assemblages. Supplementary transmission electron microscope (TEM) observations are also valuable for confirming the mineralogy of identified magnetic assemblages. FORC diagrams provide empirical information about the distributions of coercivities (B_c) and local interaction fields (B_i) for magnetic particle assemblages. For example, Yamazaki (2008) semi-quantitatively estimated the relative abundances of a non-interacting single-domain (SD) component and an interacting SD component in North Pacific Ocean sediments using FORC diagrams, and concluded that χ_{ARM}/SIRM does not necessarily reflect magnetic particle size due to the dependence of ARM acquisition on magnetostatic interactions.

Although advanced magnetic techniques, such as LT and FORC measurements, can provide more information on magnetic mineral assemblages within natural samples compared to conventional bulk magnetic parameters, their interpretations are often based on qualitative assessments and empirical "fingerprinting" (Heslop, 2015; Harrison et al., 2018). Recently, application of principal component analysis (PCA) to analyze FORC diagrams for large sample sets (FORC-PCA), as introduced by Lascu et al. (2015), has been used to discriminate magnetic mineral assemblages in sediments. For example, Channell et al. (2016) applied FORC-PCA to unmix biogenic and detrital magnetic assemblages of a sediment core from Rockall Trough to characterize glacial/interglacial sedimentation on the Northwest Iberian margin. Harrison et al. (2018) further improved the FORC-PCA method to capture both reversible and irreversible magnetization contributions and provided objective criteria to aid identification of physically realistic end members. Roberts et al. (2018) also used FORC-PCA to illustrate how magnetic properties can be used to assess diagenetic processes in reducing sedimentary environments.

In the eastern Mediterranean Sea, organic-rich sedimentary intervals known as sapropels are intercalated cyclically with marls (organic-poor sediments) from the Late Miocene to the Holocene (Emeis et al., 1996, 2000; Hilgen, 1991; Larrasoaña et al., 2003a; Liu et al., 2012b; Lourens et al., 1996; Rohling, 1994; Rohling et al., 2015; Schenau et al., 1999). Sapropels formed during phases of enhanced surface ocean productivity caused by large fluvial discharge events during North African monsoon maxima (Rossignol-Strick et al., 1982; Rossignol-Strick, 1983, 1985). Increased sedimentary organic matter preservation and its subsequent microbial degradation leads to complex post-depositional diagenesis (Larrasoaña et al., 2003a, 2006; Liu et al., 2012b; Passier et al., 2001; Roberts et al., 1999; van Santvoort et al., 1997). Sapropels

were deposited under anoxic sulphidic conditions, which promotes reductive dissolution of magnetic minerals (Dekkers et al., 1994; van Santvoort et al., 1997). When sulphate-reducing conditions are strong, excess sulphide diffuses downward into underlying marls, forming a 'dissolution front' (Larrasoaña et al., 2006; Passier et al., 2001). Mediterranean bottom waters were reoxygenated at the end of periods of sapropel formation and an 'oxidation front' then formed at the top of the most recent organic-rich layer (Higgs et al., 1994; de Lange et al., 2008; Larrasoaña et al., 2003a, 2006; Liu et al., 2012b; Passier et al., 2001; Thomson et al., 1999). Subsequently, Fe^{2+} in sapropels is oxidized to form iron oxides, which can enhance the magnetization at oxidation fronts above sapropels (Larrasoaña et al., 2003a, 2006; Liu et al., 2012b; Passier & Dekkers, 2002). Between sapropels, marls supplied by aeolian dust and fluvial inputs are deposited under oxic conditions. Therefore, eastern Mediterranean sediments contain complex mixtures of detrital and diagenetically altered magnetic minerals, and potentially biogenic magnetite, that make them a suitable subject for evaluating the effectiveness of a series of advanced techniques used in environmental magnetism compared to conventional bulk magnetic parameters.

Magnetic mineral variations have been identified in sapropel-bearing eastern Mediterranean sediments through bulk magnetic measurements and diffuse reflectance spectroscopy (Heslop et al., 2007; Kruiver & Passier, 2001; Larrasoaña et al., 2003a, 2006; Liu et al., 2012b; Roberts et al., 1999; Passier et al., 2001). However, ambiguity remains concerning some important environmental magnetic processes. For example, it has been suggested that enhanced concentrations of biogenic magnetite produced by magnetotactic bacteria (MTB) occur at oxidation fronts above sapropels (Passier et al., 2001; Kruiver and Passier, 2001), but this interpretation has not been confirmed directly by TEM observations. Magnetic mineral dissolution has been reported in sapropels and

within dissolution intervals below sapropels (Channell et al., 1990; Larrasoaña et al., 2003a, 2006; Passier et al., 2001; Roberts et al., 1999), where the extent to which magnetic minerals were dissolved depends on the intensity of sulphidization. These issues can be addressed by detailed analyses of magnetic mineral assemblages in eastern Mediterranean sediments with advanced environmental magnetic techniques as presented here. In this study, we integrate high-resolution bulk magnetic, FORC, and LT magnetic measurements, TEM observations, and FORC-PCA in conjunction with published calibrated X-ray fluorescence (XRF) core-scan data (Grant et al., 2017) to investigate magnetic mineral assemblages within sapropel-bearing sediments from the eastern Mediterranean Sea. Our aim is to make use of the variable magnetic mineral content of eastern Mediterranean sediments to assess the information provided by bulk and component-specific methods to cross-compare and illustrate the benefits of both approaches in identifying mineral magnetic assemblages in environmental magnetism.

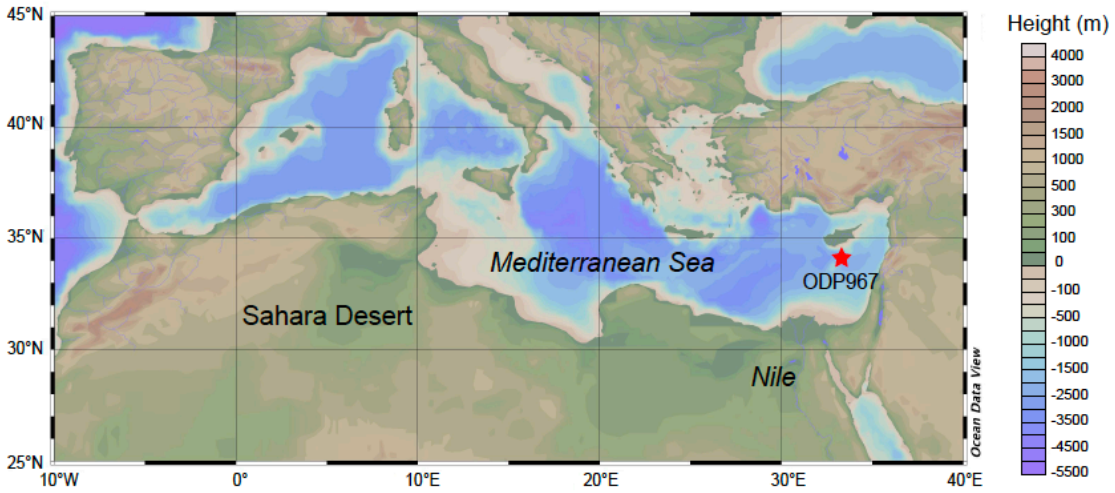

Fig. 3.1 Location of ODP Site 967 from which sediments were collected and analysed in this study. The map was generated with Ocean Date View (Schlitzer, 2014).

3.2. Samples and Methods

3.2.1 Samples

The studied eastern Mediterranean sediments contain complex magnetic mineral mixtures with detrital and diagenetically altered phases, and potentially biogenic magnetite, which are encountered widely in different geologic settings. These sediments were collected from Ocean Drilling Program (ODP) Site 967 (34°04'N, 32°43'E, water depth 2553 m), which was recovered during ODP Leg 160 (Shipboard Scientific Party, 1996) on the northern slope of Eratosthenes Seamount (Fig. 3.1). Core sections were sampled with 'u-channels' from the archive halves of cores along a continuous composite section (Sakamoto et al., 1998) at the IODP core repository in Bremen, Germany, in 1995 and have been kept in cold storage since sampling. U-channel measurements used here are from Stoner et al. (1998) and were made within two years of sampling. To obtain higher-resolution measurements in this study, u-channel samples were sliced at 1-cm intervals into discrete non-magnetic 2×2×2 cm plastic cubes and were stored thereafter in a refrigerator. The studied sequence, from Hole 967C core sections 5H6 to 5H7, spans approximately 2.7 m, which occurs at depths of between 49.99 and 52.69 meters based on the composite depth section of Grant et al. (2017). This interval ranges in age from 1.59 to 1.71 Ma based on the age model of Grant et al. (2017) for Site 967. Five sapropels of two types occur in this interval (Fig. 3.2). These two types of sapropels are representative sapropels ('type 2' sapropels with both oxidation and dissolution intervals in the classification of Larrasoaña et al. (2003b); dark grey shaded bars in Figs. 3.2-3.7) and weakly developed sapropels ('type 3' sapropels without dissolution intervals in the classification of Larrasoaña et al. (2003b); light grey shaded bars in Figs. 3.2-3.7). A total of 221 discrete samples were collected for bulk environmental magnetic measurements

across the studied stratigraphic interval. Based on bulk magnetic results, thirty-four samples were selected for more detailed analyses and were packed into non-magnetic gelatin-capsules for FORC measurements (green circles, Fig. 3.3). A further five samples were chosen for LT and TEM analyses (black circles, Fig. 3.3) (see Table S1).

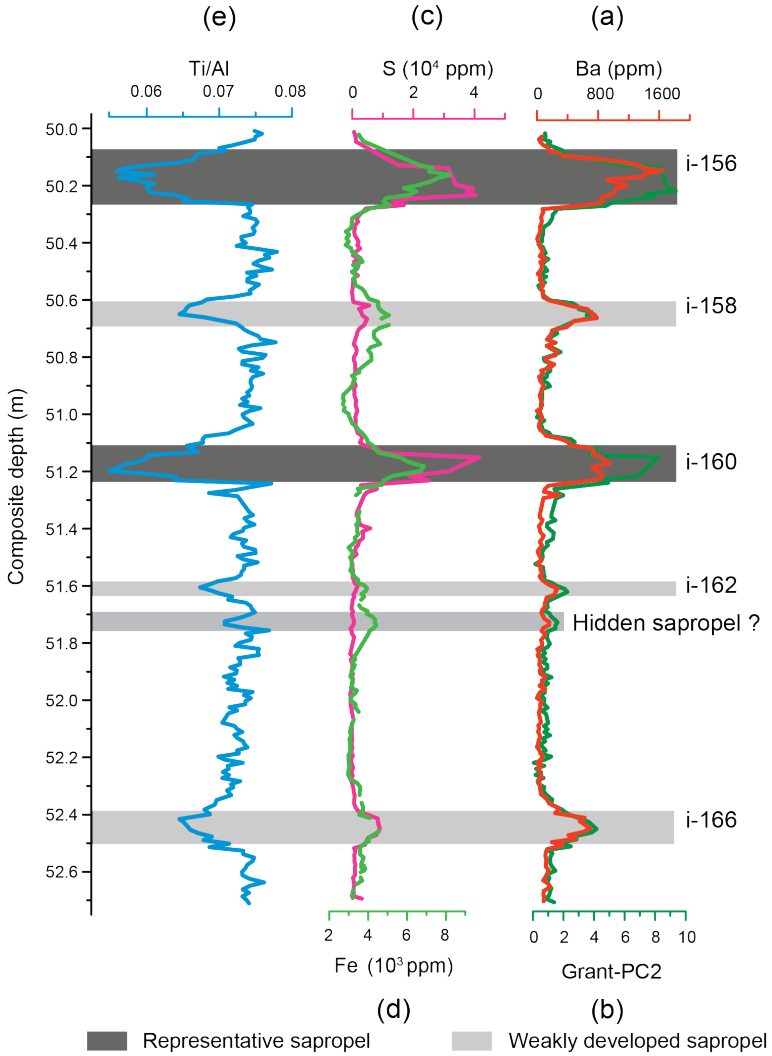

Fig. 3.2 Geochemical data from ODP Site 967 for sediments between 1.59 and 1.71 Ma (Grant et al., 2017). (a, b) Elevated Ba (orange) and Grant-PC2 (dark green) indicate sapropel boundaries (see Thomson et al. (1995) and Nijenhuis et al. (1999)), where Grant-PC2 represents the use of PCA by Grant et al. (2017) to detect sapropel boundaries based on a combination of several elements; (c) S concentration (pink); (d) Fe concentration (light green); (e) Ti/Al ratio (blue). Dark grey shaded bars indicate the positions of representative sapropels. Light grey shaded bars indicate the positions of weakly developed sapropels. A bar with intermediate grey shading indicates the position of a suspected 'hidden' sapropel with minor Ba enrichment. Sapropel stratigraphy is after Emeis et al. (2000), where "i-" followed by a number denotes the insolation cycle represented by the identified sapropels.

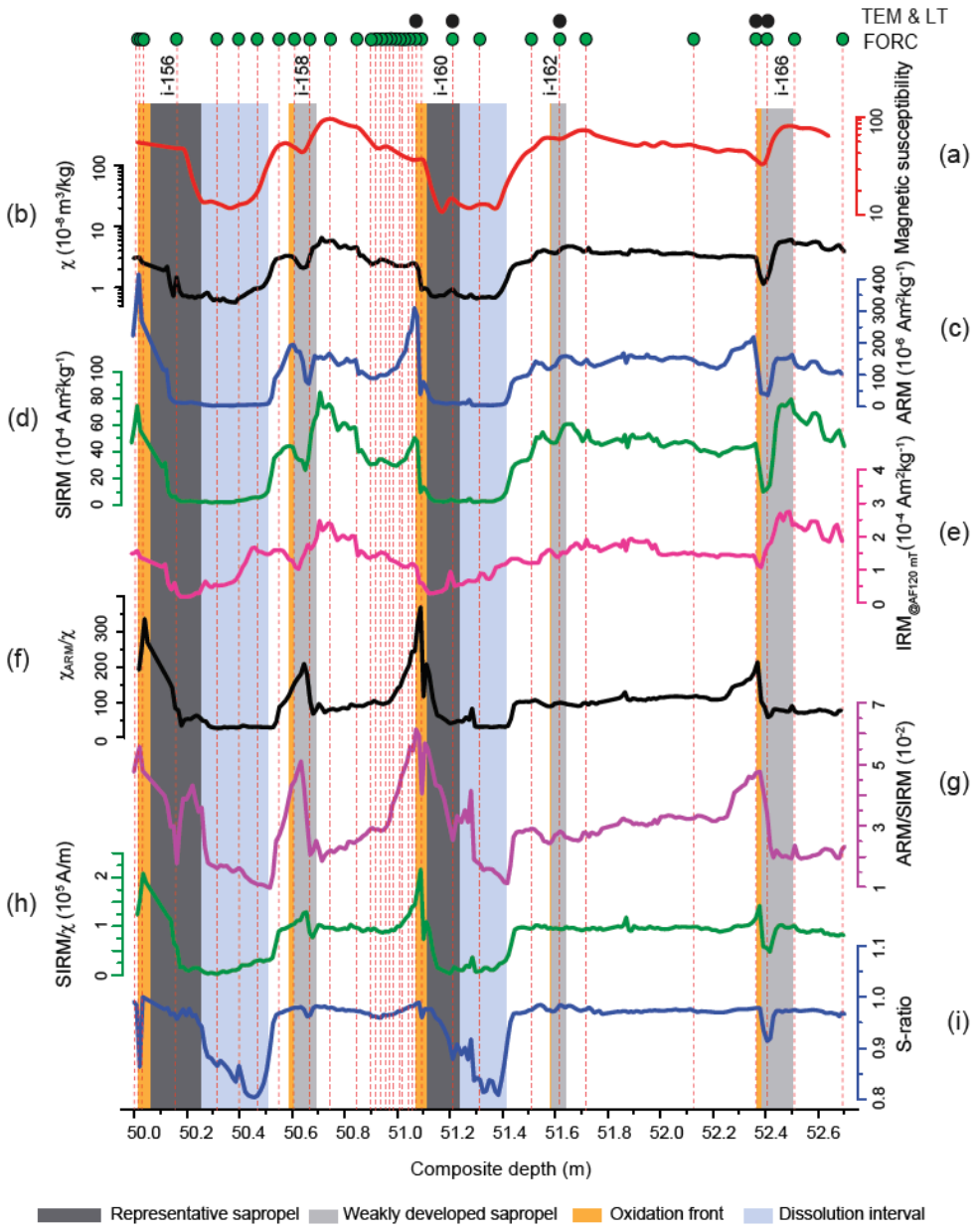

Fig. 3.3 Down-core variations of magnetic mineral concentration, particle size, and coercivity parameters. For methods used for magnetic measurements, see Section 2.2. (a) Shipboard whole-core magnetic susceptibility data for C5H6 and C5H7 from Emeis et al. (1996) (uncorrected instrument units; red); discrete sample data, including (b) χ (black); (c) ARM (blue); (d) SIRM (green); (e) $IRM_{@AF120\ mT}$ (magenta); (f) χ_{ARM}/χ (black); (g) ARM/SIRM (purple); (h) SIRM/χ (green), and (i) S-ratio (dark blue). Thirty-four green circles (top) indicate the locations of samples subjected to FORC measurements and five black circles (top) represent the locations of samples subjected to LT measurements and TEM observations. As indicated in Fig. 3.2, dark grey shaded bars indicate the positions of representative sapropels, light grey shaded bars indicate the positions of weakly developed sapropels, orange shading above sapropels indicates the positions of oxidation fronts, and light blue shading below representative sapropels indicates the positions of dissolution intervals. Sapropel stratigraphy is after Emeis et al. (2000).

3.2.2 Storage diagenesis

Changes in sediment magnetic properties can occur when organic-rich sediments oxidize during storage (e.g., Oldfield et al., 1992; Richter et al., 1999). Such susceptibility or remanence losses are referred to as "storage diagenesis" (Oldfield et al., 1992). Roberts et al. (1999) observed marked susceptibility and remanence losses in Pliocene eastern Mediterranean sapropels, which Reinholdsson et al. (2013) suggested could have been caused by the oxidation of biogenic greigite during storage. Observation of these losses in eastern Mediterranean sapropel-bearing sequences makes it reasonable to check whether other sediments recovered during ODP Leg 160 experienced similar losses. Marked remanence losses are evident when shipboard measurements are compared with U-channel measurements made within two years of sampling for Sites 966, 967, and 969 (Stoner et al., 1998). Remanence losses are most marked for Site 966; we calculate here that on average only 1% of the shipboard natural remanent magnetization (NRM) remained in the measurements of Stoner et al. (1998) for Site 966.

To assess remanence losses for the studied interval of Site 967, we compare shipboard whole-core magnetic susceptibility measurements that were made before the cores were split (Emeis et al., 1996) with our discrete sample measurements made >20 years later (Fig. 3.3a, 3.3b). Cross-calibration of volume- and mass-normalized susceptibility results has not been undertaken, but similar variations between the two data sets indicates that any storage diagenesis in the studied intervals has not obscured expression of the magnetic property cycles studied here. Comparison of shipboard NRM measurements after AF demagnetization at 25 mT (the only shipboard remanence measurement made) with the U-channel measurements of Stoner et al. (1998) for the interval of Site 967 studied here indicates that on average only 41% of the initial NRM remained at the time of u-channel measurement (for 28 measurements points) (Fig. S1a).

The original NRM cyclicity associated with variations through sapropels is clearly evident in both data sets in Fig. S1a. We did not measure the NRM in this study, so we compare our ARM data for Hole 967C with those from Stoner et al. (1998), which were measured on equivalent sections of Hole 967B (Fig. S1b). Despite the fact that the measurements are not from identical sediments, there is good agreement between the data sets with no evidence for further remanence loss. The amplitude of ARM variations for the discrete samples is larger, as would be expected because they are less smoothed. These data confirm that storage diagenesis appears to have been associated with early drying of the cores and that minimal remanence loss has occurred in the intervening 20+ years.

Oldfield et al. (1992) demonstrated that remanence losses will occur in association with iron oxide oxidation during dehydration of organic-rich sediments, and that such losses are not necessarily an indicator of greigite oxidation. The fact that remanence losses are observed throughout the studied sediment interval (Fig. S1a), including within sapropels and intervening oxic sediments, is consistent with the interpretation of Oldfield et al. (1992). We, therefore, interpret the observed storage diagenesis as indicating losses to most of the magnetic mineral fraction. Despite these losses, original cyclicities are preserved and our results below reveal the presence of original detrital and biogenic magnetic minerals, with magnetic variations driven by non-steady state diagenesis. We analyzed the studied sediments for the case study presented here because they contain these variations, which are evident regardless of the effects of storage diagenesis. Magnetic enhancement has been reported in type 1 sapropels (Roberts et al., 1999) in the classification of Larrasoaña et al. (2003b), which has been attributed by Reinholdsson et al. (2013) as due to the presence of biogenic greigite. We avoided type 1 sapropels in this study because they are dominated by major remanence losses and

do not have the variable magnetic properties observed in type 2 and 3 sapropels on which we focus here.

3.2.3 Magnetic measurements

Magnetic measurements were made at the Paleomagnetism Laboratory, Australian National University (ANU). Magnetic susceptibility was measured using a Kappabridge KLY-3 magnetic susceptibility meter (875 Hz) and the mass-specific χ was calculated. An ARM was imparted to samples with a direct current (DC) bias field of 0.05 mT and a peak alternating field (AF) of 100 mT. χ_{ARM} was calculated by normalizing ARM to the DC-bias field. $IRM_{900\ mT}$ was imparted with an induction field of 900 mT to represent SIRM, and $IRM_{-0.3\ T}$ was imparted with a backfield of 0.3 T. $IRM_{@AF120\ mT}$ was obtained after AF demagnetization of the SIRM at 120 mT, which represents the high-coercivity hematite contribution (Larrasoaña et al., 2003a). The inter-parametric ratios χ_{ARM}/χ, ARM/SIRM, and SIRM/χ were calculated to represent magnetic grain size variations (King et al., 1982; King & Channell, 1991). The S-ratio is calculated as $0.5\times[1-(IRM_{-0.3T}/SIRM)]$, which provides a measure of the relative abundance of low- to high-coercivity minerals (Bloemendal et al., 1992).

FORC measurements were made with a Princeton Measurements Corporation MicroMag vibrating sample magnetometer (VSM; Model 3900) using the irregular grid FORC protocol (Zhao et al., 2015). An averaging time of 300 ms was used for samples with remanent magnetizations less than 1 μAm^2 and a 200 ms averaging time was used for more strongly magnetized samples. FORC diagrams were processed using the xFORC software (Zhao et al., 2015). A smoothing factor (SF) of 3 or 4 was used depending on the noise level of samples. FORC data were imported into the FORCinel algorithm (Harrison & Feinberg, 2008) for FORC-PCA analysis (Harrison et al., 2018) and VARIFORC smoothing (Egli, 2013) was used for processing ($S_{c0} = 3$, $S_{c1} = 3$, $S_{b0} =$

4, S_{b1} = 4, λ_b = 0.1, λ_c = 0.1). FORCs were resampled from the irregular measurement grid to a 0.25 mT regular grid for PCA. End Members (EMs) were selected by defining a mixing space that bounds all data, with parsimonious selection of vertices that do not fall far from the data, and with guidance from the feasibility metrics of Harrison et al. (2018) that constrain solutions to fall within a physically realistic space (with monotonic changes of FORCs and without crossing of curves). EM mixing proportions and absolute contributions to the saturation magnetization were calculated based on the solution.

LT magnetic measurements were made with a Quantum Design Magnetic Property Measurement System (MPMS; model XL7). Zero-field-cooled (ZFC) and field-cooled (FC) magnetizations were measured during warming from 5 K to 300 K at 1 K intervals. Samples were first cooled to 5 K in a zero-field environment. A 5 T DC field was then applied and was switched off to impart a SIRM. SIRM curves were measured to 300 K at a heating rate of 1 K/min. A FC magnetization curve was then measured by applying a 5 T DC field throughout cooling from room temperature to 5 K. At 5 K, the field was switched off and the SIRM was then measured back to 300 K at a heating rate of 1 K/min.

3.2.4 TEM observations

Magnetic mineral extracts were obtained from bulk sediments by stirring the powdered sediment within a small volume of distilled water before thoroughly dispersing the slurry by ultrasonication. Magnetic particles were then extracted with a magnetic finger (rare Earth magnet). To concentrate and purify magnetic particles, the extraction procedure was repeated at least five times. Magnetic extracts were viewed and analyzed using a JEM-2100HR TEM operating at 200 kV, with the electron beam generated from a LaB_6 gun at the Institute of Geology and Geophysics, Chinese Academy of Sciences.

3.3. XRF-core-scanning and sapropel identification

We use the XRF core-scanning data of Grant et al. (2016, 2017) to identify sapropels, which are delineated clearly based on Ba variations (Grant et al., 2016) and Grant-PC2, which is principal component 2 from sediment geochemical data, as used by Grant et al. (2017) (Fig. 3.2a-b). Grant-PC2 corresponds to elements associated with sapropels and their various redox states and provides a more comprehensive indication of sediment geochemical changes associated with sapropel deposition and preservation/oxidation than Ba values alone (Grant et al., 2017). Down-core bulk magnetic property profiles of the studied sediments contain three main intervals: (1) representative sapropel intervals (i-156 and i-160; Fig. 3.2, dark grey shaded bars), (2) weakly developed sapropel intervals (i-158, i-162, and i-166; Fig. 3.2, light grey shaded bars), and (3) intervening marl intervals.

High Ba concentrations are observed in representative sapropels (e.g., i-156 and i-160), which indicates that sapropel deposition occurred under high productivity conditions (Fig. 3.2a). Sapropels are also characterized by S and Fe enrichments (Fig. 3.2c-d), which attests to diagenetic iron remobilization through iron sulphide formation, mostly pyrite, under sulphate-reducing conditions driven by the accumulation and microbial degradation of organic matter (Calvert & Fontugne, 2001; Pruysers et al., 1993; Thomson et al., 1995; van Santvoort et al., 1997; Warning & Brumsack, 2000; Wehausen & Brumsack, 2000). Ti/Al ratios reach minima within sapropels compared to the surrounding marls (Fig. 3.2e), which indicate increased riverine input relative to aeolian dust input during times of sapropel formation (Lourens et al., 2001). In weakly developed sapropels (e.g., i-158, i-162, and i-166), Ba contents increase compared to surrounding marls, but they have relatively lower values than in representative sapropels (Fig. 3.2a). Less pronounced Ti/Al minima occur in weakly developed sapropels compared to

representative sapropels (Fig. 3.2e), which indicate less pronounced monsoon flooding from the Nile and wider North African margin. Slightly increased S and Fe concentrations are also observed in weakly developed sapropels (Fig. 3.2b-c), which suggests that reducing conditions occurred, but were less strong, as would be expected for the lower organic matter inputs. Ba and S contents are stable at near-zero values in marls, which represent background sedimentation in the eastern Mediterranean Sea between sapropels, while Fe concentration has a small peak in marls below i-162 (Fig. 3.2a, c, d). Across this thin interval, Ba values are enhanced slightly and Ti/Al has a small minimum, which suggest the presence of a so-called hidden sapropel that is not obvious visually because of post-depositional oxidation (Larrasoaña et al., 2006). Ti/Al oscillates around high values of 0.07 in marls (Fig. 3.2e), which reflects relatively lower fluvial discharge in these intervals.

3.4. Results

3.4.1 Magnetic properties

Down-core profiles of magnetic parameters are shown in Fig. 3.3. The magnetic parameters χ, ARM, and SIRM are mainly sensitive to ferrimagnetic mineral concentration (Chaparro et al., 2008; Lascu, 2011; Liu et al., 2003). These parameters drop rapidly to low values in the upper parts of sapropels and remain low throughout underlying dissolution intervals. For representative sapropels, χ, ARM, and SIRM recover rapidly in oxidation fronts, where they typically reach their highest values (Fig. 3.3b-d). These parameters have intermediate values in the marls that occur between sapropels. χ, ARM, and SIRM have approximately similar variations with depth, except that peak values in oxidation fronts are more pronounced for ARM and SIRM. χ, ARM,

and SIRM values follow similar trends for weakly developed sapropel i-158 as for representative sapropels, except that it has a less developed oxidation front. These parameters decrease slightly from the oxidation front in weakly developed sapropel i-166 to reach minima in the upper part of the sapropel and then increase from the middle of the sapropel (Fig. 3.3b-d). For marls below representative sapropels, χ, ARM, and SIRM recover gradually from the dissolution intervals and reach high values at the next underlying oxidation front. For marls underlying weakly developed sapropels, χ, ARM, and SIRM recover rapidly from the lower part of the sapropels (Fig. 3.3b-d).

$IRM_{@AF120\ mT}$ values represent magnetic minerals with coercivity larger than 120 mT, which is mainly high-coercivity hematite. Such hematite-dominated parameters have been used previously as aeolian dust proxies in marine sediments (Larrasoaña et al., 2003b). Compared to weakly developed sapropels and marls, $IRM_{@AF120\ mT}$ has clearly lower values in representative sapropels that decrease significantly from oxidation fronts to the lower parts of sapropels and then increase gradually within dissolution intervals (Fig. 3.3e). This is indicative of a greater resistance of hematite to reductive dissolution compared to magnetite (e.g., Poulton et al., 2004; Roberts, 2015; Snowball, 1993) and indicates that the $IRM_{@AF120\ mT}$ proxy can provide a valuable indicator of subtle variations in hematite input (Larrasoaña et al., 2003b). High $IRM_{@AF120\ mT}$ values occur in the lower parts of weakly developed sapropels, while low values occur in the upper or middle parts of these sapropels.

Magnetic grain-size sensitive parameters (χ_{ARM}/χ, ARM/SIRM, and SIRM/χ) (King et al., 1982; King & Channell, 1991) have roughly parallel variations (Fig. 3.3f-h). Oxidized sediments at the tops of sapropels are marked by larger proportions of fine SD/vortex state grains, as indicated by the highest χ_{ARM}/χ, ARM/SIRM, and SIRM/χ values that drop rapidly to minima in the middle of sapropel layers and throughout the

dissolution intervals (Fig. 3.3f-h). High values of these ratios also occur in the oxidation fronts of weakly developed sapropel i-166 and in the middle of i-158. Low values occur in the lower parts of weakly developed sapropels and underlying marls, which indicates the dominance of coarser magnetic minerals (Fig. 3.3f-h). In the lower parts of the marl intervals, grain-size sensitive parameters increase markedly toward the underlying oxidation fronts.

The S-ratio indicates the relative contribution of low- to high-coercivity magnetic minerals. S-ratio values are distinctly low in dissolution intervals and in underlying marls, while the rest of the studied sequence has relatively stable values around 0.97 (Fig. 3.3i). This indicates an increased relative importance of high-coercivity minerals (hematite) within dissolution intervals.

3.4.2 Magnetic mineralogy

All measured ZFC and FC curves contain distinctive inflections associated with the Verwey transition temperature for magnetite (T_v) at ~95 K, except for a sample from the dissolution interval of representative sapropel i-160 (Fig. 3.4c). Samples from the oxidation fronts of representative sapropel i-160 and weakly developed sapropel i-166 have two inflections at ~95 and ~110 K in SIRM derivative curves (Fig. 3.4b, e). This double T_v feature represents the presence of both biogenic and inorganic magnetite (Chang et al., 2016). The double peak feature is less clear for a sample from the middle of weakly developed sapropel i-166 (Fig. 3.4f), but it is obvious in weakly developed sapropel i-162 (Fig. 3.4d). Remanence loss at ~95 K is more pronounced compared to that at ~110 K for samples from oxidation fronts (Fig. 3.4b, e) and it is less pronounced for samples from the middle part of weakly developed sapropel i-162 (Fig. 3.4d). The inflection at ~95 K is due to biogenic magnetite (Chang et al., 2016).

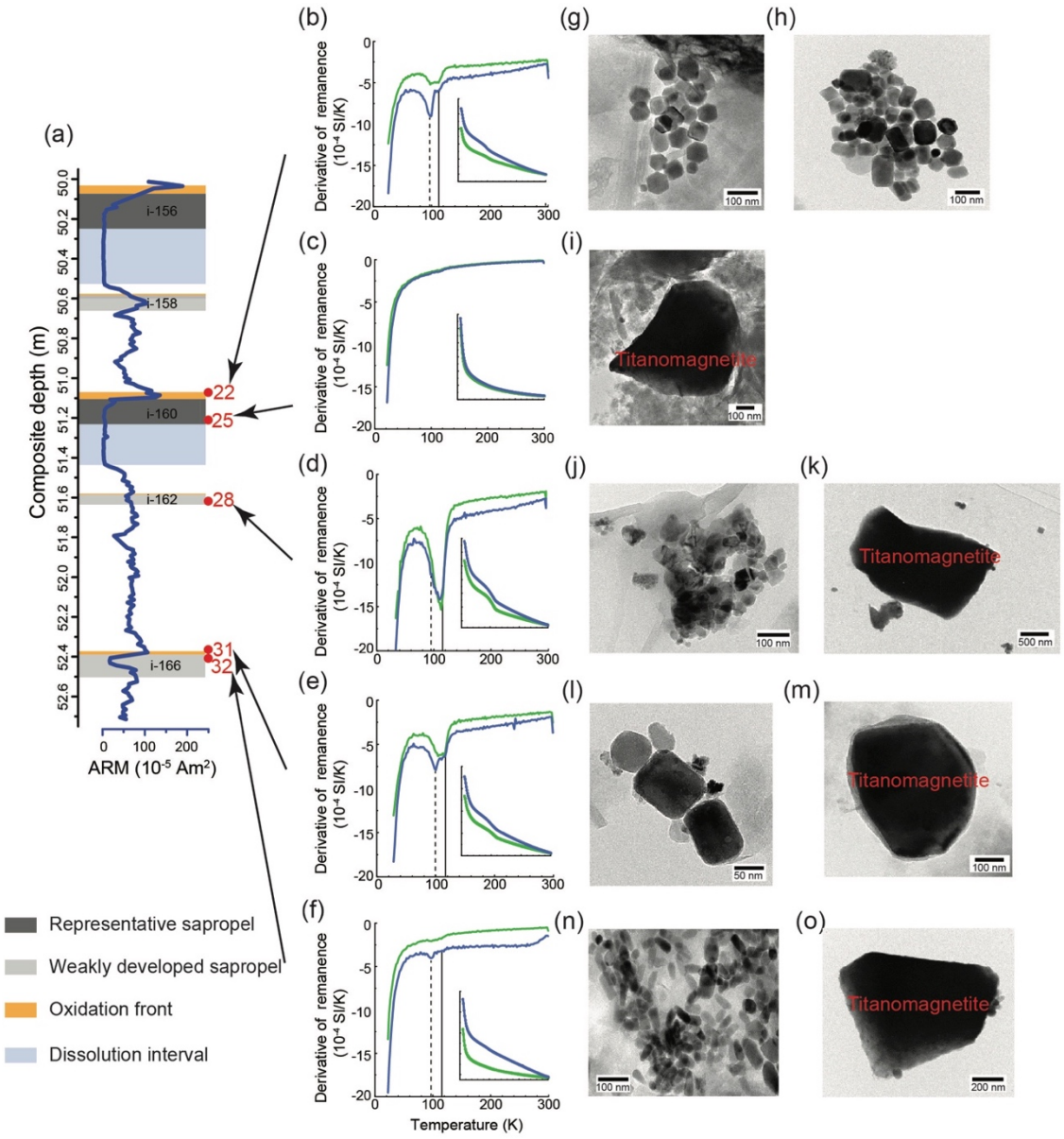

Fig. 3.4 LT magnetic measurements and TEM observations for five representative samples. (a) The locations of the five samples are indicated on an ARM profile with sapropel stratigraphy after Emeis et al. (2000). (b-f) LT magnetization curves (inset) and their derivative curves (larger; ZFC, green and FC, blue). Vertical dashed and solid lines indicate the two distinctive T_v peaks at ~95 and ~110 K, respectively. (g, h) TEM images for sample 22 from the oxidation front of representative sapropel i-160 with abundant magnetosomal magnetite; (i) TEM image for sample 25 from the middle of sapropel i-160 with a detrital titanomagnetite particle; (j, k) TEM images for sample 28 from the middle of weakly developed sapropel i-162 with both magnetosomal magnetite and titanomagnetite; (l, m) TEM images for sample 31 from the oxidation front above weakly developed sapropel i-166 with clusters of biogenic magnetite and detrital titanomagnetite; and (n, o) TEM images for sample 32 from the middle of weakly developed sapropel i-166 with abundant bullet-shaped biogenic magnetite and detrital titanomagnetite. TEM electron dispersive X-ray (TEM-EDX) spectra are indicative of mineralogy, as shown in Fig. S2.

TEM imaging of magnetic mineral extracts confirms the common presence of detrital titanomagnetite and biogenic magnetite particles within the studied sediments (Fig. 3.4g-o). Samples from oxidation fronts and weakly developed sapropels reveal the presence of abundant fine-grained biogenic magnetite particles (Fig. 3.4g, h, j, l, n). These crystals have well-defined morphologies (cubo-octaheral, prismatic, and bullet-shaped) and sizes within the SD size range for magnetite (Muxworthy & Williams, 2009) that are typical of magnetofossils (e.g., Bazylinski & Frankel, 2004; Chang et al., 2014; Kopp & Kirschvink, 2008; Petersen et al., 1986; Roberts et al., 2012). Clustering of biogenic magnetite particles in the TEM images is likely due to magnetofossil chain collapse during ultrasonication (e.g., Li et al., 2012) associated with sample preparation for magnetic extraction. Biogenic magnetite crystals are more abundant in oxidation fronts compared to sapropel layers. Titanomagnetite particles with sizes ranging from hundreds of nanometres (nm) to several micrometres (μm) are observed in samples from dissolution intervals (Fig. 3.4i) and weakly developed sapropels (Fig. 3.4k, m, o). When compared with LT results, samples with more abundant biogenic magnetite have a pronounced T_v signal at ~95 K (Fig. 3.4b, e, f) while samples with less biogenic magnetite or only titanomagnetite have a pronounced T_v signal at ~110 K or no clear T_v signal (Fig. 3.4c-d), as discussed below.

3.4.3 FORC-PCA unmixing

FORC-PCA unmixing results for all samples are shown in Fig. 3.5. Three distinctive clusters occur on the principal component 1 (PC1)-PC2 plane (Fig. 3.5a). Group 1 (G1) and Group 2 (G2) represent samples from the dissolution intervals of sapropels i-160 and i-156, respectively. PC scores in Group 3 (G3) are more tightly aggregated and represent the rest of the samples. As illustrated in Fig. 3.5b-d, G1 has elongated FORC distributions along the B_c axis, which indicates the presence of non-

interacting SD particles. G2 and G3 have mixed features with SD particles with peak coercivity of 10-20 mT and vertical spreading along the B_u axis (Fig. 3.5c-d), which is indicative of vortex state particles (Roberts et al., 2017; Lascu et al., 2018). Compared to G3 (Fig. 3.5d), G2 has a lower peak coercivity for SD particles (Fig. 3.5c).

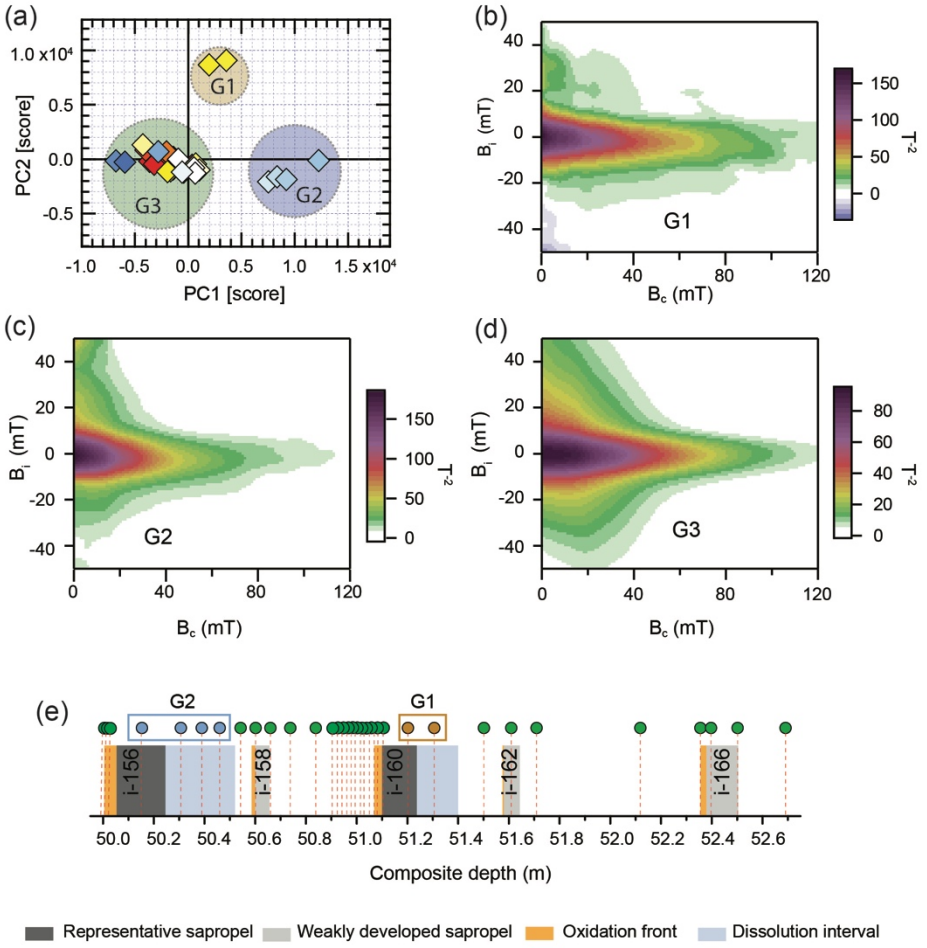

Fig. 3.5 FORC-PCA results for 34 selected samples. (a) Distribution of sample PC scores in PC1-PC2 space, from which three groups (G1, G2, and G3) are defined. Diamonds represent the PC scores for the measured FORC data, which are shown with respect to the two principal components (PC1 and PC2); (b) FORC distribution for a typical G1 sample, which has dominantly stable SD behaviour; (c) FORC distribution for a typical G2 sample, which contains mixed stable SD and vortex state behaviour; (d) FORC distribution for a typical G3 sample, which also contains mixed stable SD and vortex state components due to biogenic and detrital magnetite, respectively, and (e) stratigraphic locations of samples from each group: G1 (orange), G2 (light blue), and G3 (green) in the studied sequence. Dark grey shaded bars indicate the positions of representative sapropels. Light grey shaded bars indicate the positions of weakly developed sapropels. Light blue shading below the sapropels marks the positions of dissolution intervals, while orange shading above the sapropels indicates the positions of oxidation fronts. Sapropel stratigraphy is after Emeis et al. (2000).

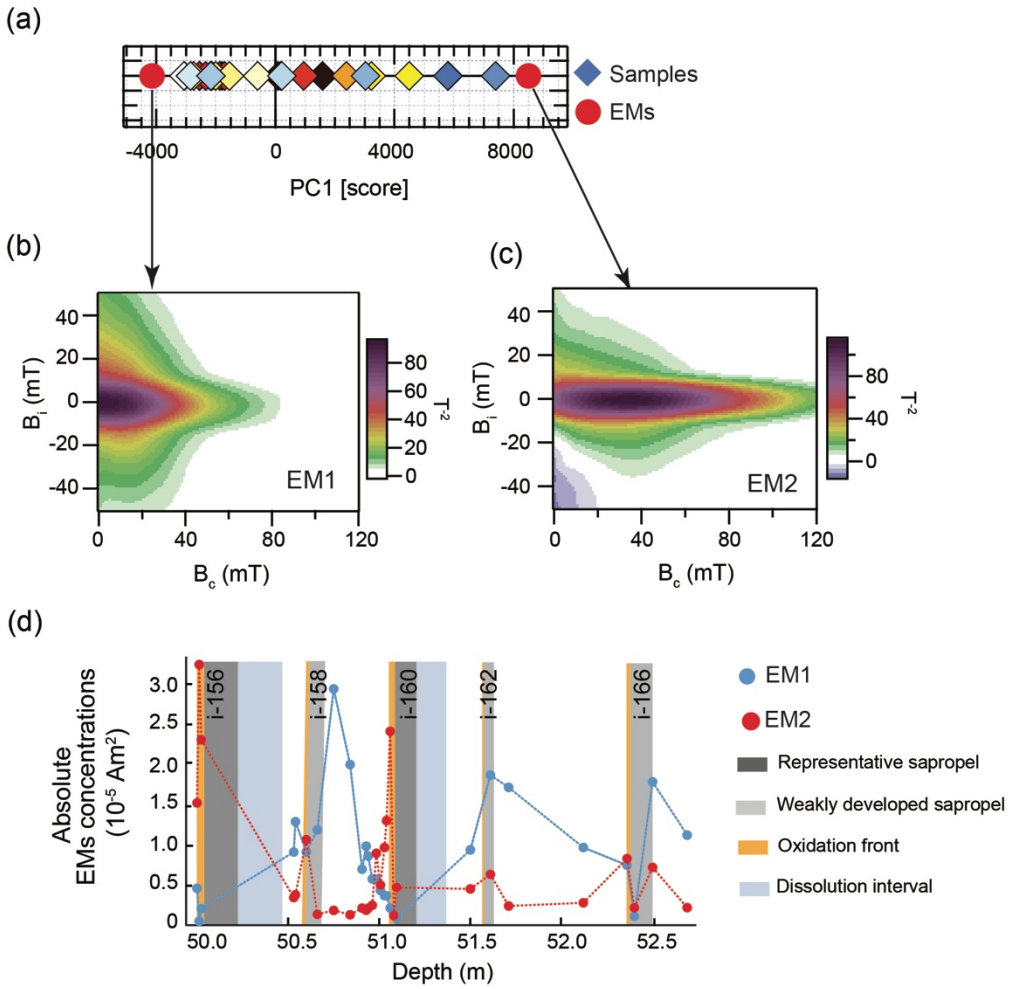

Fig. 3.6 FORC-PCA results for samples from Group 3 (G3) samples in Fig. 3.5, which is treated as a linear combination of two EMs. (a) Distribution of PC scores for 28 samples in PC1 space with FORC diagrams for the two EMs (the colour coding for diamond symbols is the same as in Fig. 3.5a); (b) EM1 consists of dominantly vortex state particles; (c) EM2 consists of dominantly non-interacting SD behaviour; and (d) magnetizations of EM1 (blue) and EM2 (red) calculated from FORC-PCA unmixing and presented with respect to depth.

As is clear in Fig. 3.5a, there is considerable variability within G3, so we extend FORC-PCA further here to assess these variations within 28 samples from oxidation fronts, the middles of sapropels, and marls. Two EMs are identified within this group (Fig. 3.6a). EM1 is represented by vortex state particles (Fig. 3.6b), while EM2 is dominated by a central ridge feature, which is characteristic of biogenic magnetite (Fig. 3.6c; e.g., Egli et al., 2010; Roberts et al., 2012). Down-core variations of the magnetization contributions of the two EMs were calculated from FORC-PCA unmixing

results and are shown in Fig. 3.6d. EM1, which represents coarser detrital magnetic minerals, is enhanced in marls and is much less abundant in oxidation fronts (Fig. 3.6d, blue). EM2, which represents biogenic magnetite, is enhanced in oxidation fronts, especially for representative sapropels, and makes a much lower contribution in other intervals (Fig. 3.6d, red).

3.5. Discussion

3.5.1 Detection of biogenic magnetic minerals

It has been suggested that magnetofossils produced by MTB formed in the oxidized zone at the tops of sapropels (Passier et al., 2001; Kruiver & Passier, 2001; Passier & Dekkers, 2002). Passier et al. (2001) reported that the high ARM and coercivity of magnetite, fine particle size, and low dispersion of the fitted IRM component in the vicinity of oxidation fronts is most likely associated with magnetofossils. Kruiver & Passier (2001) analysed coercivities in the most recent sapropel, which indicated strongly that biogenic magnetite formed in the active oxidation front. LT results of Passier & Dekkers (2002) indicate that superparamagnetic (SP) particles also exist in oxidized zones above sapropels. Although these studies provide strong indications of the presence of biogenic magnetite in oxidation fronts, it has not been proven by direct TEM imaging of magnetofossils.

Our FORC analyses provide a direct indication that central ridge features are observed not only in oxidation fronts, but also in weakly developed sapropels and marls. FORC-PCA unmixing results indicate that magnetofossils appear to occur throughout the studied sequence except within intervals with strong magnetic mineral dissolution (Fig. 3.6d). TEM observations and LT measurements confirm that EM2 identified in

FORC-PCA analysis is dominated by magnetofossils and that biogenic magnetite particles occur in most of the studied sediments (Fig. 3.4b, d, e, f, g, h, j, l, n). Membrane-bound, SD magnetite crystals are synthesized intracellularly by MTB in a genetically controlled process. MTB live within strictly limited environments, where temperature, pH, external Fe concentration, external magnetic fields, static or dynamic fluid conditions, oxygen concentration, and nutrient availability or concentrations can all affect magnetosome biomineralization in MTB (Yan et al., 2012). Widespread magnetofossils in the studied sediments indicate that sustained conditions with nitrogenous to ferruginous diagenesis existed, which favour continued MTB activity and preservation (Roberts et al., 2011b; Larrasoaña et al., 2012). In contrast, burial into sulphidic diagenetic zones, such as during periods of sapropel formation, will cause extensive magnetite dissolution, particularly of fine-grained magnetofossils (e.g., Roberts, 2015). We do not observe evidence for magnetosomal greigite (e.g., Reinholdsson et al., 2013), which is most likely to be preserved if greigite-producing MTB were active during periods of sapropel formation. The distinctive magnetic properties associated with magnetosomal greigite (e.g., Reinholdsson et al., 2013) have only been observed for type 1 sapropels, which were not studied here; if such greigite was initially present, it is unlikely to have survived drying and oxidation of the core after recovery (e.g., Roberts et al., 1999).

3.5.2 Biogenic magnetic mineral abundances

The stratigraphic distribution of EM2 identified from FORC-PCA unmixing demonstrates that biogenic magnetite concentrations are high at oxidation fronts (Figs. 3.6d, 3.7f), which indicates that redox conditions at oxidation fronts provide a habitat that enables growth of MTB populations. On the one hand, MTB productivity requires

sufficient organic carbon to release bioavailable iron. On the other hand, the organic carbon flux cannot be too high because a sulphidic diagenetic environment would form in which magnetite dissolves to prevent magnetofossil preservation (Chang et al., 2018; Larrasoaña et al., 2014; Roberts et al., 2011b). Magnetofossil preservation in sediments tends to reflect competition between MTB productivity and preservation (e.g., Dinarès-Turell et al., 2003; Hesse, 1994; Kopp et al., 2009), which can be an indicator of sediment oxygenation levels (e.g., Chang et al., 2018; Hesse, 1994; Kopp et al., 2007, 2009; Kopp & Kirschvink, 2008; Lippert & Zachos, 2007; Yamazaki, 2012; Yamazaki & Ikehara, 2012). Fe^{2+} is mobilized upward by pyrite oxidation at the tops of sapropels when bottom waters were reoxygenated immediately after periods of sapropel formation (Passier et al., 2001; van Santvoort et al., 1996) and is precipitated as mixed valence iron oxides (Fig. 3.8). MTB abundances decrease when moving upward from the top of oxidation fronts due to the gradually reduced concentration of liberated Fe^{2+} (e.g., i-160). Coincidence between ARM values and EM2 abundance variations in the oxidation fronts of sapropels i-156 and i-160 (Fig. 3.7e-f) indicates that the biogenic magnetite concentration is responsible for the enhanced magnetization of oxidation fronts. In magnetic mineral dissolution intervals, such as within and below representative sapropels, reductive dissolution has removed fine ferrimagnetic particles, so that magnetofossils are preserved rarely. Strong correlation between EM2 and ARM indicates that normal sedimentary conditions represented by marls were also suitable for MTB, although magnetizations are lower. This magnetofossil abundance variation probably reflects variations in nutrients and redox gradient strength in which MTB lived. Observed biogenic magnetite variations around oxidation fronts are consistent with the rationale of Hesse (1994) that variable oxygenation leads to variable overall MTB production and preservation.

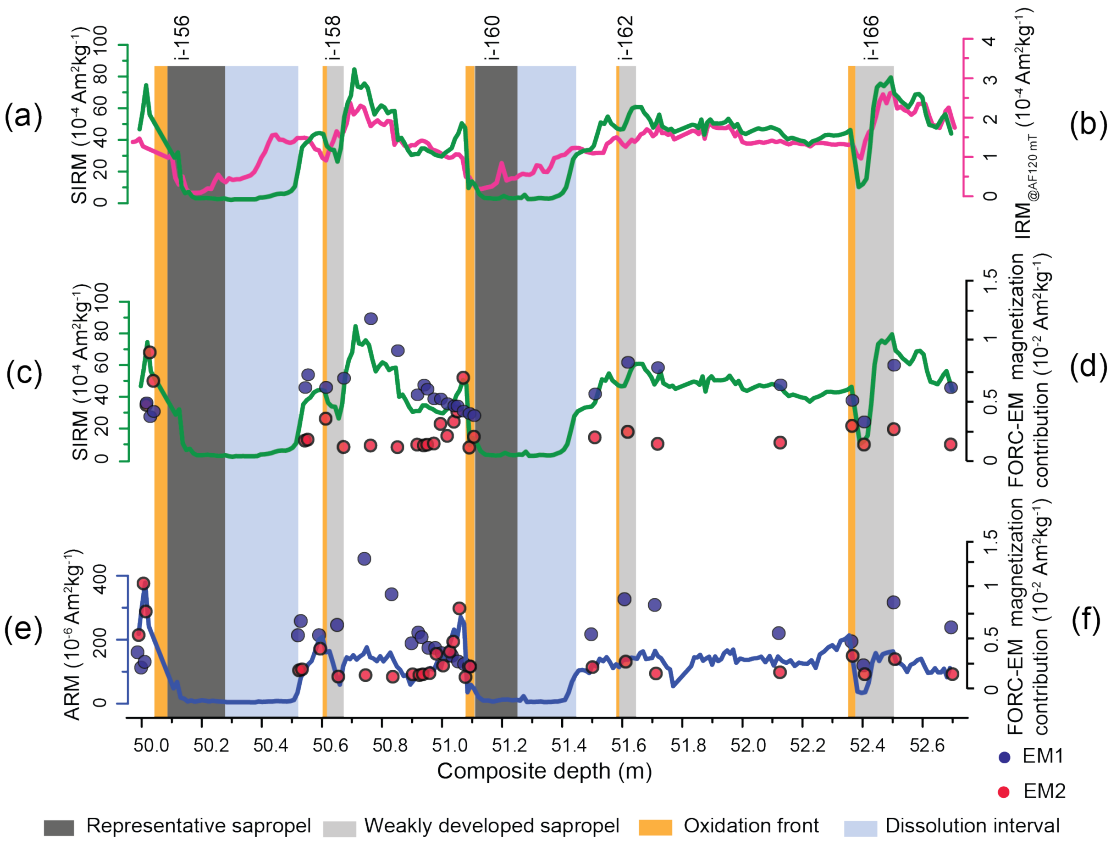

Fig. 3.7 (a, c) SIRM (green) and (b) $IRM_{@AF120\,mT}$ (magenta), which is used as a proxy for Saharan dust in the eastern Mediterranean Sea (Larrasoaña et al., 2003b); (d, f) FORC-EM magnetization contribution, which is overlain on SIRM and (e) ARM curves to illustrate their similar trends, where ARM represents the ferrimagnetic mineral concentration (blue). Blue and red circles represent EM1 (vortex state detrital magnetite) and EM2 (biogenic magnetite), respectively, as defined in Fig. 3.6. Dark grey shaded bars indicate the positions of representative sapropels. Light grey shaded bars indicate the positions of weakly developed sapropels. Light blue shading below sapropels marks the positions of dissolution fronts; orange shading above sapropels indicates the positions of oxidation fronts. Sapropel stratigraphy is after Emeis et al. (2000).

3.5.3 Detection of detrital magnetic minerals

It has been argued that aeolian dust is a major sediment source for the eastern Mediterranean Sea (Kruiver & Passier, 2001; Larrasoaña et al., 2003a; Lourens et al., 2001). $IRM_{@AF120\,mT}$ has been used as an aeolian dust proxy in this region (Larrasoaña et al., 2003a). SIRM has strong similarities with $IRM_{@AF120\,mT}$ except in representative sapropels and dissolution intervals, where magnetite dissolution has occurred (Fig. 3.7a-

b). The value of $IRM_{@AF120\ mT}$ as a high-coercivity aeolian hematite proxy has been proven in several studies (Larrasoaña et al., 2003a, 2003b, 2014), so that the strong similarity between SIRM and $IRM_{@AF120\ mT}$ suggests that the magnetic minerals represented by SIRM must also have a dominantly aeolian source outside of sapropel dissolution intervals. This interpretation is supported by the observation that there are no large magnetic mineral influxes in the more humid periods associated with representative and weakly developed sapropels, which would be taken to indicate a significant fluvial input of detrital magnetic minerals. Moreover, SIRM and $IRM_{@AF120\ mT}$ have two distinct linear relationships in marls and within dissolution intervals (Fig. 3.9). The linearity indicates that magnetic minerals within marls have a similar coercivity distribution, which is more likely to represent a single source rather than material from multiple sources. Kruiver & Passier (2001) also observed that their interpreted magnetite and hematite components have constant ratios for Holocene sediments, which indicates that the magnetic minerals have the same source.

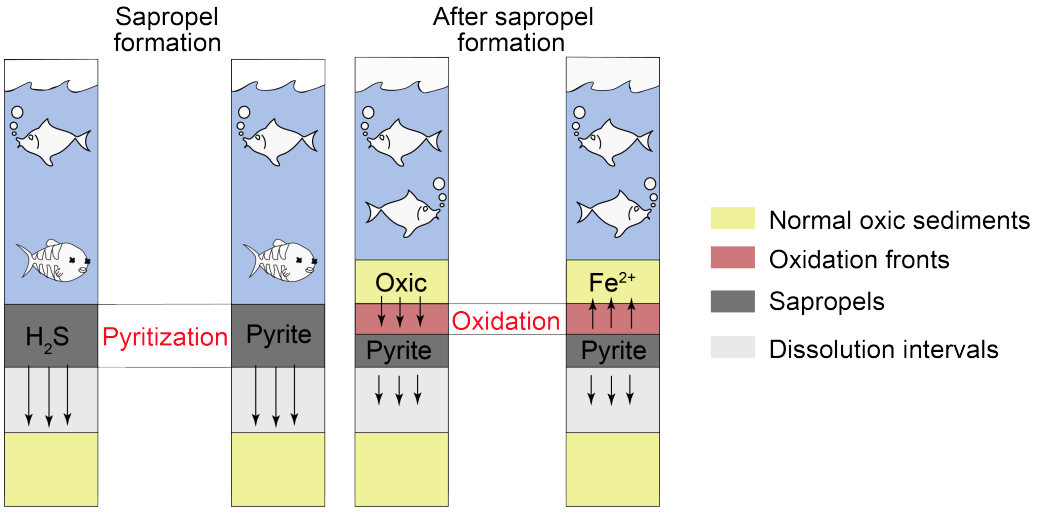

Fig. 3.8 Illustration of the effects of variable bottom water ventilation and Fe^{2+} mobilization on non-steady state diagenesis in eastern Mediterranean sediments (characteristic of a type 2 sapropel; Larrasoaña et al., 2003b). During times of sapropel formation, bottom waters were sulphidic so that H_2S diffused downward into sediments below sapropels to cause magnetite dissolution, pyrite formation, and magnetization loss. When bottom waters are reventilated, oxygen diffuses downward into formerly sulphidic sediments, which produces an oxidation front where Fe^{2+} is mobilized upward by pyrite oxidation (Passier et al., 2001; Passier and Dekkers, 2002). Figure produced by Dr Juan-Cruz Larrasoaña and used by Roberts (2015).

LT measurements and TEM observations, coupled with FORC unmixing results, further indicate that detrital magnetite is the magnetically dominant magnetic mineral in the studied sediments. LT measurements indicate that detrital magnetite particles are dominant in weakly developed sapropels (Fig. 3.4d, f). TEM observations confirm that coarse titanomagnetite is preserved in almost all samples (Fig. 3.6i, k, m, o; note: not all titanomagnetite TEM images are shown). FORC unmixing results for G1 and G2 (Fig. 3.5) from the two studied representative sapropels not only demonstrate the occurrence of detrital magnetite in representative sapropels and underlying dissolution intervals, but also that different grain sizes occur in different intervals. A representative FORC diagram for G1 has a SP/SD feature with no vortex or MD signal (Fig. 3.5b), which indicates that the magnetic minerals were reduced to a smaller size during dissolution (e.g., Roberts et al., 2018). In contrast, a representative FORC diagram for G2 has a coarser vortex state feature (Fig. 3.5c), which indicates that less magnetite dissolution has occurred in sapropel i-156 compared to i-160. The presence of dissolution intervals indicates that organic matter accumulation was sufficient to produce excess sulphide (Fig. 3.8), which migrated downward to cause magnetite dissolution (e.g., Larrasoaña et al., 2003b, 2006; Passier et al., 1996, 1999; Roberts, 2015), where dissolution intensity decreases gradually with increasing depth below sapropels. Samples from G2 lie further below their overlying sapropel than samples from G1 (Fig. 3.5e), which could explain their coarser grain sizes. Additionally, FORC diagrams (Figs. 3.5d, 3.6b) for marl and weakly developed sapropel samples have dominantly vortex state behaviour (cf. Lascu et al., 2018; Roberts et al., 2017) that reveals the dominance of coarse magnetite, with no clear evidence for SP particles (Kruiver & Passier, 2001). The absolute contribution of biogenic magnetite is generally small outside of oxidation fronts (Figs. 3.6d, 3.7f), and EM1 mainly reflects non-biogenic magnetic mineral concentrations outside of oxidation fronts. Similar trends

among EM1, SIRM, and $IRM_{@AF120\ mT}$ indicate that aeolian detrital magnetite is the main magnetic mineral in the studied sequence except for within oxidation fronts and dissolution intervals (Fig. 3.7a-d).

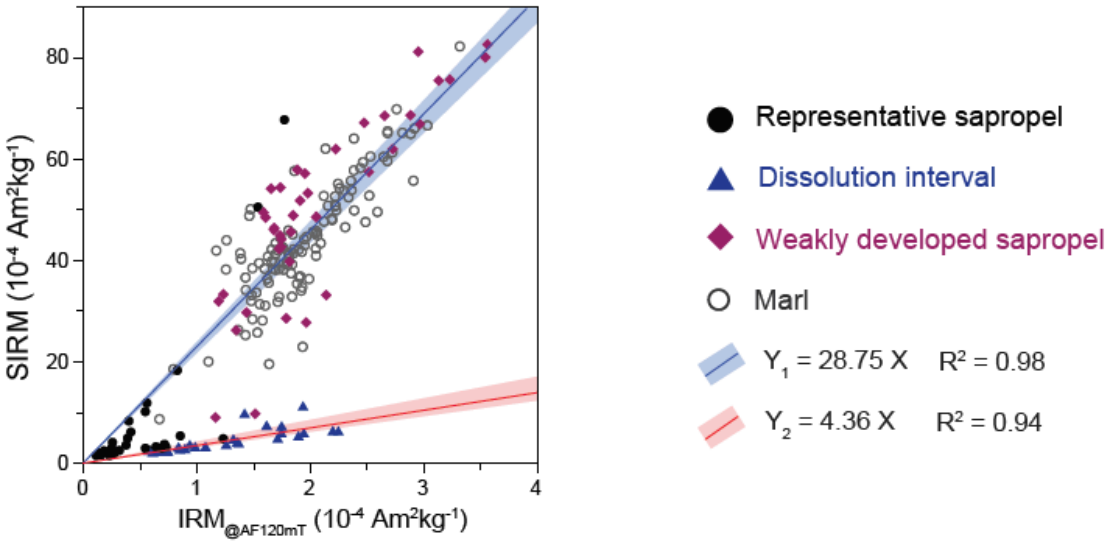

Fig. 3.9 Relationship between SIRM and the $IRM_{@AF120\ mT}$ dust proxy. Data are shown for representative sapropels (black circles) and their dissolution fronts (blue triangles), weakly developed sapropels (magenta diamonds), and intercalated marls (grey circles).

3.5.4 Benefits and limitations of advanced methods

Advanced environmental magnetic methods, such as FORC-PCA and LT measurements, with supplementary TEM observations, can provide direct indications of mineral magnetic assemblages and can enable estimation of end member abundances. However, these techniques are time-consuming, so they tend not to be used to develop high-resolution records. Conventional bulk magnetic parameters provide a rapid and nondestructive means of assessing continuous environmental magnetic variations. Those parameters mainly enable detection of magnetite or other ferrimagnetic minerals. If the aims of a study are to detect continuous ferrimagnetic variations, conventional bulk measurements are sufficient. Otherwise, the combined use of conventional bulk magnetic parameters and advanced techniques provides improved diagnosis of processes responsible for environmental magnetic signals.

3.6. Conclusions

We have applied both conventional bulk and more time-consuming advanced techniques to identify magnetic minerals within complexly mixed magnetic mineral assemblages in eastern Mediterranean sediments. Conventional bulk magnetic parameters provide continuous records of important environmental variations that have contrasting magnetic signatures, such as oxidation fronts and dissolution intervals (Fig. 3.8). However, these parameters do not necessarily enable identification of all multiple magnetic mineral components preserved in the studied sediments. Advanced environmental magnetic methods, such as LT and FORC measurements, provide crucial direct indications of mineral magnetic assemblages that enable calculation of the abundances of different end members.

FORC and LT results, along with TEM images, provide a clear demonstration that biogenic magnetite formed at oxidation fronts above eastern Mediterranean sapropels (Fig. 3.8). The abundance of biogenic magnetite (quantified through FORC-PCA) indicates that markedly enhanced biogenic magnetite abundances occur at oxidation fronts. This indicates that the strong redox gradient produced when sulphidic sapropelic sediments are exposed to oxygenated bottom waters (Fig. 3.8) provides a suitable habitat for magnetotactic bacteria. Our results also indicate that biogenic magnetite is present throughout the studied sediments, with the exception of sulphidic diagenetic intervals, in which magnetite dissolves. Furthermore, we find that detrital magnetite dominates the sediment magnetization except at oxidation fronts. Overall, our results emphasize the value of conventional continuous bulk magnetization records for environmental magnetic analysis, where use of advanced diagnostic methods adds significant interpretive power to understand the processes responsible for environmental signals.

Chapter 4

Low-temperature magnetic properties of marine sediments – quantifying magnetofossils, superparamagnetism, and maghemitization: eastern Mediterranean examples

---

This chapter has been submitted for publication as: **Qian, Y**., Heslop, D., Roberts, A. P., Hu, P., Zhao, X., Liu, Y., Li, J., Grant, K. M., & Rohling, E. J. Low-temperature magnetic properties of marine sediments – quantifying magnetofossils, superparamagnetism, and maghemitization: eastern Mediterranean examples. *Journal of Geophysical Research: Solid Earth*.

Abstract

Periodic and marked redox changes in eastern Mediterranean marine sediments drive environmental and diagenetic changes to which magnetic minerals are sensitive. Magnetic property changes, therefore, provide useful indications of paleoceanographic conditions during and after periods of organic-rich sediment (sapropel) deposition. Magnetic properties of eastern Mediterranean sediments at room temperature have been studied for decades; however, few studies have considered low-temperature magnetic properties. Here, we investigate the low-temperature (10 to 300 K) magnetic properties of different eastern Mediterranean sediment types combined with room temperature (~300 K) magnetic properties, transmission electron microscopy, and calibrated X-ray fluorescence elemental data to illustrate the valuable information that can be obtained from low-temperature magnetic analysis of sediments. Our low-temperature magnetic results suggest that magnetite magnetofossils and superparamagnetic particles occur widely in eastern Mediterranean sediments. Superparamagnetic particle contents are highest in diagenetically reduced intervals associated with sapropels. In contrast, magnetite magnetofossils are most abundant in oxidation fronts at the tops of sapropels, where strong redox gradients formed, but are also widespread throughout other sedimentary intervals that have not been subjected to extensive reductive diagenesis. Moreover, the surfaces of magnetite particles are maghemitized (i.e. partially oxidized) in oxidation fronts at the tops of sapropels, and in other oxic sediment intervals. Our results demonstrate the value of LT magnetic measurements for quantifying diverse sedimentary magnetic signals of interest in environmental magnetism when studying paleoceanographic and paleoenvironmental processes.

Plain Language Summary

Magnetic minerals are sensitive to environmental changes. Investigating their variations through sedimentary sequences can provide information about ancient environmental and climatic changes. Room temperature magnetic properties are widely measured in environmental magnetism, while low-temperature (LT) magnetic properties that are measured between room temperature and ~10 K and are studied much less, even though they can provide useful information about the presence of particular magnetic minerals and their particle size distributions. We present extensive LT analyses of Mediterranean marine sediments, together with room temperature magnetic, transmission electron microscope, and calibrated X-ray fluorescence elemental analyses to discuss redox changes of magnetic minerals within organic-rich sediment intervals to quantify these diverse magnetic particle types. Our LT results suggest that the fossilized remains of magnetotactic bacteria and tiny superparamagnetic particles occur widely in eastern Mediterranean sediments, and that the surfaces of magnetite particles are widely oxidized and provide a measure of sedimentary oxidation variations. This work demonstrates that LT magnetic measurements can be used to quantify diverse sedimentary magnetic signals, and will be widely applicable in paleoenvironmental magnetic research.

4.1. Introduction

The semi-enclosed Mediterranean Sea is land-locked with a narrow and shallow connection to the Atlantic Ocean through the Strait of Gibraltar (Fig. 4.1). Due to its small volume and limited oceanic connections, Mediterranean deep-sea sediments preserve signals of climate change and a variety of interacting physical and biogeochemical processes in an amplified manner (Rohling, 1999; Rohling et al., 2014). During insolation maxima, strengthening and northward expansion of the African summer monsoon bring enhanced precipitation to North Africa, with resulting freshwater runoff into the Mediterranean Sea via both the Nile and the wider continental margin (Amies et al., 2019; Coulthard et al., 2013; Drake et al., 2013; Grant et al., 2017; Osborne et al., 2008; Rohling et al., 2002, 2004; Rossignol-Strick et al., 1982; Scrivner at al., 2004). This increased freshwater flux reduced Mediterranean surface-water salinities, increased surface productivity, inhibited deep-water ventilation, and created conditions conducive to organic-rich sediment (sapropel) formation (e.g., Castradori, 1993; Emeis et al., 2000a; 2003; Larrasoaña et al., 2003a; Myers et al., 1998; Rohling, 1994; Rohling & Gieskes, 1989; Rohling et al., 2015; Rossignol-Strick, 1983, 1985, 1987; Rossignol-Strick et al., 1982). During summer insolation minima the monsoon rain belt lay further to the south. This resulted in low freshwater flux, low Mediterranean surface water productivity, and efficient bottom-water ventilation, which favored deposition of "normal" organic-poor marls (Emeis et al., 2000b; Lourens et al., 2001; Wehausen & Brumsack, 2000).

Increased sedimentary organic matter deposition and preservation during insolation maxima and the ensuing microbial degradation produces complicated post-depositional diagenesis, which affects the magnetic properties of sapropels and sediments that underlie them (Langereis & Dekkers, 1999; Larrasoaña et al., 2003b,

2006; Liu et al., 2012; Passier et al., 2001). Anoxic sulfidic conditions during periods of sapropel deposition cause magnetic mineral dissolution, which generally results in decreased anhysteretic remanent magnetization (ARM) values within sapropels (Fig. 4.2; Dekkers et al., 1994; van Santvoort et al., 1997). In addition, low ARM values may extend for tens of centimetres below sapropels when sulphate-reducing conditions were strong (Fig. 4.2). So-called "dissolution fronts" form in underlying marls as a result of downward diffusion of excess sulphide (Fig. 4.2; Larrasoaña et al., 2006; Passier et al., 2001). Conversely, increased ARM values exist commonly at the tops of sapropels as a result of iron oxide neoformation in reoxygenated bottom waters (Fig. 4.2; Larrasoaña et al., 2003a, 2006; Liu et al., 2012; Passier & Dekkers, 2002). This zone of elevated magnetization is referred to as the "oxidation front" (Fig. 4.2; Larrasoaña et al., 2003a, 2006; Liu et al., 2012; Passier et al., 2001). Based on these distinctive magnetic signatures, eastern Mediterranean sapropels can be grouped into three main types: those without oxidation fronts (type 1), those with both oxidation fronts and dissolution intervals (type 2), and those without dissolution fronts (type 3) (Larrasoaña et al., 2003b). These three sapropel types correspond to different surface productivity and bottom-water ventilation conditions (Larrasoaña et al., 2003b). Type 1 sapropels correspond to high productivity situations, while type 2 and 3 sapropels indicate moderate productivity. Bottom-waters were less well ventilated during the formation of type 1 sapropels and ventilation increased gradually when type 2 and 3 sapropels formed (Larrasoaña et al., 2003b). These three types of sapropels form under distinctive conditions, so developing a deeper understanding of their magnetic properties will aid paleoenvironmental reconstructions.

Magnetic minerals are sensitive to non-steady-state diagenesis associated with periodic accumulation and degradation of organic matter; thus, sedimentary magnetic

properties can provide information concerning paleoceanographic conditions both during and after sapropel formation (Dekkers et al., 1994; Larrasoaña et al., 2003b, 2006; Roberts, 2015; Roberts et al., 1999; Robinson et al., 2000; Tarduno & Wilkinson, 1996; van Hoof et al., 1993). Understanding the processes that influence sedimentary magnetism is, therefore, important for studying eastern Mediterranean paleoenvironments. Room temperature magnetic properties of different classes of eastern Mediterranean sediments have been studied widely (Larrasoaña et al., 2003b; Liu et al., 2012; Passier et al., 2001; Qian et al., 2020). The low-temperature (LT; 10 to 300 K) magnetic properties of eastern Mediterranean sediments are, however, less well understood (Roberts et al., 1999; Passier & Dekkers, 2002). LT properties can provide detailed information on a number of magnetic minerals. For example, the Néel temperatures of siderite and rhodochrosite at 30-40 K (Housen et al. 1996), the magnetic Besnus transition in monoclinic pyrrhotite at 34 K (Besnus & Meyer, 1964; Dekkers et al., 1989; Rochette et al., 1990, 2011), the Verwey transition in magnetite at 110-120 K (Verwey, 1939), and the Morin transition in hematite at 250-260 K (Morin, 1950) provide important mineral-specific information. In addition, LT analyses can demonstrate the occurrence of ultrafine-grained superparamagnetic (SP) particles (Banerjee et al. 1993; Smirnov & Tarduno 2000) and magnetite magnetofossils (Chang et al., 2016; Moskowitz et al. 1993; Passier & Dekkers, 2002). Moreover, LT measurements can provide information about the extent of maghemitization (partial surface oxidation of magnetite) (Chang et al., 2013; Özdemir & Dunlop, 2010; Passier & Dekkers, 2002; Smirnov & Tarduno, 2000, 2001). Passier & Dekkers (2002) analyzed the LT magnetic properties of the most recent eastern Mediterranean sapropel (S1). They proposed that SP particles and biogenic magnetite formed at the oxic-suboxic boundary, and that maghemitization occurred in the pyritized zone beneath sapropels. In contrast to S1, the LT magnetic

properties of other eastern Mediterranean sediments (i.e., the three sapropels types mentioned above and intercalated marls) remain unknown.

In this study, LT magnetic analyses with hysteresis loops, first-order reversal curves (FORCs), transmission electron microscope (TEM) observations, calibrated X-ray fluorescence (XRF) elemental data (Grant et al., 2017), and high-resolution bulk magnetic properties (Qian et al., 2020) are combined to investigate eastern Mediterranean sediments. Our results provide insights into various diagenetic effects on magnetic minerals under reducing conditions and illustrate the value of LT analyses in identifying environmental magnetic signals of interest in paleoceanographic and paleoenvironmental studies.

4.2. Samples

Sediments were sampled from Ocean Drilling Program (ODP) Site 967 (Fig. 4.1), eastern Mediterranean Sea (Shipboard Scientific Party, 1996). Core sections 5H6 to 5H7 from Hole 967C were studied here, which span approximately 2.7 m from 49.99 to 52.69 meters composite depth (mcd). These sections are dated to between 1.59 and 1.71 Ma in the age model of Grant et al. (2017). The studied sediments contain several well-developed sapropels of two main types, which provide a range of environmental conditions to assess the usefulness of LT magnetic analyses in paleoenvironmental studies. Forty-four samples from three representative intervals were selected for LT analyses (red circles; Figs. 4.3 and 4.4), and twenty-nine samples were selected for FORC measurements (Fig. S3). Eighty-one sediment samples were selected for hysteresis measurements (black circles; Fig. 4.4) based on their bulk magnetic properties (Qian et al., 2020).

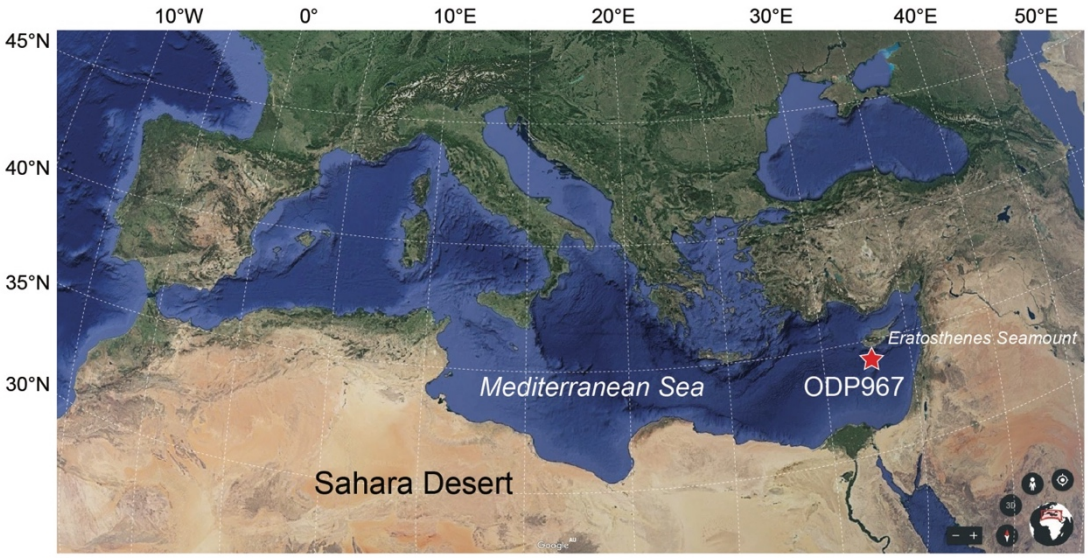

Fig. 4.1 Location of ODP Site 967 (34°04'N, 32°43'E, 2,553 m water depth) and Eratosthenes Seamount (map generated from Google Earth).

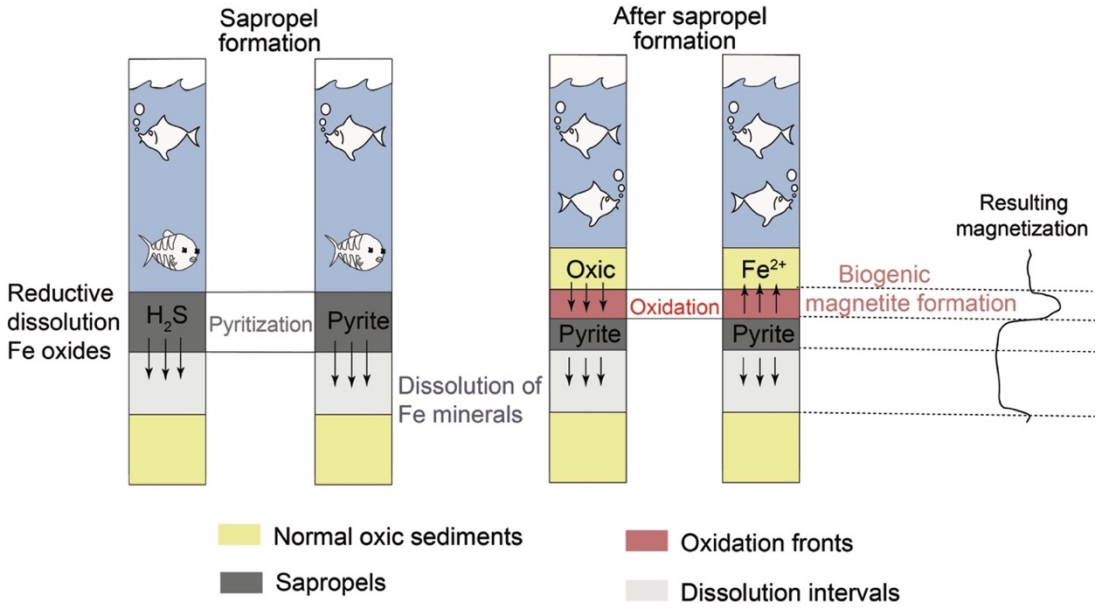

Fig. 4.2 Illustration of sapropel formation and magnetization (e.g., ARM) variations in the eastern Mediterranean Sea (characteristic of a Type 2 sapropel; Larrasoaña et al., 2003). Modified from Roberts (2015).

4.3. Methods

4.3.1 Magnetic measurements

All magnetic measurements were performed at the Paleomagnetism Laboratory, Australian National University (ANU). The studied samples were collected at 1-cm stratigraphic intervals and were placed into plastic cubes. A shielded narrow-access 2-G Enterprises cryogenic magnetometer was used to measure ARM and saturation isothermal remanent magnetization (SIRM). In this study, the ARM was imparted by applying a peak alternating field (AF) of 100 mT and a direct current (DC) bias field of 0.05 mT, and the SIRM was acquired with an induction field of 900 mT. χ_{ARM}/χ, ARM/SIRM, and SIRM/χ were measured to indicate magnetic grain size variations, where χ_{ARM} (susceptibility of ARM) is calculated as ARM/DC bias field (King et al., 1982; King & Channell, 1991). The coercivity parameter, S-ratio (= 0.5 × [1-(IRM$_{-0.3T}$/SIRM)]), is used to make inferences about the relative abundances of low- to high-coercivity minerals, where IRM$_{-0.3T}$ was imparted with a backfield of 0.3 T (Bloemendal et al., 1992).

Hysteresis loops and first-order reversal curves (FORCs; Pike et al., 1999) were measured on representative samples. Measurements were performed using a Princeton Measurements Corporation MicroMag Model 3900 vibrating sample magnetometer (VSM). Hysteresis curves were measured to ±500 mT, with field step and averaging times of 3 mT and 500 ms, respectively. Saturation magnetization (M_s), saturation remanent magnetization (M_{rs}), and coercive force (B_c) were obtained from loops, while the coercivity of remanence (B_{cr}) was obtained from backfield demagnetization curves after applying a saturation IRM along with hysteresis loops on the same system. FORCs were measured with the irregular grid FORC protocol of Zhao et al. (2015). A 300 ms averaging time was used for weakly magnetized samples (M_{rs} < 1 μAm^2), while other

samples (M_{rs} > 1 μAm^2) were measured with a 200 ms averaging time. FORC data were processed and plotted using the xFORC software with a smoothing factor of 3 or 4 based on sample noise level (Zhao et al., 2015, 2017).

A Quantum Design (QD) Magnetic Property Measurement System (MPMS; model XL7) was used for LT magnetic measurements of forty-four samples. A 5 T DC field was imparted to produce a room temperature SIRM (RTSIRM), which was then measured from 300 K to 10 K and then back to 300 K at 1 K intervals in zero field. This measurement is referred to as LT cycling (LTC) of a RTSIRM. Zero-field-cooled (ZFC) and field-cooled (FC) measurements were conducted following the method used in Qian et al. (2020). The superconducting MPMS magnet was "reset" after each field application to eliminate trapped fields. The MPMS system used here includes the QD Environmental Shield and ultra-low field option. However, small residual fields can remain after a magnet reset. Therefore, paramagnetic phases could contribute to measured LTC of RTSIRM, ZFC, and FC curves, particularly at low temperatures. We expect the remanence to dominate and this paramagnetic contribution should be minor.

4.3.2 TEM observations

Extraction and characterization of magnetic minerals from sediments were performed following Li et al. (2020a). TEM analysis was conducted at the Institute of Geology and Geophysics, Chinese Academy of Sciences (IGG-CAS) using a JEM-2100HR TEM with a LaB_6 gun and 200 kV accelerating voltage.

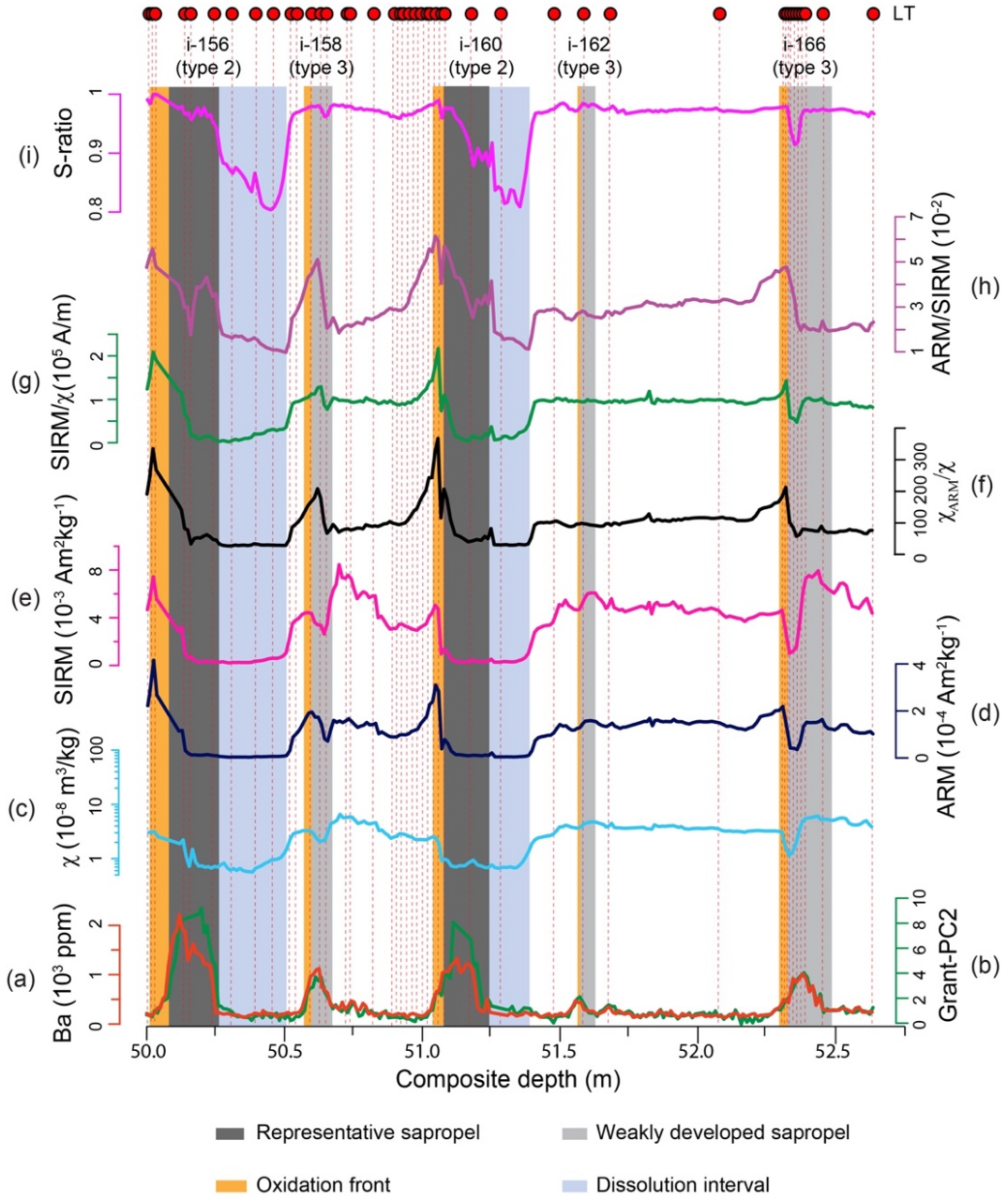

Fig. 4.3 Down-core variations of geochemical data and environmental magnetic parameters. Elevated (a) Ba (orange) and (b) Grant-PC2 (dark green) indicate the positions of sapropels. Discrete sample data include (c) χ (cyan); (d) ARM (dark blue); (e) SIRM (pink); (f) χARM/χ (black); (g) SIRM/χ (green); (h) ARM/SIRM (purple); and (i) S-ratio (magenta). Forty-four samples selected for LT analyses are indicated by red circles at the top of the figure. Dark gray and light gray shadings denote the locations of representative and weakly developed sapropels, respectively. Orange and blue shadings correspond to the locations of oxidation fronts and dissolution intervals, respectively. Sapropel stratigraphy is based on Emeis et al. (2000), where the numeric number followed by "i-" is the insolation cycle. Modified from Qian et al. (2020).

4.4. Sapropel identification

Sapropels were identified based on calibrated XRF elemental data (Grant et al., 2016) and the Grant-PC2 record (Grant et al., 2017). Grant-PC2 is a principal component estimated from geochemical results of eastern Mediterranean sediments, which contain several elements associated with sapropel formation (Grant et al., 2017; Qian et al., 2020). Using these two parameters together provides a comprehensive indication of sapropel locations. High Ba concentrations and Grant-PC2 values suggest that there are five sapropels of two types within the studied sediments. These two sapropel types are "representative" sapropels, i-156 and i-160, with well-developed oxidation fronts and dissolution intervals (type 2 according to Larrasoaña et al. (2003b); dark gray shading in Figs. 4.3-4.10) and "weakly developed" sapropels, i-158, i-162, and i-166, with well-developed oxidation fronts but without dissolution intervals (type 3 according to Larrasoaña et al. (2003b); light gray shading in Figs. 4.3-4.10), respectively. Thus, the studied sediments can be divided into three main parts: (1) representative sapropels (i-156 and i-160; Figs. 4.3-4.10), (2) weakly developed sapropels (i-158, i-162, and i-166; Figs. 4.3-4.10), and (3) background marls (Figs. 4.3-4.10).

4.5. Room temperature magnetic properties

Room temperature magnetic properties were reported by Qian et al. (2020) for the selected sediment interval. For representative sapropels, high ARM and SIRM values are observed in oxidized sediments above sapropels, which indicates a large proportion of ferrimagnetic minerals at oxidation fronts (Fig. 4.3). High χ_{ARM}/χ, ARM/SIRM, and SIRM/χ values in the oxidized sediments indicate that the ferrimagnetic minerals are more likely to be fine stable single domain (SSD)/vortex state grains (Fig. 4.3). However, ARM and SIRM values drop rapidly within sapropels and underlying dissolution

intervals due to magnetic mineral dissolution (Fig. 4.3). Low χ_{ARM}/χ, ARM/SIRM, and SIRM/χ values indicate that residual magnetic minerals in these intervals are mainly coarser grains (Fig. 4.3). This is also evident from extremely low S-ratios in the dissolution intervals (Fig. 4.3), which results from preferential removal of fine-grained magnetite. In addition, except for low ARM and SIRM values in the middle of weakly developed sapropels, other sediment intervals normally have high ARM and SIRM values (Fig. 4.3). Grain size parameters have almost the same variations in both representative sapropels and weakly developed sapropels, with high χ_{ARM}/χ, ARM/SIRM, and SIRM/χ ratios in oxidation fronts and low values within sapropels and underlying sediments (Fig. 4.3). Representative sapropels have low χ_{ARM}/χ, ARM/SIRM, and SIRM/χ ratios that persist throughout sapropels and dissolution intervals. By comparison, weakly developed sapropels have low ratios only in their lower parts before recovery commences. (Fig. 4.3). This suggests that sulfidic dissolution is not strong in weakly developed sapropels compared to representative sapropels. Furthermore, for normal sediments, all parameters remain stable. Specifically, ARM, SIRM, χ_{ARM}/χ, ARM/SIRM, and SIRM/χ change rapidly with lower values in dissolution intervals/weakly developed sapropels and higher or intermediate values between sapropels; S-ratios have relatively constant high values (Fig. 4.3).

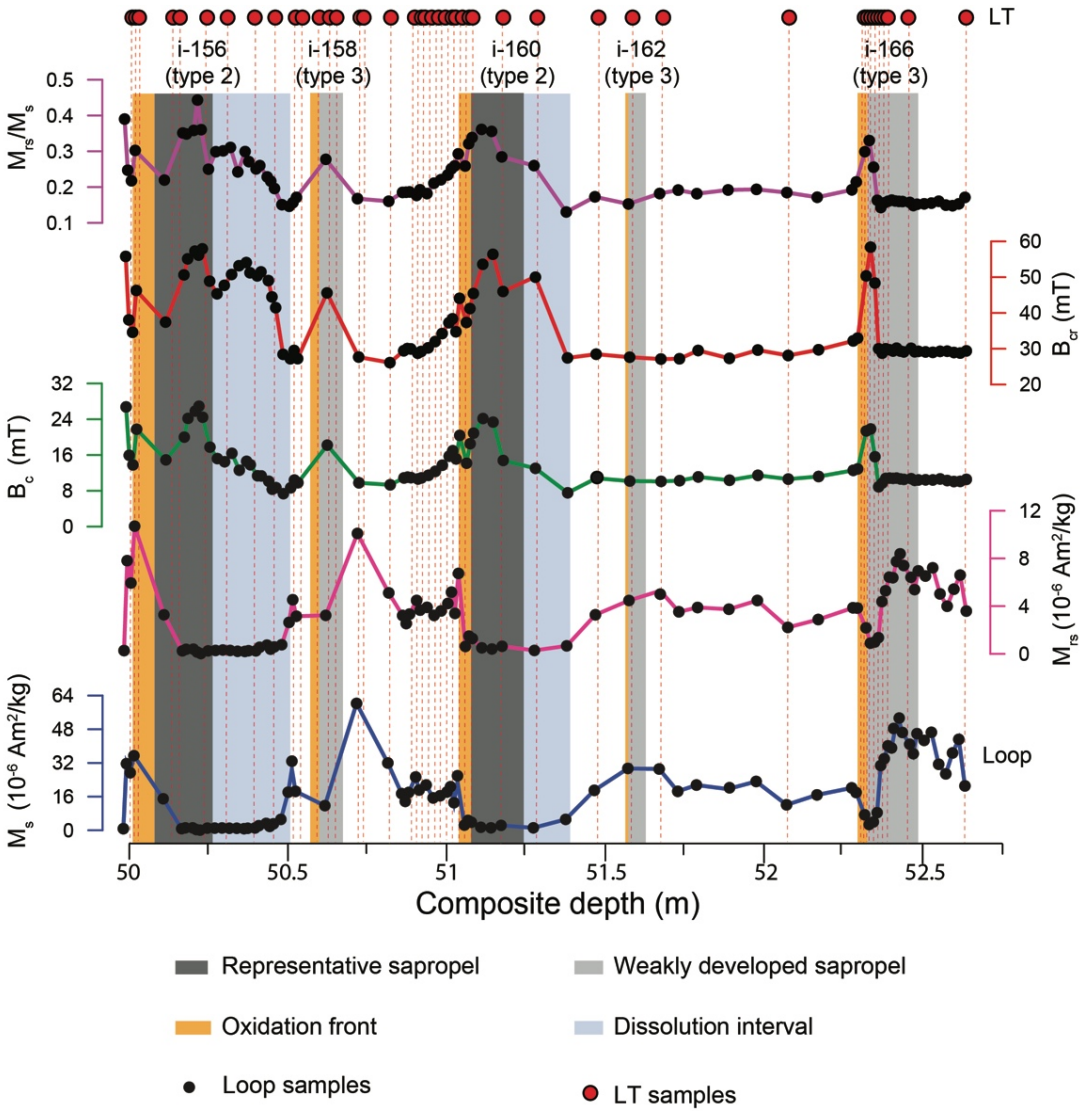

Fig. 4.4 Profiles of M_s, M_{rs}, B_c, B_{cr}, and M_{rs}/M_s versus depth. Red circles and the meaning of coloured shadings are identical to Fig. 4.3.

4.6. Results

4.6.1 Hysteresis properties

Hysteresis parameters are expressed in mass-normalized magnetic units, which account for sediment porosity variations. M_s and M_{rs} undergo similar stratigraphic variations; both increase sharply within oxidized sapropels, where maximum values are typically observed, and then decrease to minima within dissolution fronts beneath

sapropels (Fig. 4.4). M_{rs}/M_s increases within oxidation fronts from 0.15 to 0.5 (Fig. 4.4), which is indicative of SSD magnetite formation (potentially of biogenic origin) that formed at the tops of sapropels during bottom water reoxygenation (Garming et al., 2004; Kruiver & Passier, 2001; Larrasoaña et al., 2003b, 2006; Passier et al., 2001). Within marls, B_c and M_{rs}/M_s oscillate around values of 10 mT and 0.2, respectively, which is typical of many marine sediments (Fig. 4.4; Garming et al., 2004; Larrasoaña et al., 2007; Passier & Dekkers, 2002; Roberts et al., 2012). In contrast, high B_c, B_{cr}, and M_{rs}/M_s values indicate that high-coercivity minerals dominate in sapropels and dissolution intervals. This is probably a result of preferential magnetite dissolution.

4.6.2 Low-temperature magnetic properties

4.6.2.1 ZFC and FC warming

ZFC and FC warming curves have stratigraphic dependencies associated with different diagenetic zones. All ZFC and FC warming curves contain large remanence drops below 50 K, possibly due to the presence of SP grains (Fig. 4.5). Marked remanence drops between 10 and 50 K do not appear to be associated with siderite because we observe no features that could correspond to a Néel point of 38 K (Housen et al., 1996). For representative sapropels, two distinctive inflections are observed for samples from the overlying oxidation front. These inflections are related to the Verwey transition temperature (T_v) at ~95 K and ~110 K for magnetite (Fig. 4.5a) due to a combination of inorganic and biogenic magnetite. The remanence loss at ~95 K, which is related to biogenic magnetite, is more pronounced than that at ~110 K due to inorganic magnetite (Chang et al., 2016). The Verwey transition is not evident in the ZFC/FC derivatives in other regions of representative sapropels (Fig. 4.5a), which suggests that magnetite has been destroyed by reductive dissolution (Roberts, 2015). For marl samples,

all ZFC and FC curves contain a double T_v signature (Fig. 4.5c). FC curves have stronger remanences than ZFC curves. However, the remanence difference across all temperatures between FC and ZFC curves, especially around the Verwey transition, is smaller in marls than in oxidation fronts. When expressed as normalized derivatives, the remanence loss in marl samples is typically less than 0.05, while for oxidation front samples it is ~0.1 (Fig. 4.5c). The magnitude of the double T_v feature varies with depth, likely resulting from variable partial magnetite oxidation. The double T_v signature is present in all samples from the weakly developed sapropel, although it is attenuated through the middle of the sapropel (Fig. 4.5b).

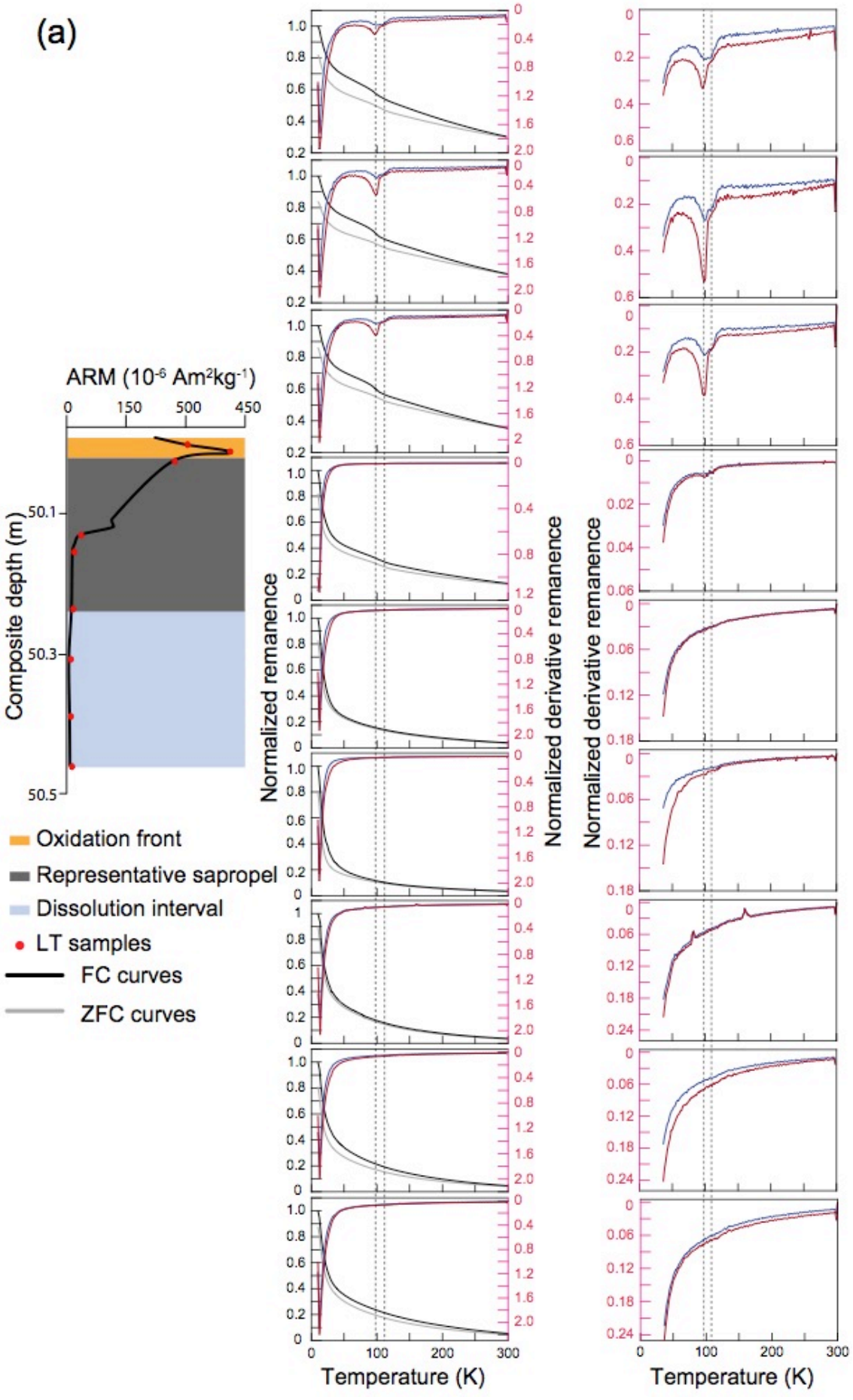
(a)
ARM (10^{-6} Am^{2}kg^{-1})
0
150
500
450
Composite depth (m)
50.1
50.3
50.5
Oxidation front
Representative sapropel
Dissolution interval
LT samples
FC curves
ZFC curves
Normalized remanence
Normalized derivative remanence
Temperature (K)
Temperature (K)

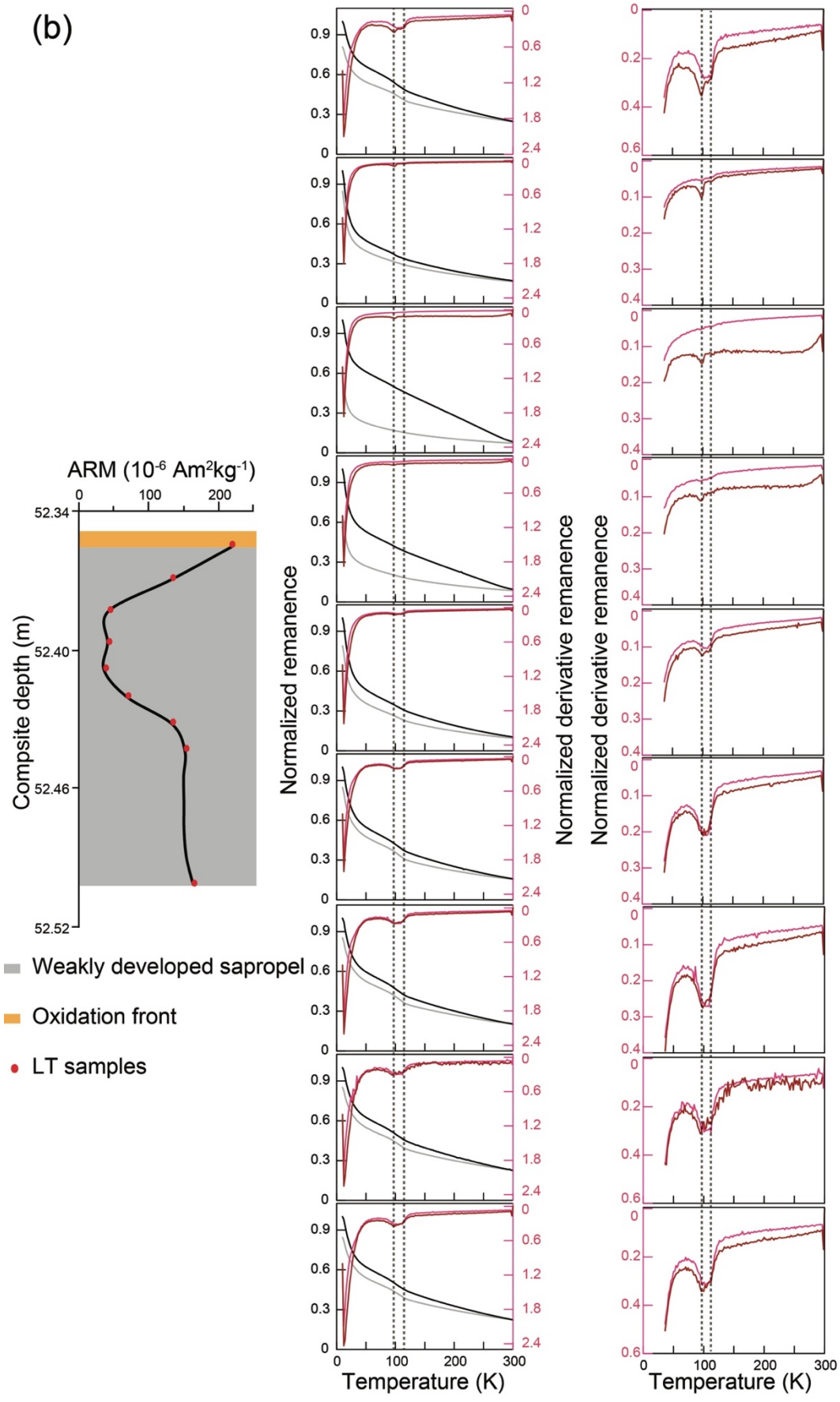
(b)
ARM (10^{-6} Am^2kg^{-1})
0
100
200
52.34
52.40
52.46
52.52
Compsite depth (m)
Weakly developed sapropel
Oxidation front
LT samples
Normalized remanence
Normalized derivative remanence
Normalized derivative remanence
Temperature (K)
Temperature (K)

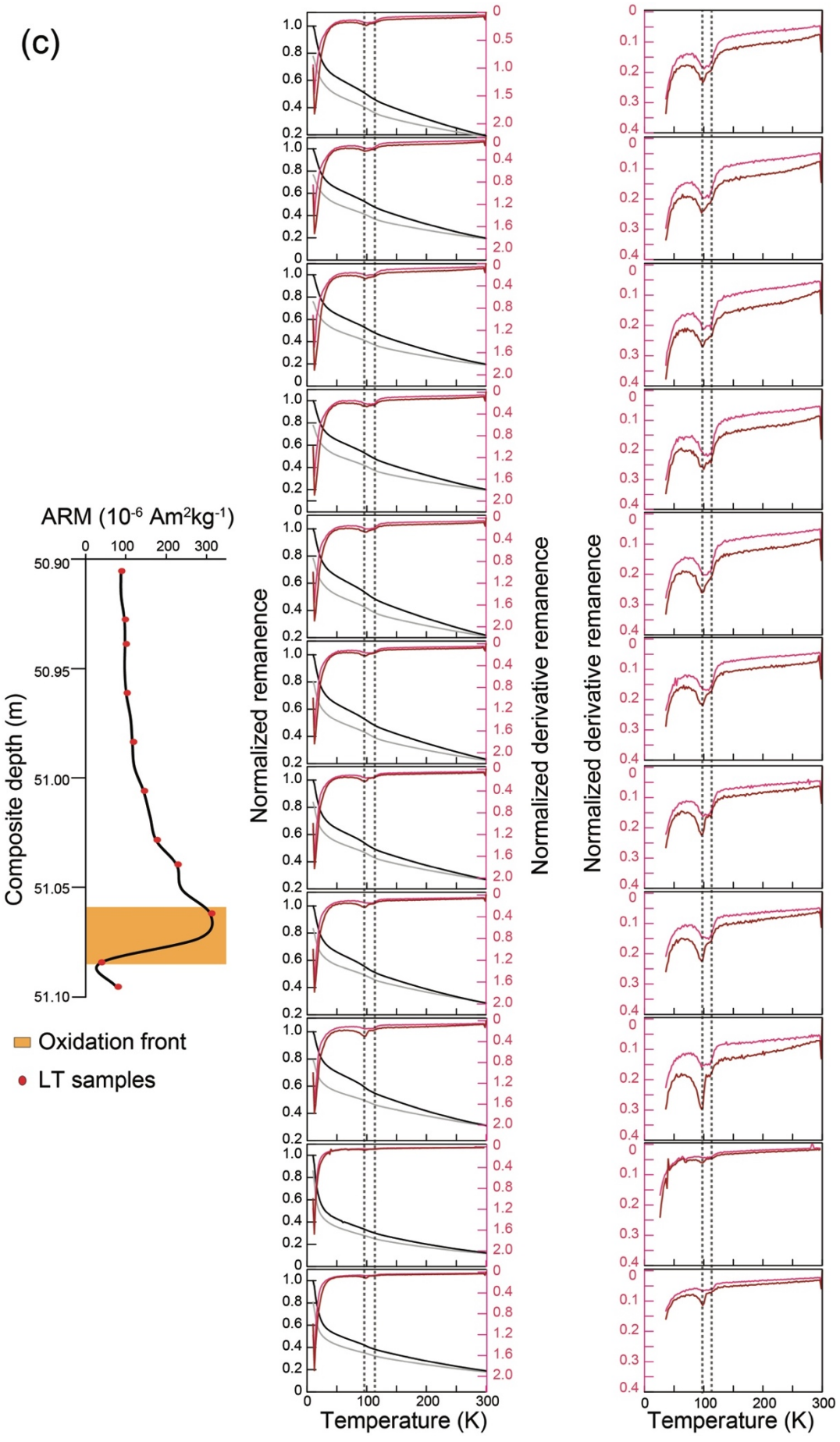
(c)
ARM (10^{-6} Am^2kg^{-1})
0 100 200 300
Composite depth (m)
50.90
50.95
51.00
51.05
51.10
Oxidation front
LT samples
Normalized remanence
Normalized derivative remanence
Temperature (K)
0 100 200 300

Fig. 4.5 ZFC and FC curves for samples from representative sedimentary intervals. ARM profile with sample locations indicated by red circles selected from (a) a representative sapropel (left), ZFC (gray) and FC (black) curves and their derivatives (blue (ZFC); red (FC)) (middle) and enlarged derivative curves (right). (b) Same as (a) but for a weakly developed sapropel (left). (c) Same as (a) but for marls. Dark gray, light gray, orange, and light blue shading indicate the respective representative sapropel, weakly developed sapropel, oxidation front, and dissolution interval, respectively.

4.6.2.2 Low-temperature cycling of RTSIRM

LTC results for a RTSIRM for the three studied intervals are shown in Fig. 4.6. Two distinctive LTC-RTSIRM patterns are observed in the representative sapropel (Fig. 4.6a), with samples from the representative sapropel and dissolution interval having different LTC behavior to the oxidation front (Fig. 4.6a). In the oxidation front, the remanence increases with cooling before decreasing to a local minimum (typically around 42 K), with a further slight increase at the lowest temperatures. The warming curves are similar to the cooling curves with <5% remanence loss between cooling and warming. Humped curves were observed by Özdemir & Dunlop (2010) for partially oxidized synthetic magnetite. The highest temperature of the hump varies between ~150 and 200 K for both warming and cooling curves (Fig. 4.6a). Samples from the sapropel and dissolution interval have almost reversible LTC curves, which increase (decrease) during cooling (warming) (Fig. 4.6a). As reported by Özdemir & Dunlop (2010), such cooling and warming curves are indicative of the occurrence of SSD maghemite. In the lower part of the weakly developed sapropel, LTC-RTSIRM curves are humped. This feature is absent from curves in the upper portion of the weakly developed sapropel (Fig. 4.6b). Samples from normal marly sediments that were deposited under oxic conditions have different LTC-RTSIRM behavior to the representative sapropel and weakly

developed sapropel (Fig. 4.6c). The hump-shaped feature is present in cooling curves but is absent from warming curves. The Verwey transition is not evident in warming curves for the marls, which is probably due to maghemitization.

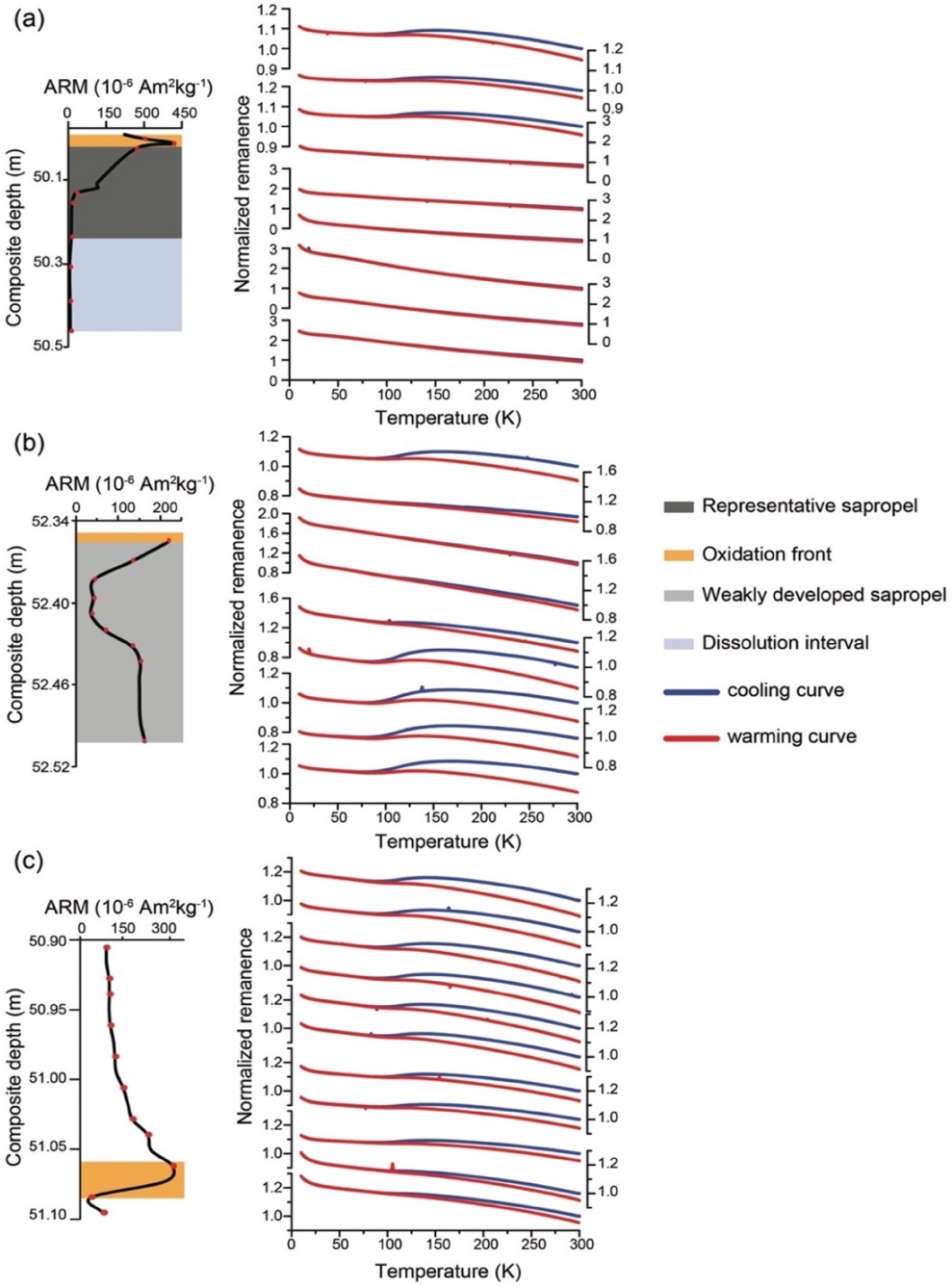

Fig. 4.6 LTC of RTSIRM for samples (red circles in ARM profiles) selected from (a) a representative sapropel (left), and their corresponding LTC curves (right); (b) as in (a) for a weakly developed sapropel, and (c) as in (a) for marls. Dark gray, light gray, orange, and blue shadings correspond to the representative sapropel, weakly developed sapropel, oxidation front, and dissolution intervals, respectively.

4.7. Discussion

4.7.1 SP particles

LT measurements are particularly useful for detecting SP particle contents (e.g., Chang et al., 2013; Dearing et al., 1997; Passier & Dekkers, 2002; Roberts, 1995; Smirnov & Tarduno, 2001). The initial slopes of ZFC and FC warming curves are mainly affected by ultrafine grained mineral phases, which unblock at low temperatures between ~10 and 40 K (Banerjee et al., 1993; Özdemir et al, 1993). This SP fraction may come from partial surface oxidation of fine magnetite particles after sapropel formation (Özdemir & Dunlop, 2010). Thus, $TD_{10\text{-}40K}$, which is equal to $[M_{rs}^{10K} - M_{rs}^{40K}]/M_{rs}^{10K}$ from FC curves, is used to represent the SP content. Moreover, as indicated by the remanence loss between low and room temperature in samples that lack a Verwey transition, the SP fraction (f_{SP}) can be estimated by the relationship (cf. Dunlop, 1973; Roberts, 1995):

$$f_{SP} = \frac{M_{rs}\,(10\,K) - M_{rs}\,(300\,K)}{M_{rs}\,(10\,K)}, \quad (1)$$

where warming occurs in zero field. As discussed in Section 4.3.1, these estimates may be influenced by paramagnetic magnetizations produced by residual fields in the MPMS superconducting magnet. Such spurious paramagnetic contributions are likely to be stronger in samples with low ferrimagnetic mineral concentrations. This caveat must be considered, although $TD_{10\text{-}40K}$ and f_{SP} are expected here to be mainly indicative of SP content.

Our LT curves have strong remanence losses, which we interpret to be indicative of SP unblocking in ZFC and FC curves below 40 K (Fig. 4.5). The parameter dM_r/dT provides a measure of the initial slope of ZFC and FC curves. It has relatively low values in dissolution intervals and, thus, does not have a strong expression compared to other SP proxies that focus on relative SP contributions (Fig. 4.7). To overcome this issue, we

normalized the initial slope by M_r to give $(dM_r/dT)/M_r$. Based on steep initial gradients of ZFC and FC curves and the highest values of f_{SP} and $TD_{10\text{-}40\ K}$ results, the SP particle content is higher at the base of representative sapropels and in the middle of weakly developed sapropels compared to other parts of the studied interval (Fig. 4.7). Although grain size parameter values decrease (e.g., ARM/SIRM) within strong dissolution intervals, which indicates removal of fine-grained material, SP particles do not influence such remanence-based ratios. Previous studies have suggested that SP behavior in diagenetically reduced sediments can have several origins: small immature magnetosomal magnetite crystals, fractions of ultrafine detrital oxidized/unoxidized magnetite, and dissolved ultrafine magnetic particles (Smirnov & Tarduno, 2000; Tarduno, 1995). SP grains may occur as a product of the breakdown of larger SD or vortex state particles in magnetic mineral reduction zones and may also be precipitated by dissimilatory iron-bearing bacteria (e.g., Moskowitz et al., 1993). Magnetosomal greigite has distinctive magnetic properties (e.g., Reinholdsson et al., 2013) that have so far only been documented in sapropels with extremely high organic carbon levels (Roberts et al., 1999; Type 1 according to Larrasoaña et al. (2003b)), so the presence of fine biogenic greigite is unlikely. High SP contents in the dissolution interval could be due to inorganic SP greigite growth as has been observed widely elsewhere (e.g., Rowan et al., 2009; Roberts et al., 2018). In contrast, the steep initial ZFC and FC slopes in oxidation fronts, for example, from representative sapropel i-160 and weakly developed sapropel i-166, are likely to have been caused by precipitation of fine-grained iron oxides in the SP state. Despite uncertainty concerning the origin of these hyperfine SP particles, LT measurements enable identification of their presence and can be used to investigate processes responsible for their presence.

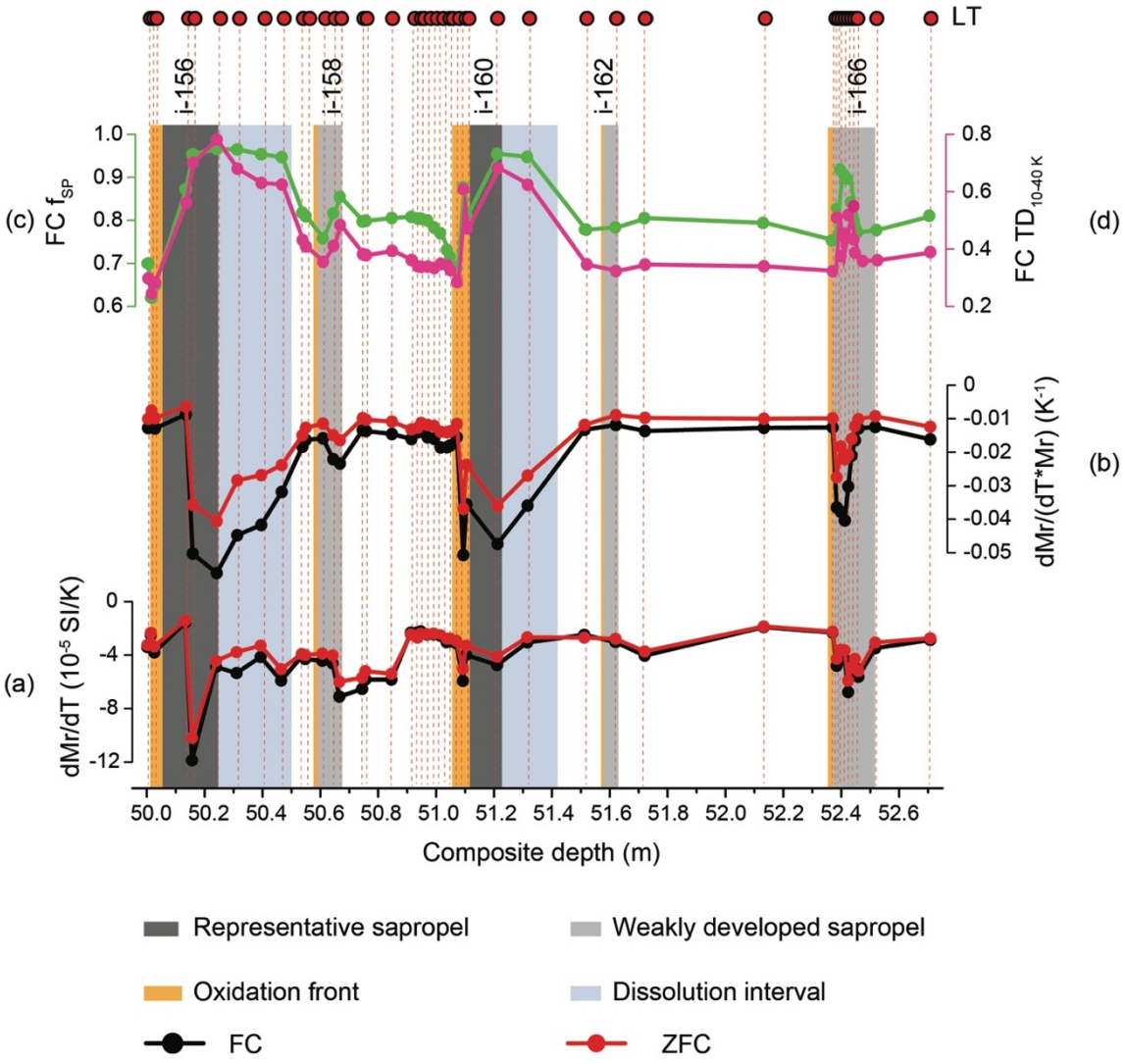

Fig. 4.7 Quantification of SP particle contents from LT magnetic and room temperature χ_{fd} measurements. (a) Estimation of SP contents from unblocking of ZFC and FC curves, as indicated from dM_r/dT data, which correspond to the absolute initial slope of warming curves; (b) ZFC and FC $(dM_r/dT)/M_r$ data, which correspond to the relative initial slope of warming curves, and (c, d) f_{SP} and $TD_{10\text{-}40\,K}$ from FC curves, which reflect the importance of SP grains. (e) Room temperature frequency dependence of magnetic susceptibility (χ_{fd}). Dark grey, light grey, orange, and light blue shadings indicate representative sapropels, weakly developed sapropels, oxidation fronts, and dissolution intervals, respectively.

4.7.2. Magnetofossils

Magnetotactic bacteria (MTB) produce highly crystalline SD magnetite within their cells. These particles typically consist of linear chains of SD magnetite, although other structures also occur (Li et al., 2020b, 2020c). After death, the magnetic remains of MTB (referred to as magnetofossils) can contribute to the natural remanent magnetization of sediments (Heslop et al., 2013; Kopp & Kirschvink, 2008; Moisescu et al., 2014; Moskowitz et al., 1993; Roberts et al., 2012). Furthermore, given the link between MTB and specific habitat conditions, magnetofossils can potentially record environmental variability (Chang et al., 2018; Heslop et al., 2014; Hesse, 1994; Li et al., 2013a; Yamazaki & Kawahata, 1998; Yamazaki & Ikehara, 2012).

LT measurements, particularly FC and ZFC curves, have been used extensively to detect magnetofossils in sediments. The δ_{FC}/δ_{ZFC} parameter has been proposed to detect magnetofossils (Moskowitz et al., 1993), where δ is the remanence lost during warming across the Verwey transition ($\delta = (M_r^{80K} - M_r^{150K})/M_r^{80K}$). When $\delta_{FC}/\delta_{ZFC} > 2$, magnetosome chains may be intact and unoxidized. When $\delta_{FC}/\delta_{ZFC} \sim 1$, magnetosome chains may be disrupted, maghemitized, or occur as part of a mixed magnetic mineral assemblage (Moskowitz et al., 1993). Based on systematic studies of diverse modern MTB and various spatial arrangements of magnetosomal magnetic particles, δ_{ZFC} versus δ_{FC}/δ_{ZFC} (i.e., a so-called δ-plot) has been proposed for identifying unoxidized magnetofossils based on the distribution of magnetosome chains (Li et al., 2012, 2013b, 2020b). From LT analysis of sapropel S1, Passier & Dekkers (2002) interpreted magnetofossils to occur predominantly in oxidized intervals above sapropels.

Our LT results indicate that magnetite magnetofossils occur in the studied interval. Double T_v features are present in samples from oxidation fronts, weakly developed sapropels, and marls, but are not found in sediments from strong dissolution intervals.

This suggests that magnetofossils exist widely in the studied sediments (Chang et al., 2016), with the exception of zones that have experienced strong magnetite dissolution. TEM images support this hypothesis (Figs. 4.8j, k, n, p, q, t, v, x, and S4). The lower T_v for biogenic magnetite has been proposed to be an intrinsic property of biogenic magnetite (Pan et al., 2005). Thus, identification of a ~95 K T_v in FC curves appears to be a powerful indicator of the presence of magnetofossils. Moreover, FC remanence loss is more pronounced at ~95 K (biogenic magnetite) compared to that at ~110 K (inorganic magnetite). The suppressed magnitude of the Verwey transition in inorganic magnetite may be due to Ti substitution in titanomagnetite.

Differences in shape and crystalline anisotropy cause different remanence losses at T_v for biogenic and inorganic magnetite (Moskowitz et al., 1993). The δ parameter quantifies remanence loss during warming through T_v. Although δ_{FC}/δ_{ZFC} does not vary significantly in the studied sediments, the data can be separated into three groups based on sediment type (Fig. 4.9a). This indicates that biogenic and inorganic magnetite proportions vary between the sediment types. Qian et al. (2020) used FORC-principal component analysis (FORC-PCA) to identify and quantify detrital (EM1) and biogenic (EM2) magnetite in the studied interval. They found that biogenic magnetite is present widely throughout the studied interval and has markedly enhanced concentrations at oxidation fronts, while detrital magnetite dominates the sediment magnetization elsewhere (Qian et al., 2020). Similar stratigraphic variations between EM2 in the FORC-PCA analysis of Qian et al. (2020) and δ_{FC}/δ_{ZFC} indicate that oxidation fronts are dominated by magnetofossils, while weakly developed sapropels and intercalated marls contain mixtures of magnetofossils and inorganic magnetite (Fig. 4.9b). This interpretation is confirmed by widespread double T_v features in samples selected from weakly developed sapropels and intercalated marls (Chang et al., 2016). δ_{FC}/δ_{ZFC} values

for our samples are relatively low (<1.4), which may be due to surface oxidation of magnetofossils or disrupted chains (Chang et al., 2013; Housen & Moskowitz, 2006; Li et al., 2010; Moskowitz et al., 1993; Passier & Dekkers, 2002; Roberts et al., 2012; Smirnov & Tarduno, 2000; Weiss et al., 2004).

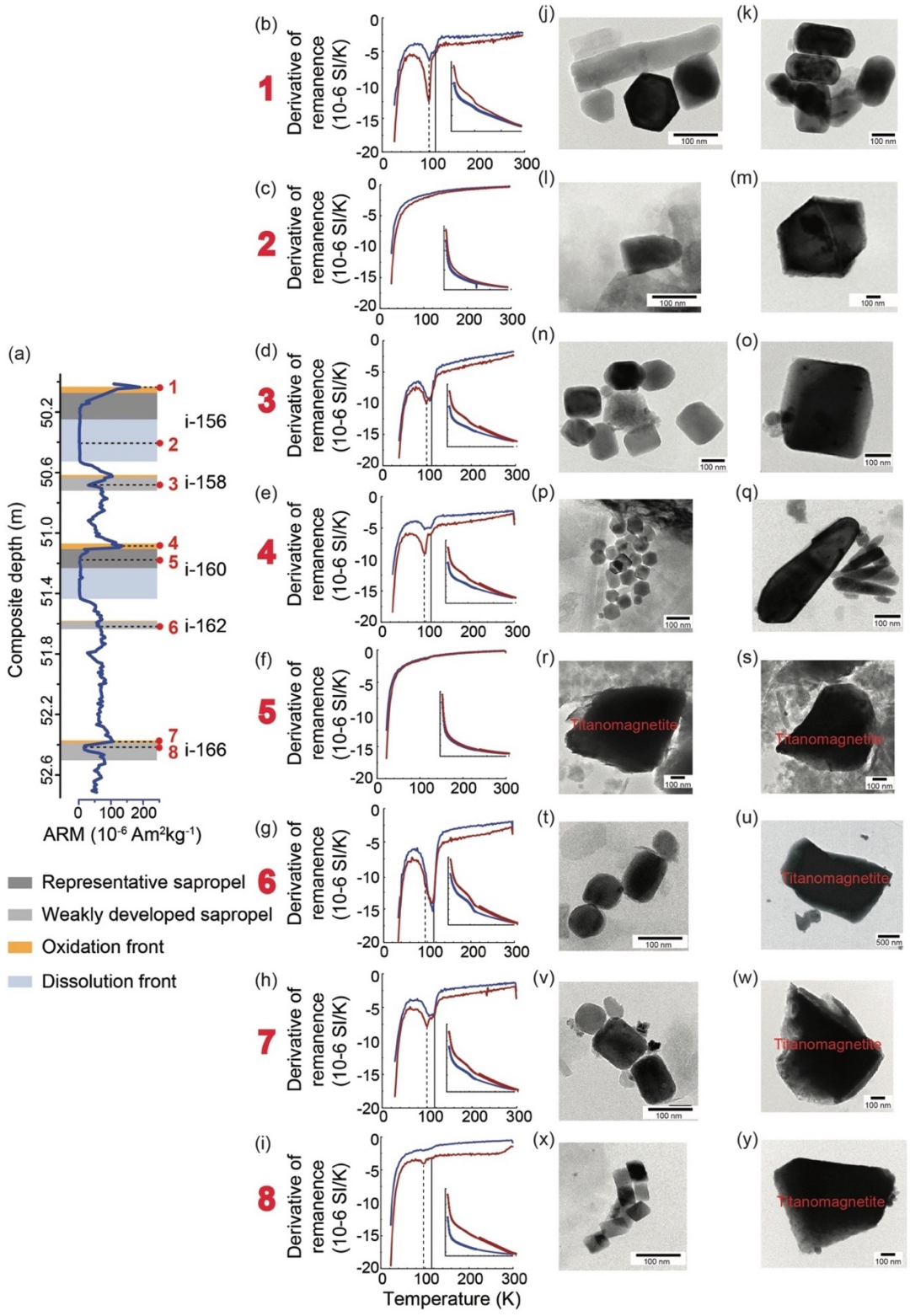

Fig. 4.8 LT magnetic measurements for eight representative samples and associated TEM images. (a) ARM profile with the eight selected sample positions indicated. (b-i) LT magnetization curves (inset) and their derivatives (ZFC curves (pink) and FC curves (red)). Distinctive double Tv peaks at ~95 and ~110 K are indicated by vertical dashed and solid lines, respectively. (j-y) TEM images for the representative samples, including (j, k) Sample 1: magnetite magnetofossils from the oxidation front above representative sapropel i-156; (l, m) Sample 2: magnetite magnetofossils and detrital titanomagnetite from the (middle) dissolution zone for representative sapropel i-156; (n, o) Sample 3: magnetite magnetofossils and detrital titanomagnetite from the middle of weakly developed sapropel i-158; (p, q) Sample 4: abundant magnetite magnetofossils from the oxidation front at the top of representative sapropel i-160; (r, s) Sample 5: detrital titanomagnetite from the middle of representative sapropel i-160; (t, u) Sample 6: magnetite magnetofossils and titanomagnetite from the middle of weakly developed sapropel i-162; (v, w) Sample 7: abundant magnetite magnetofossils and detrital titanomagnetite from the oxidation front of weakly developed sapropel i-166; and (x, y) Sample 8: abundant magnetite magnetofossils and detrital titanomagnetite from the middle of weakly developed sapropel i-166. Modified and expanded with additional data from Qian et al. (2020).

4.7.3. Maghemitization

Although the Verwey transition is not observed in representative sapropels and dissolution intervals, TEM observations demonstrate that magnetofossils and titanomagnetite particles are present (Fig. 4.9l, m, r, and s). This lack of a T_v signal could be caused either by partial magnetite oxidation or Ti substitution, which both suppress the Verwey transition, or by a low magnetofossil concentration due to dilution by organic matter or reductive dissolution. Partial magnetite oxidation (maghemitization) is common in marine sediments (Henshaw & Merrill, 1980; Karlin, 1990; Roberts, 2015; Smirnov & Tarduno, 2002; Torii 1997; Vali & Kirschvink, 1989; Yamazaki & Solheid, 2011) and can occur both at the water-sediment interface as a result of diffusion of molecular oxygen into particle surfaces and deeper in the suboxic zone of sediments as a result of bacterially mediated processes that include nitrate reduction (Kïg et al., 1997;

Smirnov & Tarduno, 2000; Torii, 1997). Magnetite oxidation can affect low-temperature magnetic properties significantly, including the Verwey transition magnitude, which compromises its detectability (Özdemir et al., 1993). Thus, maghemitization is an important process to consider in environmental magnetic reconstructions.

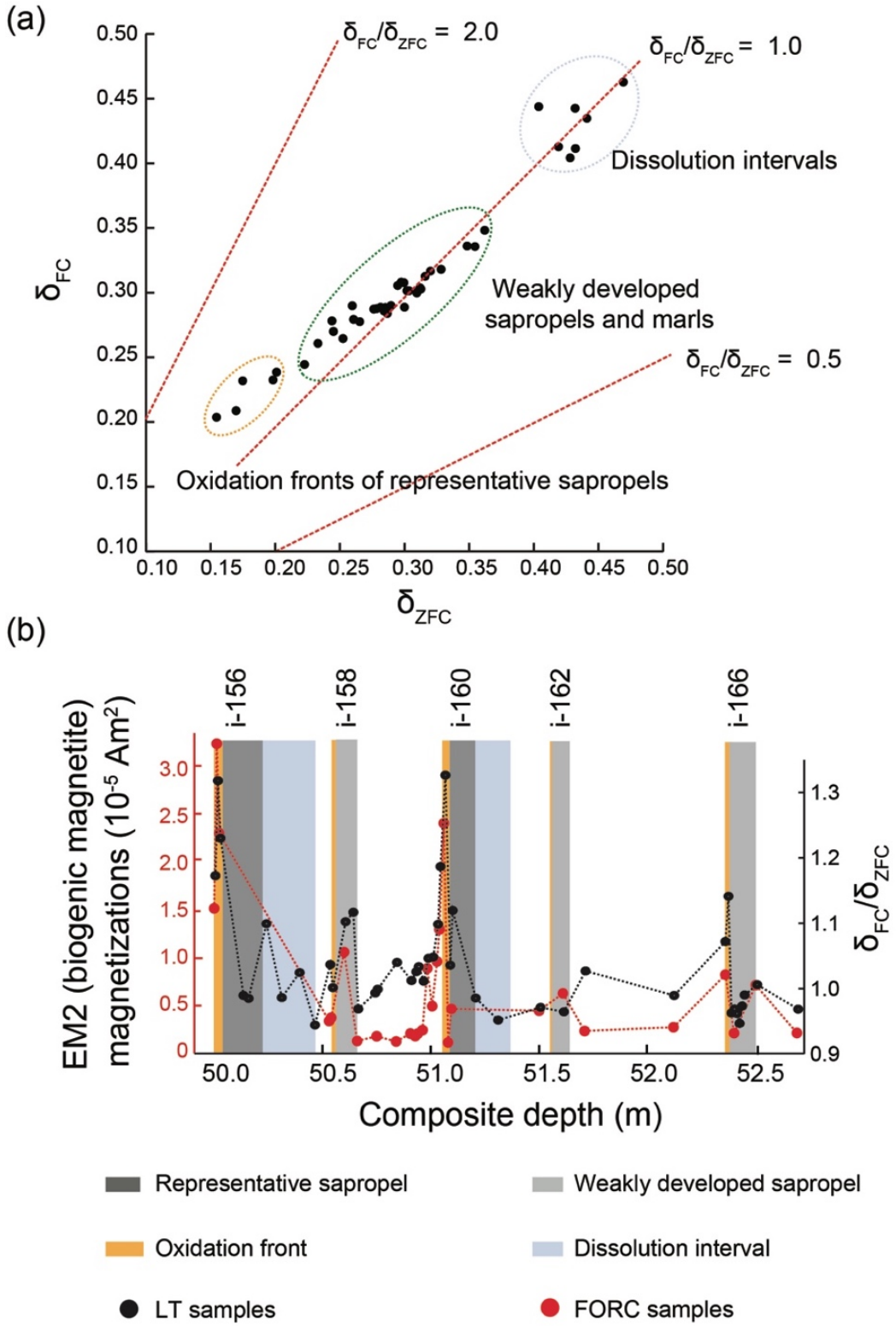

Fig. 4.9 Moskowitz test results: (a) δFC versus δZFC for all measured samples, and (b) EM2 abundance from the FORC-PCA analysis of Qian et al. (2020), which corresponds to the magnetization due to biogenic magnetite, compared to δFC/δZFC values. Dark gray, light gray, orange, and light blue shadings indicate representative sapropels, weakly developed sapropels, oxidation fronts, and dissolution intervals, respectively.

A distinctive feature of partially oxidized magnetite is the reversible hump in LTC- RTSIRM cooling and warming curves (Chang et al., 2013; Özdemir & Dunlop, 2010). During cooling, remanence increases between 300 and ~150 K and then decreases dramatically as T_v is approached. During warming, the curves are reversible. When they approach T_v, there is a modest remanence recovery above T_v, and a compensating loss as 300 K is approached. Humped curves are common in the studied sediments, except for the lower part of representative sapropels, underlying magnetite dissolution intervals, and the upper zone of weakly developed sapropels. Within the strong dissolution zones, no T_v is observed in LTC-RTSIRM and ZFC/FC SIRM curves, which suggests the absence of stoichiometric magnetite, and the lack of humped LT-SIRM curves indicates a lack of maghemitization. However, TEM observations (Qian et al. 2020) provide clear evidence that magnetite is still present in these zones, albeit in low concentrations (Fig. 4.8l and m). Thus, the absence of a detectable Verwey transition is likely indicative of a low magnetite concentration. The room temperature memory ratio, M'_{300}/M_{300}, where M_{300} is the initial M_r at 300 K, and M'_{300} is the terminal M_r value after LT cycling, is an important indicator of partially oxidized magnetite. M'_{300}/M_{300} increases with oxidation degree (Muxworthy et al., 2003; Özdemir & Dunlop, 2010). The memory ratio suggests that oxidized magnetite has minimum abundances in strong dissolution intervals, and maximum abundances in oxidation fronts of representative sapropels (Fig. 4.10b). For magnetite dissolution intervals, relatively higher M'_{300}/M_{300} values are observed in the lower parts (Fig. 4.10b), where magnetic mineral abundances are low and iron oxide

dissolution is not expected to have been as extensive as in more strongly sulfidized intervals within and immediately below the representative sapropels. This suggests that a fraction of maghemitized magnetite remains in the less extensively sulfidized lower magnetite dissolution interval.

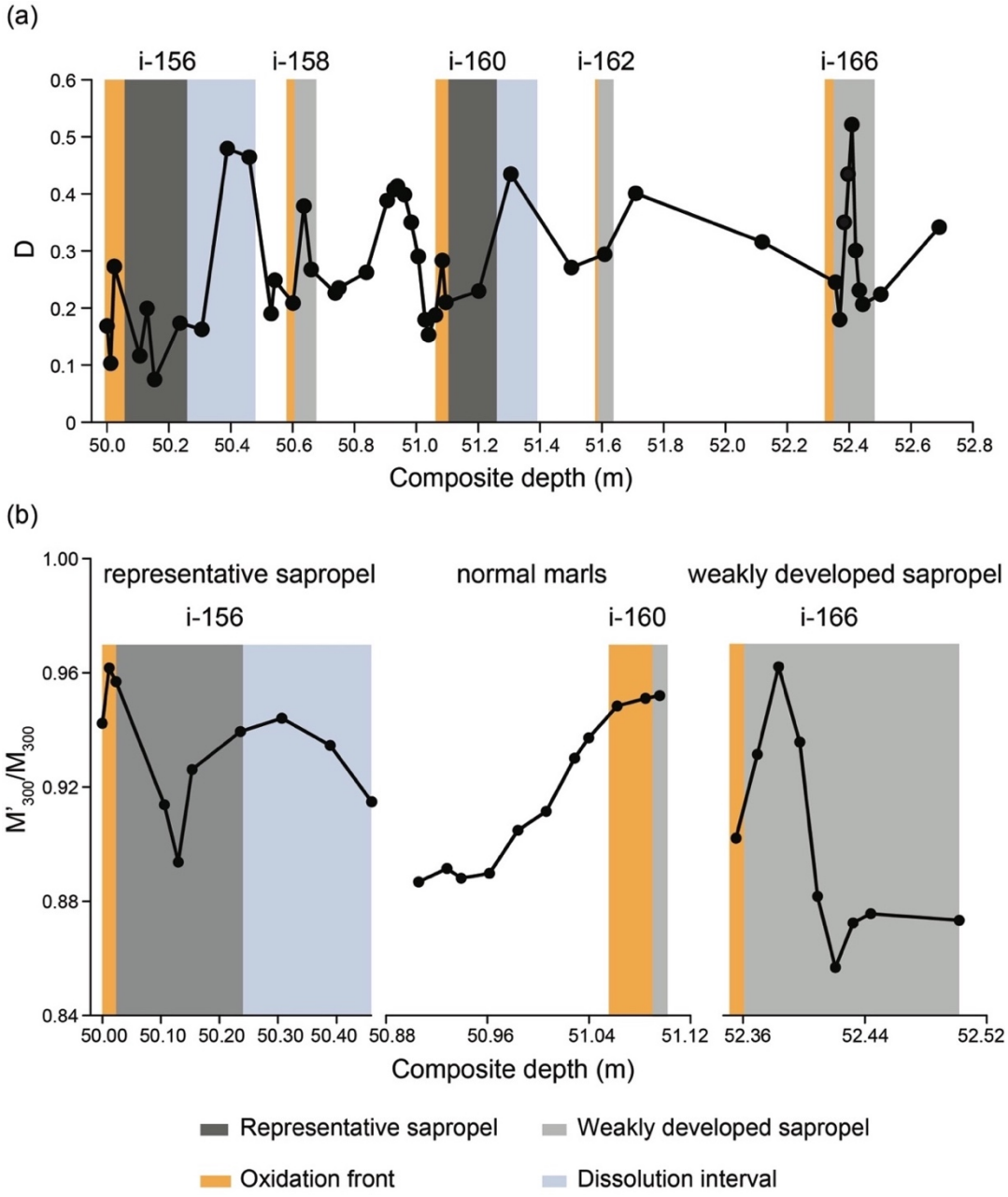

Fig. 4.10 (a) D parameter and (b) M'_{300}/M_{300} as a function of depth in the studied intervals. These parameters indicate the relative importance of maghemitization (partial surface oxidation of magnetite). Dark gray, light gray, orange, and light blue shadings indicate representative sapropels, weakly developed sapropels, oxidation fronts, and dissolution intervals, respectively.

Magnetic memory increases with decreasing grain size in submicron and larger stoichiometric magnetite (Dunlop & Argyle, 1991; Halgedahl & Jarrard, 1995; Hartstra, 1982; Heider et al., 1992; Hodych, 1991; Muxworthy et al., 2003; Özdemir et al., 1993). Finer particles are expected to be affected most by maghemitization because oxidation starts from the surface and proceeds inward, which produces an oxidized shell and a mostly unoxidized core. Fine-grained biogenic magnetite is enriched in oxidation fronts, especially in representative sapropels (Qian et al., 2020), which supports this interpretation. Thus, high M'_{300}/M_{300} values in oxidation fronts of representative sapropels suggest that magnetofossil surfaces in these zones have been maghemitized extensively.

Room temperature memory is an indicator of oxidation degree. However, due to lattice mismatch at the maghemite-magnetite interface, the internal stress between the outer maghemite shell and magnetite core could affect remanence recovery when cycling through T_v (Özdemir & Dunlop, 2010), leading to lower M'300/M300 values. To avoid the influence of the Verwey transition, Passier & Dekkers (2002) introduced a parameter, $D = \frac{M_{rs\,FC}^{150-300K} - M_{rs\,ZFC}^{150-300K}}{M_{rs\,FC}^{300K}}$, which quantifies the relative difference between the high temperature regions (150-300 K) of FC and ZFC warming curves. Across this high-temperature interval, ZFC and FC curves for unoxidized biogenic magnetite should coincide approximately. Therefore, differences between ZFC and FC curves in this high-temperature interval may be caused by oxidation of detrital magnetite (Passier & Dekkers, 2002; Smirnov & Tarduno, 2000). Low D values are observed in the representative sapropels and in the upper to middle dissolution intervals (Fig. 4.10a), which indicates a low degree of magnetite oxidation. This is consistent with the expectation that maghemitized shells in partially oxidized magnetite dissolve before the magnetite core of such composite core-shell particles (Torii, 1997; Yamazaki & Solheid, 2011).

4.8. Conclusions

Low-temperature magnetic analysis of sediments can provide valuable insights into processes of importance in environmental magnetism. Our results indicate that superparamagnetic particle contents are elevated in the lower part of representative sapropels and in the middle of weakly developed sapropels. Double T_v features in ZFC and FC warming curves suggest that magnetite magnetofossils and detrital magnetite occur widely in the studied sediments except within representative sapropels and their underlying dissolution intervals. In addition, we demonstrate that maghemitization is a common phenomenon in the studied oxic sediment intervals, which suggests that magnetite magnetofossils have experienced surficial maghemitization. The sensitivity of LT magnetic analyses to important environmental processes suggests that they deserve to be used more extensively in environmental magnetism for detecting magnetofossils, SP particles, and maghemitization on magnetite particle surfaces.

Chapter 5

Assessment of causes of increased Saharan dustiness across the mid-Pleistocene Transition

Abstract

During the Mid-Pleistocene Transition (MPT; ~1.25 to ~0.70 Ma), Earth's orbitally paced climate went through a major change with intensified glacial cycles, changing from ~41 kyr to ~100 kyr cycles that became significantly asymmetrical. Key changes during the MPT include increased dust delivery from arid source regions, especially during glacial periods, with important global biogeochemical impacts. Here, we integrate new and existing high-resolution eastern Mediterranean proxy records to discuss the cause(s) of dust intensification across the MPT from one of the world's largest source areas, the Sahara Desert. We assess previous hypotheses, including increasing source-area aridity due to reduced precipitation, expanding dust source areas, and atmospheric CO_2 reduction that led to decreased vegetation and soil cohesion. We observe that none of these hypotheses explains satisfactorily the dustiness increase across the MPT. Instead, the evidence points toward intensification of wet-dry cycles, in which increased alluvial and lacustrine silt generation and deposition during intensified African summer monsoon periods was followed by ablation during intensified arid periods. Our finding that increasing climate extremes boosted wind-blown dust fluxes is important because the resultant aeolian aerosols play major roles in both the radiative balance of climate, and biogeochemical cycles in areas where the dust settles.

5.1. Introduction

The Mid-Pleistocene Transition (MPT) occurred between around 1.25 and 0.70 Ma (Chalk et al., 2017; Clark et al., 2006; Elderfield et al., 2012). It was a transitional period for Earth's climate, during which the previously dominant, temporally symmetrical, 41-kyr glacial-interglacial (G-IG) cycles evolved into ~100-kyr cycles

(Chalk et al., 2017; Clark et al., 2006; McClymont et al., 2013). Post-MPT G-IG cycles were distinctively asymmetrical, with prolonged glaciation rates and rapid deglaciation events (Clark et al., 2006; Mudelsee & Schulz, 1997; Park & Maasch, 1993; Schmieder et al., 2000). This fundamental climate reorganization occurred in the absence of considerable changes in orbital forcing, which has led to the suggestion that the MPT involved a change of internal climate system feedbacks (Clark et al., 2006) that included important biogeochemical impacts of increasing wind-blown dust fluxes (Chalk et al., 2017). Resultant dust aerosols in addition play a major role in the radiative balance of climate (e.g., Rohling et al., 2012).

Here we focus on the dust emission history from one of the world's major dust sources, the Sahara, capitalizing on the highly resolved, continuous, multi-proxy records of MPT dust emission changes that can be constructed for this region with exceptional age control. Saharan dustiness increased through the MPT, especially during glacial periods (Fig. 5.1a). Several hypotheses have been proposed to explain G-IG changes in dust emissions: increased dust source-area aridity due to reduced precipitation (hypothesis 1 or H_1; Rea, 1994), lowered atmospheric CO_2 contents that contributed to decreased vegetation and soil cohesion (H_2; Bond et al., 2003; Mahowald et al., 2006b), and expanded dust source areas (H_3; Petit et al., 1981) (Table 5.1). Here, we propose a fourth hypothesis, based on the observation of Goudie & Middleton (2001) that silt-rich alluvium, which is easily weathered and stored in fluvial/lacustrine/wadi systems, provides the raw material for renewable dust generation. In this hypothesis (H_{new}), an increase of wet/dry cycle intensity is the primary driver of increased glacial Saharan dustiness across the MPT.

We consider a range of proxy records from eastern Mediterranean marine sediments to evaluate the four hypotheses. The records include new continuous and high-

resolution magnetic and planktic foraminiferal oxygen isotope data, published calibrated X-ray fluorescence (XRF) core-scanning data (Grant et al., 2017) from eastern Mediterranean sediments, and published atmospheric CO_2 data (Chalk et al., 2017). We test the four proposed hypotheses based on expected distinguishing proxy expressions (Table 5.1).

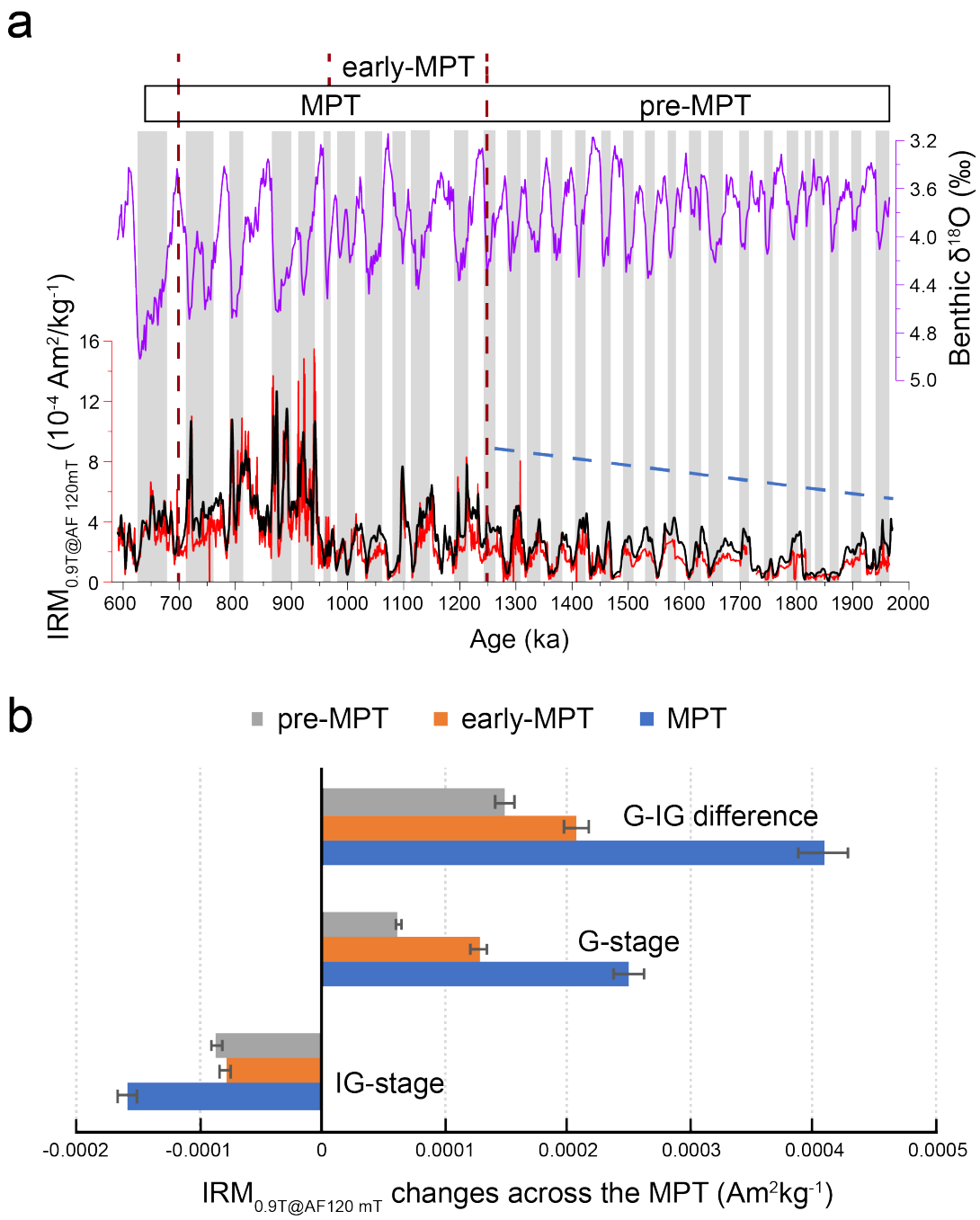

Fig. 5.1. Dust proxy changes before and through the MPT. (a) LR04 benthic foraminiferal oxygen isotope stack (Lisiecki & Raymo, 2005; purple) and our high-resolution $IRM_{0.9T@AF120mT}$ data from ODP Site 967 for discrete samples (red) and u-channel samples (Larrasoaña et al., 2003a;

black). Grey shaded bars indicate the positions of glacials (Lisiecki & Raymo, 2005). The age model is based on Grant et al. (2017). (b) Quantified $IRM_{0.9T@AF120mT}$ changes in the pre-MPT, early-MPT, and MPT intervals identified in (a). We define glacial (G) and interglacial (IG) subsets of the dataset based on a 25% cutoff criterion and quantify the change in the (bottom) IG and (middle) G $IRM_{0.9T@AF120mT}$ record and (top) the change in magnitude of IG-G $IRM_{0.9T@AF120mT}$ cycles. Thin grey bars denote error bars for the one-sided test of the sign of $IRM_{0.9T@AF120mT}$ change at the 95% significance level. Details of the $IRM_{0.9T@AF120mT}$ quantification for G, IG, and IG-G intervals are presented in the Supplementary Information.

5.2. Methods

5.2.1. Magnetic analyses

An isothermal remanent magnetization (IRM) imparted with a 0.9 T induction ($IRM_{0.9\ T}$) was then subjected to alternating field (AF) demagnetization at 120 mT ($IRM_{0.9T@AF120\ mT}$). The parameter $IRM_{0.9T@AF120\ mT}$ was measured on discrete samples using a 2-G Enterprises cryogenic magnetometer and has been used as a high-coercivity hematite concentration indicator at ODP Site 967 to avoid difficulties with IRM intensities exceeding the dynamic range of the magnetometer used for these measurements and other uncertainties associated with "hard" IRM (HIRM) calculation (Larrasoaña et al., 2003a; Liu et al., 2002). Hematite has been demonstrated as the high-coercivity magnetic mineral that is responsible for the $IRM_{0.9T@AF120\ mT}$ signal in sediments from ODP Site 967 (Larrasoaña et al., 2003a). Thus, $IRM_{0.9T@AF120\ mT}$ has been proposed as an indicator for Saharan dust input to the eastern Mediterranean Sea, and it is used for this purpose here. Larrasoaña et al. (2003a) presented a three-million-year record of $IRM_{0.9T@AF120\ mT}$ from u-channel measurements, which has 4-5 stratigraphic cm resolution (Weeks et al., 1993). The record presented here has been remeasured on discrete samples with 1-cm resolution.

5.2.2. Stable oxygen isotopes

The surface-layer dwelling planktic foraminiferal species analysed in this study is *Globigerinoides ruber (white)*, which is highly tolerant to low salinity (Rohling et al., 2004). During sapropel formation, this kind of foraminifer can occupy opportunistically less saline surface water habitats in the eastern Mediterranean Sea at the top of the water column (Amies et al., 2019; Rohling et al., 2004; Schiebel & Hemleben, 2017). This makes it the ideal species to monitor freshwater flooding associated with enhanced African monsoon runoff during sapropel events.

A 63 μm sieve was used to wash about 2 cm^3 of bulk sediment with reverse osmosis (RO) water. Then, before being sieved through 150 and 300 μm meshes, the >63 μm part was dried overnight in an oven at 45°C. *G. ruber (w)* was selected from the larger than 300 μm sediment fraction in a narrow size range (the microscope eyepiece is constrained to 35-50 μm size-windows). Foraminifera were first crushed before analysis and were then cleaned briefly with ultrasonication using methanol.

A Thermo Scientific DELTA V Isotope Ratio Mass Spectrometer equipped with a KIEL IV Carbonate Device was used for stable isotope measurements. Oxygen isotope ratios ($\delta^{18}O$) are reported in relation to VPDB (Vienna Pee Dee Belemnite) using NBS-19 ($\delta^{18}O$ = -2.20 ‰) and NBS-18 ($\delta^{18}O$ = -23.20 ‰) carbonate standards and are expressed in parts per thousand (‰):

$$\delta^{18}O\ (‰) = \left(\frac{^{18}O/^{16}O_{sample} - {}^{18}O/^{16}O_{standard}}{^{18}O/^{16}O_{standard}}\right) \times 1000, \quad (5.2.1)$$

External precision (1σ) was better than 0.08‰ for $\delta^{18}O$.

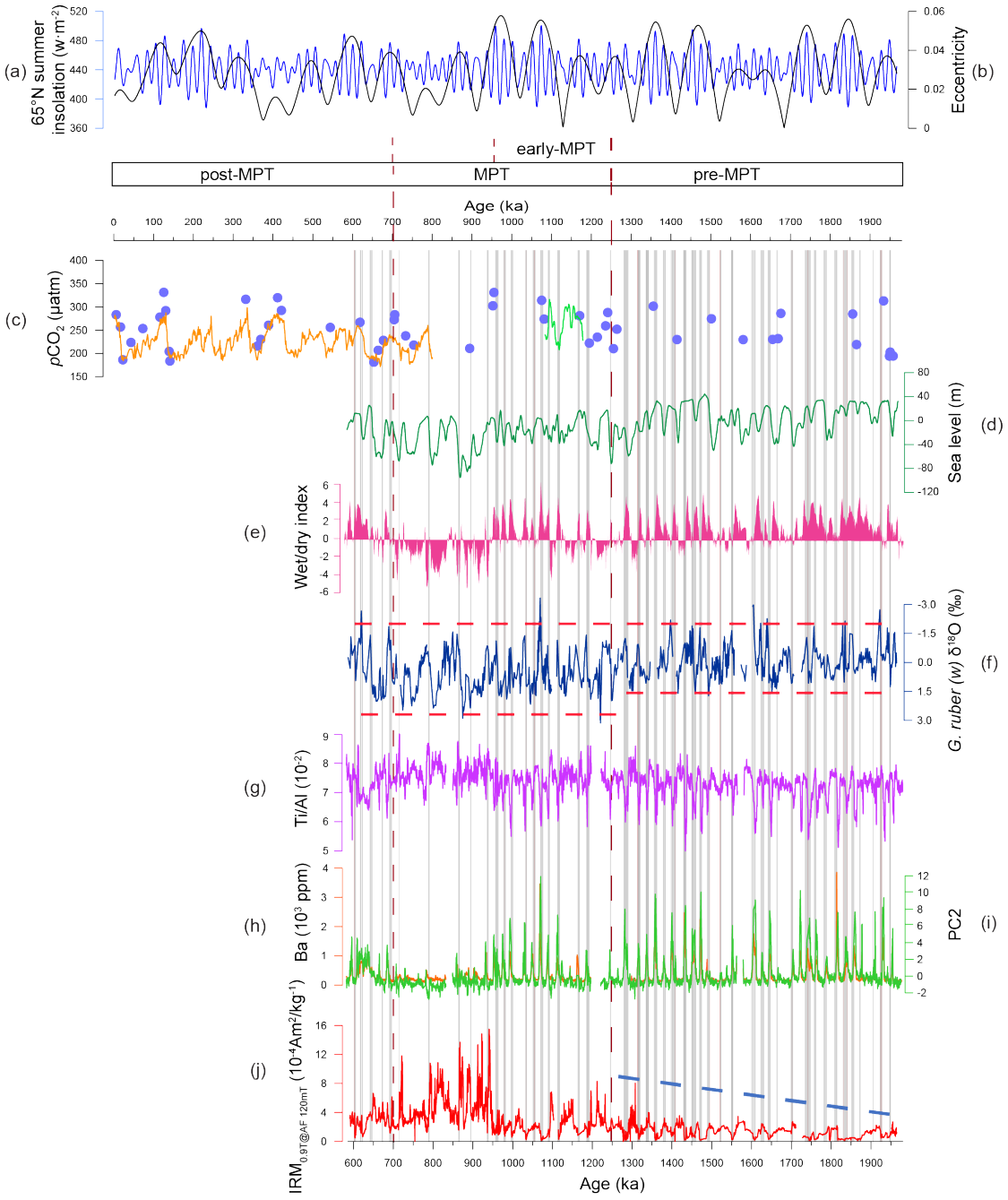

Fig. 5.2. Climate records across the MPT. Comparison of global climate with dust at ODP Site 967 between 0 and 1.98 Ma plotted against (a) northern hemisphere summer insolation (blue) and (b) eccentricity (black) from the astronomical solution of Laskar et al. (1993). (c) pCO_2 records from an ice core compilation (Bereiter et al., 2015; orange), δ^{11}B-based early-MPT data (Chalk et al., 2017; green), and δ^{11}B-based data (Hönisch et al., 2009; blue circles); (d) Mediterranean sea level reconstructed by Rohling et al. (2014) (dark green); (e) wet/dry index (Grant et al., 2017; pink); (f) δ^{18}O data from *G. ruber (w)* from ODP Site 967 (blue; this study); (g) Ti/Al (purple); (h, i) elevated Ba (orange) and PC2 (green) used to indicate sapropel boundaries (see Thomson et al. (1995) and Nijenhuis et al. (1999)), where PC2 is from the PCA

results of Grant et al. (2017), which is used to detect sapropel boundaries from a combination of elements; and (j) high-resolution $IRM_{0.9T@AF120mT}$ data from discrete samples (red, this study; the blue dashed line indicates the increasing $IRM_{0.9T@AF120mT}$ trend before the MPT). Light grey shaded bars indicate the positions of sapropels (i.e., intense African Monsoon events). Sapropel stratigraphy is after Emeis et al. (2000). The age model is based on Grant et al. (2017).

5.3. Interpretation of the proxy records

We use environmental magnetic, geochemical, and oxygen isotope records to test the hypotheses outlined above. First, we have obtained a continuous record of the magnetic parameter, $IRM_{0.9T@AF120\ mT}$, based on alternating field (AF) demagnetization at 120 mT of the isothermal remanent magnetization (IRM) imparted at 0.9 T. $IRM_{0.9T@AF120\ mT}$ indicates the high-coercivity hematite contribution in Saharan dust into eastern Mediterranean sediments (Larrasoaña et al., 2003a). Second, we use Ti/Al variations in eastern Mediterranean sediments to detect relative contributions of fluvial (Nile) and aeolian (Saharan dust) sources, where Ti is linked to aeolian transportation and Al is associated with both fluvial (e.g. smectite; Lourens et al., 2001) and aeolian (e.g., kaolinite; Foucault & Méliéres, 2000) transportation. Third, Ba contents and PC2 (a second principal component of multiple calibrated element counts) are used to detect sapropel boundaries (Grant et al., 2017). Fourth, we use negative $\delta^{18}O$ anomalies for the near-surface dwelling planktonic foraminifer *G. ruber (w)* (i.e., $\delta^{18}O_r$) to identify periods with enhanced African monsoon discharge flow into the eastern Mediterranean Sea (Amies et al., 2019; Rohling et al., 2004).

Table 5.1 Summary of proxy responses for each hypothesis tested.

		H_1	H_2	H_3	H_{new}
$IRM_{0.9T@AF120\ mT}$	Observed	Increased in glacials but stable in interglacials			
	Meets expectations?	×	×	N/A	✓
Ti/Al	Observed	High values in glacials and low values in interglacials			
	Meets expectations?	✓	N/A	N/A	✓
Ba, PC2	Observed	Low values in glacials and high values in interglacials			
	Meets expectations?	✓	N/A	N/A	✓
$\delta^{18}O$	Observed	Stable values in glacials in pre-MPT and MPT intervals and increases abruptly across the MPT			
	Meets expectations?	×	N/A	N/A	✓
wet/dry index	Observed	Widespread humidity in the pre-MPT interval			
	Meets expectations?	N/A	N/A	×	✓
sea level	Observed	Decreases gradually across the MPT			
	Meets expectations?	N/A	N/A	×	✓
✓: meets expectations		×: does not meet expectations			

References: H_1: aridity due to reduced precipitation (Rea, 1994); H_2: lower atmospheric CO_2 content (Bond et al., 2003; Mahowald et al., 2006b), H_3: expanded dust source areas (Petit et al., 1981), and H_{new}: frequent intensity changes of wet/dry periods (this study).

5.4. Discussion

5.4.1. Increased dust source area aridity (H_1)

Increased dust source-area aridity due to reduced precipitation and/or soil moisture may be the most commonly cited potential driver of increased dust flux (Rea, 1994). Aridity variations in many dry regions, notably including Saharan Africa, relate to monsoon strength, which is controlled by low-latitude precessional insolation changes (Schefuß et al., 2003). Observational data and modelling results suggest that Saharan dust emissions relate tightly to variations in African summer monsoon strength (Larrasoaña et al., 2003a; Trauth et al., 2009). Geochemical (Ti/Al ratio, Ba, and PC2) and $\delta^{18}O_r$ records from eastern Mediterranean sediments reflect humidity changes in dust source areas and are examined here to test the aridity hypothesis (H_1).

Ti/Al variations reflect relative shifts between fluvial and aeolian sediment supply. Maximum Ti/Al values in glacials indicate an increase in aeolian inputs relative to fluvial supply (Fig. 5.2g). This is consistent with the aridity hypothesis (Table 5.1). High Ba and PC2 values indicate the presence of organic-rich sediment layers (sapropels), which formed during periods with enhanced freshwater supply into the eastern Mediterranean Sea during African monsoon maxima (Rohling et al., 2015). If the main driver behind glacial dustiness is source-region aridity, then suppressed Ba and PC2 values are expected in glacials, which is consistent with our results (Fig. 5.2h-i; Table 5.1). However, variations in our $\delta^{18}O_r$ and dust proxy records ($IRM_{0.9T@AF120\ mT}$) differ substantially, in a manner that is inconsistent with expected signals for H_1. Typical $\delta^{18}O_r$ during glacial maxima is consistent in both the pre-MPT and MPT intervals, but it increases abruptly from the pre-MPT to post-MPT levels at ~1250 ka (Fig. 5.2f). This pattern does not match the abrupt dustiness increase at ~950 ka (Table 5.1). Also, the more subtle early-to-mid MPT amplitude $IRM_{0.9T@AF120\ mT}$ variations are inconsistent

with those in either our $\delta^{18}O_r$ record or the global deep-sea benthic $\delta^{18}O$ stack (Lisiecki & Raymo, 2005) (Fig 5.1, 5.2f, 5.2j). Taken together, Ti/Al, Ba and PC2, and $\delta^{18}O_r$ records indicate that increased aridity did not provide the dominant control on increased dust production across the MPT. We reject H_1.

5.4.2. Atmospheric CO_2 reduction (H_2)

In addition to aridity, lowering of atmospheric partial pressure of CO_2 (pCO_2) has been proposed as a driver of dust emissions by inhibiting vegetation growth (Bond et al., 2003; Mahowald et al., 2006b). Although high dust emissions correspond to low pCO_2 on orbital timescales, paleorecords indicate that pCO_2 does not exert a strict control on dust emissions (McGee et al., 2010). Instead, any correlation between dustiness and pCO_2 might mostly reflect dust influences on the oceanic carbon pump (Chalk et al., 2017). Regardless, we evaluate hypothesis H_2. Recent work indicates that glacial pCO_2 declined since the MPT and that interglacial pCO_2 remained stable through the transition (Chalk et al., 2017; Hönisch et al., 2009). If dustiness were driven by pCO_2 variations, then the dust proxy should undergo similar variations across the transition (Table 5.1). Instead, distinct dust production maxima are observed during glacials within the MPT versus smaller ones after the MPT (Figs. 5.1, 5.2j; Table 5.1). Overall, we reject H_2.

5.4.3. Expanded dust source areas (H_3)

In H_3, increased glacial dust emissions through the MPT are attributed to dust source-area expansion. Reduced vegetation cover due to aridity has been argued to extend dust source areas, with shorter growing seasons, increased winds, and lower temperatures during glacials all potentially helping to limit vegetation density (McGee et al., 2010). Reduced vegetation cover (desertification) then expands source regions of deflatable fine-grained material, and in hypothesis H_3 this increases glacial dustiness.

However, the wet/dry index of Grant et al. (2017), and coincident negative $\delta^{18}O_r$ peaks, Ba maxima, and PC2 all indicate substantial impacts of humid phases across Northwest/Saharan Africa and East Africa before, and in the earliest, MPT when glacial dustiness increased according to our $IRM_{0.9T@AF120\,mT}$ and Ti/Al records (especially between ~1400 and ~1050 ka; Fig. 5.2e; Table 5.1). Continental shelf exposure by low sea levels has also been suggested to increase dust source areas, causing increased glacial dust emissions (de Angelis et al., 1987). While debated, existing sea-level reconstructions (e.g., Fig. 5.2d) commonly exclude low sea-levels as a contributor in our 1250-2000 ka pre-MPT interval (for reconstruction comparisons, see Rohling et al., 2014). In sum, we reject H_3.

5.4.4. African monsoon variations and renewable silt production for dust supply (H_{new})

Based on the geochemical and isotopic records discussed here, we propose that increased amplitudes of wet/dry cycles were the primary driver of increased Saharan dustiness across the MPT. Aeolian dust in eastern Mediterranean sediments derives mainly from north of the central Saharan watershed (~21°N) (Larrasoaña et al., 2003a; 2015). This region contains abundant fossil river/wadi/lake systems sourced from the central Saharan mountain ranges (Drake et al., 2011; Gaven et al., 1981; Pachur & Hoelzmann, 2000; Rohling et al., 2002b). During high-amplitude precession minima, the African monsoon front penetrated northward beyond the central Saharan watershed (~21°N) and increased soil moisture and vegetation cover in the Northern Sahara, to form 'Green Sahara periods' (GSPs) (Larrasoaña et al., 2003a), as reflected in maximum Ba and PC2 values, minimum Ti/Al ratios, and low $\delta^{18}O_r$ anomalies (Fig. 5.2f-i). Increased monsoon activity activated widespread silt deposition in the region's extensive fluvial/lacustrine/wadi systems (Drake et al., 2011; Gaven et al., 1981; Osborne et al.,

2008; Pachur & Hoelzmann, 2000). Silt-rich alluvium is easily weathered and critically provides the raw material for dust generation (Goudie & Middleton, 2001). In addition, intervening high-amplitude precession maxima were characterized by the reduced possibility of the African monsoon front penetrating over the central Saharan watershed, which is conducive to the continuous non-vegetated, dry, desert environments (Brovkin et al., 1998; Claussen, 1998). Hematite formation is favoured during such arid phases as a result of dehydration of Fe^{3+}-bearing precursor minerals, such as goethite-rich iron crusts that form through wet periods (Nahon, 1980).

During eccentricity maxima, high-amplitude precession minima alternate consistently with high-amplitude precession maxima. At those times, alternations between particularly humid (GSP) and arid (desert) conditions would produce a renewable supply of deflatable silt. This interpretation is supported by $IRM_{0.9T@AF120\ mT}$ variations, which usually have highest values after sapropel formation (humid phases), and indicates that dust emissions peaked immediately following humid periods and then diminished. Moreover, amplitude variations are larger in $IRM_{0.9T@AF120\ mT}$ than in Ti/Al, which indicates that Saharan climate changes and weathering regimes provided proportionately more hematite than riverine inputs in intervals following GSPs.

The highest MPT $IRM_{0.9T@AF120\ mT}$ values are found in arid precession-cycle phases in the second half of the MPT, following two large eccentricity maxima with pronounced sapropel formation in the early MPT (Fig. 5.2a, j). This suggests that silt generation-dust ablation processes function over two main timescales. One is the precession timescale with silt generation in the wet phase and dust ablation in the ensuing arid phase. The other indicates a long-term build-up of “excess” silt during extended (eccentricity scale) periods with frequent humid phases and well-developed sapropels, followed by long-term alteration and ablation of this silt during ensuing extended

(eccentricity scale) periods of predominantly arid conditions with no or few sapropels. In other words, we observe an interplay between precession-scale cycles governed by immediate processes with little lag, and eccentricity-scale cycles governed by storage and alteration processes with a major lag between silt supply and deflation.

5.5. Conclusions

In summary, we provide direct evidence for increased dustiness across the MPT, especially during glacial periods. Furthermore, using multiple proxy records, we test competing hypotheses to explain the causes of G-IG dust changes across the MPT. Increased dust source-area aridity due to reduced precipitation, reduction in pCO_2 concentrations, and expansion of dust source areas fail to explain the observed proxy variations. We propose an alternative explanation, with regular humid African monsoon cycles driving supply of a renewable source of fluvial silt that could then be deflated and transported as dust during ensuing arid periods. We see evidence of both immediate processes and longer-term storage processes in this silt generation-ablation cycle.

Chapter 6

Conclusions and Future work

6.1 Conclusions

In this thesis, I present a series of studies on the environmental magnetic properties of eastern Mediterranean sediments, with the aim of comparing the benefits and limitations of both conventional bulk and more advanced component-specific measurements in identifying magnetic minerals and improving the understanding of LT measurements for detecting magnetofossils, SP particles, and maghemitization in marine sediments. Moreover, environmental magnetic proxies, Mediterranean planktic foraminiferal $\delta^{18}O$, and published geochemical data are used together to assess the causes of increased Saharan dustiness through the MPT. In this chapter, I revisit the conclusions of Chapters 3-5 and highlight specific directions for future work.

In **Chapter 3**, conventional bulk and more advanced magnetic techniques are used together to identify magnetic minerals in eastern Mediterranean sediments. More advanced techniques, such as LT measurements and FORC diagrams, indicate that biogenic magnetite formed at oxidation fronts above eastern Mediterranean sapropels. In addition, FORC-PCA analysis helps to quantify the abundance of biogenic and detrital magnetite through the studied interval. The results indicate that biogenic magnetite occurs widely throughout the studied sediments except within sulphidic diagenetic intervals, while detrital magnetite dominates the sediment magnetization except at oxidation fronts. The markedly enhanced biogenic magnetite abundances at oxidation fronts indicate that the strong redox gradient produced when sulphidic sapropelic sediments are exposed to oxygenated bottom waters provide a suitable habitat for MTB. This study also suggests that conventional bulk magnetic parameters provide valuable continuous records of magnetic property variations, without providing a direct indication of magnetic mineral components. In contrast, advanced environmental magnetic methods,

such as LT and FORC measurements, can provide crucial direct indications of multiple mineral magnetic assemblages that further enable calculation of the abundances of different magnetic mineral end members. However, such measurements are time-consuming, so they cannot be used to build high-resolution records. Overall, this study emphasizes the value of conventional continuous bulk magnetization records for environmental magnetic analysis, where use of advanced diagnostic methods adds significant interpretive power to develop quantitative understanding of the processes responsible for environmental signals.

In **Chapter 4**, eastern Mediterranean sediments are used as a case study to investigate the use of LT magnetic properties for detecting multiple magnetic particle types, such as magnetofossils and SP particles, and maghemitization of the surface of magnetite particles. The presence of magnetite magnetofossils is indicated by double T_v features in ZFC and FC warming curves. Magnetofossils occur widely in the studied sediment, except within intervals in which strong reductive dissolution has occurred. In contrast, SP particle contents are highest in diagenetically reduced intervals associated with sapropels. The commonly observed reversible hump of LTC-RTSIRM cooling and warming curves demonstrates that maghemitization of magnetite is a common phenomenon in eastern Mediterranean sediments. High values of the M'300/M300 magnetic memory parameter are observed in oxidation fronts of representative sapropels, which suggests that preserved magnetite magnetofossils are highly maghemitized. Enhanced D values also occur in background marls and intervals that have not been affected strongly by reductive dissolution of iron oxides. This work demonstrates that LT magnetic property measurements can provide valuable quantitative information about magnetofossil and SP contents, as well as maghemitization, and the environmental processes that give rise to these magnetic signatures.

In **Chapter 5**, high-resolution environmental magnetic proxy and planktic foraminiferal $\delta^{18}O$ records are presented alongside published Mediterranean geochemical records and pCO_2 data to assess hypotheses for increased Saharan dustiness across the MPT, including increasing source-area aridity due to reduced precipitation, expanded dust source areas, and atmospheric CO_2 reduction that led to decreased vegetation and soil cohesion. The results suggest that none of these hypotheses explain satisfactorily the dustiness increase across the MPT. Instead, these multi-proxy records provide direct evidence that intensification of wet-dry cycles was the main cause of increased dustiness across the MPT, especially during glacial periods. Intensified African summer monsoon cycles drove increased alluvial and lacustrine silt generation and deposition that could then be deflated and transported as dust during ensuing arid periods. The finding that increased climate extremes boosted wind-blown dust emissions is important because the resultant aeolian aerosols play major roles in both the radiative balance of climate and biogeochemical cycling in areas where the dust settles.

6.2 Future work

Magnetic minerals in eastern Mediterranean sediments have been studied widely over recent decades because their variations provide valuable information about paleoclimate changes. Hematite, which is a major magnetic mineral in eastern Mediterranean sediments, has been demonstrated to be a relatively reliable proxy for quantitative estimation of Saharan dust supply. This is because hematite is more resistant to sulphidic reductive dissolution than magnetite. However, it is difficult to detect whether hematite has dissolved within extremely strong dissolution intervals, such as within and below type 1 sapropels. Therefore, it is important to explore further the

reliability of hematite proxies and to develop additional accurate dust proxies to better understand paleoclimate changes associated with African monsoon variations that are important for understanding Green Saharan conditions. In **Chapter 3**, two distinct linear relationships are evident between SIRM and the hematite content proxy ($IRM_{@AF120\ mT}$) within marls and dissolution intervals, respectively, which provide a possibility to reconstruct dust contents in dissolution intervals to build a new dust proxy that can better reflect dust fluxes from the Sahara.

Potential causes of increased Saharan dustiness across the MPT have been examined here from multiple proxy records. The results suggest that both immediate and longer-term storage processes operate in this silt generation-ablation cycle. However, the causes behind the long-term cycles have not been studied. Spectral analysis of the dust signal indicates that a precession-scale mechanism is modulated on both short (~100 kyr) and long (~400 kyr) eccentricity time scales with strong expression of the ~41 ky obliquity cycle (Larrasoaña et al., 2003a). By comparing MPT characteristics with regard to amplitude and frequency variations in dust records, it could be possible to assess hypotheses for the origin of significant long-term Saharan dust flux cycles and its relationship to development of a major global climate shift across the MPT.

Supplementary information

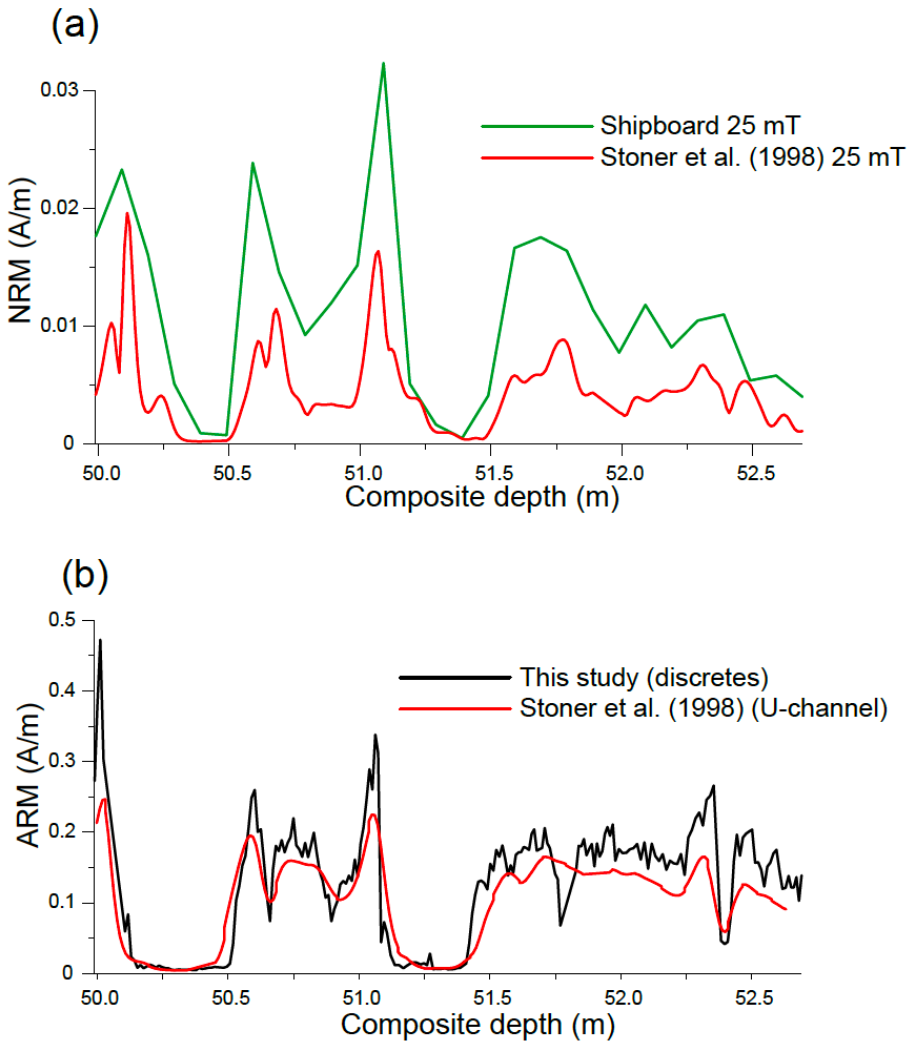

Figure S1. Comparison of (a) shipboard NRM measurements on a split half-core after AF demagnetization at 25 mT with u-channel results after AF demagnetization at 25 mT for the studied interval of Site 967 (from Stoner et al., 1998). The NRM decrease indicates that storage diagenesis has affected the studied cores. (b) Comparison of ARM measurements (acquired in a 100 mT peak alternating field with a 0.05 mT direct bias field) without demagnetization for continuous discrete samples from Hole 967C (this study) and u-channel samples from the equivalent interval from Hole 967B (Stoner et al., 1998). Minor differences between these records could result from the resolution differences and from the mode by which ARM was acquired. These minor differences suggest that minimal storage diagenesis has occurred between the measurements of Stoner et al. (1998) and those made for this study.

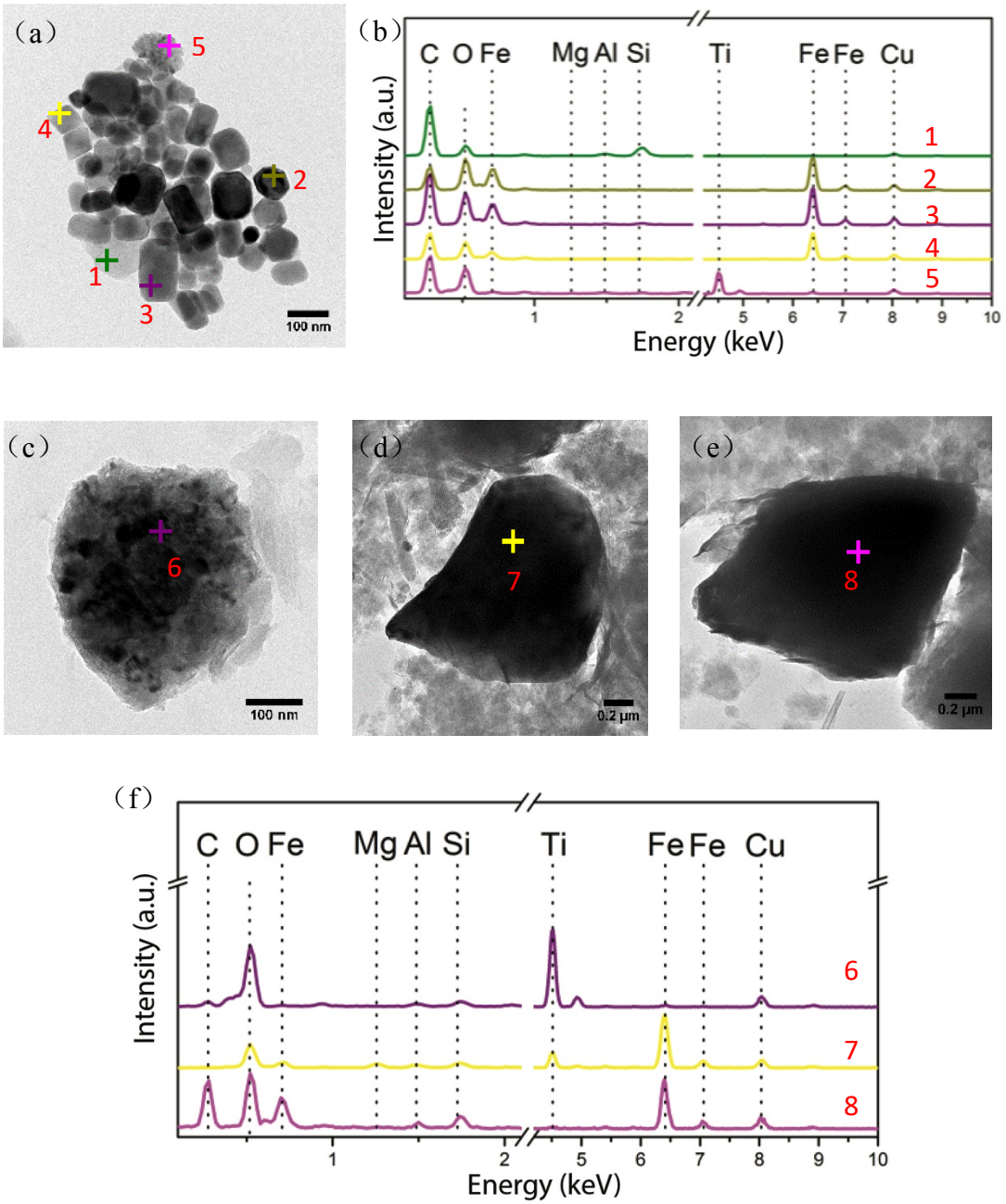

Figure S2. Transmission electron microscope (TEM) images, selected area electron diffraction (SAED) patterns, and energy-dispersive X-ray spectroscopy (EDX) analyses. (a) TEM images for magnetic extracts from Sample 22, with (b) associated EDX analyses. (c-e) TEM images for magnetic extracts from Sample 25, with (f) associated EDX analyses. Coloured numbers with crosses in (a), (c), (d), and (e) indicate locations of spot analyses that correspond to the respective EDX spectra in (b) and (f).

Table S1. Magnetic properties of samples selected for FORC and low-temperature measurements.

Number	Depth (m)	χ (10^{-8} m^3/kg)	ARM (10^{-6} Am^2kg^{-1})	SIRM (10^{-4} Am^2kg^{-1})	$IRM_{@AF120\ mT}$ (10^{-4} Am^2kg^{-1})	S-ratio	χ_{ARM}/χ	ARM/SIRM (10^{-2})	SIRM/χ (10^5 Am^{-1})
1	50.00	3.10	300.40	57.75	1.57	0.98	243.76	5.20	1.86
2	50.01	3.12	415.51	74.50	1.57	0.86	334.23	5.58	2.38
3	50.02	2.55	268.00	55.94	1.26	0.99	264.64	4.79	2.20
4	50.15	1.49	12.73	7.18	1.74	0.96	21.52	1.77	0.48
5	50.31	0.66	4.06	2.50	2.39	0.87	15.53	1.63	0.38
6	50.39	0.67	5.80	3.54	1.99	0.87	21.82	1.64	0.53
7	50.46	0.96	6.70	6.09	1.40	0.81	17.51	1.10	0.63
8	50.53	2.90	88.37	35.15	1.47	0.97	76.53	2.51	1.21
9	50.54	3.02	102.15	37.88	1.51	0.97	85.11	2.70	1.26
10	50.60	3.05	195.29	43.66	1.43	0.98	161.03	4.47	1.43
11	50.66	3.21	71.99	34.88	1.26	0.96	56.44	2.06	1.09
12	50.74	5.89	167.05	75.62	1.17	0.98	71.25	2.21	1.28
13	50.84	4.59	147.47	58.31	1.07	0.97	80.71	2.53	1.27
14	50.91	2.51	89.31	30.98	1.09	0.96	89.33	2.88	1.23
15	50.93	2.91	98.17	34.54	1.16	0.96	84.78	2.84	1.19
16	50.94	2.85	99.29	34.54	0.59	0.97	87.65	2.87	1.21
17	50.96	2.58	102.79	32.25	0.59	0.97	99.96	3.19	1.25
18	50.98	2.28	117.79	30.02	0.94	0.97	129.64	3.92	1.31
19	51.01	2.26	145.65	31.73	0.69	0.97	161.88	4.59	1.40
20	51.03	2.25	176.81	34.70	1.19	0.98	197.88	5.10	1.55
21	51.04	2.39	227.17	40.73	1.36	0.98	238.68	5.58	1.70
22*	51.06	2.43	310.16	50.48	1.68	0.99	320.96	6.14	2.08
23	51.08	0.92	39.05	9.66	1.50	0.96	106.90	4.04	1.05
24	51.10	0.98	78.53	13.79	1.43	0.98	201.77	5.69	1.41
25*	51.20	0.94	11.68	4.61	1.50	0.88	31.21	2.54	0.49
26	51.31	0.69	5.03	2.85	2.32	0.84	18.39	1.76	0.42
27	51.50	2.84	106.03	36.29	1.84	0.97	93.72	2.92	1.28
28*	51.61	4.08	144.70	51.19	1.57	0.98	89.10	2.83	1.25
29	51.71	3.99	140.42	50.63	1.57	0.98	88.36	2.77	1.27
30	52.12	3.53	149.82	46.07	1.26	0.97	106.73	3.25	1.31
31*	52.36	3.13	218.80	46.24	1.74	0.98	175.89	4.73	1.48
32*	52.40	1.38	41.14	12.11	2.39	0.91	74.94	3.40	0.88
33	52.50	5.19	163.91	69.15	1.99	0.97	79.42	2.37	1.33
34	52.69	3.88	102.59	44.01	1.40	0.97	66.40	2.33	1.13

***** Samples selected for TEM observations and LT measurements.

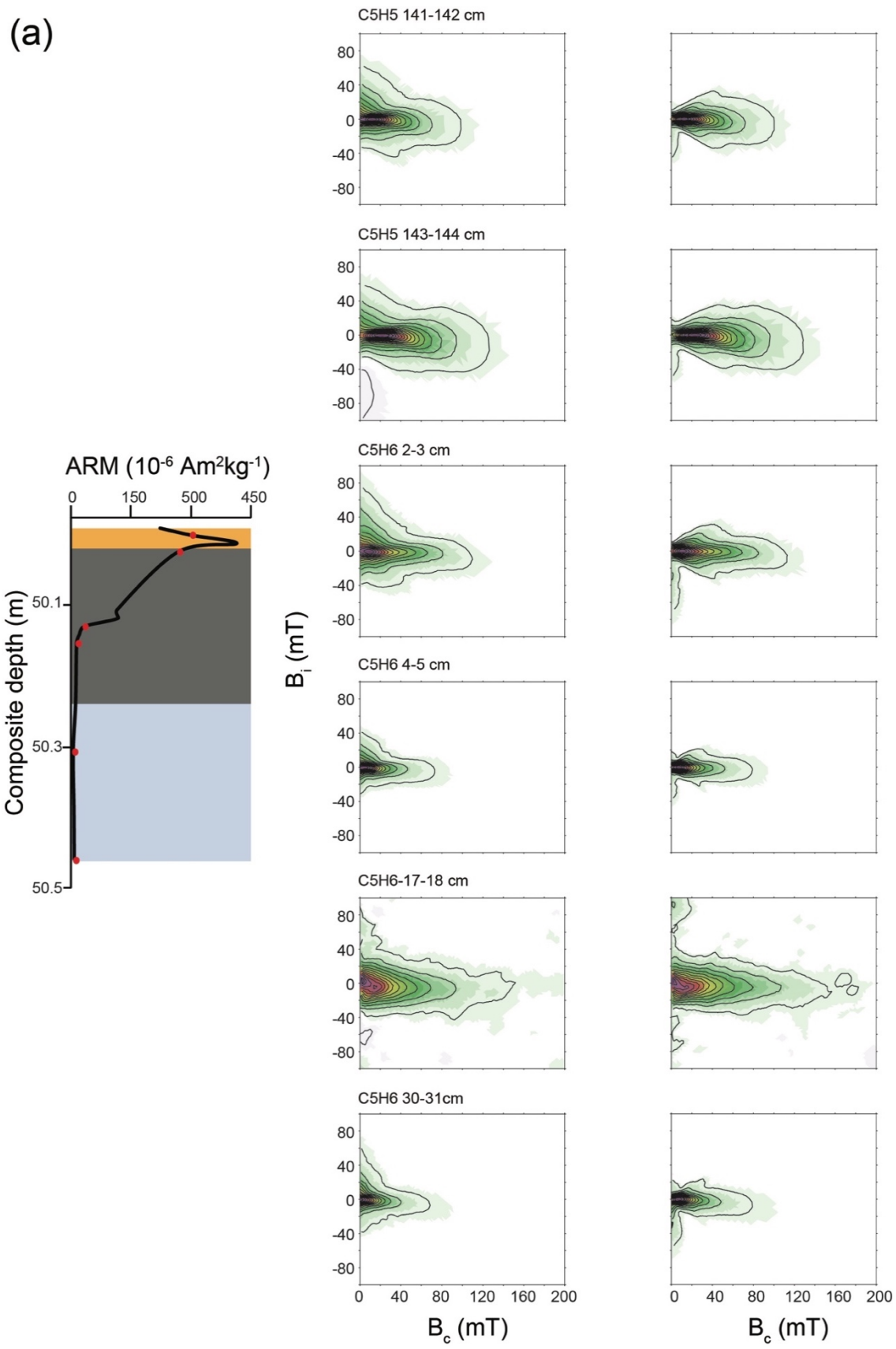
(a)
ARM (10^{-6} Am^2kg^{-1})
0
150
500
450
Composite depth (m)
50.1
50.3
50.5
C5H5 141-142 cm
C5H5 143-144 cm
C5H6 2-3 cm
C5H6 4-5 cm
C5H6-17-18 cm
C5H6 30-31cm
B_i (mT)
80
40
0
-40
-80
0
40
80
120
160
200
B_c (mT)

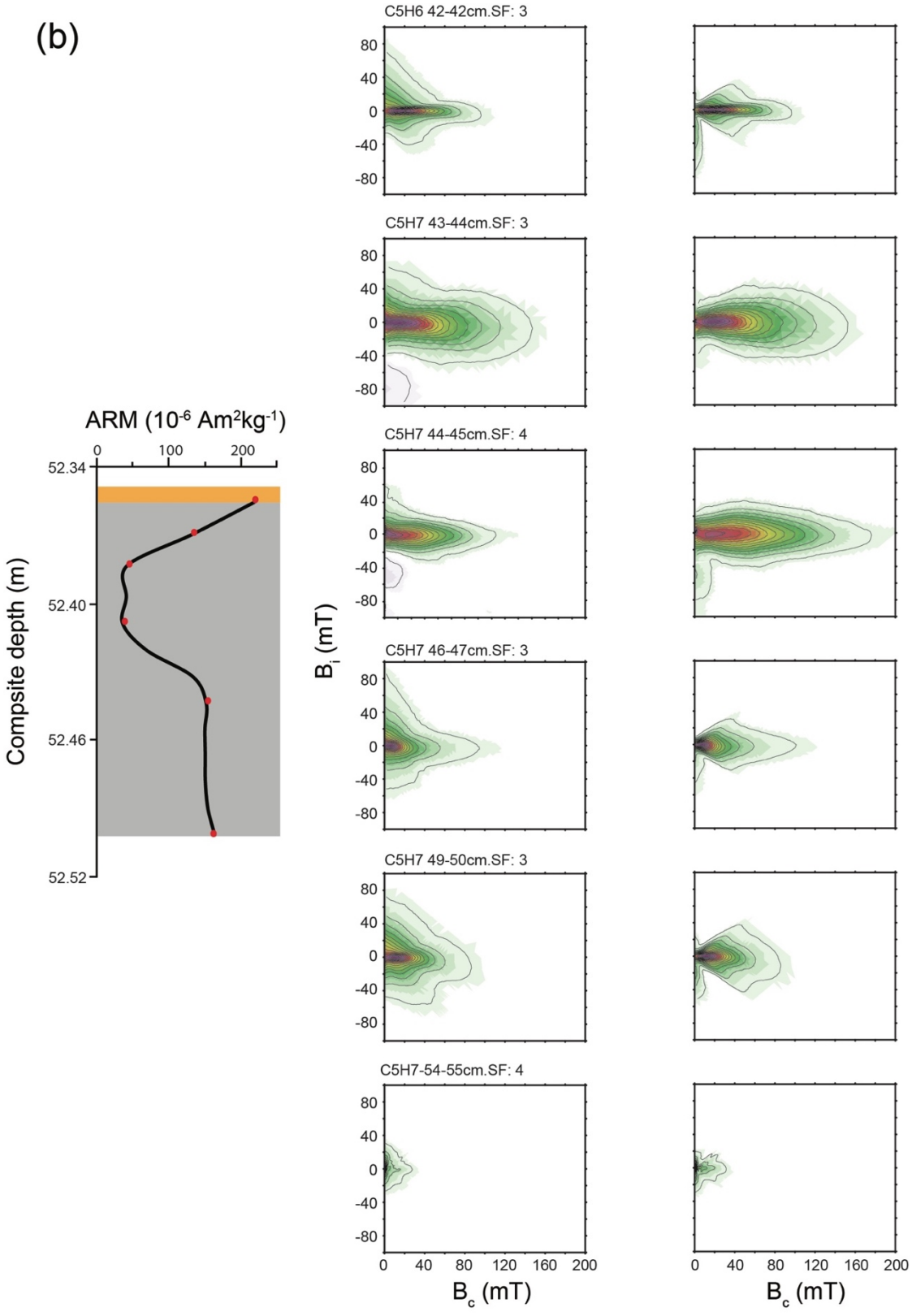
(b)
ARM (10^{-6} Am^2kg^{-1})
0
100
200
52.34
52.40
52.46
52.52
Compsite depth (m)
C5H6 42-42cm.SF: 3
C5H7 43-44cm.SF: 3
C5H7 44-45cm.SF: 4
C5H7 46-47cm.SF: 3
C5H7 49-50cm.SF: 3
C5H7-54-55cm.SF: 4
B_i (mT)
80
40
0
-40
-80
0
40
80
120
160
200
B_c (mT)

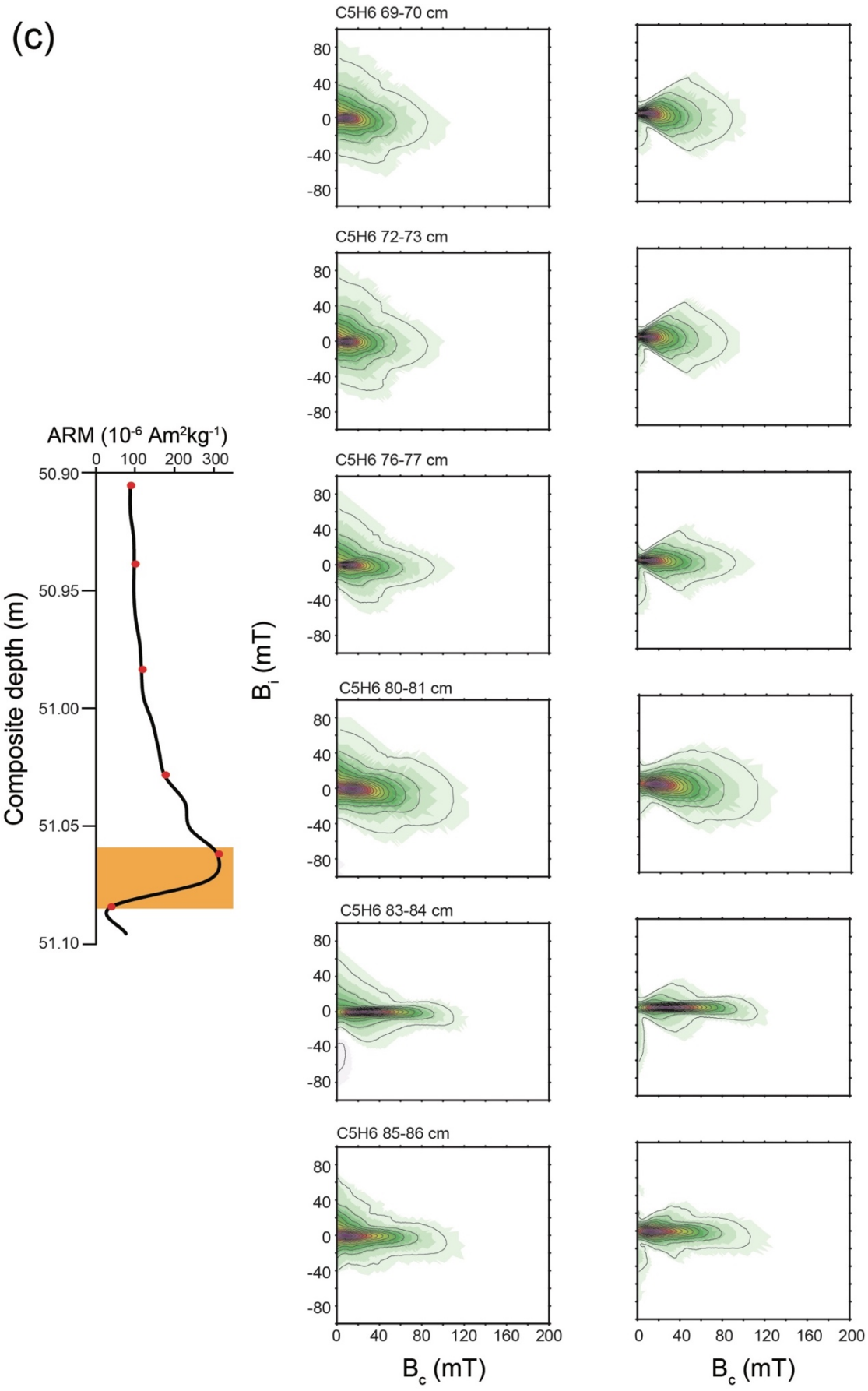
(c)
ARM (10-6 Am2kg-1)
0 100 200 300
Composite depth (m)
50.90
50.95
51.00
51.05
51.10
C5H6 69-70 cm
C5H6 72-73 cm
C5H6 76-77 cm
C5H6 80-81 cm
C5H6 83-84 cm
C5H6 85-86 cm
Bi (mT)
80
40
0
-40
-80
0 40 80 120 160 200
Bc (mT)

Fig. S3. FORC diagrams for representative samples selected from three distinctive intervals ((a) representative sapropel; (b) weakly developed sapropel; and (c) background marly sediments). Sample locations (red circles) are indicated on ARM profiles (left), FORC diagrams (centre), and remanence FORC diagrams (right), which were obtained following Zhao et al. (2017). Dark grey, light grey, orange, and light blue shadings indicate representative sapropels, weakly developed sapropels, oxidation fronts, and dissolution intervals, respectively.

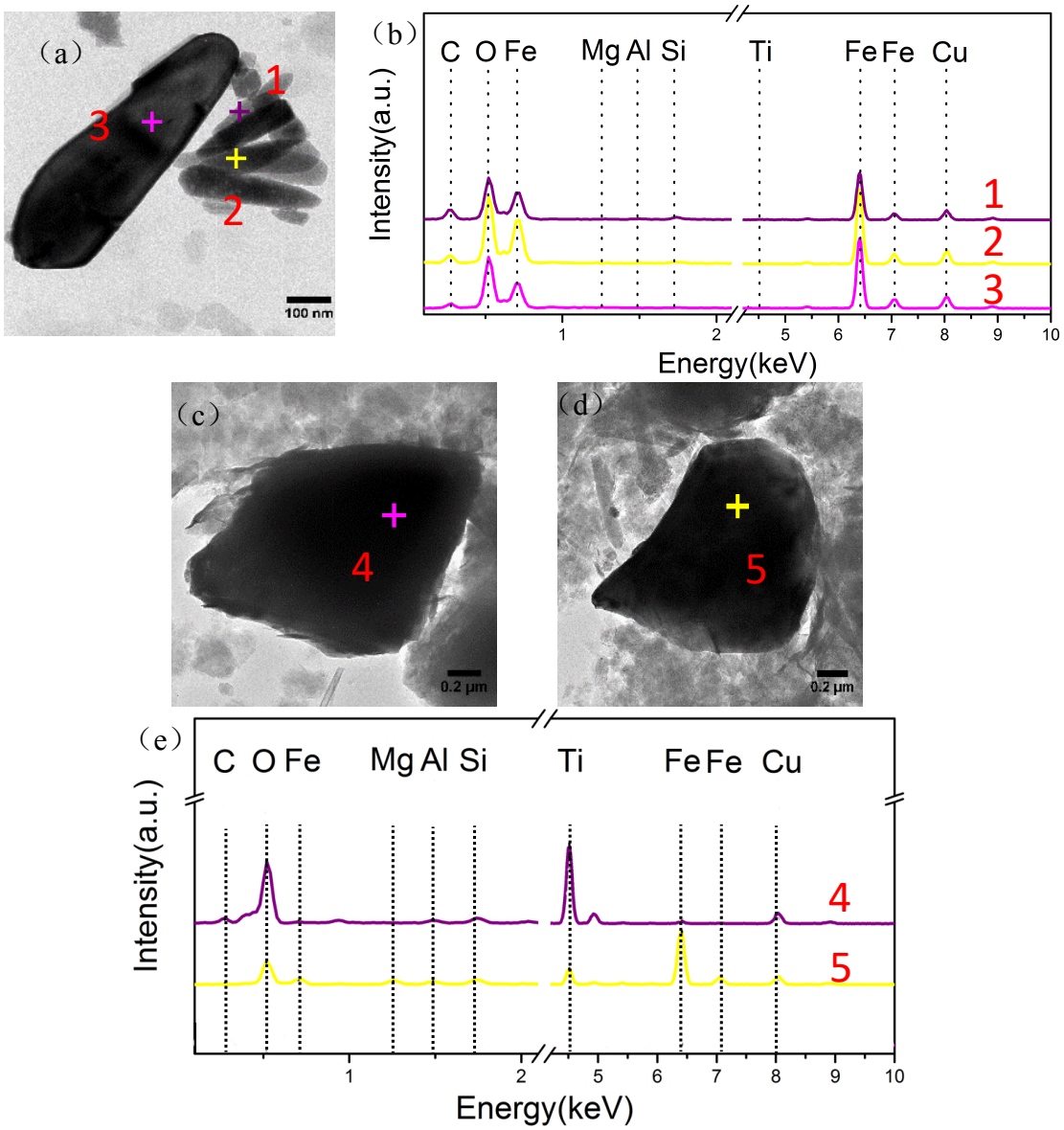

Figure S4. Transmission electron microscope (TEM) images, selected area electron diffraction patterns, and energy-dispersive X-ray spectroscopy (EDX) analyses. (a) TEM images for magnetic extracts from Sample 4 (Fig. 4.8), with (b) associated EDX analyses. (c-d) TEM images for magnetic extracts from Sample 5 (Fig. 4.8), with (e) associated EDX analyses.

Quantification of $IRM_{0.9T@AF120\ mT}$ through different climatic intervals

Our analysis of $IRM_{0.9T@AF120\ mT}$ data consists of four steps: (i) define individual data points that represent glacial (G) and interglacial (IG) conditions based on $IRM_{0.9T@AF120\ mT}$ values, respectively, (ii) estimate the average $IRM_{0.9T@AF120\ mT}$ and its uncertainty from the two data sets (i.e., G $IRM_{0.9T@AF120\ mT}$ and IG $IRM_{0.9T@AF120\ mT}$), and (iii) estimate the G-IG $IRM_{0.9T@AF120\ mT}$ difference (i.e., IG-GΔ) in the pre-, early-, and MPT intervals.

We further subsampled the G and IG $IRM_{0.9T@AF120\ mT}$ data based on a percentile cutoff criterion based on $IRM_{0.9T@AF120\ mT}$ values, using only the 25% "most IG" and the 25% "most G" data points to quantify G $IRM_{0.9T@AF120\ mT}$, IG $IRM_{0.9T@AF120\ mT}$, and IG-G $\Delta IRM_{0.9T@AF120\ mT}$. The 25% cutoff criterion is arbitrary, so we present results for 5%, 15%, 25%, 35%, and 45% cutoffs for nonoverlapping data sets (Fig. S4), with a low percentile cutoff, only the few most extreme data points are subsampled as glacial and interglacial, respectively, which maximizes the glacial/interglacial difference but also leads to a relatively larger uncertainty because few data contribute to the estimates. Conversely, for high percentile cutoffs, more data contribute to the estimate of the mean $IRM_{0.9T@AF120\ mT}$, which reduces the uncertainty and increases the robustness but also, progressively averages away the end member changes that we are seeking to quantify. As can been seen in Fig. S4, the results are robust regardless of the cutoff values used, so we use the 25% percentile cutoff in the main text (Fig. 5.1b). The second step of our analysis is to estimate G $IRM_{0.9T@AF120\ mT}$ and IG $IRM_{0.9T@AF120\ mT}$ based on their respective data sets. We sum and normalize the probability density functions for the data sets and their normally distributed uncertainty. From these cumulative subsample probability density functions, we estimate the central tendency as the mean probability (Chalk et al., 2017). To estimate IG-GΔ $IRM_{0.9T@AF120\ mT}$, we simply subtract the central

estimate of G $IRM_{0.9T@AF120\ mT}$ from IG $IRM_{0.9T@AF120\ mT}$ (Chalk et al., 2017).

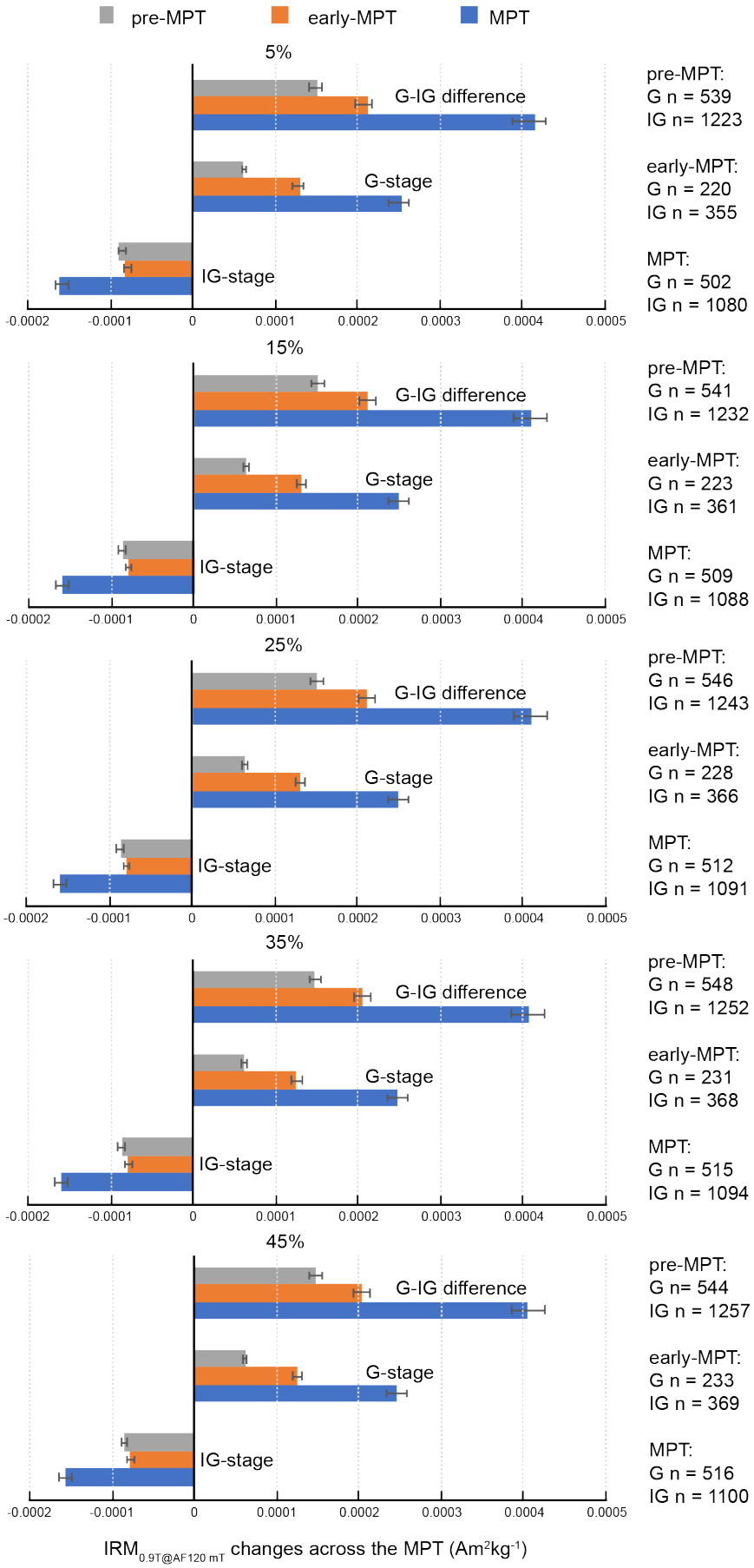

Fig. S4. Quantification of $IRM_{0.9T@AF120\ mT}$ with respect to glacial versus interglacial stages across the MPT. For this analysis, we define glacial and interglacial subsets of data based on different cutoff values (5%, 15%, 25%, 35%, and 45%) and quantify the change in (bottom) IG, (middle) G, and (top) the change in magnitude of $IRM_{0.9T@AF120mT}$ over IG-G cycles. The thin black error bars denote uncertainties in the one-sided test of the sign of $IRM_{0.9T@AF120mT}$ change at the 95% significance level. In this study, the pre-MPT interval is defined from 1.25 Ma to 1.96 Ma, the early-MPT interval is from 0.95 to 1.25 Ma, and the MPT interval began at 1.25 Ma and was complete by 0.70 Ma. Sample numbers of G and IG for each climate periods are clarified as "G n" and "IG n".

References

Abell, P. I., & Hoelzmann, P. (2000). Holocene palaeoclimates in northwestern Sudan: Stable isotope studies on molluscs. *Global and Planetary Change*, *26*(1-3), 1-12. https://doi.org/10.1016/s0921-8181(00)00030-8

Alpert, P., Neeman, B. U., & Shay-El, Y. (1990). Intermonthly variability of cyclone tracks in the Mediterranean. *Journal of Climate*, *3*(12), 1474-1478. https://doi.org/10.1175/1520-0442(1990)003<1474:ivocti>2.0.co;2

Amies, J. D., Rohling, E. J., Grant, K. M., Rodríguez-Sanz, L., & Marino, G. (2019). Quantification of African monsoon runoff during last interglacial sapropel S5. *Paleoceanography and Paleoclimatology*, *34*(8), 1487-1516. https://doi.org/10.1029/2019PA003652

Arimoto R. (2001). Eolian dust and climate: Relationships to sources, tropospheric chemistry, transport and deposition. *Earth-Science Reviews*, *54*(1-3), 29-42. https://doi.org/10.1016/s0012-8252(01)00040-x

Banerjee, S. K., Hunt, C. P., & Liu, X. M. (1993). Separation of local signals from the regional paleomonsoon record of the Chinese Loess Plateau: A rock-magnetic approach. *Geophysical Research Letters*, *20*(9), 843-846. https://doi.org/10.1029/93GL00908

Banerjee, S. K., King, J., & Marvin, J. (1981). A rapid method for magnetic granulometry with applications to environmental studies. *Geophysical Research Letters*, *8*(4), 333-336. https://doi.org/10.1029/gl008i004p00333

Bazylinski, D. A., & Frankel, R. B. (2004). Magnetosome formation in prokaryotes. *Nature Reviews Microbiology*, *2*(3), 217. https://doi.org/10.1038/nrmicro842

Bereiter, B., Eggleston, S., Schmitt, J., Nehrbass-Ahles, C., Stocker, T. F., Fischer, H., et al. (2015). Revision of the EPICA Dome C CO_2 record from 800 to 600-kyr before present. *Geophysical Research Letters*, *42*(2), 542-549. https://doi.org/10.1002/2014GL061957

Berger, W. H., & Jansen, E. (1994). Mid-Pleistocene climate shift-the Nansen connection. *The Polar Oceans and Their Role in Shaping the Global Environment*, *85*, 295-311. https://doi.org/10.1029/gm085p0295

Besnus, M. J., & Meyer, A. J. (1964). Nouvelles données expérimentales sur le magnétisme de la pyrrhotine naturelle. *Proceedings of the International Conference on Magnetism* (pp. 507-511). Nottingham.

Bethoux, J. P., El Boukhary, M. S., Ruiz-Pino, D., Morin, P., & Copin-Montégut, C. (2005). Nutrients, oxygen and carbon ratios, CO_2 sequestration and anthropogenic forcing in the Mediterranean Sea. *The Mediterranean Sea* (pp. 67-86). Springer, Berlin, Heidelberg. https://doi.org/10.1007/b107144

Beuning, K. R., Kelts, K., Russell, J., & Wolfe, B. B. (2002). Reassessment of Lake Victoria-Upper Nile River paleohydrology from oxygen isotope records of lake-sediment cellulose. *Geology*, *30*(6), 559-562. https://doi.org/10.1130/0091-7613(2002)030<0559:rolvun>2.0.co;2

Bintanja, R., van de Wal, R. S., & Oerlemans, J. (2005). Modelled atmospheric temperatures and global sea levels over the past million years. *Nature*, *437*(7055), 125-128. https://doi.org/10.1038/nature03975

Bloemendal, J., King, J. W., Hall, F. R., & Doh, S. J. (1992). Rock magnetism of Late Neogene and Pleistocene deep-sea sediments – Relationship to sediment source, diagenetic processes, and sediment lithology. *Journal of Geophysical Research: Solid Earth*, *97*(B4), 4361-4375. https://doi.org/10.1029/91jb03068

Bond, W. J., Midgley, G. F., & Woodward, F. I. (2003). The importance of low atmospheric CO_2 and fire in promoting the spread of grasslands and savannas. *Global Change Biology*, *9*(7), 973-982. https://doi.org/10.1046/j.1365-2486.2003.00577.x

Boyd, P. W., & Ellwood, M. J. (2010). The biogeochemical cycle of iron in the ocean. *Nature Geoscience*, *3*(10), 675-682. https://doi.org/10.1038/ngeo964

Brovkin, V., Claussen, M., Petoukhov, V., & Ganopolski, A. (1998). On the stability of the atmosphere-vegetation system in the Sahara/Sahel region. *Journal of Geophysical Research: Atmospheres*, *103*(D24), 31613-31624. https://doi.org/10.1029/1998JD200006

Calvert, S. E., & Fontugne, M. R. (2001). On the late Pleistocene-Holocene sapropel record of climatic and oceanographic variability in the eastern Mediterranean. *Paleoceanography*, *16*(1), 78-94. https://doi.org/10.1029/1999pa000488

Casford, J. S. L., Rohling, E. J., Abu-Zied, R. H., Fontanier, C., Jorissen, F. J., Leng, M. J., et al. (2003). A dynamic concept for eastern Mediterranean circulation and

oxygenation during sapropel formation. *Palaeogeography*, *Palaeoclimatology*, *Palaeoecology*, *190*, 103-119. https://doi.org/10.1016 /s0031-0182(02)00601-6

Castradori, D. (1993). Calcareous nannofossils and the origin of eastern Mediterranean sapropels. *Paleoceanography*, *8*(4), 459-471. https://doi.org/10.1029/93PA00756

Chalk, T. B., Hain, M. P., Foster, G. L., Rohling, E. J., Sexton, P. F., Badger, M. P. S., et al. (2017). Causes of ice age intensification across the Mid-Pleistocene Transition. *Proceedings of the National Academy of Sciences of the United States of America*, *114*(50), 13114-13119. https://doi.org/10.1073/pnas.1702143114

Chang, L., Harrison, R. J., Zeng, F., Berndt, T. A., Roberts, A. P., Heslop, D., & Zhao, X. (2018). Coupled microbial bloom and oxygenation decline recorded by magnetofossils during the Palaeocene-Eocene Thermal Maximum. *Nature Communications*, *9*(1), 4007. https://doi.org/10.1038/s41467-018-06472-y

Chang, L., Heslop, D., Roberts, A. P., Rey, D., & Mohamed, K. J. (2016). Discrimination of biogenic and detrital magnetite through a double Verwey transition temperature. *Journal of Geophysical Research: Solid Earth*, *121*(1), 3-14. https://doi.org/10.1002/2015jb012485

Chang, L., Roberts, A. P., Tang, Y., Rainford, B. D., Muxworthy, A. R., & Chen, Q. (2008). Fundamental magnetic parameters from pure synthetic greigite (Fe_3S_4). *Journal of Geophysical Research: Solid Earth*, *113*(B6), https://doi.org/10.1029/2007JB005502

Chang, L., Roberts, A. P., Winklhofer, M., Heslop, D., Dekkers, M. J., Krijgsman, W., et al. (2014). Magnetic detection and characterization of biogenic magnetic minerals: A comparison of ferromagnetic resonance and first-order reversal curve diagrams. *Journal of Geophysical Research: Solid Earth*, *119*(8), 6136-6158. https://doi.org/10.1002/2014jb011213

Chang, L., Winklhofer, M., Roberts, A. P., Heslop, D., Florindo, F., Dekkers, M. J., et al. (2013). Low-temperature magnetic properties of pelagic carbonates: Oxidation of biogenic magnetite and identification of magnetosome chains. *Journal of Geophysical Research: Solid Earth*, *118*(12), 6049-6065. https://doi.org/10.1002/2013JB010381

Channell, J. E. T., & Hawthorne, T. (1990). Progressive dissolution of titanomagnetites at ODP Site 653 (Tyrrhenian Sea). *Earth and Planetary Science Letters*, *96*(3-4), 469-480. https://doi.org/10.1016/0012-821x(90)90021-O

Channell, J. E. T., Harrison, R. J., Lascu, I., McCave, I. N., Hibbert, F. D., & Austin, W. E. (2016). Magnetic record of deglaciation using FORC-PCA, sortable-silt grain size, and magnetic excursion at 26 ka, from the Rockall Trough (NE Atlantic). *Geochemistry*, *Geophysics*, *Geosystems*, *17*(5), 1823-1841. https://doi.org/10.1002/2016gc006300

Chaparro, M. A. E., Sinito, A. M., Ramasamy, V., Marinelli, C., Chaparro, M. A. E., Mullainathan, S., & Murugesan, S. (2008). Magnetic measurements and pollutants of sediments from Cauvery and Palaru River, India. *Environmental Geology*, *56*(2), 425-437. https://doi.org/10.1007/s00254-007-1180-1

Clark, P. U., & Pollard, D. (1998). Origin of the middle Pleistocene transition by ice sheet erosion of regolith. *Paleoceanography*, *13*(1), 1-9. https://doi.org /10.1029/97pa02660

Clark, P. U., Archer, D., Pollard, D., Blum, J. D., Rial, J. A., Brovkin, V., et al. (2006). The middle Pleistocene transition: Characteristics, mechanisms, and implications for long-term changes in atmospheric pCO_2. *Quaternary Science Reviews*, *25*(23-24), 3150-3184. https://doi.org/10.1016/j.quascirev.2006.07. 008

Claussen, M. (1998). Modelling global terrestrial vegetation-climate interaction. *Philosophical Transactions of the Royal Society B*, *353*(1365), 53-63. https://doi.org/10.1098/rstb.1998.0190

Coulthard, T. J., Ramirez, J. A., Barton, N., Rogerson, M., & Brücher, T. (2013). Were rivers flowing across the Sahara during the last interglacial? Implications for human migration through Africa. *PloS One*, *8*(9), e74834. https://doi.org/10.1371/annotation/0a0303fa-ae35-4100-9f8d-c9ad65d49897

Cracknell, A. P. (1975). *Magnetism in crystalline materials: Applications of the theory of groups of cambiant symmetry*. Elsevier, Oxford.

Cramp, A., & O'Sullivan, G. (1999). Neogene sapropels in the Mediterranean: A review. *Marine Geology*, *153*(1-4), 11-28. https://doi.org/10.1016/s0025-3227(98)00092-9

Cui, Y., Verosub, K. L., & Roberts, A. P. (1994). The effect of low-temperature oxidation on large multi-domain magnetite. *Geophysical Research Letters*, *21*(9), 757-760. https://doi.org/10.1029/94GL00639

Dayan, U. (1986). Climatology of back trajectories from Israel based on synoptic analysis. *Journal of Applied Meteorology and Climatology*, *25*(5), 591-595.

https://doi.org/10.1175/1520-0450(1986)025<0591:cobtfi>2.0.co;2

de Angelis, M., Barkov, N. I., & Petrov, V. N. (1987). Aerosol concentrations over the last climatic cycle (160 kyr) from an Antarctic ice core. *Nature*, *325*, 318-321. https://doi.org/10.1038/325318a0

de Kaenel, E., Siesser, W. G., & Murat, A. (1999). Pleistocene calcareous nannofossil biostratigraphy and the western Mediterranean sapropels, sites 974 to 977 and 979. *Proceedings of the Ocean Drilling Program, Scientific Results* (vol. 161, pp. 159-183). Ocean Drilling Program, College Station, TX. https://doi.org/10.2973/odp.proc.sr. 161.250.1999

de Lange, G. J., Thomson, J., Reitz, A., Slomp, C. P., Principato, M. S., Erba, E., & Corselli, C. (2008). Synchronous basin-wide formation and redox-controlled preservation of a Mediterranean sapropel. *Nature Geoscience*, *1*(9), 606-610. https://doi.org/10.1038/ngeo283

Dearing, J. A., Bird, P. M., Dann, R. J. L., & Benjamin, S. F. (1997). Secondary ferrimagnetic minerals in Welsh soils: A comparison of mineral magnetic detection methods and implications for mineral formation. *Geophysical Journal International*, *130*(3), 727-736. https://doi.org/10.1111/j.1365246X.1997.tb01867.x

Dekkers, M. J. (1989). Magnetic properties of natural goethite-II. TRM behaviour during thermal and alternating field demagnetization and low-temperature treatment. *Geophysical Journal International*, *97*(2), 341-355. https://doi.org/10.1111/j.1365-246X.1989.tb00505.x

Dekkers, M. J., Langereis, C. G., Vriend, S. P., van Santvoort, P. J. M., & de Lange, G. J. (1994). Fuzzy c-means cluster analysis of early diagenetic effects on natural remanent magnetisation acquisition in a 1.1 Myr piston core from the Central Mediterranean. *Physics of the Earth and Planetary Interiors*, *85*(1-2), 155-171. https://doi.org/10.1016/0031-9201(94)90014-0

Dekkers, M. J., Mattéi, J. L., Fillion, G., & Rochette, P. (1989). Grain-size dependence of the magnetic behavior of pyrrhotite during its low-temperature transition at 34 K. *Geophysical Research Letters*, *16*(8), 855-858. https://doi.org/10.1029/GL016i008p00855

deMenocal, P., Ortiz, J., Guilderson, T., & Sarnthein, M. (2000). Coherent high-and low-latitude climate variability during the Holocene warm period. *Science*, *288*(5474), 2198-2202. https://doi.org/10.1126/science.288.5474.2198

Dinarès-Turell, J., Hoogakker, B. A. A., Roberts, A. P., Rohling, E. J., & Sagnotti, L. (2003). Quaternary climatic control of biogenic magnetite production and eolian dust input in cores from the Mediterranean Sea. *Palaeogeography, Palaeoclimatology, Palaeoecology*, *190*, 195-209. https://doi.org/10.1016/s0031-0182(02)00605-3

Drake, N. A., Blench, R. M., Armitage, S. J., Bristow, C. S., & White, K. H. (2011). Ancient watercourses and biogeography of the Sahara explain the peopling of the desert. *Proceedings of the National Academy of Sciences*, *108*(2), 458-462. https://doi.org/10.1073/pnas.1012231108

Drake, N. A., Breeze, P., & Parker, A. (2013). Palaeoclimate in the Saharan and Arabian Deserts during the Middle Palaeolithic and the potential for hominin dispersals. *Quaternary International*, *300*, 48-61. https://doi.org/10.1016/j.quaint.2012.12.018

Dunlop, D. J. (1973). Superparamagnetic and single-domain threshold sizes in magnetite. *Journal of Geophysical Research*, *78*(11), 1780-1793. https://doi.org/10.1029/JB078i011p01780

Dunlop, D. J., & Argyle, K. S. (1991). Separating multidomain and single-domain-like remanences in pseudo-single-domain magnetites (215-540 nm) by low-temperature demagnetization. *Journal of Geophysical Research: Solid Earth*, *96*(B2), 2007-2017. https://doi.org/10.1029/90JB02338

Dunlop, D. J., & Özdemir, Ö. (1997). *Rock Magnetism: Fundamentals and Frontiers*. Cambridge University Press, Cambridge. https://doi.org/10.1063/1.882466

Dunlop, D. J., Özdemir, Ö., & Schmidt, P. W. (1997). Paleomagnetism and paleothermometry of the Sydney Basin 2. Origin of anomalously high unblocking temperatures. *Journal of Geophysical Research: Solid Earth*, *102*(B12), 27285-27295. https://doi.org/10.1029/97JB02478

Dymond, J., Suess, E., & Lyle, M. (1992). Barium in deep-sea sediment: A geochemical proxy for paleoproductivity. *Paleoceanography*, *7*(2), 163-181. https://doi.org/10.1073/pnas.1012231108

Egli, R. (2013). VARIFORC: An optimized protocol for calculating non-regular first-order reversal curve (FORC) diagrams. *Global and Planetary Change*, *110*, 302-320. https://doi.org/10.1016/j.gloplacha.2013.08.003

Egli, R., Chen, A. P., Winklhofer, M., Kodama, K. P., & Horng, C. S. (2010). Detection of noninteracting single domain particles using first-order reversal curve diagrams. *Geochemistry*, *Geophysics*, *Geosystems*, *11*(1). https://doi.org/10.1029/2009GC002916

Elderfield, H., Ferretti, P., Greaves, M., Crowhurst, S., McCave, I. N., Hodell, D., & Piotrowski, A. M. (2012). Evolution of ocean temperature and ice volume through the mid-Pleistocene climate transition. *Science*, *337*(6095), 704-709. https://doi.org/10.1126/science.1221294

Emeis, K. C., Camerlenghi, A., McKenzie, J. A., Rio, D., & Sprovieri, R. (1991). The occurrence and significance of Pleistocene and Upper Pliocene sapropels in the Tyrrhenian Sea. *Marine Geology*, *100*(1-4), 155-182. https://doi.org/10.1016 /0025-3227(91)90231-r

Emeis, K. C., Robertson, A. H. F., & Richter, C. (1996). Shipboard Scientific Party ODP Leg 160. *Proceedings of the Ocean Drilling Program*, *Initial Reports* (pp. 972). Ocean Drilling Program, College Station, TX.

Emeis, K. C., Sakamoto, T., Wehausen, R., & Brumsack, H. J. (2000a). The sapropel record of the eastern Mediterranean Sea-results of Ocean Drilling Program Leg 160. *Palaeogeography*, *Palaeoclimatology*, *Palaeoecology*, *158*(3-4), 371-395. https://doi.org/10.1016/s0031-0182(00)00059-6

Emeis, K. C., Struck, U., Schulz, H. M., Rosenberg, R., Bernasconi, S., Erlenkeuser, H., et al. (2000b). Temperature and salinity variations of Mediterranean Sea surface waters over the last 16,000 years from records of planktonic stable oxygen isotopes and alkenone unsaturation ratios. *Palaeogeography*, *Palaeoclimatology*, *Palaeoecology*, *158*(3-4), 259-280. https://doi.org/10.1016/s00310182(00)0005 3-5

Emeis, K. C., Schulz, H. M., Struck, U., Sakamoto, T., Doose, H., Erlenkeuser, H., et al. (1998). Stable isotope and alkenone temperature records of sapropels from Sites 964 and 967: Constraining the physical environmental of sapropel formation in the Eastern Mediterranean Sea. *Proceedings of the Ocean Drilling Program*, *Scientific Results* (vol. 160). Ocean Drilling Program, College Station, TX. https://doi.org/10.2973 /odp.proc.sr.160.011.1998

Emeis, K. C., Schulz, H., Struck, U., Rossignol-Strick, M., Erlenkeuser, H., Howell, M. W., et al. (2003). Eastern Mediterranean surface water temperatures and $\delta^{18}O$

composition during deposition of sapropels in the late Quaternary. *Paleoceanography*, *18*(1). https://doi.org/10.1029/2000pa000617

Evans, M. E., & Heller, F. (2003). *Environmental magnetism: Principles and applications of enviromagnetics*, Academic, San Diego, Calif.

Foucault, A., & Méliéres, F. (2000). Palaeoclimatic cyclicity in central Mediterranean Pliocene sediments: The mineralogical signal. *Palaeogeography*, *Palaeoclimatology*, *Palaeoecology*, *158*(3-4), 311-323. https://doi.org/10.1016/S0031-0182(00)00056-0

Fritsch, E., Morin, G., Bedidi, A., Bonnin, D., Balan, E., Caquineau, S., & Calas, G. (2005). Transformation of haematite and Al-poor goethite to Al-rich goethite and associated yellowing in a ferralitic clay soil profile of the middle Amazon basin (Manaus, Brazil). *European Journal of Soil Science*, *56*(5), 575-588. https://doi.org/10.1111/j.1365-2389.2005.00693.x

Garming, J. F. L., de Lange, G. J., Dekkers, M. J., & Passier, H. F. (2004). Changes in magnetic parameters after sequential iron phase extraction of eastern Mediterranean sapropel S1 sediments. *Studia Geophysica et Geodaetica*, *48*(2), 345-362. https://doi.org/10.1023/b:sgeg.0000020837.18450.76

Gasse, F. (2000). Hydrological changes in the African tropics since the Last Glacial Maximum. *Quaternary Science Reviews*, *19*(1-5), 189-211. https://doi.org /10.1016/s0277-3791(99)00061-x

Gaven, C., Hillaire-Marcel, C., & Petit-Maire, N. (1981). A Pleistocene lacustrine episode in southeastern Libya. *Nature*, *290*(5802), 131-133. https://doi.org/ 10.1038/290131a0

Goudie, A. S., & Middleton, N. J. (2001). Saharan dust storms: Nature and consequences. *Earth-Science Reviews*, *56*(1-4), 179-204. https://doi.org/ 10.1016/S0012-8252(01)00067-8

Grant, K. M., Grimm, R., Mikolajewicz, U., Marino, G., Ziegler, M., & Rohling, E. J. (2016). The timing of Mediterranean sapropel deposition relative to insolation, sea-level and African monsoon changes. *Quaternary Science Reviews*, *140*, 125-141. https://doi.org/10.1016/j.quascirev.2016.03.026

Grant, K. M., Rohling, E. J., Westerhold, T., Zabel, M., Heslop, D., Konijnendijk, T., & Lourens, L. (2017). A 3 million year index for North African humidity/aridity

and the implication of potential pan-African Humid periods. *Quaternary Science Reviews*, *171*, 100-118. https://doi.org/10.1016/j.quascirev.2017.07.005

Halgedahl, S. L., & Jarrard, R. D. (1995). Low-temperature behavior of single-domain through multidomain magnetite. *Earth and Planetary Science Letters*, *130*(1-4), 127-139. https://doi.org/10.1016/0012-821X(94)00260-6

Harrison, R. J., & Feinberg, J. M. (2008). FORCinel: An improved algorithm for calculating first-order reversal curve distributions using locally weighted regression smoothing. *Geochemistry*, *Geophysics*, *Geosystems*, *9*. https://doi.org/Artn Q0501610.1029/2008gc001987

Harrison, R. J., Muraszko, J., Heslop, D., Lascu, I., Muxworthy, A. R., & Roberts, A. P. (2018). An improved algorithm for unmixing first-order reversal curve diagrams using principal component analysis. *Geochemistry*, *Geophysics*, *Geosystems*, *19*(5), 1595-1610. https://doi.org/10.1029/2018gc007511

Hartstra, R. L. (1982). Grain-size dependence of initial susceptibility and saturation magnetization-related parameters of four natural magnetites in the PSD-MD range. *Geophysical Journal International*, *71*(2), 477-495. https://doi.org/10.1111/j.1365-246X.1982.tb05998.x

Hecht, A., & Gertman, I. (2001). Physical features of the eastern Mediterranean resulting from the integration of POEM data with Russian Mediterranean cruises. *Deep Sea Research I*, *48*(8), 1847-1876. https://doi.org/10.1016/s0967-0637(00)00113-8

Heider, F., Dunlop, D. J., & Soffel, H. C. (1992). Low-temperature and alternating field demagnetization of saturation remanence and thermoremanence in magnetite grains (0.037 μm to 5 mm). *Journal of Geophysical Research: Solid Earth*, *97*(B6), 9371-9381. https://doi.org/10.1029/91JB03097

Henshaw Jr, P. C., & Merrill, R. T. (1980). Magnetic and chemical changes in marine sediments. *Reviews of Geophysics*, *18*(2), 483-504. https://doi.org/10.1029/RG018i002p00483

Heslop, D. (2015). Numerical strategies for magnetic mineral unmixing. *Earth-Science Reviews*, *150*, 256-284. https://doi.org/10.1016/j.earscirev.2015.07.007

Heslop, D., Roberts, A. P., & Chang, L. (2014). Characterizing magnetofossils from first-order reversal curve (FORC) central ridge signatures. *Geochemistry*, *Geophysics*, *Geosystems*, *15*(6), 2170-2179. https://doi.org/10.1002/2014GC00 5291

Heslop, D., Roberts, A. P., Chang, L., Davies, M., Abrajevitch, A., & De Deckker, P. (2013). Quantifying magnetite magnetofossil contributions to sedimentary magnetizations. *Earth and Planetary Science Letters*, *382*, 58-65. https://doi.org/10.1016/j.epsl.2013.09.011

Heslop, D., Von Dobeneck, T., & Höcker, M. (2007). Using non-negative matrix factorization in the "unmixing" of diffuse reflectance spectra. *Marine Geology*, *241*(1-4), 63-78. https://doi.org/10.1016/j.margeo.2007.03.004

Hesse, P. P. (1994). Evidence for bacterial palaeoecological origin of mineral magnetic cycles in oxic and sub-oxic Tasman Sea sediments. *Marine Geology*, *117*(1-4), 1-17. https://doi.org/10.1016/0025-3227(94)90003-5

Higgs, N. C., Thomson, J., Wilson, T. R. S., & Croudace, I. W. (1994). Modification and complete removal of eastern Mediterranean sapropels by post depositional oxidation. *Geology*, *22*(5), 423-426. https://doi.org/10.1130/0091-7613(1994)022<0423:macroe>2.3.co;2

Hilgen, F. J. (1987). Sedimentary rhythms and high-resolution chronostratigraphic correlations in the Mediterranean Pliocene. *Newsletters on Stratigraphy*, *17*(2), 109-127. https://doi.org/10.1127/nos/17/1987/109

Hilgen, F. J. (1991). Astronomical calibration of Gauss to Matuyama sapropels in the Mediterranean and implication for the geomagnetic polarity time scale. *Earth and Planetary Science Letters*, *104*(2), 226-244. https://doi.org/10.1016/0012-821x(91)90206-w

Hilgen, F. J., & Langereis, C. G. (1993). A critical re-evaluation of the Miocene/Pliocene boundary as defined in the Mediterranean. *Earth and Planetary Science Letters*, *118*(1-4), 167-179. https://doi.org/10.1016/0012-821x(93)90166-7

Hilgen, F. J., Aziz, H. A., Krijgsman, W., Raffi, I., & Turco, E. (2003). Integrated stratigraphy and astronomical tuning of the Serravallian and lower Tortonian at Monte dei Corvi (Middle-Upper Miocene, northern Italy). *Palaeogeography, Palaeoclimatology, Palaeoecology*, *199*(3-4), 229-264. https://doi.org /10.1016/s0031-0182(03)00505-4

Hilgenfeldt, K. (2000). Diagenetic dissolution of biogenic magnetite in surface sediments of the Benguela upwelling system. *International Journal of Earth Sciences*, *88*(4), 630-640. https://doi.org/10.1007/s005310050293

Hodych, J. P. (1991). Low-temperature demagnetization of saturation remanence in rocks bearing multidomain magnetite. *Physics of the Earth and Planetary Interiors*, *66*(3-4), 144-152. https://doi.org/10.1016/0031-9201(91)90073-Q

Hoelzmann, P., Kruse, H. J., & Rottinger, F. (2000). Precipitation estimates for the eastern Saharan palaeomonsoon based on a water balance model of the West Nubian Palaeolake Basin. *Global and Planetary Change*, *26*(1-3), 105-120. https://doi.org/10.1016/s0921-8181(00)00038-2

Hönisch, B., Hemming, N. G., Archer, D., Siddall, M., & McManus, J. F. (2009). Atmospheric carbon dioxide concentration across the mid-Pleistocene transition. *Science*, *324*(5934), 1551-1554. https://doi.org/10.7551/mitpress/8876.003.0036

Housen, B. A., & Moskowitz, B. M. (2006). Depth distribution of magnetofossils in near-surface sediments from the Blake/Bahama Outer Ridge, western North Atlantic Ocean, determined by low-temperature magnetism. *Journal of Geophysical Research: Biogeosciences*, *111*(G1). https://doi.org/10.1029/2005 jg000068

Housen, B. A., Banerjee, S. K., & Moskowitz, B. M. (1996). Low-temperature magnetic properties of siderite and magnetite in marine sediments. *Geophysical Research Letters*, *23*(20), 2843-2846. https://doi.org/10.1029/96GL01197

IPCC (Intergovernmental Panel on Climate Change). (2007). Summary for policymakers. *Climate change 2007: The physical science basis. Contribution of working group I to the Fourth Assessment Report of the Intergovernmental Panel on Climate Change*, 1-18.

Jickells, T. D., An, Z. S., Andersen, K. K., Baker, A. R., Bergametti, G., Brooks, N., et al. (2005). Global iron connections between desert dust, ocean biogeochemistry, and climate. *Science*, *308*(5718), 67-71. https://doi.org/10.1126/science.1105959

Just, J., Dekkers, M. J., von Dobeneck, T., van Hoesel, A., & Bickert, T. (2012). Signatures and significance of aeolian, fluvial, bacterial and diagenetic magnetic mineral fractions in Late Quaternary marine sediments off Gambia, NW Africa. *Geochemistry*, *Geophysics*, *Geosystems*, *13*(9). https://doi.org/10.1029/2012gc004146

Karlin, R. (1990). Magnetite diagenesis in marine sediments from the Oregon continental margin. *Journal of Geophysical Research: Solid Earth*, *95*(B4), 4405-4419. https://doi.org/10.1029/JB095iB04p04405

Kaufman, Y. J., Tanré, D., & Boucher, O. (2002). A satellite view of aerosols in the

climate system. *Nature*, *419*(6903), 215-223. https://doi.org/10.1038/nature01091

Kent, D. V. (1982). Apparent correlation of palaeomagnetic intensity and climatic records in deep-sea sediments. *Nature*, *299*(5883), 538-539. https://doi.org/10.1038/299538a0

Kïg, I., Drodt, M., Suess, E., & Trautwein, A. X. (1997). Iron reduction through the tan-green color transition in deep-sea sediments. *Geochimica et Cosmochimica Acta*, *61*(8), 1679-1683. https://doi.org/10.1016/S0016-7037(97)00007-0

King, J. W., & Channell, J. E. T. (1991). Sedimentary magnetism, environmental magnetism, and magnetostratigraphy. *Reviews of Geophysics*, *29*(S1), 358-370. https://doi.org/10.1002/rog.1991.29.s1.358

King, J., Banerjee, S. K., Marvin, J., & Özdemir, Ö. (1982). A comparison of different magnetic methods for determining the relative grain-size of magnetite in natural materials: Some results from lake-sediments. *Earth and Planetary Science Letters*, *59*(2), 404-419. https://doi.org/10.1016/0012-821x(82)90142-X

Kopp, R. E., & Kirschvink, J. L. (2008). The identification and biogeochemical interpretation of fossil magnetotactic bacteria. *Earth-Science Reviews*, *86*(1-4), 42-61. https://doi.org/10.1016/j.earscirev.2007.08.001

Kopp, R. E., Raub, T. D., Schumann, D., Vali, H., Smirnov, A. V., & Kirschvink, J. L. (2007). Magnetofossil spike during the Paleocene-Eocene thermal maximum: Ferromagnetic resonance, rock magnetic, and electron microscopy evidence from Ancora, New Jersey, United States. *Paleoceanography*, *22*(4), PA4103. https://doi.org/10.1029/2007PA001473

Kopp, R. E., Schumann, D., Raub, T. D., Powars, D. S., Godfrey, L. V., Swanson-Hysell, N. L., et al. (2009). An Appalachian Amazon? Magnetofossil evidence for the development of a tropical river-like system in the mid-Atlantic United States during the Paleocene-Eocene thermal maximum. *Paleoceanography*, *24*(4). https://doi.org/10.1029/2009PA001783

Krijgsman, W., Fortuin, A. R., Hilgen, F. J., & Sierro, F. J. (2001). Astrochronology for the Messinian Sorbas basin (SE Spain) and orbital (precessional) forcing for evaporite cyclicity. *Sedimentary Geology*, *140*(1-2), 43-60. https://doi.org/10.1016/s0037-0738(00)00171-8

Krijgsman, W., Hilgen, F. J., Langereis, C. G., Santarelli, A., & Zachariasse, W. J. (1995). Late Miocene magnetostratigraphy, biostratigraphy and cyclostratigraphy in the Mediterranean. *Earth and Planetary Science Letters*, *136*(3-4), 475-494. https://doi.org/10.1016/0012-821x(95)00206-r

Kruiver, P. P., & Passier, H. F. (2001). Coercivity analysis of magnetic phases in sapropel S1 related to variations in redox conditions, including an investigation of the S ratio. *Geochemistry*, *Geophysics*, *Geosystems*, *2*(12). https://doi.org/10.1029/2001gc000181

Labeyrie, L. D., Duplessy, J. C., & Blanc, P. L. (1987). Variations in mode of formation and temperature of oceanic deep waters over the past 125,000 years. *Nature*, *327*(6122), 477-482. https://doi.org/10.1038/327477a0

Laberty, C., & Navrotsky, A. (1998). Energetics of stable and metastable low-temperature iron oxides and oxyhydroxides. *Geochimica et Cosmochimica Acta*, *62*(17), 2905-2913. https://doi.org/10.1016/S0016-7037(98)00208-7

Langereis, C. G., & Dekkers M. J. (1999). Magnetic cyclostratigraphy: High-resolution dating in and beyond the Quaternary and analysis of periodic changes in diagenesis and sedimentary magnetism. *Quaternary Climates, Environments and Magnetism* (pp. 352-382). Cambridge University Press.

Langereis, C. G., & Hilgen, F. J. (1991). The Rossello composite: A Mediterranean and global reference section for the Early to early Late Pliocene. *Earth and Planetary Science Letters*, *104*(2-4), 211-225. https://doi.org/10.1016/0012-821x(91)90205-v

Langereis, C. G., Dekkers, M. J., De Lange, G. J., Paterne, M., & Van Santvoort, P. J. M. (1997). Magnetostratigraphy and astronomical calibration of the last 1.1 Myr from an eastern Mediterranean piston core and dating of short events in the Brunhes. *Geophysical Journal International*, *129*(1), 75-94. https://doi.org/10.1111/j.1365-246x.1997.tb00938.x

Larrasoaña, J. C., Liu, Q., Hu, P., Roberts, A. P., Mata, P., Civis, J., et al. (2014). Paleomagnetic and paleoenvironmental implications of magnetofossil occurrences in late Miocene marine sediments from the Guadalquivir Basin, SW Spain. *Frontiers in Microbiology*, *5*, 71. https://doi.org/10.3389/fmicb.2014.00071

Larrasoaña, J. C., Roberts, A. P., & Rohling, E. J. (2013). Dynamics of green Sahara periods and their role in hominin evolution. *PLoS One*, *8*(10), e76514. https://doi.org/10.1371/journal.pone.0076514

Larrasoaña, J. C., Roberts, A. P., Chang, L., Schellenberg, S. A., Fitz Gerald, J. D., Norris, R. D., & Zachos, J. C. (2012). Magnetotactic bacterial response to Antarctic dust supply during the Palaeocene-Eocene thermal maximum. *Earth and Planetary Science Letters*, *333*, 122-133. https://doi.org/10.1016/j.epsl.2012.04.003

Larrasoaña, J. C., Roberts, A. P., Hayes, A., Wehausen, R., & Rohling, E. J. (2006). Detecting missing beats in the Mediterranean climate rhythm from magnetic identification of oxidized sapropels (Ocean Drilling Program Leg 160). *Physics of the Earth and Planetary Interiors*, *156*(3-4), 283-293. https://doi.org/10.1016/j.pepi.2005.04.017

Larrasoaña, J. C., Roberts, A. P., Liu, Q. S., Lyons, R., Oldfield, F., Rohling, E. J., & Heslop, D. (2015). Source-to-sink magnetic properties of NE Saharan dust in Eastern Mediterranean marine sediments: Review and paleoenvironmental implications. *Frontiers in Earth Science*, *3*, 19. https://doi.org/10.3389/feart.2015.00019

Larrasoaña, J. C., Roberts, A. P., Musgrave, R. J., Gràcia, E., Piñero, E., Vega, M., & Martínez-Ruiz, F. (2007). Diagenetic formation of greigite and pyrrhotite in gas hydrate marine sedimentary systems. *Earth and Planetary Science Letters*, *261*(3-4), 350-366. https://doi.org/10.1016/j.epsl.2007.06.032

Larrasoaña, J. C., Roberts, A. P., Rohling, E. J., Winklhofer, M., & Wehausen, R. (2003a). Three million years of monsoon variability over the northern Sahara. *Climate Dynamics*, *21*(7-8), 689-698. https://doi.org/10.1007/s00382-003-0355-z

Larrasoaña, J. C., Roberts, A. P., Stoner, J. S., Richter, C., & Wehausen, R. (2003b). A new proxy for bottom-water ventilation in the eastern Mediterranean based on diagenetically controlled magnetic properties of sapropel-bearing sediments. *Palaeogeography*, *Palaeoclimatology*, *Palaeoecology*, *190*, 221-242. https://doi.org/10.1016/s0031-0182(02)00607-7

Lascu, I., Banerjee, S. K., & Berquó, T. S. (2010). Quantifying the concentration of ferrimagnetic particles in sediments using rock magnetic methods. *Geochemistry*, *Geophysics*, *Geosystems*, *11*, Q08Z19. https://doi.org/10.1029/2010GC003182

Lascu, I., Einsle, J. F., Ball, M. R., & Harrison, R. J. (2018). The vortex state in geologic materials: A micromagnetic perspective. *Journal of Geophysical Research: Solid Earth*, *123*(9), 7285-7304. https://doi.org/10.1029/2018jb015909

Lascu, I., Harrison, R. J., Li, Y., Muraszko, J. R., Channell, J. E. T., Piotrowski, A. M., & Hodell, D. A. (2015). Magnetic unmixing of first-order reversal curve diagrams using principal component analysis. *Geochemistry*, *Geophysics*, *Geosystems*, *16*(9), 2900-2915. https://doi.org/10.1002/2015gc005909

Laskar, J., Joutel, F., & Boudin, F. (1993). Orbital, precessional, and insolation quantities for the Earth from -20 Myr to +10 Myr. *Astronomy and Astrophysics*, *270*, 522-533.

Levin, Z., Ganor, E., & Gladstein, V. (1996). The effects of desert particles coated with sulfate on rain formation in the eastern Mediterranean. *Journal of Applied Meteorology*, *35*(9), 1511-1523. https://doi.org/10.1175/1520-0450(1996)035<1511:teodpc>2.0.co;2

Li, J. H., Wu, W. F., Liu, Q. S., & Pan, Y. X. (2012). Magnetic anisotropy, magnetostatic interactions and identification of magnetofossils. *Geochemistry*, *Geophysics*, *Geosystems*, *13*(109), Q10Z51. https://doi.org/10.1029/2012GC004384

Li, J., Benzerara, K., Bernard, S., & Beyssac, O. (2013a). The link between biomineralization and fossilization of bacteria: Insights from field and experimental studies. *Chemical Geology*, *359*, 49-69. http://dx.doi.org/10.1016/j.chemgeo.2013.09.013

Li, J., Ge, K., Pan, Y., Williams, W., Liu, Q., & Qin, H. (2013b). A strong angular dependence of magnetic properties of magnetosome chains: Implications for rock magnetism and paleomagnetism. *Geochemistry*, *Geophysics*, *Geosystems*, *14*(10), 3887-3907. https://doi.org/10.1002/Ggge.20228

Li, J., Menguy, N., Roberts, A. P., Gu, L., Leroy, E., Bourgon, J., et al. (2020a). Bullet-shaped magnetite biomineralization within a magnetotactic deltaproteobacterium: Implications for magnetofossil identification. *Journal of Geophysical Research: Biogeosciences*, *125*(7), e2020JG005680. https://doi.org/10.1029/2020jg005680

Li, J., Liu, Y., Liu, S., Roberts, A. P., Pan, H., Xiao, T., et al. (2020b). Classification of a complexly mixed magnetic mineral assemblage in Pacific Ocean surface sediment by electron microscopy and supervised magnetic unmixing. *Frontiers in Earth Science*, *8*, 648. https://doi.org/10.3389/feart.2020.609058

Li, J., Menguy, N., Leroy, E., Roberts, A. P., Liu, P., & Pan, Y. (2020c). Biomineralization and magnetism of uncultured magnetotactic coccus strain THC-1 with non-chained magnetosomal magnetite nanoparticles. *Journal of Geophysical Research: Solid Earth*, *125*, e2020JB020853. https://doi.org/10.1029/2020JB020853

Li, J., Pan, Y., Liu, Q., Yu-Zhang, K., Menguy, N., Che, R., et al. (2010). Biomineralization, crystallography and magnetic properties of bullet-shaped magnetite magnetosomes in giant rod magnetotactic bacteria. *Earth and Planetary Science Letters*, *293*(3-4), 368-376. https://doi.org/10.1016/j.epsl.2010.03.007

Li, J., Wu, W., Liu, Q., & Pan, Y. (2012). Magnetic anisotropy, magnetostatic interactions and identification of magnetofossils. *Geochemistry*, *Geophysics*, *Geosystems*, *13*(12). https://doi.org/10.1029/2012GC004384

Lippert, P. C., & Zachos, J. C. (2007). A biogenic origin for anomalous fine-grained magnetic material at the Paleocene-Eocene boundary at Wilson Lake, New Jersey. *Paleoceanography*, *22*, PA4104. https://doi.org/10.1029/2007PA001471

Lisiecki, L. E., & Raymo, M. E. (2005). A Pliocene-Pleistocene stack of 57 globally distributed benthic $\delta^{18}O$ records. *Paleoceanography*, *20*(1). https://doi.org/10.1029/2004pa001071

Lisiecki, L. E., & Raymo, M. E. (2007). Plio-Pleistocene climate evolution: Trends and transitions in glacial cycle dynamics. *Quaternary Science Reviews*, *26*(1-2), 56-69. https://doi.org/10.1016/j.quascirev.2006.09.005

Liu, H., Zhu, R. X., & Li, G. X. (2003). Rock magnetic properties of the fine-grained sediment on the outer shelf of the East China Sea: Implication for provenance. *Marine Geology*, *193*(3-4), 195-206. https://doi.org/10.1016/s0025-3227(02)00660-6

Liu, Q., Roberts, A. P., Larrasoaña, J. C., Banerjee, S. K., Guyodo, Y., Tauxe, L., & Oldfield, F. (2012a). Environmental magnetism: Principles and applications. *Reviews of Geophysics*, *50*(4). https://doi.org/10.1016/j.palaeo.2012.02.036

Liu, Q. S., Larrasoaña, J. C., Torrent, J., Roberts, A. P., Rohling, E. J., Liu, Z. F., & Jiang, Z. X. (2012b). New constraints on climate forcing and variability in the circum-Mediterranean region from magnetic and geochemical observations of sapropels

S1, S5 and S6. *Palaeogeography*, *Palaeoclimatology*, *Palaeoecology*, *333*, 1-12. https://doi.org/10.1016/j.palaeo.2012.02.036

Liu, Q., Banerjee, S. K., Jackson, M. J., Zhu, R., & Pan, Y. (2002). A new method in mineral magnetism for the separation of weak antiferromagnetic signal from a strong ferrimagnetic background. *Geophysical Research Letters*, *29*(12), 6-1. https://doi.org/10.1029/2002GL014699

Liu, Q., Roberts, A. P., Torrent, J., Horng, C. S., & Larrasoaña, J. C. (2007). What do the HIRM and *S*-ratio really measure in environmental magnetism? *Geochemistry*, *Geophysics*, *Geosystems*, *8*(9). https://doi.org/10.1029/2007GC001717

Lolis, C. J., Bartzokas, A., & Katsoulis, B. D. (2002). Spatial and temporal 850 hPa air temperature and sea-surface temperature covariances in the Mediterranean region and their connection to atmospheric circulation. *International Journal of Climatology: A Journal of the Royal Meteorological Society*, *22*(6), 663-676. https://doi.org/10.1002/joc.759

Lourens, L. J., Antonarakou, A., Hilgen, F. J., Van Hoof, A. A. M., Vergnaud-Grazzini, C., & Zachariasse, W. J. (1996). Evaluation of the Plio-Pleistocene astronomical timescale. *Paleoceanography*, *11*(4), 391-413. https://doi.org/10.1029/96pa01125

Lourens, L. J., Wehausen, R., & Brumsack, H. J. (2001). Geological constraints on tidal dissipation and dynamical ellipticity of the Earth over the past three million years. *Nature*, *409*(6823), 1029-1033. https://doi.org/10.1038/35059062

Lowenstam, H. A. (1981). Minerals formed by organisms. *Science*, *211*(4487), 1126-1131. https://doi.org/10.1126/science.7008198

Loye-Pilot, M. D., Martin, J. M., & Morelli, J. (1986). Influence of Saharan dust on the rain acidity and atmospheric input to the Mediterranean. *Nature*, *321*(6068), 427-428. https://doi.org/10.1038/321427a0

Maasch, K. A. (1988). Statistical detection of the mid-Pleistocene transition. *Climate Dynamics*, *2*(3), 133-143. https://doi.org/10.1007/bf01053471

Maher, B. A. (1988). Magnetic properties of some synthetic sub-micron magnetites. *Geophysical Journal International*, *94*(1), 83-96. https://doi.org/10.1111/j.1365-246X.1988.tb03429.x

Maher, B. A. (2011). The magnetic properties of Quaternary aeolian dusts and sediments, and their palaeoclimatic significance. *Aeolian Research*, *3*, 87-144. https://doi.org/10.1016/j.aeolia.2011.01.005

Maher, B. A., Prospero, J. M., Mackie, D., Gaiero, D., Hesse, P. P., & Balkanski, Y. (2010). Global connections between aeolian dust, climate and ocean biogeochemistry at the present day and at the last glacial maximum. *Earth-Science Reviews*, *99*(1-2), 61-97. https://doi.org/10.1016/j.earscirev.2009.12. 001

Maher, B. A., & Thompson, R. (1999). *Quaternary climates, environments and magnetism* (pp. 390). Cambridge University Press, Cambridge.

Mahowald, N. M., Yoshioka, M., Collins, W. D., Conley, A. J., Fillmore, D. W., & Coleman, D. B. (2006a). Climate response and radiative forcing from mineral aerosols during the last glacial maximum, pre-industrial, current and doubled-carbon dioxide climates. *Geophysical Research Letters*, *33*(20). https://doi.org/10.1029/2006gl026126

Mahowald, N. M., Muhs, D. R., Levis, S., Rasch, P. J., Yoshioka, M., Zender, C. S., & Luo, C. (2006b). Change in atmospheric mineral aerosols in response to climate: Last glacial period, preindustrial, modern, and doubled carbon dioxide climates. *Journal of Geophysical Research: Atmospheres*, *111*(10). https://doi.org/10.1029/2005JD006653

Malanotte-Rizzoli, P., & Hecht, A. (1988). The general circulation of the eastern Mediterranean Sea: A review of its phenomenology and modeling. *Oceanologica Acta*, *11*(4), 323-335.

Martínez-Garcia, A., Rosell-Melé, A., Geibert, W., Gersonde, R., Masqué, P., Gaspari, V., & Barbante, C. (2009). Links between iron supply, marine productivity, sea surface temperature, and CO_2 over the last 1.1 Ma. *Paleoceanography*, 24(1). https://doi.org/10.1029/2008pa001657

Maslin, M. A., Brierley, C. M., Milner, A. M., Shultz, S., Trauth, M. H., & Wilson, K. E. (2014). East African climate pulses and early human evolution. *Quaternary Science Reviews*, *101*, 1-17. https://doi.org/10.1016/j.quascirev.2014.06.012

Mayergoyz, I. (1986). Mathematical models of hysteresis. *IEEE Transactions on Magnetics*, *22*(5), 603-608. https://doi.org/10.1109/TMAG.1986.1064347

McClymont, E. L., Sosdian, S. M., Rosell-Melé, A., & Rosenthal, Y. (2013). Pleistocene sea-surface temperature evolution: Early cooling, delayed glacial intensification, and implications for the mid-Pleistocene climate transition. *Earth-Science Reviews*, *123*, 173-193. https://doi.org/10.1016/j.earscirev. 2013.04.006

McGee, D., Broecker, W. S., & Winckler, G. (2010). Gustiness: The driver of glacial

dustiness? *Quaternary Science Reviews*, *29*(17-18), 2340-2350. https://doi.org/10.1016/j.quascirev.2010.06.009

McKenzie, J. A. (1993). Pluvial conditions in the eastern Sahara following the penultimate deglaciation: Implications for changes in atmospheric circulation patterns with global warming. *Palaeogeography*, *Palaeoclimatology*, *Palaeoecology*, *103*(1-2), 95-105. https://doi.org/10.1016/0031-0182(93)90054-M

MEDOC group. (1970). Observation of formation of deep water in the Mediterranean Sea, 1969. *Nature*, *277*, 1037-1040. https://doi.org/10.1038/2271037a0

Mercone, D., Thomson, J., Abu-Zied, R. H., Croudace, I. W., & Rohling, E. J. (2001). High resolution geochemical and micropalaeontological profiling of the most recent eastern Mediterranean sapropel. *Marine Geology*, *177*(1-2), 25-44. https://doi.org/10.1016/s0025-3227(01)00122-0

MerMex Group. (2011). Marine ecosystems' responses to climatic and anthropogenic forcings in the Mediterranean. *Progress in Oceanography*, *91*(2), 97-166. https://doi.org/10.1016/j.pocean.2011.02.003

Meyers, P. A. (2006). Paleoceanographic and paleoclimatic similarities between Mediterranean sapropels and Cretaceous black shales. *Palaeogeography*, *Palaeoclimatology*, *Palaeoecology*, *235*(1-3), 305-320. https://doi.org/10.1016/j.palaeo.2005.10.025

Meyers, P. A., & Doose, H. (1999). Sources, preservation, and thermal maturity of organic matter in Pliocene-Pleistocene organic-carbon-rich sediments of the Western Mediterranean Sea. *Proceedings of the Ocean Drilling Program, Scientific Results* (vol. 161, pp. 383-390). Ocean Drilling Program, College Station, TX. https://doi.org/10.2973/odp.proc.sr.161.235.1999

Miller, A. R., Tchernia, P., Charnock, H., & McGill, D. A. (1970). Mediterranean Sea Atlas of temperature, salinity, and oxygen. *Profiles and Data from Cruises of RV Atlantis and RV Chain*. Alpine, Braintree, Mass.

Millot, C., & Taupier-Letage, I. (2005). Circulation in the Mediterranean Sea. *The Mediterranean Sea* (pp. 29-66). Springer, Berlin, Heidelberg. https://doi.org/10.1007/b107143

Moisescu, C., Ardelean, I., & Benning, L. G. (2014). The effect and role of environmental conditions on magnetosome synthesis. *Frontiers in Microbiology*, *5*, 49. https://doi.org/10.3389/fmicb.2014.00049

Mollo, S., Putirka, K., Iezzi, G., & Scarlato, P. (2013). The control of cooling rate on titanomagnetite composition: Implications for a geospeedometry model applicable to alkaline rocks from Mt. Etna volcano. *Contributions to Mineralogy and Petrology*, *165*(3), 457-475. https://doi.org/10.1007/s00410-012-0817-6

Morin, F. J. (1950). Magnetic susceptibility of αFe_2O_3 and αFe_2O_3 with added titanium. *Physical Review*, *78*(6), 819. https://doi.org/10.1016/j.aeolia.2011.01.005

Morris, R. V., & Lauer, H. V. (1981). Stability of goethite (α-FeOOH) and lepidocrocite (γ-FeOOH) to dehydration by UV radiation: Implications for their occurrence on the Martian surface. *Journal of Geophysical Research: Solid Earth*, *86*, 10893-10899. https://doi.org/10.1029/JB086iB11p10893

Moskowitz, B. M., Frankel, R. B., & Bazylinski, D. A. (1993). Rock magnetic criteria for the detection of biogenic magnetite. *Earth and Planetary Science Letters*, *120*(3-4), 283-300. https://doi.org/10.1016/0012-821X(93)90245-5

Moulin, C., Lambert, C. E., Dayan, U., Masson, V., Ramonet, M., Bousquet, P., et al. (1998). Satellite climatology of African dust transport in the Mediterranean atmosphere. *Journal of Geophysical Research: Atmospheres*, *103*(D11), 13137-13144. https://doi.org/10.1029/98jd00171

Mudelsee, M., & Schulz, M. (1997). The Mid-Pleistocene climate transition: Onset of 100 ka cycle lags ice volume build-up by 280 ka. *Earth and Planetary Science Letters*, *151*(1-2), 117-123. https://doi.org/10.1016/s0012-821x(97)00114-3

Mulitza, S., Heslop, D., Pittauerova, D., Fischer, H. W., Meyer, I., Stuut, J. B., et al. (2010). Increase in African dust flux at the onset of commercial agriculture in the Sahel region. *Nature*, *466*(7303), 226-228. https://doi.org/10.1038/ nature09213

Murat, A. (1999). Pliocene-Pleistocene occurrence of sapropels in the Western Mediterranean Sea and their relation to Eastern Mediterranean Sapropels. *Proceedings of the Ocean Drilling Program, Scientific Results* (vol. 161, pp. 519-527). Ocean Drilling Program, College Station, TX. https://doi.org/10.2973/odp.proc.sr.161.244.1999

Muxworthy, A. R., & Williams, W. (2009). Critical superparamagnetic/single-domain grain sizes in interacting magnetite particles: Implications for magnetosome crystals. *Journal of the Royal Society Interface*, *6*(41), 1207-1212. https://doi.org/10.1098/rsif.2008.0462

Muxworthy, A., Williams, W., & Virdee, D. (2003). Effect of magnetostatic interactions on the hysteresis parameters of single-domain and pseudo-single-domain grains. *Journal of Geophysical Research: Solid Earth*, *108*(B11). https://doi.org/10.1029/2003JB002588

Myers, P. G., Haines, K., & Rohling, E. J. (1998). Modeling the paleocirculation of the Mediterranean: The Last Glacial Maximum and the Holocene with emphasis on the formation of sapropel S1. *Paleoceanography*, *13*(6), 586-606. https://doi.org/10.1029/98PA02736

Nahon, D. (1980). Soil accumulations and climatic variations in western Sahara. *Palaeoecology of Africa and of the Surrounding Islands and Antarctica* (pp. 63-68). Balkema, Cape Town, South Africa.

Néel, L. (1936). Propriétés magnétiques de l'état métallique et énergie d'interaction entre atomes magnétiques. *Annales de Physique, 11*(5), 232-279. https://doi.org/10.1051/anphys/193611050232

Néel, L. (1948). Propriétés magnétiques des ferrites; ferrimagnétisme et antiferromagnétisme. *Annales de physique, 12*(3), 137-198. https://doi.org/10.1051/anphys/ 194812030137

Nijenhuis, I. A., Bosch, H. J., Damste, J. S. S., Brumsack, H. J., & de Lange, G. J. (1999). Organic matter and trace element rich sapropels and black shales: A geochemical comparison. *Earth and Planetary Science Letters*, *169*(3-4), 277-290. https://doi.org/10.1016/S0012-821x(99)00083-7

Nijenhuis, I. A., Schenau, S. J., Van der Weijden, C. H., Hilgen, F. J., Lourens, L. J., & Zachariasse, W. J. (1996). On the origin of upper Miocene sapropelites: A case study from the Faneromeni section, Crete (Greece). *Paleoceanography*, *11*, 633-645. https://doi.org/10.1029/96pa01963

O'Reilly, W. (1984). *Rock and Mineral Magnetism* (pp. 220). Glasgow, Blackie. https://doi.org/10.1007/978-1-4684-8468-7

Oldfield, F. (1991), Environmental magnetism – A personal perspective, *Quaternary Science Reviews*, *10*(1), 73-85. https://doi.org/10.1016/0277-3791(91)90031-O

Oldfield, F., Darnley, I., Yates, G., France, D. E., & Hilton, J. (1992). Storage diagenesis versus sulphide authigenesis: Possible implications in environmental magnetism. *Journal of Paleolimnology*, *7*(3), 179-189. https://doi.org/10.1007/bf00181713

Osborne, A. H., Vance, D., Rohling, E. J., Barton, N., Rogerson, M., & Fello, N. (2008). A humid corridor across the Sahara for the migration of early modern humans out

of Africa 120,000 years ago. *Proceedings of the National Academy of Sciences of the United States of America*, *105*(43), 16444-16447. https://doi.org/10.1073/pnas.0804472105

Özdemir, Ö., & Dunlop, D. J. (2010). Hallmarks of maghemitization in low-temperature remanence cycling of partially oxidized magnetite nanoparticles. *Journal of Geophysical Research: Solid Earth*, *115*(B2). https://doi.org/10.1029/2009JB006756

Özdemir, Ö., Dunlop, D. J., & Moskowitz, B. M. (1993). The effect of oxidation on the Verwey transition in magnetite. *Geophysical Research Letters*, *20*(16), 1671-1674. https://doi.org/10.1029/93GL01483

Pachur, H. J., & Hoelzmann, P. (2000). Late Quaternary palæoecology and palæoclimates of the eastern Sahara. *Journal of African Earth Sciences*, *30*(4), 929-939. https://doi.org/10.1016/S0899-5362(00)00061-0

Pan, Y., Petersen, N., Winklhofer, M., Davila, A. F., Liu, Q., Frederichs, T., et al. (2005). Rock magnetic properties of uncultured magnetotactic bacteria. *Earth and Planetary Science Letters*, *237*(3-4), 311-325. https://doi.org/10.1016/j.epsl.2005.06.029

Park, J., & Maasch, K. A. (1993). Plio-Pleistocene time evolution of the 100-kyr cycle in marine paleoclimate records. *Journal of Geophysical Research: Solid Earth*, *98*(B1), 447-461. https://doi.org/10.1029/92jb01815

Passier, H. D., de Lange, G. J., & Dekkers, M. J. (2001). Magnetic properties and geochemistry of the active oxidation front and the youngest sapropel in the eastern Mediterranean Sea. *Geophysical Journal International*, *145*(3), 604-614. https://doi.org/10.1046/j.0956-540x.2001.01394.x

Passier, H. F., & Dekkers, M. J. (2002). Iron oxide formation in the active oxidation front above sapropel S1 in the eastern Mediterranean Sea as derived from low-temperature magnetism. *Geophysical Journal International*, *150*(1), 230-240. https://doi.org/10.1046/j.1365-246X.2002.01704.x

Passier, H. F., Middelburg, J. J., de Lange, G. J., & Böttcher, M. E. (1999). Modes of sapropel formation in the eastern Mediterranean: Some constraints based on pyrite properties. *Marine Geology*, *153*(1-4), 199-219. https://doi.org/10.1016/S0025-3227(98)00081-4

Passier, H. F., Middelburg, J. J., van Os, B. J., & de Lange, G. J. (1996). Diagenetic

pyritisation under eastern Mediterranean sapropels caused by downward sulphide diffusion. *Geochimica et Cosmochimica Acta*, *60*(5), 751-763. https://doi.org/10.1016/0016-7037(95)00419-x

Peña, L. D., & Goldstein, S. L. (2014). Thermohaline circulation crisis and impacts during the mid-Pleistocene transition. *Science*, *345*(6194), 318-322. https://doi.org/10.1126/science.1249770

Petersen, N., von Dobeneck, T., & Vali, H. (1986). Fossil bacterial magnetite in deep-sea sediments from the South-Atlantic Ocean. *Nature*, *320*(6063), 611-615. https://doi.org/10.1038/320611a0

Petit, J. R., Briat, M., & Royer, A. (1981). Ice age aerosol content from East Antarctic ice core samples and past wind strength. *Nature*, *293*, 391-394. https://doi.org/10.1038/293391a0

Pike, C. R., Roberts, A. P., & Verosub, K. L. (1999). Characterizing interactions in fine magnetic particle systems using first order reversal curves. *Journal of Applied Physics*, *85*(9), 6660-6667. https://doi.org/10.1063/1.370176

Pinardi, N., & Masetti, E. (2000). Variability of the large scale general circulation of the Mediterranean Sea from observations and modelling: A review. *Palaeogeography, Palaeoclimatology, Palaeoecology*, *158*(3-4), 153-173. https://doi.org/10.1016/s0031-0182(00)00048-1

Pinardi, N., Zavatarelli, M., Adani, M., Coppini, G., Fratianni, C., Oddo, P., et al. (2015). Mediterranean Sea large-scale low-frequency ocean variability and water mass formation rates from 1987 to 2007: A retrospective analysis. *Progress in Oceanography*, *132*, 318-332. https://doi.org/10.1016/j.pocean.2013.11.003

Pisias, N. G., & Moore Jr, T. C. (1981). The evolution of Pleistocene climate: A time series approach. *Earth and Planetary Science Letters*, *52*(2), 450-458. https://doi.org/10.1016/0012-821x(81)90197-7

POEM group. (1992). General circulation of the eastern Mediterranean Sea. *Earth-Science Reviews*, *32*(4), 285-308. https://doi.org/10.3989/scimar.2006.70n3457

Pollard, D., & DeConto, R. M. (2009). Modelling West Antarctic ice sheet growth and collapse through the past five million years. *Nature*, *458*(7236), 329-332. https://doi.org/10.1038/nature07809

Pouillard, E. (1950). The behavior of alumina and titanium oxide with oxides of iron. *Annales de Chimie (Paris)*, *5*, 164-214.

Poulton, S. W., Krom, M. D., & Raiswell, R. (2004). A revised scheme for the reactivity of iron (oxyhydr) oxide minerals towards dissolved sulfide. *Geochimica et Cosmochimica Acta*, *68*(18), 3703-3715. https://doi.org/10.1016/j.gca.2004.03.012

Pruysers, P. A., de Lange, G. J., Middelburg, J. J., & Hydes, D. J. (1993). The diagenetic formation of metal-rich layers in sapropel-containing sediments in the eastern Mediterranean. *Geochimica et Cosmochimica Acta*, *57*(3), 527-536. https://doi.org/10.1016/0016-7037(93)90365-4

Qian, Y., Roberts, A. P., Liu, Y., Hu, P., Zhao, X., Heslop, D., et al. (2020). Assessment and integration of bulk and component-specific methods for identifying mineral magnetic assemblages in environmental magnetism. *Journal of Geophysical Research: Solid Earth*, *125*(8), e2019JB019024. https://doi.org/10.1029/2019JB019024

Raymo, M. E., & Horowitz, M. (1996). Organic carbon paleo-pCO_2 and marine-ice core correlations and chronology. *Geophysical Research Letters*, *23*(4), 367-370. https://doi.org/10.1029/96gl00254

Raymo, M. E., Lisiecki, L. E., & Nisancioglu, K. H. (2006). Plio-Pleistocene ice volume, Antarctic climate, and the global $\delta^{18}O$ record. *Science*, *313*(5786), 492-495. https://doi.org/10.1126/science.1123296

Rea, D. K. (1994). The paleoclimatic record provided by eolian deposition in the deep sea: The geologic history of wind. *Reviews of Geophysics*, *32*(2), 159-195. https://doi.org/10.1029/93RG03257

Reinholdsson, M., Snowball, I., Zillén, L., Lenz, C., & Conley, D. J. (2013). Magnetic enhancement of Baltic Sea sapropels by greigite magnetofossils. *Earth and Planetary Science Letters*, *366*, 137-150. https://doi.org/10.1016/j.epsl.2013.01.029

Ribera d'Alcalà, M., Civitarese, G., Conversano, F., & Lavezza, R. (2003). Nutrient ratios and fluxes hint at overlooked processes in the Mediterranean Sea. *Journal of Geophysical Research*, *108*(C9), 8106. https://doi.org/10.1029/2002jc0016 50

Richter, C., Hayashida, A., Guyodo, Y., Valet, J.-P., & Verosub, K. L. (1999). Magnetic intensity loss and core diagenesis in long-core samples from the East Cortez Basin and the San Nicolas Basin (California Borderland). *Earth Planets Space*, *51*, 329-336. https:// doi.org/10.1186/BF03352237

Ritchie, J. C., Eyles, C. H., & Haynes, C. V. (1985). Sediment and pollen evidence for an early to mid-Holocene humid period in the eastern Sahara. *Nature*, *314*(6009), 352-355. https://doi.org/10.1038/314352a0

Roberts, A. P. (1995). Magnetic properties of sedimentary greigite (Fe_3S_4). *Earth and Planetary Science Letters*, *134*(3), 227-236. https://doi.org/10.1016/0012-821x(95)00131-u

Roberts, A. P. (2015). Magnetic mineral diagenesis. *Earth-Science Reviews*, *151*, 1-47. https://doi.org/10.1016/j.earscirev.2015.09.010

Roberts, A. P., Almeida, T. P., Church, N. S., Harrison, R. J., Heslop, D., Li, Y., et al. (2017). Resolving the origin of pseudo-single domain magnetic behavior. *Journal of Geophysical Research: Solid Earth*, *122*(12), 9534-9558. https://doi.org/10.1002/2017jb014860

Roberts, A. P., Chang, L., Heslop, D., Florindo, F., & Larrasoaña, J. C. (2012). Searching for single domain magnetite in the "pseudo-single-domain" sedimentary haystack: Implications of biogenic magnetite preservation for sediment magnetism and relative paleointensity determinations. *Journal of Geophysical Research: Solid Earth*, *117*, B08104. https://doi.org/Artn B0810410.1029/2012jb009412

Roberts, A. P., Chang, L., Rowan, C. J., Horng, C. S., & Florindo, F. (2011a). Magnetic properties of sedimentary greigite (Fe_3S_4): An update. *Reviews of Geophysics*, *49*(1). https://doi.org/10.1029/2010RG000336

Roberts, A. P., Florindo, F., Villa, G., Chang, L., Jovane, L., Bohaty, S. M., et al. (2011b). Magnetotactic bacterial abundance in pelagic marine environments is limited by organic carbon flux and availability of dissolved iron. *Earth and Planetary Science Letters*, *310*(3-4), 441-452. https://doi.org/10.1016/j.epsl.2011.08.011

Roberts, A. P., Pike, C. R., & Verosub, K. L. (2000). First-order reversal curve diagrams: A new tool for characterizing the magnetic properties of natural samples. *Journal of Geophysical Research: Solid Earth*, *105*(B12), 28461-28475. https://doi.org/10.1029/2000JB900326

Roberts, A. P., Stoner, J. S., & Richter, C. (1999). Diagenetic magnetic enhancement of sapropels from the eastern Mediterranean Sea. *Marine Geology*, *153*(1-4), 103-116. https://doi.org/10.1016/S0025-3227(98)00087-5

Roberts, A. P., Tauxe, L., & Heslop, D. (2013). Magnetic paleointensity stratigraphy and high-resolution Quaternary geochronology: Successes and future challenges.

Quaternary Science Reviews, *61*, 1-16. https://doi.org/10.1016/j.quascirev.2012.10.036

Roberts, A. P., Zhao, X., Harrison, R. J., Heslop, D., Muxworthy, A. R., Rowan, C. J., et al. (2018). Signatures of reductive magnetic mineral diagenesis from unmixing of first-order reversal curves. *Journal of Geophysical Research: Solid Earth*, *123*(6), 4500-4522. https://doi.org/10.1029/2018jb015706

Robinson, S. G., Sahota, J. T., & Oldfield, F. (2000). Early diagenesis in North Atlantic abyssal plain sediments characterized by rock-magnetic and geochemical indices. *Marine Geology*, *163*(1-4), 77-107. https://doi.org/10.1016/s0025-3227(99)00108-5

Rochette, P., Fillion, G., & Dekkers, M. J. (2011). Interpretation of low-temperature data Part 4: The low-temperature magnetic transition of monoclinic pyrrhotite. *The IRM Quarterly*, *21*(1), 1-7.

Rochette, P., Fillion, G., Mattéi, J. L., & Dekkers, M. J. (1990). Magnetic transition at 30-34 Kelvin in pyrrhotite: Insight into a widespread occurrence of this mineral in rocks. *Earth and Planetary Science Letters*, *98*(3-4), 319-328. https://doi.org/10.1016/0012-821X(90)90034-U

Rogerson, M., Cacho, I., Jimenez-Espejo, F., Reguera, M. I., Sierro, F. J., Martinez-Ruiz, F., et al. (2008). A dynamic explanation for the origin of the western Mediterranean organic-rich layers. *Geochemistry*, *Geophysics*, *Geosystems*, *9*(7). https://doi.org/10.1029/2007gc001936

Rohling, E. J. (1994). Review and new aspects concerning the formation of eastern Mediterranean sapropels. *Marine Geology*, *122*(1-2), 1-28. https://doi.org/10.1016/0025-3227(94)90202-x

Rohling, E. J. (1999). Environmental control on Mediterranean salinity and $\delta^{18}O$. *Paleoceanography*, *14*(6), 706-715. https://doi.org/10.1029/1999PA900042

Rohling, E. J., & De Rijk, S. (1999a). Holocene Climate Optimum and Last Glacial Maximum in the Mediterranean: The marine oxygen isotope record. *Marine Geology*, *153*(1-4), 57-75. https://doi.org/10.1016/S0025-3227(98)00020-6

Rohling, E. J., & De Rijk, S. (1999b). Erratum to "Holocene climate optimum and last glacial maximum in the Mediterranean: The marine oxygen isotope record. *Marine Geology*, *161*(2-4), 385-387. https://doi.org/10.1016/s0025-3227(99)00083-3

Rohling, E. J., & Gieskes, W. W. (1989). Late Quaternary changes in Mediterranean intermediate water density and formation rate. *Paleoceanography*, *4*(5), 531-545. https://doi.org/10.1029/PA004i005p00531

Rohling, E. J., & Hilgen, F. J. (1991). The eastern Mediterranean climate at times of sapropel formation: A review. *Netherlands Journal of Geosciences/Geologie en Mijnbouw*, *70*, 253-264.

Rohling, E. J., & Thunell, R. C. (1999). Five decades of Mediterranean palaeoclimate and sapropel studies. *Marine Geology*, *153*(1-4), 7-10. https://doi.org/10.1016/s0025-3227(98)00093-0

Rohling, E. J., Abu-Zied, R., Casford, J. S. L., Hayes, A., & Hoogakker, B. A. A. (2009). The marine environment: Present and past. *The Physical Geography of the Mediterranean* (pp. 33-67). Oxford University Press, Oxford. https://doi.org/10.1093/oso/9780199268030.003.0012

Rohling, E. J., Cane, T. R., Cooke, S., Sprovieri, M., Bouloubassi, I., Emeis, K. C., et al. (2002a). African monsoon variability during the previous interglacial maximum. *Earth and Planetary Science Letters*, *202*(1), 61-75. https://doi.org/10.1016/s0012-821x(02)00775-6

Rohling, E. J., Kemp, A. E. S., Cooke, S., & Pearce, R. B. (2002b). High-resolution stratigraphic framework for Mediterranean sapropel S5: Defining temporal relationships between records of Eemian climate variability. *Palaeogeography, Palaeoclimatology, Palaeoecology*, *183*(1-2), 87-101. https://doi.org/10.1016/S0031-0182(01)00461-8

Rohling, E. J., Foster, G. L., Grant, K. M., Marino, G., Roberts, A. P., Tamisiea, M. E., et al. (2014). Sea-level and deep-sea-temperature variability over the past 5.3 million years. *Nature*, *508*(7497), 477-482. https://doi.org/10.1038/nature13230

Rohling, E. J., Grant, K. M., Roberts, A. P., & Larrasoaña, J. C. (2013). Paleoclimate variability in the Mediterranean and Red Sea regions during the last 500,000 years: Implications for hominin migrations. *Current Anthropology*, *54*(S8), S183-S201. https://doi.org/10.1086/673882

Rohling, E. J., Jorissen, F. J., & De Stigter, H. C. (1997). 200 year interruption of Holocene sapropel formation in the Adriatic Sea. *Journal of Micropalaeontology*, *16*(2), 97-108. https://doi.org/10.1144/jm.16.2.97

Rohling, E. J., Jorissen, F. J., Vergnaud-Grazzini, C., & Zachariasse, W. J. (1993). Northern Levantine and Adriatic Quaternary planktic foraminifera;

Reconstruction of paleoenvironmental gradients. *Marine Micropaleontology*, *21*(1-3), 191-218. https://doi.org/10.1016/0377-8398(93)90015-P

Rohling, E. J., Marino, G., & Grant, K. M. (2015). Mediterranean climate and oceanography, and the periodic development of anoxic events (sapropels). *Earth-Science Reviews*, *143*, 62-97. https://doi.org/10.1016/j.earscirev. 2015.01.008

Rohling, E. J., Medina-Elizalde, M., Shepherd, J. G., Siddall, M., & Stanford, J. D. (2012). Sea surface and high-latitude temperature sensitivity to radiative forcing of climate over several glacial cycles. *Journal of Climate, 25*, 1635-1656. https://doi.org/10.1175/2011jcli4078.1

Rohling, E. J., Sprovieri, M., Cane, T., Casford, J. S., Cooke, S., Bouloubassi, I., et al. (2004). Reconstructing past planktic foraminiferal habitats using stable isotope data: A case history for Mediterranean sapropel S5. *Marine Micropaleontology*, *50*(1-2), 89-123. https://doi.org/10.1016/S0377-8398(03)00068-9

Rossignol-Strick, M. (1983). African monsoons, an immediate climate response to orbital insolation. *Nature*, *304*(5921), 46-49. https://doi.org/10.1038/304046a0

Rossignol-Strick, M. (1985). Mediterranean Quaternary sapropels, an immediate response of the African monsoon to variation of insolation. *Palaeogeography*, *Palaeoclimatology*, *Palaeoecology*, *49*(3-4), 237-263. https://doi.org/10.1016 /0031-0182(85)90056-2

Rossignol-Strick, M. (1995). Sea-land correlation of pollen records in the eastern Mediterranean for the glacial-interglacial transition: Biostratigraphy versus radiometric time-scale. *Quaternary Science Reviews*, *14*(9), 893-915. https://doi.org/10.1016/0277-3791(95)00070-4

Rossignol-Strick, M. (1987). Rainy periods and bottom water stagnation initiating brine accumulation and metal concentrations: The late Quaternary. *Paleoceanography*, *2*(3), 333-360. https://doi.org/10.1029/PA002i003p00333

Rossignol-Strick, M., Nesteroff, W., Olive, P., & Vergnaud-Grazzini, C. (1982). After the deluge: Mediterranean stagnation and sapropel formation. *Nature*, *295*(5845), 105-110. https://doi.org/10.1038/295105a0

Rowan, C. J., Roberts, A. P., & Broadbent, T. (2009). Reductive diagenesis, magnetite dissolution, greigite growth and paleomagnetic smoothing in marine sediments: A new view. *Earth and Planetary Science Letters*, *277*(1-2), 223-235. https://doi.org/10.1016/j.epsl.2008.10.016

Rozanski, K. (1985). Deuterium and oxygen-18 in European groundwaters-Links to atmospheric circulation in the past. *Chemical Geology*, *52*(3-4), 349-363. https://doi.org/10.1016/0168-9622(85)90045-4

Ruddiman, W. F., Raymo, M., Martinson, D. G., Clement, B. M., & Backman, J. (1989). Pleistocene evolution: Northern hemisphere ice sheets and North Atlantic Ocean. *Paleoceanography*, *4*(4), 353-412. https://doi.org/10.1029/ pa004i004p00353

Ruddiman, W. F. (2011). *Earth's Climate: Past and future* (pp. 465). Macmillan Higher Freeman and Company, New York.

Rutherford, S., & D'Hondt, S. (2000). Early onset and tropical forcing of 100,000-year Pleistocene glacial cycles. *Nature*, *408*(6808), 72-75. https://doi.org/10.1038/ 35040533

Sakamoto, T., Janecek, T., & Emeis, K.-C. (1998). Continuous sedimentary sequences from the eastern Mediterranean Sea: Composite depth sections. *Proceedings of the Ocean Drilling Program*, *Scientific Results* (vol. 160, pp. 37-59). Ocean Drilling Program, College Station, TX.

Saltzman, B., & Maasch, K. A. (1991). A first-order global model of late Cenozoic climatic change II. Further analysis based on a simplification of CO_2 dynamics. *Climate Dynamics*, *5*(4), 201-210. https://doi.org/10.1007/bf00210005

Samuel, S., Haines, K., Josey, S., & Myers, P. G. (1999). Response of the Mediterranean Sea thermohaline circulation to observed changes in the winter wind stress field in the period 1980-1993. *Journal of Geophysical Research*, *104*(C4), 7771-7784. https://doi.org/10.1029/1998jc900130

Sassen, K., DeMott, P. J., Prospero, J. M., & Poellot, M. R. (2003). Saharan dust storms and indirect aerosol effects on clouds: Crystal-face results. *Geophysical Research Letters*, *30*(12). https://doi.org/10.1029/2003gl017371

Schefuß, E., Schouten, S., Jansen, J. H. F., & Damsté, J. S. S. (2003). African vegetation controlled by tropical sea surface temperatures in the mid-Pleistocene period. *Nature*, *422*(6930), 418-421. https://doi.org/10.1038/nature01500

Schenau, S. J., Antonarakou, A., Hilgen, F. J., Lourens, L. J., Nijenhuis, I. A., van der Weijden, C. H., & Zachariasse, W. J. (1999). Organic-rich layers in the Metochia section (Gavdos, Greece): Evidence for a single mechanism of sapropel formation during the past 10 My. *Marine Geology*, *153*(1-4), 117-135. https://doi.org/10.1016/S0025-3227(98)00086-3

Schiebel, R. & Hemleben, C. (2017). *Planktic Foraminifers in the Modern Ocean*. Springer, Berlin. https://doi.org/10.1007/978-3-662-50297-6

Schlitzer, R. (2014). Ocean Data View. http://odv.awi.de

Schmieder, F., von Dobeneck, T., & Bleil, U. (2000). The Mid-Pleistocene climate transition as documented in the deep South Atlantic Ocean: Initiation, interim state and terminal event. *Earth and Planetary Science Letters*, *179*(3-4), 539-549. https://doi.org/10.1016/S0012-821X(00)00143-6

Schmiedl, G., Mitschele, A., Beck, S., Emeis, K. C., Hemleben, C., Schulz, H., et al. (2003). Benthic foraminiferal record of ecosystem variability in the eastern Mediterranean Sea during times of sapropel S5 and S6 deposition. *Palaeogeography*, *Palaeoclimatology*, *Palaeoecology*, *190*, 139-164. https://doi.org/10.1016/s0031-0182(02)00603-x

Scrivner, A. E., Vance, D., & Rohling, E. J. (2004). New neodymium isotope data quantify Nile involvement in Mediterranean anoxic episodes. *Geology*, *32*(7), 565-568. https://doi.org/10.1130/G20419.1

Send, U., Font, J., Krahmann, G., Millot, C., Rhein, M., & Tintoré, J. (1999). Recent advances in observing the physical oceanography of the western Mediterranean Sea. *Progress in Oceanography*, *44*(1-3), 37-64. https://doi.org/10.1016/s0079-6611(99)00020-8

Sexton, P. F., & Barker, S. (2012). Onset of 'Pacific-style' deep-sea sedimentary carbonate cycles at the mid-Pleistocene transition. *Earth and Planetary Science Letters*, *321*, 81-94. https://doi.org/10.1016/j.epsl.2011.12.043

Shackleton, N. J. (1967). Oxygen isotope analyses and Pleistocene temperatures re-assessed. *Nature*, *215*(5096), 15-17. https://doi.org/10.1038/215015a0

Sierro, F. J., Flores, J. A., Zamarreno, I., Vázquez, A., Utrilla, R., Francés, G., et al. (1999). Messinian pre-evaporite sapropels and precession-induced oscillations in western Mediterranean climate. *Marine Geology*, *153*(1-4), 137-146. https://doi.org/10.1016/s0025-3227(98)00085-1

Smirnov, A. V., & Tarduno, J. A. (2000). Low-temperature magnetic properties of pelagic sediments (Ocean Drilling Program Site 805C): Tracers of maghemitization and magnetic mineral reduction. *Journal of Geophysical Research: Solid Earth*, *105*(B7), 16457-16471. https://doi.org/10.1029/2000JB900140

Smirnov, A. V., & Tarduno, J. A. (2001). Estimating superparamagnetism in marine sediments with the time dependency of coercivity of remanence. *Journal of Geophysical Research: Solid Earth*, *106*(B8), 16135-16143. https://doi.org/10.1029/2001JB000152

Smirnov, A. V., & Tarduno, J. A. (2002). Magnetic field control of the low-temperature magnetic properties of stoichiometric and cation-deficient magnetite. *Earth and Planetary Science Letters*, *194*(3-4), 359-368. https://doi.org/10.1016/S0012-821X(01)00575-1

Snowball, I. F. (1993). Geochemical control of magnetite dissolution in subarctic lake sediments and the implications for environmental magnetism. *Journal of Quaternary Science*, 8(4), 339-346. https://doi.org/10.1002/jqs.3390080405

Sonntag, C., Muennich, K. O., Junghans, C., Klitzsch, E., Thorweihe, U., Weistroffer, K., et al. (1979). Palaeoclimatic information from deuterium and oxygen-18 in carbon-14-dated north Saharan groundwaters. Groundwater formation in the past. *Isotope Hydrology 1978* (vol. 8, pp. 569-581). International Atomic Energy Agency, Vienna.

Sosdian, S., & Rosenthal, Y. (2009). Deep-sea temperature and ice volume changes across the Pliocene-Pleistocene climate transitions. *Science*, *325*(5938), 306-310. https://doi.org/10.1126/science.1169938

Spracklen, D. V., Carslaw, K. S., Kulmala, M., Kerminen, V. M., Sihto, S. L., Riipinen, I., et al. (2008). Contribution of particle formation to global cloud condensation nuclei concentrations. *Geophysical Research Letters, 35*(6). https://doi.org/10.1029/2007gl033038

Stoner, J. S., Richter, C., & Roberts, A. P. (1998). High resolution study of magnetic properties of sapropel-bearing sediments from ODP sites 966, 967, and 969, eastern Mediterranean Sea, *Proceedings of the Ocean Drilling Program*, *Scientific Results* (vol. 160, pp. 75-82). Ocean Drilling Program, College Station, TX.

Tarduno, J. A. (1995). Superparamagnetism and reduction diagenesis in pelagic sediments: Enhancement or depletion? *Geophysical Research Letters*, *22*(11), 1337-1340. https://doi.org/10.1029/95GL00888

Tarduno, J. A., & Wilkison, S. L. (1996). Non-steady state magnetic mineral reduction, chemical lock-in, and delayed remanence acquisition in pelagic sediments. *Earth and Planetary Science Letters*, *144*(3-4), 315-326. https://doi.org/

10.1016/s0012-821x(96)00174-4

Tauxe, L. (1993). Sedimentary records of relative paleointensity of the geomagnetic field: Theory and practice. Reviews of Geophysics, 31(3), 319-354. https://doi.org/10.1029/93RG01771

Tegen, I., Lacis, A. A., & Fung, I. (1996). The influence on climate forcing of mineral aerosols from disturbed soils. *Nature*, *380*(6573), 419-422. https://doi.org/10.1038/380419a0

Theocharis, A., Klein, B., Nittis, K., & Roether, W. (2002). Evolution and status of the Eastern Mediterranean Transient (1997-1999). *Journal of Marine Systems*, *33*, 91-116. https://doi.org/10.1016/s0924-7963(02)00054-4

Thompson, R., & Oldfield, F. (1986). *Environmental magnetism* (pp. 227). Allen and Unwin, London. https://doi.org/10.1007/978-94-011-8036-8_4

Thompson, R., Stober, J. C., Turner, G. M., Oldfield, F., Bloemendal, J., Dearing, J. A., & Rummery, T. A. (1980). Environmental applications of magnetic measurements. *Science*, *207*(4430), 481-486. https://doi.org/10.1126/science.207.4430.481

Thomson, J., Higgs, N. C., Wilson, T. R. S., Croudace, I. W., de Lange, G. J., & van Santvoort, P. J. M. (1995). Redistribution and geochemical behavior of redox-sensitive elements around S1, the most recent eastern Mediterranean sapropel. *Geochimica et Cosmochimica Acta*, *59*(17), 3487-3501. https://doi.org/10.1016/0016-7037(95)00232-O

Thomson, J., Mercone, D., de Lange, G. J., & Van Santvoort, P. J. M. (1999). Review of recent advances in the interpretation of eastern Mediterranean sapropel S1 from geochemical evidence. *Marine Geology*, *153*(1-4), 77-89. https://doi.org/10.1016/S0025-3227(98)00089-9

Timmermann, A., & Friedrich, T. (2016). Late Pleistocene climate drivers of early human migration. *Nature*, *538*(7623), 92-95. https://doi.org/10.1038/nature 19365

Torii, M. (1997). Low-temperature oxidation and subsequent downcore dissolution of magnetite in deep-sea sediments, ODP Leg 161 (Western Mediterranean). *Journal of Geomagnetism and Geoelectricity*, *49*(10), 1233-1245. https://doi.org/10.5636/jgg.49.1233

Trauth, M. H., Larrasoaña, J. C., & Mudelsee, M. (2009). Trends, rhythms and events in Plio-Pleistocene African climate. *Quaternary Science Reviews*, *28*(5-6), 399-411.

https://doi.org/10.1016/j.quascirev.2008.11.003

Trauth, M. H., Maslin, M. A., Deino, A. L., Strecker, M. R., Bergner, A. G., & Dühnforth, M. (2007). High-and low-latitude forcing of Plio-Pleistocene East African climate and human evolution. *Journal of Human Evolution*, *53*(5), 475-486. https://doi.org/10.1016/j.jhevol.2006.12.009

Vali, H., & Kirschvink, J. L. (1989). Magnetofossil dissolution in a palaeomagnetically unstable deep-sea sediment. *Nature*, *339*(6221), 203-206. https://doi.org/10.1038/339203a0

Van Hoof, A. A. M., Van Os, B. J. H., Rademakers, J. G., Langereis, C. G., & de Lange, G. J. (1993). A paleomagnetic and geochemical record of the upper Cochiti reversal and two subsequent precessional cycles from Southern Sicily (Italy). *Earth and Planetary Science Letters*, *117*(1-2), 235-250. https://doi.org/ 10.1016/0012-821X(93)90130-2

Van Santvoort, P. J. M., de Lange, G. J., Langereis, C. G., Dekkers, M. J., & Paterne, M. (1997). Geochemical and paleomagnetic evidence for the occurrence of "missing" sapropels in eastern Mediterranean sediments. *Paleoceanography*, *12*(6), 773-786. https://doi.org/10.1029/97PA01351

Van Santvoort, P. J. M., de Lange, G. J., Thomson, J., Cussen, H., Wilson, T. R. S., Krom, M. D., & Strohle, K. (1996). Active post-depositional oxidation of the most recent sapropel (S1) in sediments of the eastern Mediterranean Sea. *Geochimica et Cosmochimica Acta*, *60*(21), 4007-4024. https://doi.org/10.1016/S0016-7037(96)00253-0

Verosub, K. L., & Roberts, A. P. (1995). Environmental magnetism: Past, present, and future. *Journal of Geophysical Research: Solid Earth*, *100*(B2), 2175-2192. https://doi.org/10.1029/94JB02713

Verwey, E. J. W. (1939). Electronic conduction of magnetite (Fe_3O_4) and its transition point at low temperatures. *Nature*, *144*(3642), 327-328. https://doi.org/10.1038/144327b0

Wang, L. (2000). Isotopic signals in two morphotypes of *Globigerinoides ruber* (white) from the South China Sea: Implications for monsoon climate change during the last glacial cycle. *Palaeogeography*, *Palaeoclimatology*, *Palaeoecology*, *161*(3-4), 381-394. https://doi.org/10.1016/S0031-0182(00)00094-8

Warning, B., & Brumsack, H. J. (2000). Trace metal signatures of eastern Mediterranean sapropels. Palaeogeography, Palaeoclimatology, Palaeoecology, 158(3-4), 293-

309. https://doi.org/10.1016/S0031-0182(00)00055-9

Weeks, R., Laj, C., Endignoux, L., Fuller, M., Roberts, A., Manganne, R., et al. (1993). Improvements in long-core measurement techniques: Applications in palaeomagnetism and palaeoceanography. *Geophysical Journal International*, *114*(3), 651-662. https://doi.org/10.1111/j.1365-246X.1993.tb06994.x

Wehausen, R., & Brumsack, H. J. (1999). Cyclic variations in the chemical composition of eastern Mediterranean Pliocene sediments: A key for understanding sapropel formation. *Marine Geology*, *153*(1-4), 161-176. https://doi.org/10.1016/S0025-3227(98)00083-8

Wehausen, R., & Brumsack, H. J. (2000). Chemical cycles in Pliocene sapropel-bearing and sapropel-barren eastern Mediterranean sediments. *Palaeogeography*, *Palaeoclimatology*, *Palaeoecology*, *158*(3-4), 325-352. https://doi.org/10.1016/S0031-0182(00)00057-2

Weiss, B. P., Kim, S. S., Kirschvink, J. L., Kopp, R. E., Sankaran, M., Kobayashi, A., & Komeili, A. (2004). Ferromagnetic resonance and low-temperature magnetic tests for biogenic magnetite. *Earth and Planetary Science Letters*, *224*(1-2), 73-89. https://doi.org/10.1016/j.epsl.2004.04.024

Wolff, E. W., Fischer, H., Fundel, F., Ruth, U., Twarloh, B., Littot, G. C., et al. (2006). Southern Ocean sea-ice extent, productivity and iron flux over the past eight glacial cycles. *Nature*, *440*(7083), 491-496. https://doi.org/10.1038 /nature04614

Worm, H. U. (1998). On the superparamagnetic-stable single domain transition for magnetite, and frequency dependence of susceptibility. *Geophysical Journal International*, *133*(1), 201-206. https://doi.org/10.1046/j.1365-246X.1998.1331468.x

Wu, M., John, S. T., & Pan, Y. (2016). Electronic structures of greigite (Fe_3S_4): A hybrid functional study and prediction for a Verwey transition. *Scientific Reports*, *6*(1), 1-7. https://doi.org/10.1038/srep21637

Wüst, G. (1961). On the vertical circulation of the Mediterranean Sea. *Journal of Geophysical Research*, *66*(10), 3261-3271. https://doi.org/10.1029/JZ066i010p03261

Yamazaki, T. (2008). Magnetostatic interactions in deep-sea sediments inferred from first-order reversal curve diagrams: Implications for relative paleointensity

normalization. *Geochemistry*, *Geophysics*, *Geosystems*, *9*(2), Q02005. https://doi.org/10.1029/2007gc001797

Yamazaki, T. (2012). Paleoposition of the Intertropical Convergence Zone in the eastern Pacific inferred from glacial-interglacial changes in terrigenous and biogenic magnetic mineral fractions. *Geology*, *40*(2), 151-154. https://doi.org/10.1130/g32646.1

Yamazaki, T., & Ikehara, M. (2012). Origin of magnetic mineral concentration variation in the Southern Ocean. *Paleoceanography*, *27*(2). https://doi.org/10.1029/2011pa002271

Yamazaki, T., & Solheid, P. (2011). Maghemite-to-magnetite reduction across the Fe-redox boundary in a sediment core from the Ontong-Java Plateau: Influence on relative palaeointensity estimation and environmental magnetic application. *Geophysical Journal International*, *185*(3), 1243-1254. https://doi.org/10.1111/j.1365-246x.2011.05021.x

Yan, L., Zhang, S., Chen, P., Liu, H., Yin, H., & Li, H. (2012). Magnetotactic bacteria, magnetosomes and their application. *Microbiological Research*, *167*(9), 507-519. https://doi.org/10.1016/j.micres.2012.04.002

Zhao, X., Heslop, D., & Roberts, A. P. (2015). A protocol for variable-resolution first-order reversal curve measurements. *Geochemistry*, *Geophysics*, *Geosystems*, *16*(5), 1364-1377. https://doi.org/10.1002/2014gc005680

Zhao, X., Roberts, A. P., Heslop, D., Paterson, G. A., Li, Y., & Li, J. (2017), Magnetic domain state diagnosis using hysteresis reversal curves, *Journal of Geophysical Research: Solid Earth*, *122*, 4767-4789. https://doi.org/10.1002/2016JB013683